



# MBE Growth and Characterization of Multilayer Structures for Vertically Emitting Laser Devices

## **DISSERTATION**

to obtain the academic degree of

## **DOKTOR-INGENIEUR (DR.-ING.)**

from the Faculty of Engineering Science and Computer Sciences  
Ulm University

by

**Fernando Rinaldi**  
**from Catanzaro, Italy**

Referees: Prof. Dr. rer. nat. Peter Unger  
Prof. Carl E. Krill III, Ph.D.

Dean of the faculty: Prof. Dr. rer. nat. Helmuth Partsch

Oral examination: Ulm, April 23rd, 2008

To Antje, the woman I love.

# Abstract

This work concerns molecular beam epitaxy (MBE) growth and characterization of multilayer structures for vertically emitting laser devices. In particular, this thesis is focused on the fabrication of novel VCSEL (vertical-cavity surface-emitting laser) and VECSEL (vertical-external-cavity surface-emitting laser) multilayer structures grown on GaAs substrate.

Several VCSEL structures for emitting wavelengths of 760, 850, and 980 nm were realized and the corresponding devices show high performance and have direct technological applications. As example, single-mode 760 nm VCSELs are successfully employed in oxygen sensing, or integrated VCSELs-photodetector systems allow bidirectional data transmission in full-duplex mode at 2.5 Gbit/s over 50 m graded-index multimode fiber.

As far as regard VECSELs, samples for devices having emitting wavelengths of 850 nm and 980 nm were produced. High-performance 850 nm quantum-well-pumped VECSELs having a slope efficiency of 67% were demonstrated.

The calibration techniques of the MBE system are described and applied to the practical cases of the growth of complex laser structures, therefore, an important part of this work is devoted to HRXRD (high-resolution x-ray diffraction) analysis of the grown samples. This is a powerful tool to characterize not only the strain configuration and the compositional profile of the layers, but also to indirectly monitor the molecular fluxes improving the reliability of the MBE system.

# Acknowledgment

It is a pleasure for me to salute all the people that made possible the realization of this work. I start with Frank Demaria, Ihab Kardosh, and Steffen Lorch, they are the special friends I found in the Institute of Optoelectronics. For us there was no separation between work and freetime, between work and fun. I wish everybody to find friends like them. Also my thanks go to Dr. Manfred Mundbrod, he used to motivate me and he really understood me.

A special thank goes to Susanne Menzel, we work close together since many years. I learned everything about MBE exclusively from her, and this was a luck, because nobody else has so much experience and so much understanding of this technique. I am also very thankful to Michael Riedl, we spent together so much time on the MBE, that still runs because Michael worked so hard also for me. I cannot forget Dr. Wladimir Schoch, he is always ready to help me, to give good advice, and share his experience.

This thesis is ready just because all my colleagues transformed the samples I grew in high-performance devices, these are Frank Demaria, Ihab Kardosh, Andrea Kroner, Martin Stach, Abdel Sattar, Hendrik Roscher, Wolfgang Schwarz and were (because they are already "Doktoren") Dr. Eckart Gester, Dr. Manmohan Singh, Dr. Johannes Michael Ostermann and of course again the master of coatings Dr. Steffen Lorch. I am also thankful to Ivan Savonov, Dr. Uwe Brauch from the University of Stuttgart for sharing with us his expertise, and to Benjamin Scherer from the Fraunhofer-Institut in Freiburg.

Other people helped me and supported me everyday, like Sükran Kilic, who used to cheer me up very often, and Rudolf Rösch, who is the kind of person one can trust completely.

I am grateful to the Prof. Ferdinand Scholz and to all the other members of the GaN group for the support they gave me all over the years, especially Peter Brückner and Joachim Hertkorn.

So many students worked close to me as tight team, they are so many that I cannot list them all, I want to make an exception for Onur Atilla, I thank him for the work he did programming the  $p$ -doping control of the MBE I and for being my friend.

I still want to remember Dr. James O'Callaghan and Dr. Vincent Voignier, we had a great time together.

I want to mention Shunyi Li, who had the misfortune of being my first and only student I ever had. He had to stand and tolerate my egocentrism, my disorganization, and my mood.

In this page there is obviously a place for Dietmar Wahl, we really have so much fun working together, even though I can be arrogant, I hope he will forgive me for that. I learned from him the basics of quantum dots and many other things.

I am so thankful to Dr. Rainer Michalzik for all the aid he gives to me in the V.O.I. group and the work and time he spent with me bringing always new ideas.

To conclude, I am happy to greet my Professor, Prof. Peter Unger, who trusted in me, giving me all the assistance I need and also the freedom in my work.

My life it is not just work, I also had my life outside the Institute. Therefore, I should mention the complete Hagen family, and between them Martin, Andrea, Sabine

and Markus, these are people I can rely on, and they were my first German friends together with Frank Fiedler, now on his way in Sweden.

A special place is reserved for Stephanie Wagner for staying always close to me. We are the best friends one can imagine, and I feel I am a part of her family. It is really not possible to express her my gratitude in this few lines.

I think I should apologize for my bad English, but nobody was happy when I propose to write this work in Italian!

The last line is dedicated to my family, who tried to encourage me despite the distance.



# Contents

<b>1</b>	<b>Introduction</b>	<b>1</b>
1.1	Motivation . . . . .	1
1.2	Structure of the thesis . . . . .	1
1.3	Remarks . . . . .	2
<b>2</b>	<b>Basics of molecular beam epitaxy</b>	<b>4</b>
2.1	Overview of the MBE apparatus . . . . .	4
2.2	Effusion cells . . . . .	5
2.3	Thermodynamic approach . . . . .	7
<b>3</b>	<b>Elasticity and physical properties in crystals</b>	<b>12</b>
3.1	The strain tensor . . . . .	12
3.2	The stress tensor . . . . .	14
3.3	Hooke's law in crystals . . . . .	15
3.4	The $c$ and $s$ tensors in cubic crystals . . . . .	16
3.5	The Poisson's ratio . . . . .	18
3.6	Pseudomorphic (001) growth . . . . .	19
3.7	The wafer bowing . . . . .	21
3.8	Critical thickness and strain compensation . . . . .	25
3.9	Nonlinear optical crystals . . . . .	29
<b>4</b>	<b>Basics of VCSELs and VECSELs</b>	<b>33</b>
4.1	VCSELs . . . . .	33
4.2	VECSELs or semiconductor disk lasers . . . . .	35
4.3	Fresnel's formulae . . . . .	36
4.4	Multilayers, the transfer-matrix method . . . . .	38
<b>5</b>	<b>Basic x-ray diffraction theory</b>	<b>41</b>
5.1	X-ray reflectometry . . . . .	41
5.2	Dynamical theory of x-ray diffraction . . . . .	46
5.3	Detection of thin layers . . . . .	47
<b>6</b>	<b>The molecular beam epitaxy system</b>	<b>50</b>
6.1	Introduction . . . . .	50
6.2	The effusion cells . . . . .	52
6.3	Calibration of the sources . . . . .	54

6.4	Calibration of the growth rates . . . . .	55
6.5	AlGaAs calibrations based on photoluminescence . . . . .	59
6.6	Growth rate profile . . . . .	62
6.7	Pyrometer . . . . .	63
6.8	Doping calibration . . . . .	63
6.9	The arsenic source . . . . .	66
6.10	Residual gas analyzer (RGA) . . . . .	67
<b>7</b>	<b>Reflection high-energy electron diffraction</b>	<b>73</b>
7.1	Electron wavelength . . . . .	73
7.2	Kinematical approach to RHEED . . . . .	74
7.3	RHEED patterns on GaAs (001) . . . . .	75
<b>8</b>	<b>High Performance VCSELs emitting at 760 nm</b>	<b>82</b>
8.1	Introduction . . . . .	82
8.2	Layer structure . . . . .	83
8.3	Wafer-level characterization . . . . .	83
8.4	Lasers fabrication . . . . .	85
8.5	Standard and inverted relief 760 nm VCSELs . . . . .	85
8.6	Inverted grating relief 760 nm VCSELs . . . . .	88
8.7	Oxygen sensing . . . . .	90
<b>9</b>	<b>VCSEL devices emitting at 850 nm</b>	<b>94</b>
9.1	High-power single-mode 850 nm VCSELs . . . . .	94
9.2	Monolithically integrated transceivers . . . . .	97
9.3	Flip-chip highly packed VCSEL arrays . . . . .	101
9.4	The real VCSELs profile . . . . .	102
<b>10</b>	<b>VCSEL devices emitting at 980 nm</b>	<b>109</b>
10.1	VCSEL layer structure for 980 nm emission . . . . .	109
10.2	Fabrication and performances of the devices . . . . .	110
10.3	Electrically pumped VECSELs . . . . .	111
<b>11</b>	<b>VECSELs</b>	<b>114</b>
11.1	Device design and fabrication . . . . .	114
11.2	Quantum well pumped VECSELs . . . . .	117
11.3	HRXRD on VECSELs, a special case . . . . .	120
<b>12</b>	<b>Conclusions</b>	<b>122</b>
<b>A</b>	<b>Publications</b>	<b>124</b>
	<b>Bibliography</b>	<b>129</b>



# Chapter 1

## Introduction

This work regards the growth and characterization of semiconductor laser structures by means of molecular beam epitaxy (MBE). The growth process is based on the GaAs technology.

### 1.1 Motivation

Since their development, semiconductor laser devices have been used for a vast range of applications, like data storage or transmission, laser printing, high-performance light source, projection, gas sensing, micromanipulation, and more. This wide range of applications justifies the enormous effort to improve the performances of these devices.

The largest class of semiconductor laser devices technology is based on GaAs and its corresponding AlGaAs alloy. This alloy has the unique feature of being almost lattice matched to GaAs, making these materials perfect for the growth of complex multilayer structures.

Despite the proliferation of commercially available GaAs-based semiconductor lasers, there is a huge interest to investigate novel device structures or tailor the characteristics of the ones already known for specific applications. In fact, even minor design changes can dramatically vary the characteristics and performances of the device. However, this type of study requires the new growth of the structures with the same quality of the ones produced by the large industrial facilities. In addition, the versatility of the experimental setup is not always available in a production line and this type of investigation is only possible in a research laboratory.

The aim of the work described in this thesis is the the creation of new device structures and their improvement for novel applications. New structures were grown by MBE and characterized with various experimental techniques.

### 1.2 Structure of the thesis

In chapter 2, a basic and general introduction to the MBE technique is given, pointing the attention to the III/V compound semiconductors. Furthermore in this chapter, a detailed description of the effusion cells, that are key components in a MBE apparatus,

is reported. It follows an analysis of the growth process based on a thermodynamical approach.

Chapter 3 discusses the fundamentals of the theory of elasticity applied to crystals by means of the tensor formalism. These concepts allow a quantitative description of the crystal configuration in multilayer systems grown pseudomorphically. In addition to this, it is reported the calculation of the wafer bowing supported by experimental results and a theoretical analysis of the strain compensation. A brief mention is also given to the rank 3 tensor which is introduced to describe the susceptibility of the non-linear crystals that are used for frequency doubling at optical wavelengths.

Chapter 4 focuses on the theoretical description of vertical-cavity surface-emitting lasers (VCSELs) and vertical-external-cavity surface-emitting lasers (VECSELs). The transfer-matrix method for electromagnetic wave propagation in dielectrics is also reviewed.

In chapter 5, the dynamical theory of x-ray diffraction is introduced. This theory has been chosen, in this work, as a physical model to achieve accurate quantitative results, using a transfer-matrix method similar to the one introduced in chapter 4. The x-ray reflectometry (XRR) is reviewed since this technique is used to characterize metals or amorphous layers such as oxides.

The MBE apparatus used in this work are described extensively in chapter 6. Emphasis is given to the material sources and calibration methods.

Chapter 7 is dedicated to reflection high-energy electron diffraction (RHEED) that is conventionally used to monitor the growth. The main RHEED patterns related to the GaAs (001) surface are reported and discussed.

In chapters 8, 9, 10, and 11 the fabrication of the devices and their characterization are described. The chapters 8 and 9 are dedicated to the performance of VCSELs emitting at 760 and 850 nm including a detailed high-resolution x-ray diffraction (HRXRD) analysis of the compositional profile. In chapter 10, VCSELs and electrically pumped VECSELs (emission at 980 nm) are described with particular interest to the HRXRD characterization.

Similarly, several optically pumped VECSELs and their HRXRD characterization, are presented in chapter 11.

The last chapter summarizes the main results and the achieved goals.

## 1.3 Remarks

The experiments, the growth of the samples, and devices, that are described in this work were performed in the Institute of Optoelectronics at the Ulm University, while the characterization of processed quantum-well-pumped VECSELs devices was carried out in the Institute für Strahlwerkzeuge by Dr. Uwe Brauch at the University of Stuttgart. Oxygen absorption spectroscopy experiments, described in chapter 8, were performed, instead, in the Fraunhofer Institut für physikalische Messtechnik in Freiburg by Benjamin Scherer and Dr. J. Wöllenstein. The samples containing phosphorus were grown by M. C. Riedl.

The fabrication and the characterization of a finished semiconductor laser device is a complex multi-step process that includes the design of the device structure, the growth of

the sample, the characterization of the sample and the finished device. The work of the author consisted in the design, the growth and characterization of the structures used for the finished devices that were tested separately. It follows that the work described here is the result of a continuous feedback with the rest of the group.

# Chapter 2

## Basics of molecular beam epitaxy

In this chapter is given a general description of the molecular beam epitaxy (MBE) system, followed by a thermodynamic description of the growth process.

### 2.1 Overview of the MBE apparatus

Molecular beam epitaxy is a technique for epitaxial growth via the interaction of one or several atomic/molecular beams that occurs on the surface of a crystalline substrate.

In Fig. 2.1 is shown a scheme of a typical MBE system. The apparatus consists of an ultra-vacuum chamber in which there are several material sources that provide the molecular beams that hit the sample that is kept under temperature control. When needed, the sample is maintained in rotation to improve the growth homogeneity.

The molecular beam condition, for which the mean free path  $\lambda$  of the particles has to be larger than the geometrical size of the chamber, is easily fulfilled if the total pressure does not exceed  $10^{-5}$  Torr (Fig. 2.2). However, effective MBE growth is obtained when the condition for sufficiently clean epilayer is satisfied. This occurs when the monolayer deposition time of the beam  $t_b$  is sufficiently smaller than the one corresponding to the background residual vapor  $t_{\text{res}}$ , e.g.,  $t_b < 10^{-5} t_{\text{res}}$ . For example, for a typical flux of gallium of  $10^{19} \text{ atoms m}^{-2} \text{ s}^{-1}$  corresponding to a growth rate of the order of  $1 \mu\text{m/h}$ , the condition for a clean epilayer is that  $p_{\text{res}} < 10^{-11}$  Torr. Since the fraction of the gallium atoms that “stick” on the substrate is, in normal operating conditions, approximately 1, in opposition to the sticking coefficient of most of the typical residual gas species which is much lower, the condition above results to be not so stringent, nevertheless ultra-high vacuum (UHV) is required.

Therefore, the rate of gas evolution from the components of the chamber has to be controlled and reduced as much as possible. For example, pyrolytic boron nitride (pBN) is typically chosen for the crucibles since it gives low rate of gas evolution and chemical stability up to  $1400^\circ\text{C}$ . Molybdenum and tantalum are, instead, widely used for shutters, heaters and other components, and only ultrapure materials are used as source. Furthermore, whenever the system has been vented for maintenance, a bakeout of the whole chamber for 24 h at almost  $200^\circ\text{C}$  is required. A liquid nitrogen cryogenic screening around the substrate minimizes spurious fluxes of molecules from the walls of the chamber.

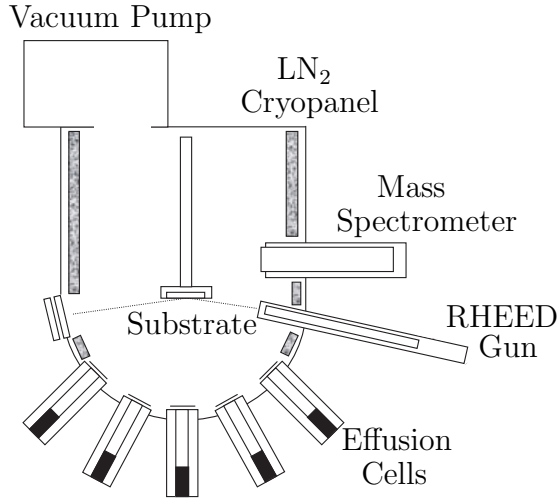
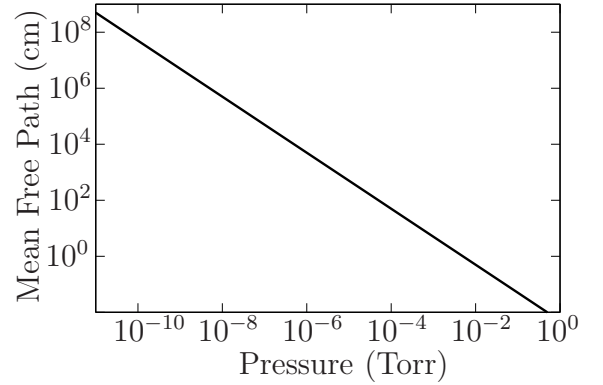


Figure 2.1: A typical MBE system.

Figure 2.2: Mean free path  $\lambda$  for nitrogen molecules at 300 K.

The MBE system allows a fine control of composition and doping of the growing structure at monolayer level. The composition of the incoming beam is controlled by mechanical shutters whose operation time (approximately 0.1 s) is normally much shorter than the time needed to grow one monolayer (typically 1–5 s). The temperatures of the effusion cells, adjusted by PID controllers, tunes the intensity of the fluxes of any single molecular species with a precision better than 1%.

Unlike other growth techniques, like chemical vapor deposition (CVD), the UHV environment allows the use of many in-situ characterization tools as, for example, reflection high-energy electron diffraction (RHEED), whose signal oscillation correspond to the time needed to grow a monolayer. Furthermore, the diffraction pattern on the RHEED window gives a direct indication of the surface morphology (chapter 7).

## 2.2 Effusion cells

The effusion cells are essentially the crucibles where the source materials are placed and are thermally evaporated to generate the molecular flux. The evaporation process from a realistic effusion cell is extremely complicated, but can be effectively described with a simplified ideal model, i.e., the Knudsen cell, or if necessary, taking into account the characteristics of a realistic cell.

In a closed enclosure, for pure substances, an equilibrium is established between the gas and the condensed phase. Such systems have only one degree of freedom, and the pressure  $p_{\text{eq}}$  is a function of the absolute temperature  $T$  and can be approximately expressed by the Clapeyron equation [1]

$$p_{\text{eq}}(T) = C \exp\left(-\frac{\Delta H}{k_B T}\right), \quad (2.1)$$

where  $\Delta H$  is the evaporation enthalpy and  $k_B$  the Boltzmann constant. Under this

equilibrium condition, when the  $p_{\text{eq}}$  is sufficiently low, it is possible to treat independently the incoming and outgoing fluxes at the interface between gas and condensed phase. The maximum value for the outgoing flux  $\Gamma_{\text{m}}$  is given by [2]

$$\Gamma_{\text{m}} = \frac{p_{\text{eq}}}{\sqrt{2\pi m k_{\text{B}} T}} \quad (2.2)$$

where  $m$  is the mass of the evaporated particle. This follows from the assumption that each molecule from the gas phase is trapped by the surface and an equal opposite flux leaves the condensed phase to maintain the equilibrium pressure. If the impinging beam is partially reflected, then only a fraction  $a$  is accommodated on the surface and the flux leaving the surface is

$$\Gamma = a \Gamma_{\text{m}}. \quad (2.3)$$

The factor  $a$  depends on the microscopic state of the surface and is practically unpredictable and as consequence the flux of material  $\Gamma$ .

The Knudsen evaporating method overcomes this problem providing a molecular beam that is independent of  $a$ . An ideal Knudsen cell is a large enclosure where the condensed material is in thermodynamic equilibrium with the gas phase and the molecular flux flows out from an orifice so small that the equilibrium pressure  $p_{\text{eq}}$  is not perturbed. Therefore, the orifice diameter  $d$  has to fulfill the condition  $d \ll \lambda$  at  $p_{\text{eq}}$ , and the enclosure wall thickness  $L$  has to be infinitely thin. Under these conditions, the orifice is a surface with an evaporating pressure  $p_{\text{eq}}$  and does not reflect the incoming molecules, resulting in  $a = 1$ . According to this, the number of molecules per unit of time of the outgoing beam is  $\Gamma_{\text{m}}$ .

The ideal Knudsen cell exhibits an angular distribution of the fluxes of the evaporated particles that follows the cosine law

$$\frac{d\Gamma_{\theta}}{d\Omega} = \frac{\Gamma_{\text{m}}}{\pi} \cos \theta, \quad (2.4)$$

where the angle  $\theta$  is referred to the normal to the orifice area. Using the Clausing's model [3], for the conductance of a molecular flow in a cylindrical tube, Dayton has studied the deviation from ideality given when  $L/d$  is not longer 0. In this model the interaction of the molecules with the orifice walls is described by random reflections. However, a more complicated model, that involves temporary adsorption and surface diffusion, has also been developed [4], but an estimation of  $a$  for the surface of the condensed material is still not required. When  $L/d$  increases, the beam is more focused on the normal direction and already for  $L/d = 1$  the deviation from the cosine law is relevant. These models are important tools to measure  $p_{\text{eq}}$  and  $\Delta H$  starting from the equation (2.1).

Instead, the value of the coefficient  $a$  is needed when it is not possible to consider the enclosure as infinitely large and it is therefore important to take into account the influences of the main body of the cell [5]. This is the case of cylindrical and conical cells, that are widely used in actual MBE systems. Using the aforementioned models, it is possible to estimate the angular distribution of the outgoing vapor beam, when the factor  $a$  is assumed to be homogeneous on the condensed phase material surface. Many variables describing the cell geometry are involved in this problem, like shown in Fig. 2.3.

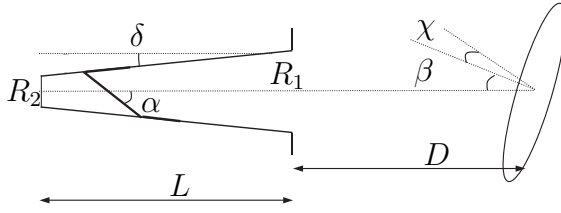


Figure 2.3: Example of the geometrical configuration for a conical effusion cell.

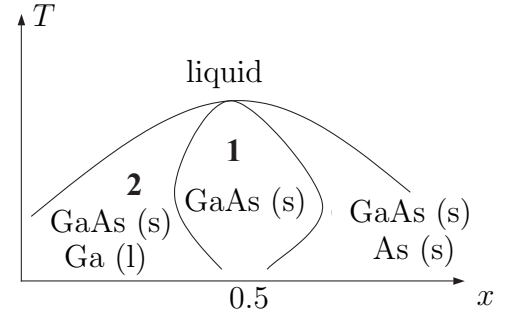


Figure 2.4: Simplified phase diagram ( $T$ – $x$  section) for GaAs. (s) is the solid and (l) is liquid phase. A gas phase is always present.

For example, very often the source material is in liquid form (gallium, aluminum, indium) and so an additional angle  $\alpha$  is required to set up the geometry of the cell. Some materials wet the crucible surface (e.g., aluminum in pBN crucibles), so other variables are needed to specify the position of the evaporating surface.

A complex work of optimization is therefore necessary in relation to the fact that in a MBE system many cells operate and for each one a suitable geometrical configuration cell–substrate must be properly chosen. Control and homogeneity of the cell temperatures are crucial, because of the strong dependence of the flux on temperature. Therefore, W-Re thermocouples are used due to their chemical stability at high temperatures and their very low outgassing rates. Tantalum heater elements and radiative shields are chosen by virtue of the excellent refractory property of this metal. These elements are often self-supporting preventing the use of material that does not have such low rate of gas evolution. Great care is also needed to decrease the temperature difference between heater and crucible. This is necessary to avoid very high temperature outgassing from tantalum, and to reduce the dissipated heat, which causes possible uncontrolled outgassing from other parts of the vacuum chamber.

## 2.3 Thermodynamic approach

In the 1980s, MBE was developing experimentally very successfully and most of the problems, particularly regarding AlGaAs and InGaAlAs materials, were solved empirically. But in recent years, the need for MBE growth with newer materials revealed the importance of a closer theoretical modeling, like the possibility of applying thermodynamics to the growth processes in MBE.

In the case of MBE, it may seem that the system cannot be described by a thermodynamic representation because the different components, like sources, substrate, and chamber walls, are at different temperatures. However, if the thermalization time is much shorter than the time required to grow a monolayer, it is possible to assume that the temperature of the system is equal to the temperature of the substrate. Consequently, it

is considered an equilibrium state in which the partial pressures are the ones relative to fluxes of atoms/molecules leaving the substrates surface at its temperature. This assumption is confirmed by observing that the fluxes of atoms/molecules leaving the substrate have its temperature, irrespective of the temperature of the fluxes arriving at the surface and furthermore, in the GaAs system, the nature of the arsenic molecules leaving the substrate is independent of the nature of the arsenic molecules that reach the surface. In this case, the dissociation reaction of the arsenic tetramers has to be considered together with the relative mass action equation [6]

$$2\text{As}_2(\text{g}) \rightleftharpoons \text{As}_4(\text{g}) \quad \text{and} \quad p_{\text{As}_2}^2 p_{\text{As}_4}^{-1} = 3.97 \times 10^8 \exp\left(-\frac{2.35 \text{ eV}}{k_B T}\right) \text{ atm}, \quad (2.5)$$

where the pressures are measured in atmospheres and  $k_B T$  in eV. The dimeric fraction of arsenic molecules leaving the substrate follows exactly the temperature behavior predicted by (2.5) [7].

Starting by these assumptions, it is possible to model the basic behavior of the III/V binary compounds under MBE working conditions. For a binary compound the  $x - T$  phase diagram, like the one sketched for GaAs in Fig. 2.4, must be considered, where  $x$  is the gallium molar fraction and  $T$  is the absolute temperature. In the region labeled with 1 GaAs(s) is present in equilibrium with Ga(g), As<sub>2</sub>(g), and As<sub>4</sub>(g). A small deviation from the Ga<sub>0.5</sub>As<sub>0.5</sub> stoichiometry is possible via the presence of point defects that is always much smaller than  $10^{-4}$  even at high temperatures, this is exaggerated in the figure. Using the Gibbs' phase rule  $f = c - p + 2$  [8], that relates the number of components  $c$  and the number of different phases  $p$  to the number of degrees of freedom  $f$ , it is easy to recognize that in the region 1 of the phase diagram  $f = 2$ . Therefore, temperature and pressure are independent. In region 2, liquid gallium is present and hence  $f = 1$  as three phases are present. Consequently a function  $p = p(T)$  exists. In the region 1, the reactions between the components are



and the relative mass action equations is given by

$$p_{\text{Ga}} p_{\text{As}_2}^{\frac{1}{2}} = K_{\text{GaAs}} = 2.73 \times 10^{11} \exp\left(-\frac{4.72 \text{ eV}}{k_B T}\right) \text{ atm}^{3/2}, \quad (2.7)$$

that should be fulfilled together with (2.5).

Under normal MBE growth conditions, i.e., when  $T > 450^\circ\text{C}$ , it is possible to neglect the  $p_{\text{As}_4}$  contribution to the total pressure  $p_T$ . Therefore, the total pressure is given by

$$p_T = p_{\text{Ga}} + p_{\text{As}_2} = \frac{K_{\text{GaAs}}}{p_{\text{As}_2}^{\frac{1}{2}}} + p_{\text{As}_2}. \quad (2.8)$$

The gallium pressure is maximum on the left side of the diagram in Fig. 2.4, where it corresponds to the gallium vapor pressure on pure liquid gallium. Moving to the right, because of (2.7), the partial pressure decreases while the arsenic pressure increases.



For some range in temperature, the total pressure exhibits a minimum for a suitable stoichiometry of the solid phase. This minimum condition has to be applied to find the flux in free sublimation, i.e., sublimation in vacuum.

The reason for the minimum condition is very general [9]. In a compound  $A_xB_{1-x}$ , the total pressure is the sum of the pressures of its components. If the partial pressure of the component B is bigger than the one of the component A, the composition of the condensed phase will be enriched with A, moving the system to a lower partial pressure. If a minimum total pressure for a certain  $x$  exists, this will be asymptotically reached. In this point the sublimation is congruent. In the case of GaAs, the equation for a minimum of the pressure is

$$\frac{dp_T}{dp_{\text{As}_2}} = \frac{dp_T}{dp_{\text{Ga}}} = 0. \quad (2.9)$$

Solving this equation together with the formula (2.8) brings to

$$p_{\text{Ga}}^s = 2 p_{\text{As}_2}^s = (2 K_{\text{GaAs}}^2)^{\frac{1}{3}}, \quad (2.10)$$

where the superscript "s" indicates free sublimation. This last result corresponds to congruent sublimation of GaAs. When the temperature increases over a certain temperature  $T_{\text{max}}$ , the pressure of the more volatile component, in this case arsenic, increases faster and there will be no minimum in the region 1. Under this condition, a liquid gallium phase is created. The temperature  $T_{\text{max}}$  is called "temperature of maximum sublimation".  $T_{\text{max}}$  is calculated imposing  $p_{\text{Ga}}^s$  from (2.10) equal to the value of the gallium pressure over the liquid gallium

$$p_{\text{Ga}}^L = 2.88 \times 10^5 \exp\left(-\frac{2.74 \text{ eV}}{k_B T}\right) \text{ atm}. \quad (2.11)$$

The value of  $T_{\text{max}}$  is approximately 630 °C, and the GaAs free sublimation rate is so given by

$$v = -V \frac{p_{\text{Ga}}^s}{\sqrt{2 \pi m_{\text{Ga}} k_B T}}, \quad (2.12)$$

where  $p_{\text{Ga}}^s$  is defined by (2.10) and  $V$  is the volume occupied by a pair of gallium and arsenic atoms in GaAs and it is equal to  $a^3/4$ , where 4 is the number of gallium and arsenic atoms present in the zinc blende GaAs structure and  $a$  is its lattice constant. The negative sign in front of (2.12) indicates that material is lost from the crystal. It is important to emphasize that, in the previous calculations, the sticking coefficient of gallium on an atomically clean GaAs surface is assumed  $\approx 1$ , indeed the outcoming flux, and so the related pressure, is always given by (2.3).

For many important binary compounds, equations like (2.11) can be used to calculate the  $T_{\text{max}}$  as summarized in Tab. 2.1.

When an external  $\text{As}_2$  flux of pressure  $p_{\text{As}_2}^{\text{ext}}$  is supplied, so that  $p_{\text{As}_2}^{\text{ext}} \gg p_{\text{As}_2}^s$ , a reduced gallium evaporated flux is obtained directly from the equation (2.7)

$$p_{\text{Ga}} = \frac{K_{\text{GaAs}}}{(p_{\text{As}_2}^{\text{ext}})^{\frac{1}{2}}}, \quad (2.13)$$

and a suppression of the sublimation occurs. Hence, the rate of evaporation is inversely proportional to the square root of the arsenic flux to the substrate, like experimentally

Compound	$K_{\text{III/V}}(\text{atm}^{3/2})$	$T_{\text{max}}(^{\circ}\text{C})$
AlAs	$1.63 \times 10^{10} \exp\left(-\frac{5.39 \text{ eV}}{k_B T}\right)$	902
GaAs	$2.73 \times 10^{11} \exp\left(-\frac{4.72 \text{ eV}}{k_B T}\right)$	630
GaP	$2.26 \times 10^{11} \exp\left(-\frac{4.71 \text{ eV}}{k_B T}\right)$	571
InAs	$7.76 \times 10^{11} \exp\left(-\frac{4.34 \text{ eV}}{k_B T}\right)$	508
InP	$8.34 \times 10^{11} \exp\left(-\frac{4.02 \text{ eV}}{k_B T}\right)$	268

Table 2.1: Action mass equation constants  $K_{\text{III/V}}$  and temperatures of maximum sublimation  $T_{\text{max}}$  for some III/V compound semiconductors [10].

observed in MBE systems. The case of an external  $\text{As}_4$  flux brings to the similar result just by substituting  $p_{\text{As}_2}^{\text{ext}}$  for  $2p_{\text{As}_4}^{\text{ext}}$  in equation (2.13).

When an external gallium flux of pressure  $p_{\text{Ga}}^{\text{ext}}$  is added, the growth rate can be expressed by

$$v = -V \frac{p_{\text{Ga}} - p_{\text{Ga}}^{\text{ext}}}{\sqrt{2\pi m_{\text{Ga}} k_B T}}, \quad (2.14)$$

and considering that the external arsenic flux is practically always much bigger than the gallium one, for the growth rate one gets

$$v = C \left[ p_{\text{Ga}}^{\text{ext}} - \frac{K_{\text{GaAs}}}{(p_{\text{As}_2}^{\text{ext}})^{\frac{1}{2}}} \right], \quad (2.15)$$

where the fraction of arsenic that takes part in the growth process has been neglected, and the condition  $p_{\text{As}_2} \gg p_{\text{As}_4}$  has also been considered. Also the temperature dependence implicit in (2.15) was experimentally found [11].

For typical values of  $p_{\text{As}_2}^{\text{ext}}$ , ranging between  $10^{-6} - 10^{-4}$  Torr, the growth rate is mainly controlled by the gallium flux and a solid arsenic phase is never formed, because the vapor arsenic pressure at standard growth temperatures, namely  $T > 500^{\circ}\text{C}$ , would be in Torr range. Nevertheless, the excess arsenic flux fixes a point in the phase diagram and so determines the type and concentration of point defects. This considerations are valid for many III/V compounds [10].

Ternary alloys, composed by two group-III elements like  $\text{Al}_x\text{Ga}_{1-x}\text{As}$ ,  $\text{Ga}_x\text{In}_{1-x}\text{As}$ , and  $\text{Al}_x\text{In}_{1-x}\text{As}$ , can be successfully analyzed with the same theory. However, in these materials the estimation of the activity coefficient  $\gamma$ , that takes into account the non-ideal nature of the alloy, is difficult.  $\text{Al}_x\text{Ga}_{1-x}\text{As}$  is a special case having  $\gamma_{\text{GaAs}} = \gamma_{\text{AlAs}} = 1$ . For ternary compounds having two group-V elements, like  $\text{GaAs}_x\text{P}_{1-x}$ , the mass action equations are

$$p_{\text{Ga}} p_{\text{As}_2}^{\frac{1}{2}} = \gamma_{\text{GaAs}} K_{\text{GaAs}} x \quad \text{and} \quad p_{\text{Ga}} p_{\text{P}_2}^{\frac{1}{2}} = \gamma_{\text{GaP}} K_{\text{GaP}} (1-x), \quad (2.16)$$

together with the mass equations relative to the arsenic molecules (2.5) and the similar ones corresponding to the phosphorus dissociation  $2\text{P}_{2(\text{g})} \rightleftharpoons \text{P}_{4(\text{g})}$ . The resulting final

composition of  $\text{GaAs}_x\text{P}_{1-x}$  is given by

$$\frac{1}{x} = 1 + \left( \frac{\gamma_{\text{GaAs}} K_{\text{GaAs}}}{\gamma_{\text{GaP}} K_{\text{GaP}}} \right) \left( \frac{p_{\text{P}_2}^{\text{ext}}}{p_{\text{As}_2}^{\text{ext}}} \right)^{\frac{1}{2}}, \quad (2.17)$$

where the amount of group-V elements that take part in the growth process is neglected and  $T > 500^\circ\text{C}$  is considered, so that the dimers are the dominating molecular species. Even neglecting the influence of the activity coefficients in (2.17), a good qualitative agreement can be found with the experimental data [12].

# Chapter 3

## Basics of elasticity and physical properties in crystals

In this chapter, an introduction to the elasticity theory in crystals is presented, in order to apply it to the case of pseudomorphic growth. In addition, the definition of the elastic constants is analyzed in detail, in fact, their role is central in the simulation of high-resolution x-ray diffraction (HRXRD) spectra that are extensively measured to characterize the samples. The concepts of critical thickness and strain compensation are also introduced, because of their importance in the present work. The tensor formalism is used in a general way and it can be applied to other field of great interest for optoelectronics, such as the nonlinear optical crystals and birefringence.

### 3.1 The strain tensor

In Fig. 3.1, a schematic sketch of a deformed body is depicted, each point of the object is moved a certain amount which is function of the original position. The displacement field  $\vec{u}(\vec{r})$  is defined as

$$\vec{u}(\vec{r}) = \vec{r}' - \vec{r}, \quad (3.1)$$

where the primed symbols are used to refer to quantities after the transformation. It is obvious that rotations or translations do not stretch the object, but if two points change their distance then a deformation occurred. The deformation, as function of  $\vec{r}$ , can be analyzed by studying the effect of the displacement on the infinitesimal length of the segment  $dl$

$$dl^2 = dx^2 + dy^2 + dz^2 = dx_i^2, \quad (3.2)$$

where the Einstein summation convention on the repeated indices is used. Using the def-

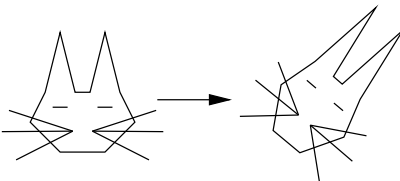


Figure 3.1: Each point in the picture is displaced as function of its original position, but rotations or translations does not deform the object.

inition (3.1), the square of the transformed infinitesimal segment length can be rewritten as

$$dl'^2 = (dx_i + du_i)^2 = \left( dx_i + \frac{\partial u_i}{\partial x_j} dx_j \right)^2, \quad (3.3)$$

and just expanding

$$dl'^2 = dx_i^2 + 2 \frac{\partial u_i}{\partial x_j} dx_j dx_i + \frac{\partial u_i}{\partial x_j} \frac{\partial u_i}{\partial x_k} dx_j dx_k = dx_i^2 + \left( 2 \frac{\partial u_i}{\partial x_j} + \frac{\partial u_k}{\partial x_j} \frac{\partial u_k}{\partial x_i} \right) dx_j dx_i, \quad (3.4)$$

where in the second term of last equation the indices  $i$  and  $k$  are just swapped. Equation (3.4) can be written in a more symmetric way, therefore

$$dl'^2 = dl^2 + \left( \frac{\partial u_i}{\partial x_j} + \frac{\partial u_j}{\partial x_i} + \frac{\partial u_k}{\partial x_j} \frac{\partial u_k}{\partial x_i} \right) dx_j dx_i. \quad (3.5)$$

Finally, the components of the strain  $\epsilon$  are defined as

$$\epsilon_{ij}(\vec{r}) = \frac{1}{2} \left( \frac{\partial u_i}{\partial x_j} + \frac{\partial u_j}{\partial x_i} + \frac{\partial u_k}{\partial x_j} \frac{\partial u_k}{\partial x_i} \right), \quad (3.6)$$

and it is evident that  $\epsilon$  is a tensor and it is symmetric, it is also a function of the position as it is put in evidence in (3.6). As a consequence of the  $\epsilon$  symmetry, it is always possible to find, at any point  $\vec{r}$ , an orthogonal basis that diagonalize the  $\epsilon$  and in the principal axes representation, the equation (3.5) can be expressed using the tensor (3.6) giving

$$dl'^2 = dl^2 + 2\epsilon_{ii} dx_i^2. \quad (3.7)$$

In the case  $dl$  is chosen along the  $x_1$  direction, one gets directly

$$dx_1'^2 = dx_1^2 + 2\epsilon_{11} dx_1^2 \quad \text{and} \quad dx_1' = dx_1 \sqrt{1 + 2\epsilon_{11}}, \quad (3.8)$$

and for small deformations (3.8) can be approximated by

$$dx_1' \simeq dx_1 (1 + \epsilon_{11}). \quad (3.9)$$

The last expression shows that the generic diagonal component  $\epsilon_{ii}$  is indeed the relative linear elongation along the direction  $x_i$ . Furthermore, it is explained the presence of the factor  $1/2$  in the definition (3.6).

Another consequence of the assumption of small deformation is the negligibility of the second derivative terms allowing the simplification of (3.6), that can be easily rewritten as

$$\epsilon_{ij}(\vec{r}) \simeq \frac{1}{2} \left( \frac{\partial u_i}{\partial x_j} + \frac{\partial u_j}{\partial x_i} \right). \quad (3.10)$$

Considering that the trace of a tensor of rank two is invariant under basis transformation, a useful and simple expression for the local change of volume is obtained for every coordinate basis starting from (3.9), giving

$$dV' \simeq dV (1 + \epsilon_{ii}). \quad (3.11)$$

## 3.2 The stress tensor

The stress tensor  $\sigma$  describes the force field in matter. Referring to Fig. (3.2), the forces, applied on the surface of an infinitesimal cubic volume  $dV$  of a body, directly define the components of the strain tensor by

$$P_i = \sigma_{ij}n_j, \quad (3.12)$$

where  $\vec{P}dS = \vec{F}$  is the force applied on the surface of extension  $dS$  with normal vector  $\vec{n}$ .

Geometrical arguments prove the symmetry of the stress tensor in case of statical equilibrium and when the force field is homogeneous throughout the body, and in absence of body-forces (like gravity) and body-torques. In fact, it is evident from equation (3.12) that, in order to have zero total force, the vectors are oriented like shown in Fig. 3.3, and the other equilibrium condition of zero total torque implies directly the symmetry of the

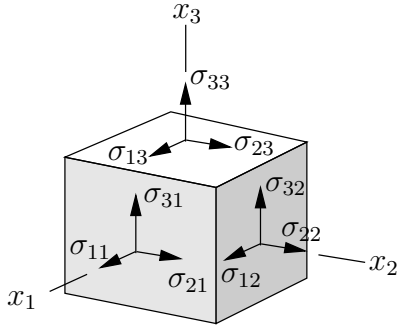


Figure 3.2: The forces on the faces of a cube inside a homogeneously stressed body.

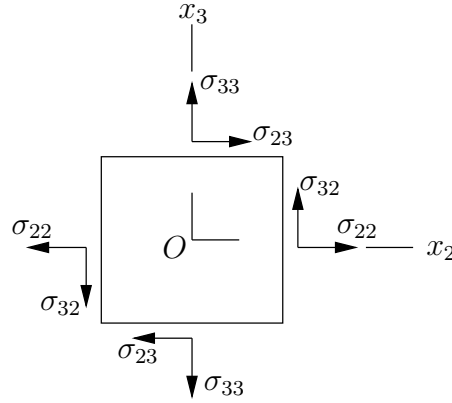


Figure 3.3: Section perpendicular to axis  $x_1$  of the Fig. 3.2.

strain tensor

$$\sigma_{ij} = \sigma_{ji}. \quad (3.13)$$

It can be proved that the stress tensor remains symmetric when the stress field is inhomogeneous, body-forces are present, and in the non-static case [13, 14]. On the other hand, the tensor symmetry is broken when a distributed body-torque is present, i.e., a torque proportional to the volume generated by a long-range force.

It is important to write the equilibrium equations in case the stress field is inhomogeneous, it is easy to prove that the Newton's law can be written as

$$\rho \ddot{x}_i = \rho g_i + \frac{\partial \sigma_{ij}}{\partial x_j}, \quad (3.14)$$

where  $\rho$  is the material density and  $g_i$  are the components of an eventual body force.

### 3.3 Hooke's law in crystals

Strain and stress were defined, so far, independently onto each other. Elasticity theory studies the reversible deformation of a body and not the irreversible one, that are called plastic. In what follows, just elastic deformations are considered and there is always a relation between stress and strain and it is reasonable to approximate it linearly for small loads, this is the Hooke's law. The more general linear expressions are namely

$$\epsilon_{ij} = s_{ijkl}\sigma_{kl} \quad \text{and} \quad \sigma_{ij} = c_{ijkl}\epsilon_{kl}, \quad (3.15)$$

where  $s$  and  $c$  are respectively the compliance and the stiffness tensors. Due to the presence of four indices,  $3^4 = 81$  components are needed to specify these rank-four tensors, but the symmetry of the stress and strain tensors reduces the number of the independent components to 36, in fact holds

$$c_{ijkl} = c_{ijlk} = c_{jilk} \quad \text{and} \quad s_{ijkl} = s_{ijlk} = s_{jilk}. \quad (3.16)$$

The variation of the stored elastic energy in the material can be expressed as function of the variation  $d\epsilon$  of the strain tensor, which is also a symmetric tensor and considering, for example, the component  $d\epsilon_{11}$ , in the diagonal representation of  $d\epsilon$ , it is clear that the work per unit of volume to strain the material from  $\epsilon_{11}$  to  $\epsilon_{11} + d\epsilon_{11}$  can be written as

$$dW = \sigma_{11}d\epsilon_{11}, \quad (3.17)$$

and considering all the three components one gets

$$dW = \sigma_{ii}d\epsilon_{ii}. \quad (3.18)$$

This expression can be easily generalized to any non diagonal representation of  $d\epsilon$ , giving for the variation of the elastic energy per unit of volume

$$dW = \sigma_{ij}d\epsilon_{ij}. \quad (3.19)$$

Therefore, it follows that the components of  $\sigma$  can be formally obtained by partial derivation of  $W$  as

$$\sigma_{ij} = \frac{\partial W}{\partial \epsilon_{ij}}, \quad (3.20)$$

but an additional factor  $1/2$  has to be introduced in the mixed terms when the energy is considered as function of the  $i \geq j$  strain component only [13]. The elemental work from equation (3.19) is invariant under basis transformation, which is consistent with the fact that  $dW$  is a scalar quantity with physical meaning and, using the Hooke's law (3.15), it can be further expanded as

$$dW = c_{ijkl}\epsilon_{kl}d\epsilon_{ij}. \quad (3.21)$$

The elastic energy  $W$  is a function of the strain components  $\epsilon_{ij}$  only and it is a state function for the system, it follows that the differential (3.21) is exact. In virtue of these assumptions one can derivate twice the primitive function  $W$  obtaining

$$\frac{\partial^2 W}{\partial \epsilon_{ij} \partial \epsilon_{kl}} = c_{ijkl}, \quad (3.22)$$

and thus the primitive function  $W$  can be written as direct consequence of (3.22) as

$$W = \frac{1}{2} c_{ijkl} \epsilon_{kl} \epsilon_{ij}, \quad (3.23)$$

where it is assumed to have zero elastic energy when the strain tensor has all the components equal to zero. Furthermore, it can be noticed that inverting the derivation order in equation (3.22) does not affect the result and it follows immediately that

$$c_{ijkl} = c_{klij}. \quad (3.24)$$

This last relation together with the (3.16) can be resumed as

$$c_{ijkl} = c_{jikl} = c_{ijlk} = c_{klij}, \quad (3.25)$$

the number of independent components of the stiffness tensor  $c$  is thus reduced to 21. The same procedure is valid for the compliance tensor  $s$ . In fact, starting from (3.19) one can rewrite (3.21) and (3.23) in function of the stress tensor by using (3.15) and analogously as (3.24) one can show that

$$s_{ijkl} = s_{jikl} = s_{ijlk} = s_{klij}. \quad (3.26)$$

In virtue of (3.25), it is possible to represent the fourth-rank elastic tensors in a practical matricial form, where two indices are used instead of four, substituting the first two and the last two, respectively, following the convention

$$11 \rightarrow 1 \quad 22 \rightarrow 2 \quad 33 \rightarrow 3 \quad 23, 32 \rightarrow 4 \quad 13, 31 \rightarrow 5 \quad 12, 21 \rightarrow 6. \quad (3.27)$$

As example, in this notation  $c_{3123}$  can be written as  $c_{54} = c_{45}$ , and a matrix can be formally used to represent the  $c$  or the  $s$  tensors, e.g.,

$$c = \begin{pmatrix} c_{11} & c_{12} & c_{13} & c_{14} & c_{15} & c_{16} \\ & c_{22} & c_{23} & c_{24} & c_{25} & c_{26} \\ & & c_{33} & c_{34} & c_{35} & c_{36} \\ & & & c_{44} & c_{45} & c_{46} \\ & & & & c_{55} & c_{56} \\ & & & & & c_{66} \end{pmatrix}, \quad (3.28)$$

where the blanks in (3.28) are always intended to be filled using the symmetry of this pseudo-matrix, that of course it is not a second-rank tensor.

### 3.4 The $c$ and $s$ tensors in cubic crystals

It is important to point out that the stress tensor represents the perturbation introduced to a system and it can be arbitrary, using (3.15) it is also possible to realize that also an arbitrary strain can be applied. On the other hand, the tensors stiffness  $c$  and compliance  $s$  are given intrinsic properties of the material and are deeply influenced from its internal symmetry.



Any material property is influenced by the symmetry of the material itself and, in case of crystals, the Neumann's Principle is valid: *The symmetry elements of any physical property of a crystal must include the symmetry elements of the point group of the crystal.* This means that a crystal property should at least have the same symmetry of the crystal.

Focusing on GaAs, which belongs to the  $\bar{4}3m$  point group, it is possible to find the symmetries of the  $c$  tensor by direct inspection. The starting point is the general transformation rule of a tensor of rank  $n$ , which transforms like the product of  $n$  coordinates by definition. For this reason, the  $\bar{4}$  operation (a four-fold rotation around one of the principal axis followed by inversion) can act on the coordinates as

$$1 \rightarrow -2 \quad 2 \rightarrow 1 \quad 3 \rightarrow -3, \quad (3.29)$$

where just the coordinate index is shown, and using the six indices notation, it is obtained

$$1 \rightarrow 2 \quad 2 \rightarrow 1 \quad 3 \rightarrow 3 \quad 4 \rightarrow -5 \quad 5 \rightarrow 4 \quad 6 \rightarrow -6. \quad (3.30)$$

As example, using (3.30) it is proved that the  $\bar{4}$  operation transforms  $c_{45}$  in  $-c_{54} = -c_{45}$ , but the invariance of the crystal under this transformation implies that  $c_{45} = -c_{45} = 0$ . Similarly it is obtained for the complete pseudo-matrix in a base set like the crystal axes that

$$c = \begin{pmatrix} c_{22} & c_{12} & c_{23} & -c_{25} & c_{24} & -c_{26} \\ & c_{11} & c_{13} & -c_{15} & c_{14} & -c_{16} \\ & & c_{33} & -c_{35} & c_{34} & -c_{36} \\ & & & c_{55} & -c_{45} & c_{56} \\ & & & & c_{44} & -c_{46} \\ & & & & & c_{66} \end{pmatrix} = \begin{pmatrix} c_{11} & c_{12} & c_{13} & 0 & 0 & c_{16} \\ & c_{11} & c_{13} & 0 & 0 & -c_{16} \\ & & c_{33} & 0 & 0 & 0 \\ & & & c_{44} & 0 & 0 \\ & & & & c_{44} & 0 \\ & & & & & c_{66} \end{pmatrix}. \quad (3.31)$$

After this operation the tensor  $c$  has just 7 independent entries. Using the three-fold symmetry along the body diagonal it can be obtained analogously

$$1 \rightarrow 2 \quad 2 \rightarrow 3 \quad 3 \rightarrow 1, \quad (3.32)$$

and using the six indices notation

$$1 \rightarrow 2 \quad 2 \rightarrow 3 \quad 3 \rightarrow 1 \quad 4 \rightarrow 5 \quad 5 \rightarrow 6 \quad 6 \rightarrow 4, \quad (3.33)$$

that, substituted in the last (3.31) expression, gives for the  $c$  tensor the form

$$c = \begin{pmatrix} c_{22} & c_{23} & c_{12} & 0 & 0 & c_{24} \\ & c_{22} & c_{12} & 0 & 0 & -c_{24} \\ & & c_{11} & 0 & 0 & 0 \\ & & & c_{55} & 0 & 0 \\ & & & & c_{55} & 0 \\ & & & & & c_{44} \end{pmatrix} = \begin{pmatrix} c_{11} & c_{12} & c_{12} & 0 & 0 & 0 \\ & c_{11} & c_{12} & 0 & 0 & 0 \\ & & c_{11} & 0 & 0 & 0 \\ & & & c_{44} & 0 & 0 \\ & & & & c_{44} & 0 \\ & & & & & c_{44} \end{pmatrix}. \quad (3.34)$$

It can be shown by inspection that using the  $m$  symmetry, a mirror plane of the face diagonals, it is not possible to simplify the form of the tensor any further. In fact, this symmetry can transform the indices as

$$1 \rightarrow -2 \quad 2 \rightarrow -1 \quad 3 \rightarrow 3, \quad (3.35)$$

and using the six indices notation

$$1 \rightarrow 2 \quad 2 \rightarrow 1 \quad 3 \rightarrow 3 \quad 4 \rightarrow -5 \quad 5 \rightarrow -4 \quad 6 \rightarrow 6. \quad (3.36)$$

So just 3 independent elastic constants are needed. In addition, it is also possible to show [13, 14] that for all the cubic symmetries the stiffness tensor has the form (3.34). The compliance tensor  $s$ , written in the pseudo-matrix form, has exactly the same (3.34) structure, because the crystal symmetry can be exploited in the same way. By inverting the linear system (3.15), the components of  $s$  can be expressed in function of the components of  $c$

$$s_{11} = \frac{c_{11} + c_{12}}{(c_{11} - c_{12})(c_{11} + 2c_{12})}, \quad s_{12} = \frac{-c_{12}}{(c_{11} - c_{12})(c_{11} + 2c_{12})}, \quad s_{44} = \frac{1}{c_{44}}. \quad (3.37)$$

### 3.5 The Poisson's ratio

When a compressive stress  $\sigma_{33}$  is applied to an isotropic body, a contraction  $\epsilon_{33}$  results in the stress direction and, typically, a lateral elongation  $\epsilon_{11} = \epsilon_{22}$  perpendicular to the applied stress is observed, as schematically indicated in Fig. 3.4. The opposite behavior is typically expected in case of tensile stress. The negative of the ratio between the perpendicular and the parallel strain is the Poisson's ratio

$$\nu = -\frac{\epsilon_{11}}{\epsilon_{33}} = -\frac{\epsilon_{22}}{\epsilon_{33}}, \quad (3.38)$$

and it is a material property for isotropic bodies. It can be proved, from general thermodynamical considerations, that only Poisson's ratios between -1 and 1/2 are allowed [13], the case of 1/2 corresponds to ideally incompressible materials, as can be seen applying (3.11) together with (3.38). Most of the materials have Poisson's ratios ranging between 1/3 and 1/2.

The elastic behavior of an isotropic body is characterized by a second material constant, in fact, if just  $\sigma_{33}$  stress is applied, the relations between the strain and the stress are

$$\epsilon_{33} = \sigma_{33}/E \quad \text{and} \quad \epsilon_{11} = \epsilon_{22} = -\frac{\nu}{E}\sigma_{33}, \quad (3.39)$$

where  $E$  is the Young's modulus and  $\nu$  is the already defined Poisson's ratio.

It is interesting to underline that an isotropic medium can be treated as a special case of material having cubic symmetry. Therefore, the form of the  $c$  tensor (3.34) can be taken as starting point, but any other additional symmetry can also be included, for example, the invariance of  $c$  under 45° rotation brings an extra condition for  $c_{44}$ , namely

$$c_{44} = \frac{c_{11} - c_{12}}{2}, \quad (3.40)$$

and relations between the elastic constants are

$$c_{11} = \frac{1 - \nu}{(1 + \nu)(1 - 2\nu)}E, \quad c_{12} = \frac{\nu}{(1 + \nu)(1 - 2\nu)}E, \quad (3.41)$$

or using the Lamé coefficients  $\mu$  and  $\lambda$

$$c_{11} = 2\mu + \lambda, \quad c_{12} = \lambda. \quad (3.42)$$

It is clear from Fig. 3.4 that the definition of the Poisson's ratio is unique for isotropic materials, instead other definitions are adopted in case of anisotropy [15]

$$\nu_{ij} = -\frac{s_{ij}}{s_{jj}}. \quad (3.43)$$

In this work, cubic crystal GaAs is always used as substrate and the growth is always intended to be pseudomorphic in the (001) direction, here also called the  $x_3$  or  $z$  direction. Therefore, it is of particular interest to calculate the already defined Poisson's ratios  $\nu_{13}$  and  $\nu_{23}$  in function of the elastic constants  $c_{11}$ ,  $c_{12}$ , and  $c_{44}$  appearing in (3.34). In case of

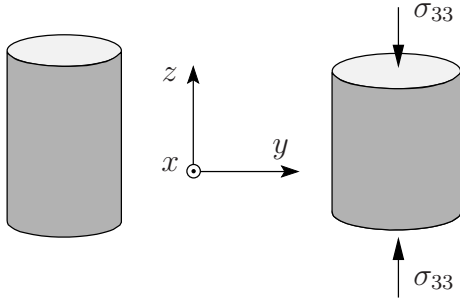


Figure 3.4: Lateral expansion of an object perpendicularly to the stress in a homogeneous material.

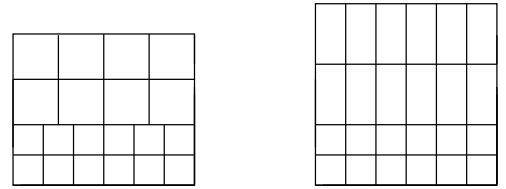


Figure 3.5: Schematic picture of totally relaxed (left) and pseudomorphic (right) growth.

a cubic crystal, the strain is introduced by  $\sigma_{33}$ , the only non zero component of the stress tensor, and is given by applying the compliance tensor. The non zero component of the strain are

$$\epsilon_{11} = s_{12}\sigma_{33} \quad \epsilon_{22} = s_{12}\sigma_{33} \quad \epsilon_{33} = s_{11}\sigma_{33} \quad (3.44)$$

where the symmetry properties of the compliance tensor in cubic crystals are used. Using the definitions (3.43) and (3.37) it results that

$$\nu_{23} = \nu_{13} = \nu_{(001)} = -\frac{s_{12}}{s_{11}} = \frac{c_{12}}{c_{11} + c_{12}}. \quad (3.45)$$

The equality between  $\nu_{23}$  and  $\nu_{13}$  allows to consider the Poisson's ratio in the sense of (3.38), this is due to the high symmetry of the (001) direction on which the stress is applied. Furthermore, it is possible to show, that also for the direction (111) a Poisson's ratio following (3.38) can be defined.

## 3.6 Pseudomorphic (001) growth

In pseudomorphic (001) growth the materials are strained perpendicular to the growth direction  $x_3$ , in order to accommodate completely the substrate lattice mismatch, see

Fig. 3.5. In the case of cubic crystal substrates and layers, the latter is tetragonal distorted by biaxial stress. The  $\epsilon_{33}$  strain component can be expressed in function of the elastic constant and in particular in function of the previously defined  $\nu_{(001)}$ . The strain components  $\epsilon_{11}$  and  $\epsilon_{22}$  are known and are equal, because the layer matches the lattice mismatch relative to the cubic substrate. Using (3.34) three equations can be written

$$\sigma_{11} = c_{11}\epsilon_{11} + c_{12}(\epsilon_{22} + \epsilon_{33}) \quad \sigma_{22} = c_{12}(\epsilon_{11} + \epsilon_{33}) + c_{11}\epsilon_{22} \quad (3.46)$$

$$\sigma_{33} = c_{12}(\epsilon_{11} + \epsilon_{22}) + c_{11}\epsilon_{33} = 0. \quad (3.47)$$

From (3.46) and  $\epsilon_{11} = \epsilon_{22}$  it follows directly that the in-plane stresses  $\sigma_{11}$  and  $\sigma_{22}$  are equal. From equation (3.47) the important relation between perpendicular and in-plane strain can be derived, in fact, in case of pseudomorphic growth the extra condition of no perpendicular stress can be imposed. This allows to solve the equations giving

$$\epsilon_{33} = -2\frac{c_{12}}{c_{11}}\epsilon_{22} = -2\frac{\nu_{(001)}}{1 - \nu_{(001)}}\epsilon_{22}, \quad (3.48)$$

and for the stress

$$\sigma_{11} = \frac{\epsilon_{22}}{c_{11}}(c_{11}^2 + c_{11}c_{12} - 2c_{12}^2). \quad (3.49)$$

These equations are of great importance in the characterization of pseudomorphic epitaxial multilayers. In fact, considering the case of (001) growth, the HRXRD spectra recorded on symmetric reflections are very sensitive to the  $\epsilon_{33}$  values of the layers in the stack. Using formula (3.48), it is possible to retrieve the composition of the layer, considering that not only the in-plane  $\epsilon_{22}$ , but also the components of the stiffness tensor are material dependent. The knowledge of the stiffness tensor for different materials and alloys is of great importance for a precise characterization of the grown samples.

Values of the components of the stiffness tensor together with the lattice constant of many important III/V semiconductors, that have the same crystal structure as GaAs, are listed in Tab. 3.1. For the relative alloys, linear interpolation (Vegard's rule) is commonly used.

Compound	$a_0$ (nm)	$c_{11}$ (GPa)	$c_{12}$ (GPa)	$c_{44}$ (GPa)
GaAs	0.565325	122.1	56.6	60.0
AlAs	0.56611	125.0	53.4	54.2
InAs	0.60583	83.3	45.3	39.6
GaP	0.54505	140.5	62.0	70.3
AlP	0.54672	133.0	63.0	61.5
InP	0.58697	101.1	56.1	45.6
GaSb	0.60959	88.4	40.3	43.2
AlSb	0.61355	87.7	43.4	40.8
InSb	0.64794	68.5	37.6	31.1

Table 3.1: The values of the component of the stiffness tensor together with the lattice constant for some III/V zinc blend semiconductor at 300 K after [16].

### 3.7 The wafer bowing

The pseudomorphic growth of multilayers stores elastic energy in the structure. This effect is evident by observing the curvature of the grown samples. The control of the radius of curvature of the grown samples is important, because in microelectronic many technological steps, for example lithography, require a flat sample. Therefore, the control and the prediction of the curvature is an important topic. In this section, the calculation of the curvature is presented using a simple phenomenological model.

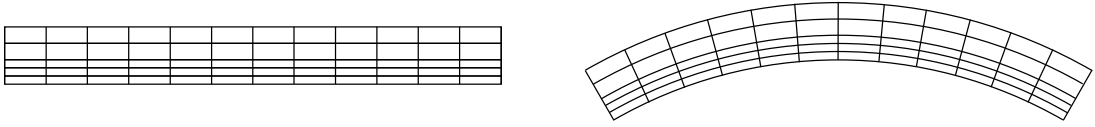


Figure 3.6: Flat and curved sample, schematic representation.

In Fig. 3.6 a substrate with a pseudomorphic layer is depicted in flat and curved configuration. As long as no plastic deformation occurs, the curvature introduces an additional strain that reduces the total elastic energy of the system, in particular, referring to Fig. 3.6, the top layers are stretched and the bottom ones are compressed. In the following, the shape of the bowed wafer is assumed to be spherical. This assumption, that is supported by the experimental observation, simplifies the calculations, since just the radius of curvature  $R$  and the in-plane lattice constant  $a_{\parallel}(0)$  at the sample surface are to be determined. These two parameters define completely the configuration of the sample and also its elastic energy. The in-plane lattice constant as function of  $z$  is given by

$$a_{\parallel}(z) = \frac{R+z}{R}a = (1 + \kappa z)a, \quad (3.50)$$

where  $\kappa$  is the sample curvature and  $z = 0$  corresponds to the surface. The  $i$ -th layer has a thickness  $d_i$  and it is a cubic crystal material of bulk lattice constant  $a_i$  and relative mismatch  $m_i$  to the substrate defined as

$$m_i = \frac{a_i - a_{\text{sub}}}{a_{\text{sub}}}. \quad (3.51)$$

In cubic crystals, the elastic energy per unit of surface, stored in a layer of infinitesimal thickness  $dz$ , can be written as

$$dW = \frac{1}{2}c_{11}(\epsilon_{11}^2 + \epsilon_{22}^2 + \epsilon_{33}^2)dz + c_{12}(\epsilon_{11}\epsilon_{22} + \epsilon_{11}\epsilon_{33} + \epsilon_{22}\epsilon_{33})dz, \quad (3.52)$$

where all the elastic constants and the strain components are function of  $z$ . The components  $\epsilon_{11}$  and  $\epsilon_{22}$  are equal to the in-plane strain, that for the material of the  $i$ -th layer is

$$\epsilon_{\parallel} = \epsilon_{11} = \epsilon_{22} = \frac{a_{\parallel}(z) - a_i}{a_i}. \quad (3.53)$$

Furthermore, the relation (3.48) is valid for the perpendicular component  $\epsilon_{33}$  and results in

$$\epsilon_{\perp} = \epsilon_{33} = -2\frac{c_{12}}{c_{11}}\epsilon_{\parallel}. \quad (3.54)$$

The formula (3.52) can so be rewritten as

$$dW = \frac{c_{11}^2 + c_{11}c_{12} - 2c_{12}^2}{c_{11}}\epsilon_{\parallel}^2 dz = C\epsilon_{\parallel}^2 dz, \quad (3.55)$$

and it can be easily integrated over  $z$ , separating the contribution of each layer  $i$ , giving the elastic energy of the sample

$$W(\kappa, a) = \sum_i \int_{z_{i,\text{start}}}^{z_{i,\text{end}}} C_i \epsilon_{\parallel,i}^2 dz. \quad (3.56)$$

In the integrand of (3.56) the term  $C$  and the in-plane strain  $\epsilon_{\parallel}$  are indexed with  $i$ , and the substrate is also considered as a layer. In case of layers with graded composition, a  $z$  dependence in  $C_i$  and  $a_i$  can be introduced. The function  $W(\kappa, a)$  should be minimized to find the equilibrium configuration, hence the two equations are

$$\frac{\partial W}{\partial \kappa} = 0 \quad \text{and} \quad \frac{\partial W}{\partial a} = 0, \quad (3.57)$$

and can be solved numerically in all practical cases. In particular, it is easy to approximate (3.56) in the typical case in which the substrate is much thicker than the strained layers, and the neutral plane, that is the plane with no strain, lies almost in the middle of the substrate. Under these assumptions the substrate energy is

$$W(\kappa)_{\text{sub}} \simeq \int_{-\frac{d_{\text{sub}}}{2}}^{\frac{d_{\text{sub}}}{2}} C_{\text{sub}} \kappa^2 z^2 dz = \frac{C_{\text{sub}} \kappa^2 d_{\text{sub}}^3}{12}. \quad (3.58)$$

The in-plane strain of the other layers can be written considering that the distance of each layer from the neutral line is approximately half of the substrate thickness. Using this simplification the strain (3.53) can be rewritten as

$$\epsilon_{\parallel,i} \simeq \frac{a_{\text{sub}}}{a_i} \left( -m_i + \frac{\kappa d_{\text{sub}}}{2} \right) \simeq \left( -m_i + \frac{\kappa d_{\text{sub}}}{2} \right) \quad (3.59)$$

and the elastic energy of the layers can be simplified in

$$W(\kappa)_{\text{layers}} \simeq \sum_i C_i \left( -m_i + \frac{\kappa d_{\text{sub}}}{2} \right)^2 d_i \simeq \sum_i C_i (m_i^2 - \kappa m_i d_{\text{sub}}) d_i, \quad (3.60)$$

where in the last two formulae the index  $i$  is referred to the layers only. The elastic energies (3.58) and (3.60) are just function of  $\kappa$ , because the dependence on  $a$  is implicitly eliminated by defining the position of the neutral line. It follows that the minimum of the elastic energy is then given by

$$\frac{\partial(W_{\text{sub}} + W_{\text{layers}})}{\partial \kappa} = 0. \quad (3.61)$$

By solving (3.61) one gets the Stoney's formula [17]

$$\kappa \simeq \frac{6}{C_{\text{sub}} d_{\text{sub}}^2} \sum_i C_i m_i d_i. \quad (3.62)$$

The curvature of a sample can be measured with high precision by monitoring the reflection of a laser beam on the sample surface, with this technique commercial systems can reach a resolution of  $10^{-5} \text{ m}^{-1}$  [18]. It is clear that such high precision may not always be achievable in in-situ applications, where the sample rotation, for example, can be a severe limiting factor.

The radii of curvature can be measured using HRXRD, as shown in Fig. 3.7, where several different samples are analyzed. The angle  $\omega$  of the substrate diffraction peak, in this case the (004) Bragg reflection, is determined on different sample points lying at different  $x$  positions on the intersection line between the sample surface and the diffractometer plane. The radius of curvature can be calculated considering the ratio between the increments of  $\Delta x$  and  $\Delta \omega$

$$R = \frac{\Delta x}{\Delta \omega} = \frac{1}{\kappa}, \quad (3.63)$$

where  $\Delta \omega$  is measured in radians. The sample number 2 is a GaAs substrate and has negligible curvature, the linear fit of the data points in Fig. 3.7 results in a radius of curvature of more that 130 m, nevertheless, it is easy to realize that this method does not allow an higher resolution, in fact, the data points are not perfectly aligned and the measurement suffers of random and systematic errors. Despite HRXRD is less precise than optical methods, these two measurement procedures have a slightly different meaning. In fact, no direct information about the absolute elastic configuration of the system is given

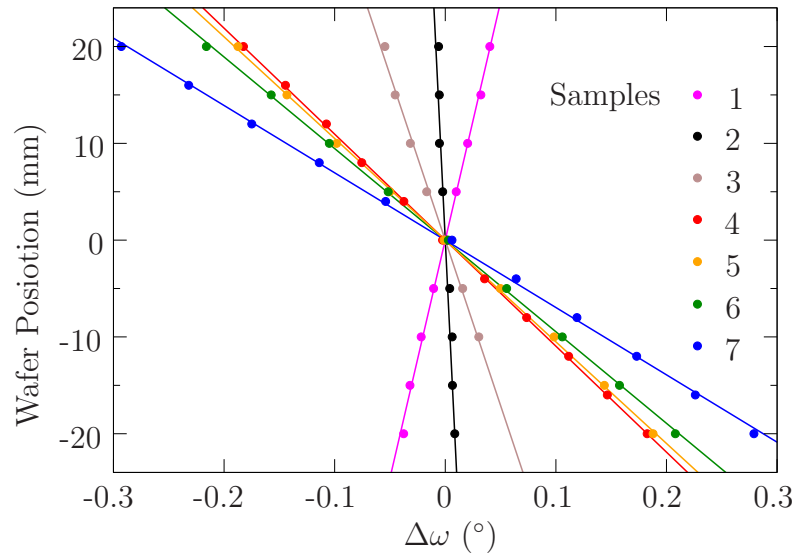


Figure 3.7: Deviation of the substrate position of the (004) Bragg reflection in function of the wafer position in the diffractometer plane, the slope is a direct measurement of the radius of curvature.

Sample	$r_{\text{meas.}}(\text{m})$	$r_{\text{sim.}}(\text{m})$	$\Delta E_{\text{curved}}$	description
1	-28.2	-25	-0.1%	100 nm GaNAs on GaAs
2	134	$+\infty$	0%	GaAs substrate
3	19.6	28	-0.1%	Test structure, 6 QWs for 980 nm emission 980 nm VECSEL
4	6.3	6.1	-1.2%	
5	6.0	6.3	-6%	850 nm VCSEL on 500 $\mu\text{m}$ thick substrate
6	5.4	4.8	-3%	Bottom emitter 980 nm VCSEL
7	4.0	3.7	-7%	Standard 850 nm VCSEL

Table 3.2: Measured (from Fig. 3.7) and simulated, using (3.62), radii of curvature of different samples. The calculated percental elastic energy change between curved and non curved configuration is showed in the fourth column.

when the curvature of a reflecting surface is measured optically, and, for example, an unstrained sample may exhibit curvature just as result of a polishing process, nevertheless the high resolution of the technique allows to measure very small curvature changes. On the other hand, the same sample will result flat for HRXRD investigations, because not the curvature of the surface is measured, but the curvature of the atomic planes, and thus direct information on the elastic sample configuration is obtained.

The values of the samples curvatures extracted from Fig. 3.7 are reported in Tab. 3.2 followed by the calculated ones. The relative variation of elastic energy due to wafer bowing is also listed. All samples were grown on 350  $\mu\text{m}$  thick substrates, except sample 5, in this case the substrate thickness was 500  $\mu\text{m}$ . The sample 1 consists of a 100 nm thick GaNAs layer with a nitrogen concentration of almost 4% and a in-plane strain of 0.8%, which means that this layer is tensile strained. In contrast to all the other samples of the series, this is the only one that shows a concave surface, this is clearly seen by the slope sign in Fig. 3.7, and from the negative value of the radius of curvature in Tab. 3.2. The second sample is just a GaAs substrate, in this case no strain should be present, and the measured radius of curvature is due to statistical errors or to unintentional bowing of the sample when mounted on the holder. This problem can affect all the measurement with large radius of curvature, like sample 3, where six  $\text{In}_{0.165}\text{Ga}_{0.835}\text{As}$  QWs of 8 nm thickness are separated by 130 nm GaAs and are confined by two AlGaAs layers. This clarify that a typical InGaAs QW, designed for an emission wavelength of 980 nm, which has an in-plane strain of approximately -1.2%, stores, because of the quadratic dependence on the strain (3.55), almost 100 times more elastic energy density than AlAs which is almost unstrained with just -0.14% in-plane strain.

In optical devices the number of QWs is very limited (typically 3 to 6 in VCSELs and less than 20 in VECSELs), and their thickness is just of few nanometers. In contrast, AlGaAs layers, with an average aluminum composition around 50%, can reach in a standard VCSEL structure a total thickness of almost 10  $\mu\text{m}$ . Following this arguments, the QWs do not contribute substantially to the total elastic energy of the sample, but the sample bowing is just dominated by thickness and composition of the AlGaAs layers. For example, in sample 4 there are less DBR pairs than respectively in sample 6 and 7, as



consequence the radius of curvature of sample 4 is higher.

The thickness of the substrate plays also an important role, the samples 5 and 7 are almost identical, except in the substrate thickness. The choice of a thicker substrate for sample 5 was dictated by the need of reducing the sample curvature in order to facilitate the lithographic processes on large chips.

It is also interesting to underline, as evidenced in the fourth column of Tab. 3.2, that the higher is the curvature, the higher is the elastic energy, relatively to the non curved configuration, that can be accommodated by bowing the structure.

### 3.8 Critical thickness and strain compensation

It is evident from equation (3.55) that the growth of pseudomorphic layers always increases the elastic energy stored in the sample, in comparison to the relaxed configuration. If the mismatch is less than 7% the layer start to grow pseudomorphically [19]. But, as long as the thickness is increased, it is energetically convenient for the layer to accommodate partially the strain via the introduction of misfit dislocations, because a complete relaxation requires to overcome a much higher energy barrier. This process only starts after a certain critical thickness is reached, before this point, the layer is thermodynamically stable and is perfectly pseudomorphic.

As it will be seen later in this section, the self energy of a dislocation is proportional to the length of the Burgers vector  $\vec{b}$ , and therefore dislocations with small  $|\vec{b}|$  are favored. In face centered cubic crystals of lattice constant  $a$ , the smallest allowed Burgers vectors that create perfect dislocations are of type  $\frac{a}{2} < 110 >$ , and the possible slip planes, that should contain these directions, are for example  $\{001\}$ ,  $\{011\}$ , and  $\{111\}$ , but just the latter are actually experimentally observed [20].

A dislocation can release elastic energy because can expand (shrink) the in-plane length of the layer by the quantity  $\vec{b}_{\parallel}$ , for this reason dislocation lines placed at the film–substrate interface partially accommodate the lattice mismatch. The only kind of dislocations that are experimentally observed, in pseudomorphic layers grown on (001) GaAs, have Burgers vectors forming  $45^\circ$  with the surface normal [21, 22, 23], it follows that just

$$\vec{b} = \pm \frac{1}{2}a[101], \pm \frac{1}{2}a[10\bar{1}], \pm \frac{1}{2}a[011], \text{ and } \pm \frac{1}{2}a[01\bar{1}] \quad (3.64)$$

are allowed resulting in an induced in-plane shift of  $a/2$ . The relative dislocation lines corresponds to the  $[110]$  and  $[\bar{1}\bar{1}0]$  directions, forming an angle of  $60^\circ$  with the Burgers vectors, so they are mixed dislocations.

The calculation of the self energy of a dislocation is an hard task, but, introducing the strong simplification that considers the solid as an isotropic and continuous medium, this can be done easily [13, 20]. One can consider a right-handed screw dislocation having Burgers vector  $(0, 0, b)$  by choosing the coordinate system so that the dislocation line coincides to the  $z$  axis. A plausible displacement function due to the introduction of such dislocation can be

$$\vec{u} = \left( 0, 0, -\frac{b}{2\pi} \arctan \frac{y}{x} \right). \quad (3.65)$$

This function satisfies the properties of a screw dislocation, in fact, the multivalued function "arctan" guarantees that the  $\vec{u}$  component parallel to the dislocation line changes of  $-b$  along every close circuit around the dislocation. It follows that the strain tensor can be derived by the definition (3.10) obtaining

$$\epsilon_{13} = \frac{b}{4\pi} \frac{y}{x^2 + y^2}, \quad \epsilon_{23} = -\frac{b}{4\pi} \frac{x}{x^2 + y^2}, \quad \epsilon_{12} = \epsilon_{11} = \epsilon_{22} = \epsilon_{33} = 0. \quad (3.66)$$

The corresponding stress tensor follows using the formulae (3.15), (3.34), (3.40), and (3.42) and, as long as just shear components are present, one can write

$$\sigma_{ij} = 2\mu\epsilon_{ij}. \quad (3.67)$$

The Newton's equation written in (3.14) is also fulfilled by the calculated stress field, in fact

$$\frac{\partial \sigma_{ij}}{\partial x_j} = 0 \quad (3.68)$$

is the equilibrium condition when no body-forces are taken into account because gravity is typically negligible in solids. Therefore, the density of elastic energy can be written from (3.23), and in this particular case is

$$W = 2\mu(\epsilon_{13}^2 + \epsilon_{23}^2) = \frac{\mu b^2}{8\pi^2} \frac{1}{r^2}. \quad (3.69)$$

The density of energy,  $\xi$ , per unit length of dislocation line is given by integration of  $W$  obtaining

$$\xi = \int_0^{2\pi} \int_{r_1}^{r_2} \frac{\mu b^2}{8\pi^2} \frac{1}{r^2} r d\theta dr = \frac{\mu b^2}{4\pi} \ln \frac{r_2}{r_1}, \quad (3.70)$$

where the integration boundary  $r_2$  cannot be greater than the crystal dimensions and it is set as the layer thickness  $h$ . The value of  $r_1$  cannot be zero, where the continuous media elastic theory is not valid, therefore, the cutoff value  $r_1 = b/\beta$  is introduced, where  $0.7 < \beta < 2.7$  is normally considered [17, 24]. It follows that the linear self-energy density of a screw dislocation of Burgers vector length  $b$  is given by

$$\xi_{\text{screw}} = \frac{\mu b^2}{4\pi} \ln \frac{\beta h}{b}. \quad (3.71)$$

The inaccuracy introduced by the estimation of the ratio  $r_2/r_1$  is mitigated by the logarithmic function and the strong dependence on  $b^2$  of  $\xi$  is demonstrated.

The calculation of  $\xi$  for an edge dislocation is more laborious, but the result [13, 20] is very similar

$$\xi_{\text{edge}} = \frac{\mu b^2}{4\pi(1-\nu)} \ln \frac{\beta h}{b}. \quad (3.72)$$

The screw and edge components of the Burgers vector has to be considered in case of a  $60^\circ$  mixed dislocation giving

$$\xi_{60^\circ} = \alpha \frac{\mu b^2}{4\pi} \ln \frac{\beta h}{b}, \quad (3.73)$$

where some coefficients depending on the dislocation geometry and on  $\nu$  are grouped in the factor  $\alpha$ . It should be remarked that, in these calculations of  $\xi$ , the core energy of the dislocations are not taken into account, an additional contribution of 10–20% on the value of  $\xi$  is typically considered.

The critical thickness for a pseudomorphically grown film of thickness  $h$  can be now calculated. The energy of the layer is

$$W = Ch\epsilon_{\parallel}^2, \quad (3.74)$$

where the equation (3.55) is used considering an in-plane strain  $\epsilon_{\parallel}$  given by the mismatch to the substrate. When the layer thickness is further increased, a net of orthogonal lines appears on the layer surface, this is the so called cross hatched surface and it is typical of strained samples. This can be seen in Fig. 3.8, where the steps produced by the dislocations can be observed with equal density along the  $[110]$  and  $[\bar{1}\bar{1}0]$  directions. If the average distance between the dislocation edges in these specific directions is  $D$ , there will be  $2/D$  dislocations per unit of area, and considering that each dislocation introduces an in-plane shift equal to  $|\vec{b}_{\parallel}| = a/2$ , it follows that the in-plane strain is reduced of  $\frac{a}{2D}$  and the new total energy can be rewritten as

$$W_{\text{dis.}} = Ch \left( |\epsilon_{\parallel}| - \frac{a}{2D} \right)^2 + \alpha \frac{\mu a^2}{16\pi} \ln \left( \frac{2\beta h}{a} \right) \frac{2}{D}. \quad (3.75)$$

In the last equation, the first term represents the reduced elastic energy, and the second term is the energy needed to introduce  $2/D$  dislocation per unit of area (dislocation density).

The introduction of dislocations is not energetically convenient as long as the layer does not exceed a critical thickness, in fact, the energy is just a function of the dislocation density, and the equilibrium configuration is given by

$$\frac{\partial W_{\text{dis.}}}{\partial \frac{1}{D}} = -aCh \left( |\epsilon_{\parallel}| - \frac{a}{2D} \right) + \alpha \frac{\mu a^2}{8\pi} \ln \frac{2\beta h}{a} = 0. \quad (3.76)$$

This equation gives, for a given thickness, the equilibrium dislocation density. On the other hand, the critical thickness  $h_c$  is given imposing the minimum condition at zero dislocation density, namely

$$h_c = \alpha \frac{\mu a}{8\pi |\epsilon_{\parallel}| C} \ln \frac{2\beta h_c}{a}. \quad (3.77)$$

Just when this value is exceeded, it is convenient for the system to introduce dislocations.

In Fig. 3.9, the critical thickness versus the strain of the layer is plotted using the expression (3.77) from [21], who first introduced this concept. It is important to point out that the minimum energy condition (3.76) guarantees that the system is stable, while it is proved that epitaxial layers can be metastable, in the sense that the critical thickness can be largely exceeded without forming dislocations, this phenomenon was studied extensively in the SiGe material system [25].

In optoelectronics devices, for example in VECSELs, it is typical to work with an area of the dimension of  $0.1 \text{ mm}^2$  that emits several watts of output power, taking into

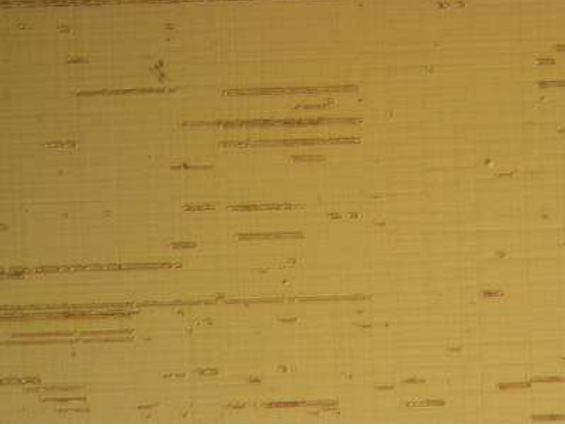


Figure 3.8: Optical microscope picture using Nomarsky contrast at  $200\times$  of a 0.6% tensile strained  $6\mu\text{m}$  thick layer on GaAs. A dislocation net is present together with some fractures.

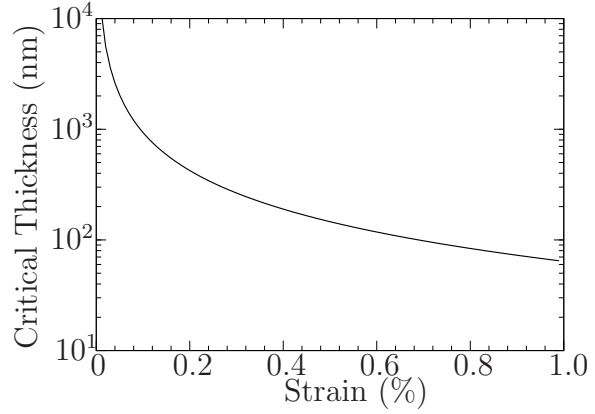


Figure 3.9: Critical thickness versus in-plane strain for a strained layer on GaAs substrate after [21].

account the device efficiency, one can infer that more than  $100\text{ W/cm}^2$  of heat is locally produced in the nanometer range thick QW regions. As a result these structures need to be particularly stable, aging effects of the operating devices can be surprisingly fast and detrimental.

A drastic improvement in the devices lifetime is obtained with the strain compensation, where the compressive strained layer are balanced with tensile strained ones. In fact, the formulae (3.75) and (3.76), can be rewritten for layers of thickness  $d_i$  and in-plane strain  $\epsilon_{\parallel,i}$  giving

$$W_{\text{dis.}} = \sum_i C_i d_i \left( \epsilon_{\parallel,i} - \frac{a}{2D} \right)^2 + \alpha \frac{\mu a^2}{16\pi} \ln \left( \frac{2\beta h}{a} \right) \frac{2}{D}, \quad (3.78)$$

$$\left. \frac{\partial W_{\text{dis.}}}{\partial \frac{1}{D}} \right|_{\frac{1}{D}=0} = - \sum_i C_i d_i \epsilon_{\parallel,i} + \alpha \frac{\mu a}{8\pi} \ln \frac{2\beta h_c}{a} = 0. \quad (3.79)$$

where  $h$  is here the total thickness of the grown layers. It is important to underline that in these formulae the average strain, weighted with the thickness and elastic constants, is responsible for the critical thickness of the whole structure. The main idea of the strain compensation is to try to increase  $h_c$ , reducing as much as possible the value of the summation in (3.79), where, in contrast to formula (3.75),  $\epsilon_{\parallel,i}$  is not taken with absolute value, in fact, a dislocation can increase or decrease the strain depending on its sign. In case most of the strain arise from the compressive strained InGaAs QWs, where more than 1% mismatch is accommodated, the strain can be compensated using GaAsP layers with phosphorus concentration between 10 and 25%, as can be seen in chapters 10, and 11.

The critical thickness expression (3.79) deserves some further comments. In fact, the  $h_c$  values should be not exceeded during the growth, namely when the structure is still incomplete, and should be also not be exceeded by just a part of the layer stack, so the

stability condition, given by this simplified model, is more strict than it may seem looking at (3.79).

### 3.9 Nonlinear optical crystals

The influence of the cubic symmetry has been analyzed in the particular case of the fourth-rank tensors  $c$  and  $s$ . The same direct inspection procedure can be applied, always for cubic crystals, to any second-rank tensor that represents a physical property of the material. It can be proved that such second-rank tensor is always proportional to the identity, therefore, its components are proportional to  $\delta_{ij}$  and it can be handled like a scalar. It follows that a cubic crystal material like GaAs exhibits, for example, scalar susceptibility, electrical and thermal conductivity, and cannot be birefringent, in fact, the index of refraction  $n(\omega)$  is defined from the susceptibility  $\chi(\omega)$  as

$$\vec{P}(\omega, t) = \varepsilon_0 \chi(\omega) \vec{E}(\omega, t) \quad \text{and} \quad n(\omega) = \sqrt{1 + \chi(\omega)}, \quad (3.80)$$

where  $\vec{P}$  is the polarization and  $\vec{E}$  is the electric field vector with pulsation  $\omega$ . If the susceptibility is a scalar, then also the refractive index is isotropic. On the other hand, an orthorhombic crystal like LBO (lithium triborate,  $\text{LiB}_3\text{O}_5$ ), that belongs to the point group  $mm2$  and has two mirrors planes perpendicular to the axis  $x_1$  and  $x_2$  and a two-fold rotation symmetry on  $x_3$ , exhibits a lower symmetry in the corresponding second-rank tensors. It can be proved by inspection, applying the  $mm2$  symmetries given by

$$1 \rightarrow -1 \quad 2 \rightarrow 2 \quad 3 \rightarrow 3, \quad (3.81)$$

$$1 \rightarrow 1 \quad 2 \rightarrow -2 \quad 3 \rightarrow 3, \quad (3.82)$$

$$1 \rightarrow -1 \quad 2 \rightarrow -2 \quad 3 \rightarrow 3, \quad (3.83)$$

on a generic second-rank tensor  $S$ , that its form, in a base set like the crystal axes, is given by

$$S = \begin{pmatrix} S_{11} & 0 & 0 \\ 0 & S_{22} & 0 \\ 0 & 0 & S_{33} \end{pmatrix}. \quad (3.84)$$

This expression holds for all orthorhombic crystals [14] and it means that orthorhombic crystals may show three different refractive indices along the three principal axes, namely they may have two optical axes, like LBO does.

The example of LBO crystal is important, because this material is one of the nonlinear crystals that are widely used in optoelectronics. In fact, as long as it is possible to have efficient VECSELs emitting in the infrared region, it is convenient to use nonlinear crystals to double the frequency of the output lasers beam and obtain a shorter emission wavelength, for example in the visible range. With this technique, blue [26, 27], green-yellow [28, 29] and orange [30] emission can be obtained.

The susceptibility in crystals can be written as a second-rank tensor as

$$P_i(\omega, t) = \varepsilon_0 \chi_{ij}(\omega) E_j(\omega, t), \quad (3.85)$$

and if the material is linear, this last equation represents the more general relationship between  $\vec{E}$  and  $\vec{P}$ , but for very intense electric fields, like in a laser cavity, the medium exhibits nonlinearity, in this case the expression (3.85) can be generalized introducing higher order terms, for example the second one, resulting in

$$P_i = \varepsilon_0 \chi_{ij} E_j + d_{ijk} E_j E_k. \quad (3.86)$$

The third-rank tensor  $d$  in the last equation is responsible for the frequency doubling because, if the vector  $\vec{E}$  has a time dependence  $\cos \omega t$ , then it results from the relation (3.86) that one part of the polarization vector has a time dependence  $\cos 2\omega t$  and so it can generate a field with  $2\omega$  pulsation, the so called second harmonic. In the following, it is more practical to consider just the the term of the polarization that generates the second harmonic defining

$$p_i = d_{ijk} E_j E_k, \quad (3.87)$$

and, to simplify the further derivation, the nonlinear process is assumed to be non-dispersive and lossless. This assumption is experimentally valid for many nonlinear crystals, nevertheless a complete derivation can be found in [31].

It follows directly from the tensor transformation rule, that if a material possess the inversion symmetry then

$$d_{ijk} = -d_{ijk} = 0, \quad (3.88)$$

and the tensor  $d$  is identically zero. This simple consideration proves that silicon and all the diamond-like crystals cannot be used to produce second harmonic, because they posses the inversion symmetry. The same is valid for all the amorphous materials, that are essentially isotropic, and so they posses all the symmetries.

The third-rank tensor  $d$ , generally speaking, has 27 components and has some intrinsic symmetries, for example, as long as it is possible to swap the indices  $j$  and  $k$  in (3.87) leaving  $p_i$  unchanged, it results that

$$d_{ijk} = d_{ikj}, \quad (3.89)$$

these equalities reduce the number of independent components of the tensor to 18. Starting from the definition

$$\vec{D} = \varepsilon_0 \vec{E} + \vec{P}, \quad (3.90)$$

and (3.86), it directly follows that

$$D_i = \varepsilon_0 E_i + \varepsilon_0 \chi_{ij} E_j + d_{ijk} E_j E_k, \quad (3.91)$$

and the energy per unit of volume  $w$  stored in the material because of the electric field can be expressed as

$$dw = E_i dD_i = \varepsilon_0 E_i dE_i + \varepsilon_0 \chi_{ij} E_i dE_j + 2d_{ijk} E_i E_j dE_k, \quad (3.92)$$

where the relations (3.89) are used. It is possible to proceed like in Sect. 3.3 where one can recognize that the differential (3.92) should be exact and it follows that

$$\left. \frac{\partial^2 w}{\partial E_i \partial E_j} \right|_{\vec{E}=0} = \varepsilon_0 (\delta_{ij} + \chi_{ij}) \quad \text{and} \quad \frac{\partial^3 w}{\partial E_i \partial E_j \partial E_k} = 4d_{ijk}, \quad (3.93)$$

and considering that one can exchange the order of derivation, this implies

$$\chi_{ij} = \chi_{ji} \quad \text{and} \quad d_{ijk} = d_{jki} = d_{kij}. \quad (3.94)$$

The energy density, which is the primitive function of the differential (3.92), can be thus obtained assuming that the energy is zero when no electric field is present

$$w = \frac{1}{2}\varepsilon_0 E_i^2 + \frac{1}{2}\varepsilon_0 \chi_{ij} E_i E_j + \frac{2}{3} d_{ijk} E_i E_j E_k. \quad (3.95)$$

The second group of equations in (3.94) represents the Kleinman symmetry [32], and it is also valid for the more general case of a complex tensor  $d$ . Considering that the order of the indices is unimportant, the number of the independent components of the tensor reduce to 10, and the  $d$  tensor is typically represented in form of a  $3 \times 6$  matrix. The general component  $d_{ijk}$  is written considering the smaller index as first and by grouping the remaining two using the six indices notation (3.27), so for example  $d_{332} = d_{233} = d_{23}$ . The complete pseudo-matrix is

$$d = \begin{pmatrix} d_{11} & d_{12} & d_{13} & d_{14} & d_{15} & d_{16} \\ d_{16} & d_{22} & d_{23} & d_{24} & d_{14} & d_{12} \\ d_{15} & d_{24} & d_{33} & d_{23} & d_{13} & d_{14} \end{pmatrix}. \quad (3.96)$$

The invariance of the tensor  $d$  under the  $\bar{4}3m$  symmetries of GaAs should be imposed like it was done for the tensor  $c$ , starting with the  $\bar{4}$  symmetry of the cube facets (3.29) one gets

$$d = \begin{pmatrix} -d_{22} & -d_{16} & -d_{23} & d_{14} & -d_{24} & d_{12} \\ d_{12} & d_{11} & d_{13} & -d_{15} & d_{14} & -d_{16} \\ -d_{24} & -d_{15} & -d_{33} & d_{13} & -d_{23} & d_{14} \end{pmatrix} = \begin{pmatrix} 0 & 0 & 0 & d_{14} & d_{15} & 0 \\ 0 & 0 & 0 & -d_{15} & d_{14} & 0 \\ d_{15} & -d_{15} & 0 & 0 & d_{15} & d_{14} \end{pmatrix} \quad (3.97)$$

and operating with the three-fold symmetry on the cube diagonals (3.32) one obtains

$$d = \begin{pmatrix} 0 & 0 & 0 & d_{14} & d_{12} & 0 \\ 0 & 0 & 0 & -d_{12} & d_{14} & 0 \\ d_{12} & -d_{12} & 0 & 0 & d_{12} & d_{14} \end{pmatrix} = \begin{pmatrix} 0 & 0 & 0 & d_{14} & 0 & 0 \\ 0 & 0 & 0 & 0 & d_{14} & 0 \\ 0 & 0 & 0 & 0 & 0 & d_{14} \end{pmatrix}. \quad (3.98)$$

It is easy to prove, that the mirror symmetry does not simplify the tensor any further and this result shows how a crystal like GaAs can generate second harmonic.

In a GaAs based VCSEL, grown on (001) substrate, the only strong components of the electric field present are  $E_1$  and  $E_2$ , because the electrical field in the cavity is mainly parallel to this plane, namely the  $x_1 x_2$  plane. Because of the form (3.98) of  $d$ , it follows that only a component  $p_3$  is present. As consequence, a frequency doubled emission is limited to the VCSEL plane where it is strongly absorbed. This explains why a GaAs based VCSEL device with emitting second harmonic was demonstrated on (113) substrate [33].

The case of LBO, that can be efficiently used, for example in VECSELs, can be also analyzed. LBO is an orthorhombic crystal having  $mm2$  symmetry, where each symbol

is referred to one of the three orthogonal principal axes. For this reason the reflection symmetry referred to the first axis is given by the transformations

$$1 \rightarrow -1 \quad 2 \rightarrow 2 \quad 3 \rightarrow 3, \quad (3.99)$$

the action of this symmetry on the tensor is obvious, all the  $d_{ijk}$  component with an uneven repetition of the index 1 have to be set to zero and so it directly follows

$$d = \begin{pmatrix} 0 & 0 & 0 & 0 & d_{15} & d_{16} \\ d_{16} & d_{22} & d_{23} & d_{24} & 0 & 0 \\ d_{15} & d_{24} & d_{33} & d_{23} & 0 & 0 \end{pmatrix}, \quad (3.100)$$

the same happens with the second reflection symmetry with the index 2, giving

$$d = \begin{pmatrix} 0 & 0 & 0 & 0 & d_{15} & 0 \\ 0 & 0 & 0 & d_{24} & 0 & 0 \\ d_{15} & d_{24} & d_{33} & 0 & 0 & 0 \end{pmatrix} \quad (3.101)$$

the third symmetry will not simplify further the tensor.

The actual use of LBO crystals, in order to have an improved efficiency of the second harmonic generation in a laser resonator, is rather complex, application in VECSEL can be found in [26]. A detailed review on nonlinear optics can be found in [31].



# Chapter 4

## Basics of VCSELs and VECSELs

In this chapter, the basic principles of VCSELs and VECSELs are shortly described, followed by a section regarding the Fresnel's formulae for the propagation of electromagnetic waves through a plane interface. As conclusion, the transfer-matrix method which generalizes the Fresnel's formulae to multilayer structures is reported and applied to the calculation of the threshold gain in VCSELs and VECSELs. A deeper theoretical introduction on VCSEL and VECSEL devices can be found in [34] and [35] respectively, a general overview on semiconductor laser is given in [36].

### 4.1 VCSELs

The vertical-cavity surface-emitting laser is a type of semiconductor laser diode with laser beam emission perpendicular to the wafer surface, in contrast to edge-emitting lasers that exhibit laser emission from the cleaved facets. This main difference is the key of the VCSEL success, making it suitable for large scale production, because many lasers can be processed on-wafer simultaneously.

A typical VCSEL, depicted in Fig. 4.1, is composed of two high-reflectivity periodic stacks of layers presenting a modulation in the refraction index, the so called distributed Bragg reflectors (DBRs), that create the optical resonator. When GaAs substrates are used, the easiest DBR is obtained by growing a periodic stack of GaAs and AlAs layers having a respective optical thickness of a quarter of wavelength and, in order to reach the wanted reflectivity, it is common to pile up more than 20 pairs. The resulting reflector may have a thickness of several micrometers and should be practically unstrained to remain pseudomorphic. For this reason, on GaAs the only material which is suitable is AlGaAs, because  $\text{Al}_x\text{Ga}_{1-x}\text{As}/\text{Al}_y\text{Ga}_{1-y}\text{As}$  pairs can be easily grown without any relaxation. Anyhow, the reflectivity of the DBRs is strongly dependent on the refractive index contrast of the pairs and GaAs/AlAs exhibits the highest performances. An obvious limitation in the DBR design is given by the absorption edge of the materials constituting the layers, considering that the GaAs bandgap is situated at approximately 873 nm at room temperature, it is obvious that for shorter wavelengths a progressively higher aluminum content is needed, decreasing the DBR contrast.

Always referring to Fig. 4.1, it can be noticed that the bottom DBR ( $n$ -doped reflector) is constituted of more pairs than the relative top stack ( $p$ -doped reflector), improving the

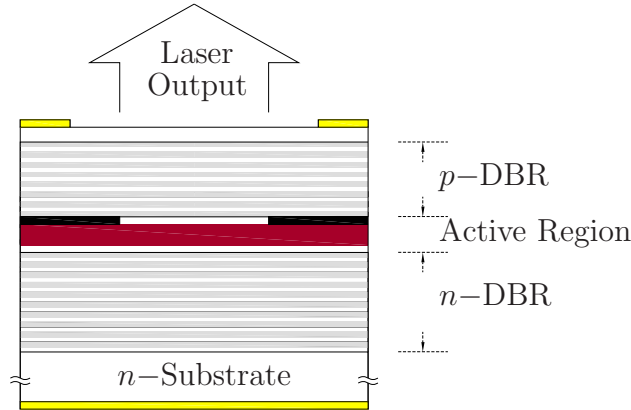


Figure 4.1: Sketch of a VCSEL device.

top/bottom emission ratio. The doping profile is a crucial feature in VCSELs, that are diode lasers operating when the junction is forward biased. Considering that the best GaAs substrates are silicon  $n$ -doped, it is natural to start the device with the  $n$ -DBR which exhibits also a lower optical absorption.

The typical layer sequence, close to the middle of a VCSEL cavity, is reported in Fig. 9.2, where at the left side of the picture the last two  $n$ -doped pairs can be seen. Moving to the center of the figure, the doping level is decreasing, going to zero in connection with the active zone (intrinsic material), which is in this case constituted of three 8 nm thick GaAs QWs separated by 10 nm  $\text{Al}_{0.3}\text{Ga}_{0.7}\text{As}$  layers. The  $p$ -doped DBR stack is placed on the other side of the intrinsic active region.

When the diode is forward biased, the majority carriers are injected in the active region, where they can recombine radiatively. In this situation, the QWs in the intrinsic region are the active material, in fact, the presence of electrons in conduction band and of holes in valence band allows photons of the right wavelength to stimulate the emission of other photons of the same wavelength and with the same phase. As result, laser operation is possible if the carrier injection is high enough to sustain this process continuously.

The main difference between a semiconductor laser and a simple light-emitting diode (LED) is the presence of the optical resonator, which is designed to decrease the threshold current necessary to achieve the laser emission.

The active layers are typically made of QWs, where a high carrier density can be reached and the density of states in conduction and in valence band is a step-like function of the energy, in contrast to bulk material where the square root functional dependence is given.

In VCSELs the current should be confined spatially, in order to reach an high injection density of carriers, this scope is achieved by the partial lateral oxidation of an highly  $p$ -doped AlAs layer having a typical thickness of 20–40 nm. This oxidation is very selective and the layers containing even few percent of gallium are not involved in the process [37].

A good VCSEL design is a compromise between the optical, the electrical and even the thermal problems, which are tightly coupled. In fact, not only the standing wave

pattern should be calculated and optimized to improve the device performances, but also the right doping levels should be chosen. A simple DBR made of two different materials, separated by abrupt interfaces, creates heterojunctions that increase the series resistance of the device, hence composition-graded DBRs are usually preferred. The same is valid for the position of the highly doped AlAs oxidation layer that is situated in a node of the standing wave pattern, in order to minimize the free carrier absorption, even though this position is not optimal in the resonator. Furthermore, the doping profile is modulated in order to reduce the free carrier absorption in the cavity. In the chapters 8,9, and 10 are reported more details regarding these VCSEL structures.

## 4.2 VECSELs or semiconductor disk lasers

A VECSEL or semiconductor disk laser is sketched in Fig. 4.2. In this kind of device, the optical resonator is not monolithic, but an external curved mirror is placed outside the sample. An inverted structure is typically grown on the GaAs substrate, which is then removed in order to mount the epitaxial layers directly on a heat sink. The structure consists of the semiconductor DBR that is followed by a periodic gain structure, as can be seen in more detail in the simplified band diagram of Fig. 4.3.

In optically pumped VECSELs, the inversion of population in the QW region is generated by an external laser beam that is strongly absorbed in the region close to the QWs (in Fig. 4.3 the absorption region), the carriers can just diffuse to the QWs, where they can recombine by stimulated emission. Another possibility is to pump the structure with a laser wavelength very close to the emission one, pumping the QWs directly. This second pump mode can be very inefficient, unless special design is used, like resonant pumping. In QW-pumped VECSELs, the quantum defect can be drastically reduced and net energy conversion efficiency of this devices can be as high as 50% [38].

The advantage of VECSELs is that the energy flux, supplied by an array of laser beams characterized by a bad beam quality factor, can be converted in a single laser having a drastically improved beam quality. Another advantage is that the external cavity can be

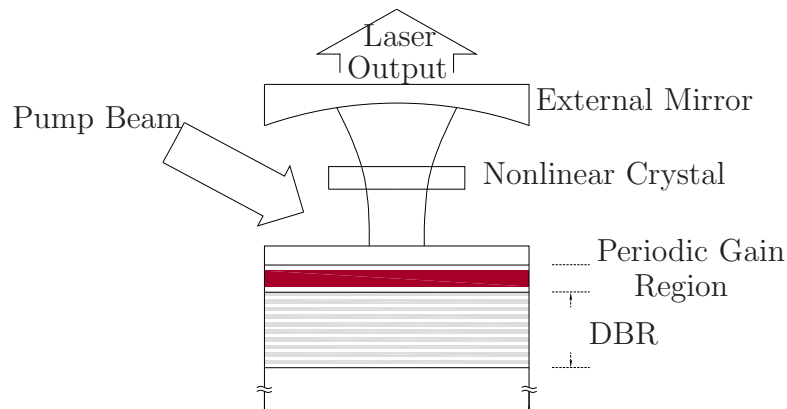


Figure 4.2: Sketch of a VECSEL device.

used to sense gases or, by inserting a nonlinear crystal like LBO, to obtain visible laser emission by frequency doubling. As example, second harmonic blue emission at 490 nm can be obtained from a VECSEL device working in the infrared at 980 nm.

A VECSEL can also be pumped electrically and the laser structure is similar to the one of a standard VCSEL, but the number of the top DBR pairs is drastically reduced, in order to increase the optically coupling between the monolithic cavity and the external one. Some electrically pumped VECSELs are presented in chapter 10.

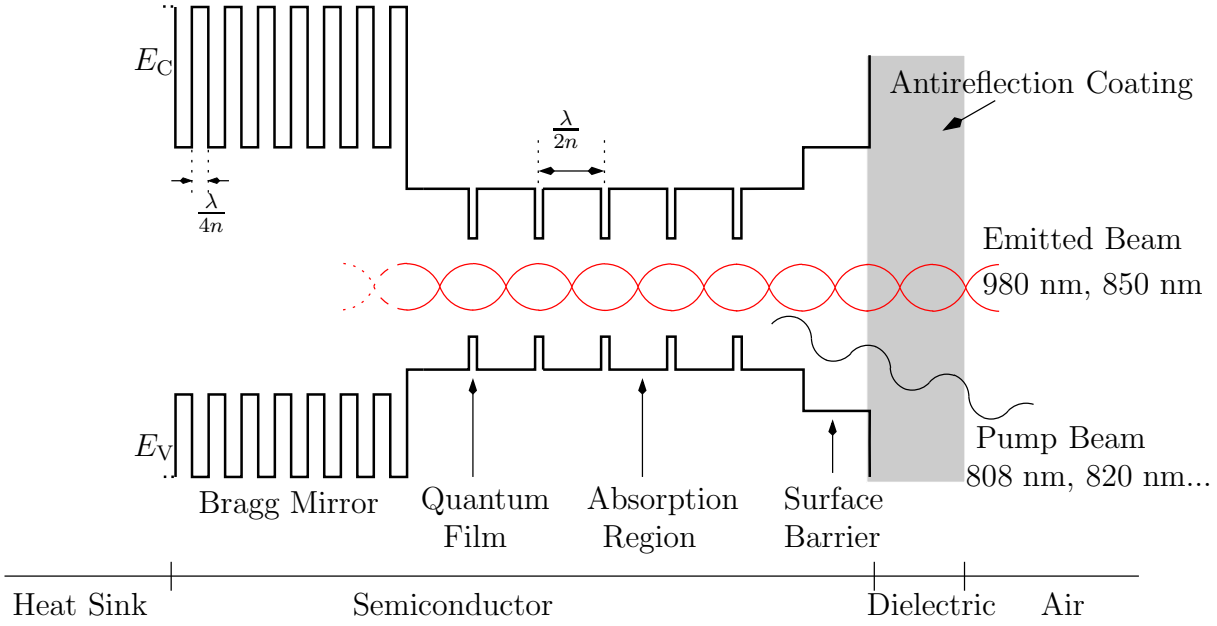


Figure 4.3: Schematic band diagram of a VECSEL structure.

### 4.3 Fresnel's formulae

The problem of the reflection and transmission of an electromagnetic plane wave at the plane interface between two media is solved by the Fresnel's formulae. These equations are here reported just to introduce the suitable formalism that is also used in the next section, where a generic multilayer system is considered in order to analyze laser structures.

An incident plane wave propagates to the interface between two isotropic media characterized by the refractive indexes  $n_1$  and  $n_2$  and, as seen in chapter 3, cubic crystals always exhibits an isotropic refractive index, so what follows can be applied to GaAs and all the other alloys having cubic crystal structure.

It is natural to search the solutions in the plane wave form like

$$\vec{E}_j = A_j e^{-i\vec{k}_j \cdot \vec{r}} \quad \text{where} \quad k_{j,x}^2 + k_{j,y}^2 + k_{j,z}^2 = \left(n_j \frac{\omega}{c}\right)^2, \quad (4.1)$$

where  $\omega$  is the pulsation of all the waves, and the time dependence is not written for simplicity.

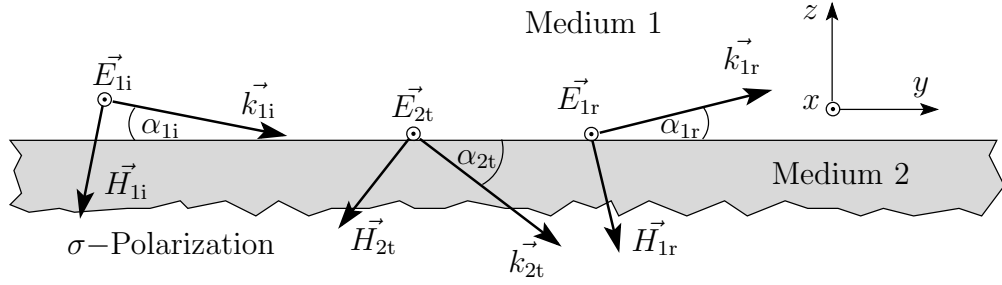


Figure 4.4: The three waves in the  $\sigma$ -polarization case,  $\vec{E}$  is perpendicular to the plane defined by  $\vec{k}$  and the normal to the surface.

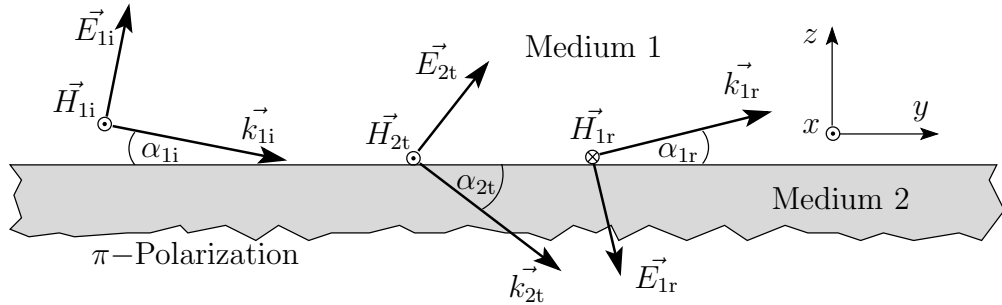


Figure 4.5: The three waves in the  $\pi$ -polarization case,  $\vec{E}$  is parallel to the plane defined by  $\vec{k}$  and the normal to the surface.

Referring now to Fig. 4.4 and 4.5, the three waves, incident, reflected, and transmitted, can be considered in the two polarization states  $\sigma$  and  $\pi$ . In the pictures, the angles are measured relative to the surface, this is commonly done in literature for x-ray, in optics the angles are usually measured relative to the surface normal. The boundary conditions deriving from the Maxwell's equations can be applied at the interface for the three plane waves. This procedure will result in relations between the waves amplitudes  $A_j$ , the Fresnel's formulae:

for the  $\sigma$ -polarization

$$r_{1,2} = \frac{A_{1r}}{A_{1i}} = \frac{k_{1i,z} - k_{2t,z}}{k_{1i,z} + k_{2t,z}} = -r_{2,1} \quad (4.2)$$

$$t_{1,2} = \frac{A_{2t}}{A_{1i}} = \frac{2k_{1i,z}}{k_{1i,z} + k_{2t,z}} = 1 + r_{1,2} \quad (4.3)$$

and for the  $\pi$ -polarization

$$r_{1,2} = \frac{A_{1r}}{A_{1i}} = \frac{n_1^2 k_{2t,z} - n_2^2 k_{1i,z}}{n_2^2 k_{1i,z} + n_1^2 k_{2t,z}} = -r_{2,1} \quad (4.4)$$

$$t_{1,2} = \frac{A_{2t}}{A_{1i}} = \frac{2n_1 n_2 k_{1i,z}}{n_2^2 k_{1i,z} + n_1^2 k_{2t,z}} = \frac{n_1}{n_2} (1 - r_{1,2}) . \quad (4.5)$$

Some comments are needed for the calculation of  $k_{2t,z}$  in the previous equations, it holds

$$k_{1i,y} = k_{2t,y} \quad (4.6)$$

which is the Snell's law written for the  $\vec{k}$  vectors and is also valid for complex refractive indices and it follows

$$k_{2t,z} = -\sqrt{(n_2^2 - n_1^2) \left(\frac{\omega}{c}\right)^2 + k_{1i,z}^2} \quad \text{with} \quad k_{1i,z} = -n_1 \frac{\omega}{c} \sin \alpha_{1i}, \quad (4.7)$$

considering that all the  $k_{j,x}$  are zero and that  $\alpha_{1i}$  is the incidence angle of the incoming wave. The right solution for the square root in (4.7) should be correctly selected, therefore, its imaginary part should be positive in case the medium 2 absorbs, and negative in case the medium 2 is active.

## 4.4 Multilayers, the transfer-matrix method

The presence of more than two materials can be treated by taking into account all the reflected waves generated at any interface. This task can be efficiently performed using the transfer-matrix method [39]. In Fig. 4.6, a generic multilayer structure is depicted as reference. The field in any layer can be described as composed of two waves propagating backward and forward. The incoming wave has an amplitude  $T_1 = 1$  and an incidence angle  $\alpha_1$ , the reflected wave  $R_1$  is the unknown, together with the amplitudes of the waves in each layer,  $T_j$  and  $R_j$ . The Snell's law is still valid for each layer and so it follows

$$n_1 \cos \alpha_1 = n_j \cos \alpha_j \quad \text{or} \quad k_{1,y} = k_{j,y}, \quad (4.8)$$

where the second expression is preferred in case of complex refractive indices. In the same way, the  $z$  component of  $\vec{k}_j$  of the transmitted wave in each layer can be calculated using (4.7), while the same value, but with opposite sign, should be assigned to the respective reflected wave. The Fresnel's formulae hold for a generic interface between medium  $j$  and medium  $j + 1$

$$r_{j,j+1} = \frac{A_{jr}}{A_j} = \frac{k_{j,z} - k_{j+1,z}}{k_{j,z} + k_{j+1,z}} = -r_{j+1,j} \quad (4.9)$$

$$t_{j,j+1} = \frac{A_{j+1}}{A_j} = \frac{2k_{j,z}}{k_{j,z} + k_{j+1,z}} = 1 + r_{j,j+1}, \quad (4.10)$$

where just the formulae for the  $\sigma$ -polarization are here written, just to clarify the formalism. At every interface the amplitude of the two waves can be defined. Referring to Fig. 4.6, the amplitudes at the interface  $j$  and  $j + 1$  can be written as

$$R_j = t_{j+1,j} \tilde{R}_{j+1} + r_{j,j+1} T_j \quad (4.11)$$

and

$$\tilde{T}_{j+1} = t_{j,j+1} T_j + r_{j+1,j} \tilde{R}_{j+1}. \quad (4.12)$$

The last two equations can be written in matrix form by defining the objects

$$V_j = \begin{pmatrix} T_j \\ R_j \end{pmatrix} \quad \text{and} \quad \tilde{V}_j = \begin{pmatrix} \tilde{T}_j \\ \tilde{R}_j \end{pmatrix}, \quad (4.13)$$

and writing formally

$$V_j = B_j \tilde{V}_{j+1} \quad \text{where} \quad B_j = \frac{1}{t_{j,j+1}} \begin{pmatrix} 1 & r_{j,j+1} \\ r_{j,j+1} & -r_{j,j+1}r_{j+1,j} + t_{j,j+1}t_{j+1,j} \end{pmatrix}, \quad (4.14)$$

where the expression of the matrix  $B_j$  can be further simplified, depending on the polarization. The matrix  $B_j$  transforms the amplitudes through the interface  $j$ . Another matrix can be defined to propagate the waves amplitudes from the back surface to the top surface of the generic  $j$ -th layer as follows

$$\tilde{V}_{j+1} = \Phi_{j+1} V_{j+1} \quad \text{with} \quad \Phi_{j+1} = \begin{pmatrix} e^{-ik_{j+1,z}d_{j+1}} & 0 \\ 0 & e^{ik_{j+1,z}d_{j+1}} \end{pmatrix}. \quad (4.15)$$

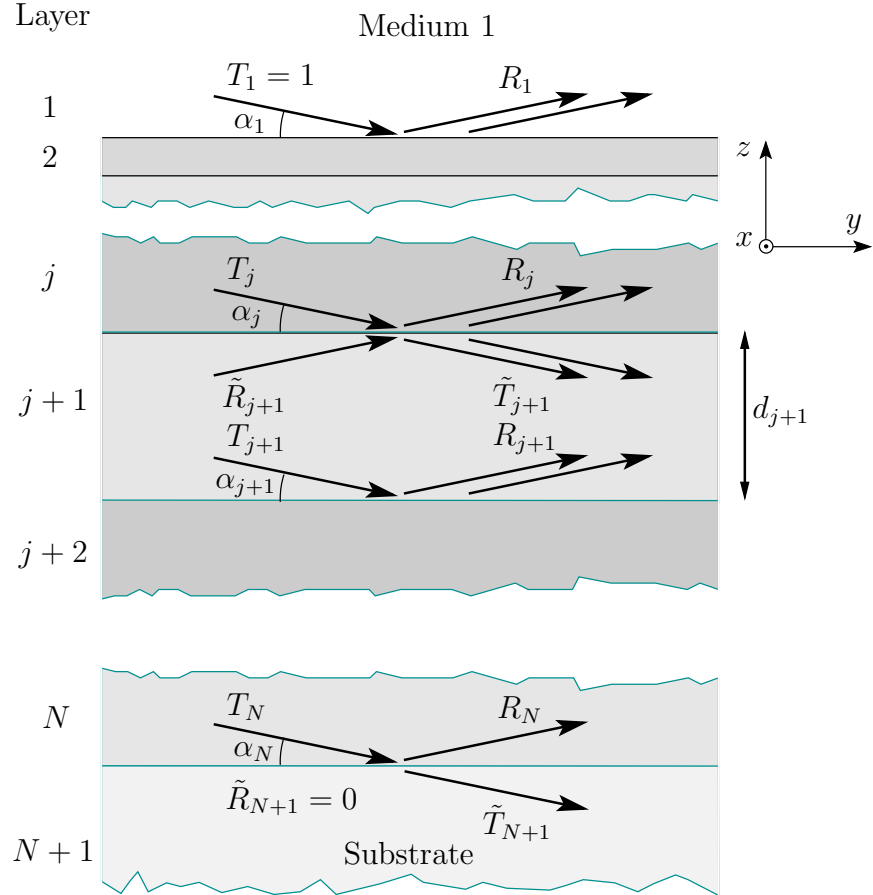


Figure 4.6: Scheme of a multilayer structure.

The defined matrices can be multiplied in sequence obtaining

$$V_1 = \left( \prod_{j=1}^{N-1} B_j \Phi_{j+1} \right) B_N \tilde{V}_{N+1} = M \tilde{V}_{N+1} \quad \text{with} \quad \tilde{V}_{N+1} = \begin{pmatrix} \tilde{T}_{N+1} \\ 0 \end{pmatrix}. \quad (4.16)$$

As can be seen in Fig. 4.6, the second component of the vector  $\tilde{V}_{N+1}$  is zero, while its first component can be calculated from the value of  $T_1$ . Hence, the reflectivity of the multilayer is given by

$$\mathbf{R}(\alpha_1) = \left| \frac{R_1}{T_1} \right|^2 = \left| \frac{M_{21}}{M_{11}} \right|^2, \quad (4.17)$$

where  $M_{11}$  and  $M_{21}$  are the respective components of the matrix  $M$ . It is possible to calculate the field in every point of the structure, using the proper matrix in (4.16).

In case of a laser device, some layers in the structure are active media and are characterized by a gain  $\alpha$  associated to a positive imaginary part of the refractive index  $\beta$  by the relation

$$\beta = \frac{\lambda \alpha}{4\pi}. \quad (4.18)$$

The value of  $\alpha$  or correspondly  $\beta$  is function of the population inversion level in the active media. In particular, there is a value of the gain that should be reached in order to have an emission from the laser sides without any incoming beam. When this gain is reached the structure lases. The transfer-matrix methods allows to calculate the so defined threshold gain. In fact the structure is lasing when the additional condition  $T_1 = 0$  is fulfilled. Considering that  $\tilde{R}_{N+1}$  is already set to zero, the aforementioned condition requires that no waves are impinging into the structures, but just two waves are emitted, with the amplitudes  $R_1$  and  $\tilde{T}_{N+1}$ , from the top and the bottom of the structure respectively. By increasing continuously the value of  $\beta$ , which is treated as variable parameter in the structure, the condition  $T_1 = 0$  can be satisfied and the relative value of the gain is then the threshold gain.

Transfer-matrix calculation were performed in this thesis using the REFLEX code [40], in order to calculate the threshold gain of the structures and the relative standing wave patterns.



# Chapter 5

## Basic x-ray diffraction theory

In this chapter, the basic theory of x-ray reflectometry and x-ray diffraction is discussed. The behavior of x-ray waves in matter can be described using the same matrix formalism defined in the chapter 4.

Examples regarding some particular structures illustrate how these techniques can be fruitfully used to characterize the grown samples.

### 5.1 X-ray reflectometry

X-ray reflectometry (XRR) is a technique that allows to characterize bulk materials or multilayer systems. In contrast to other diffraction methods, XRR also allows the investigation of amorphous materials.

XRR experiments are performed by illuminating at low incidence angle the surface of the sample, that is supposed to be flat, with a monochromatic x-ray beam and by collecting the elastically scattered photons at the specular reflection angle. This means that the difference between the exit and incidence wave vectors,  $\Delta\vec{k} = \vec{k}_e - \vec{k}_i = \vec{q}$ , is normal to the sample surface. The typically used x-ray wavelength  $\lambda$  ranges between 0.1 and 0.3 nm and the angular scan is recorded in the region of small incidence angles, commonly in the range 0–4°.

A vast literature on the argument was produced after the publication of the pioneering work of Parratt in 1954 [41] and good reviews on this topic are [42, 43, 44]. As already mentioned, in x-ray reflectometry the 2×2 transfer-matrix formalism is used exactly like in optics, in fact, it is possible to define, for x-rays at low incidence angles, a refractive index and, in contrast to x-ray diffraction experiments, a periodic disposition of atoms is not required. In fact, the integrals that are needed to calculate the scattered field amplitude  $\vec{E}$  can be approximated by

$$\vec{E}(\vec{r}) \sim \frac{e^{ikr}}{r} f(\vec{q}) \quad \text{with} \quad f(\vec{q}) = \int \rho(\vec{r}') e^{-i\vec{q} \cdot \vec{r}'} d\vec{r}' \quad \text{and} \quad k = \frac{2\pi}{\lambda}, \quad (5.1)$$

where  $\rho(\vec{r}')$  is the electron density [45]. It follows that at low angles, the transferred vector  $\vec{q}$  is so small that fast spatial variations of  $\rho(\vec{r}')$  can be neglected. In practice, in XRR the electron density  $\rho(\vec{r}')$  can be approximated by its averaged value,  $\bar{\rho}(\vec{r}')$ , taken

on a microscopic scale, smoothing the atom-to-atom variations. This allows to define a material susceptibility for x-ray and therefore a refractive index.

The susceptibility  $\chi(\vec{r})$  should be introduced to define a refractive index, and it can be written as a function of the local electron density. Just using semiclassical arguments, it holds

$$\chi(\vec{r}) = -r_{\text{el}} \frac{\lambda^2}{\pi} \tilde{\rho}(\vec{r}) \quad \text{with} \quad r_{\text{el}} = 2.82 \times 10^{-15} \text{ m} , \quad (5.2)$$

where  $r_{\text{el}}$  is the classical electron radius constant. The formula (5.2) can be proved simply imagining that the electrons in an atom are attracted by the nucleus with an elastic force characterized by  $\omega_0$  and are subjected to a periodic electric field of angular frequency  $\omega$ . Thence one can write

$$m\ddot{\vec{r}} = -m\omega_0^2 \vec{r} - e\vec{E}e^{i\omega t} , \quad (5.3)$$

where  $e$  and  $m$  are the electron charge and mass respectively. The solution for the displacement  $\vec{r}$  is

$$\vec{r} = \frac{-e}{m(\omega_0^2 - \omega^2)} \vec{E}e^{i\omega t} \quad (5.4)$$

and it is proportional to the electrical field. From the definitions of  $\chi$  and of the polarization vector  $\vec{P}$  one has

$$\vec{P}(\vec{r}) = -e\tilde{\rho}(\vec{r})\vec{r} = \varepsilon_0\chi(\vec{r})\vec{E}e^{i\omega t} , \quad (5.5)$$

where  $\varepsilon_0$  is the vacuum permittivity. Substituting (5.4) in (5.5), the susceptibility is obtained

$$\chi(\vec{r}) = \frac{e^2 \tilde{\rho}(\vec{r})}{m\varepsilon_0(\omega_0^2 - \omega^2)} . \quad (5.6)$$

In this formula  $\omega_0$  has the physical meaning of plasma angular frequency and, in the case of x-ray, the formula (5.6) can be further approximated and finally compared with (5.2). It follows that

$$\chi(\vec{r}) \simeq -\frac{e^2 \tilde{\rho}(\vec{r})}{m\varepsilon_0\omega^2} = -r_{\text{el}} \frac{\lambda^2}{\pi} \tilde{\rho}(\vec{r}), \quad \omega \gg \omega_0 \quad \text{and} \quad r_{\text{el}} = \frac{e^2}{4\pi\varepsilon_0 mc^2} , \quad (5.7)$$

where  $c$  is the speed of light and so  $r_{\text{el}}$  is expressed in term of universal constants. The refractive index is defined directly by

$$n(\vec{r}) = \sqrt{1 + \chi(\vec{r})} \quad (5.8)$$

and considering that for x-rays  $\chi \ll 1$  one can write

$$n(\vec{r}) \simeq 1 + \frac{\chi(\vec{r})}{2} = 1 - \delta(\vec{r}) - i\beta(\vec{r}) \quad \text{with} \quad (5.9)$$

$$\delta(\vec{r}) = \frac{\lambda^2}{2\pi} r_{\text{el}} \rho(\vec{r}) \quad \text{and} \quad \beta(\vec{r}) = \frac{\lambda}{4\pi} \mu(\vec{r}) , \quad (5.10)$$

The existence of the imaginary part  $\beta$  of the refractive index can be proved theoretically using better models that include the quantum behavior of the electrons. The physical

	$\delta$ ( $10^{-6}$ )	$\beta$ ( $10^{-7}$ )	$1/\mu$ ( $\mu\text{m}$ )	$\alpha_c$ ( $^\circ$ )
Vacuum	0	0	$+\infty$	0
PMMA( $\text{C}_5\text{H}_8\text{O}_2$ ) $_n$	4.0	0.09	1400	0.162
PVC ( $\text{C}_2\text{H}_3\text{Cl}$ ) $_n$	4.6	1.05	120	0.174
Quartz ( $\text{SiO}_2$ )	7.1	1.04	120	0.21
Silicon	7.6	1.73	70.9	0.223
Nickel	27.4	4.99	24.6	0.424
Gold	49.6	51.1	2.40	0.570

Table 5.1: Values of  $\delta$ ,  $\beta$ , intensity penetration depth  $1/\mu$ , and critical angle  $\alpha_c$  for different materials at  $\lambda = 0.154$  nm after [43].

meaning of  $\beta$  is related directly related to the x-ray linear absorption coefficient  $\mu$ , and  $1/\mu$  is the penetration depth, where the wave intensity is reduced by a factor  $e$ , namely

$$\frac{1}{\mu} = \frac{\lambda}{4\pi\beta}. \quad (5.11)$$

It is important to underline that, in virtue of (5.10), the real part of  $n$  is smaller than 1 and total reflection on the sample surface occurs under a critical angle  $\alpha_c$ . This angle is always very small because  $n \simeq 1$ . A refractive index lower than 1 implies just a phase velocity higher than speed of light in vacuum  $c$  and this is, of course, not in contradiction with any physical principle.

In Table 5.1 values of  $\delta$ ,  $\beta$ ,  $1/\mu$ , and  $\alpha_c$  are given for different materials.

Despite its simplicity, the susceptibility model, previously reported, allows to estimate  $\delta$  in a easy way for every material. For example, a silicon crystal has a diamond-like structure with 8 atoms in the unit cell, considering that the silicon atom has 14 electrons, the electronic density can be calculated using the silicon crystal lattice constant of  $a_{\text{Si}} = 0.357$  nm and so  $\delta$

$$\delta_{\text{Si}} \simeq \frac{\lambda^2}{2\pi} r_e \rho_{\text{Si}} = \frac{\lambda^2}{2\pi} r_e \frac{8 \times 14}{a_{\text{Si}}^3} \simeq 7.4 \times 10^{-6}, \quad (5.12)$$

this value is very close to the tabulated one (see Table 5.1).

The knowledge of the refractive index allows to simulate the reflectivity curve recorded at low angles, by applying the transfer-matrix method introduced in chapter 4. In this way, information about layered samples can be extracted by fitting the experimental data with the simulation.

In optoelectronics the use of XRR permits to characterize non-crystalline materials, like oxide coatings, or to measure with high precision the thickness of deposited metal. In particular, XRR allows the modeling of the layer interfaces, because the roughness of the interfaces can be estimated even for buried layers.

In Fig. 5.1, the XRR spectra of three coated samples are shown, the coating thicknesses of 98, 97, and 98 nm could be measured with high precision. At very low angle the spectra

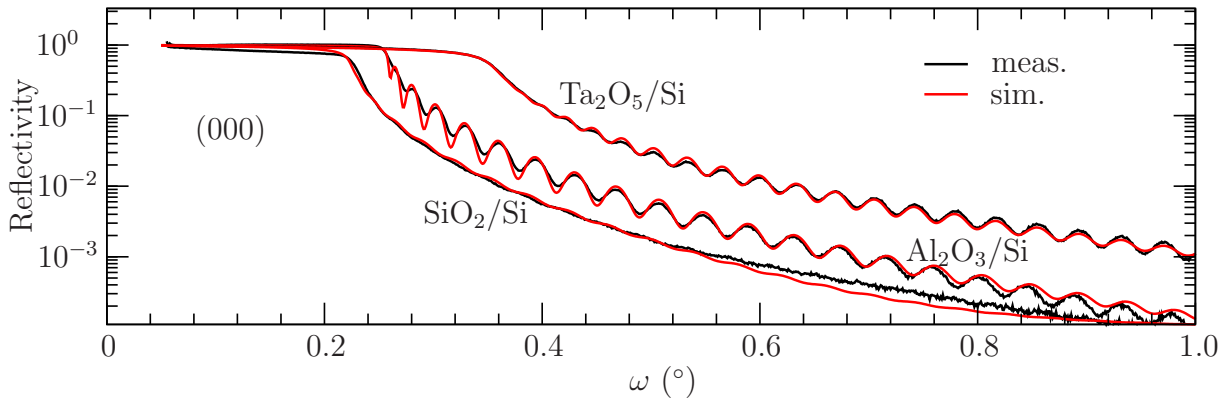


Figure 5.1: XRR spectra and simulation curves of three coated samples. The plateau at low angles are corrected to take into account some experimental setup artefacts. The thickness of the three coatings are 98, 97, and 98 nm from top to bottom respectively.

should be corrected (see Fig.5.1), because at grazing incidence the x-ray beam typically irradiates an area larger than the sample itself.

Another group of measurements are shown in Fig. 5.2, where the samples consist of platinum thin films of different thicknesses deposited on glass substrates. The platinum

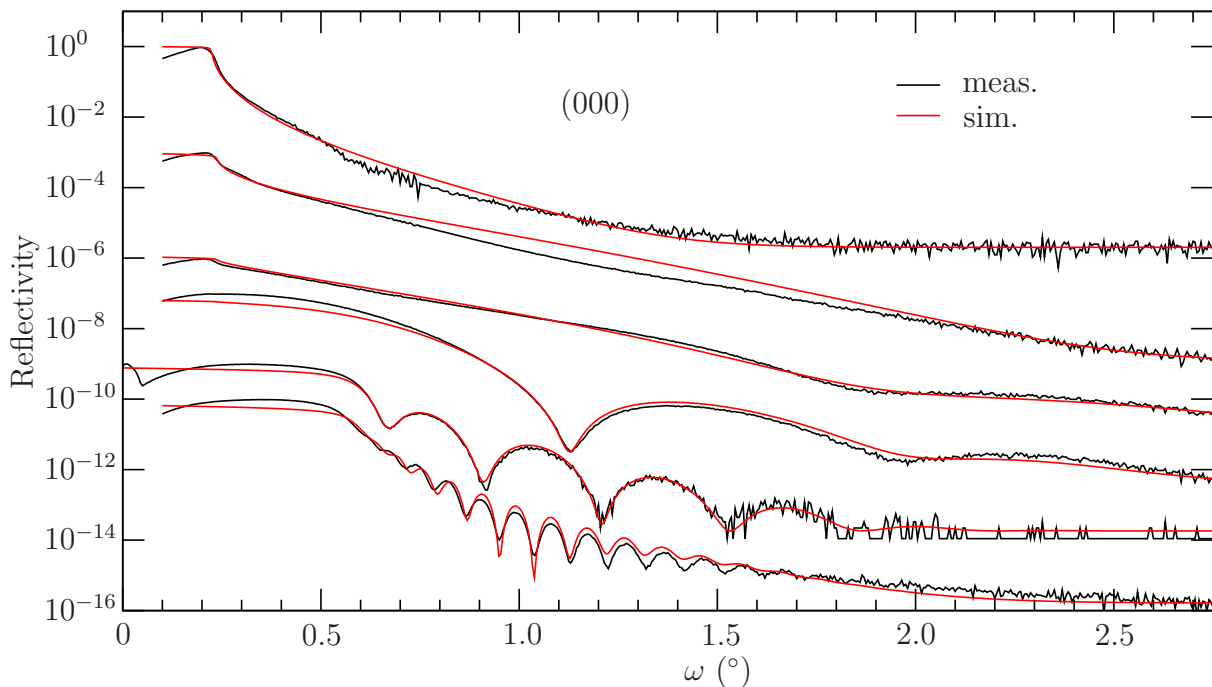


Figure 5.2: XRR recorded spectra, non corrected at low angles, and simulations for platinum on glass. From top to bottom, the nominal platinum thicknesses are 0, 1, 2, 5, 15, and 50 nm.

Nominal thickness (nm)	Measured thickness (nm)	Roughness Pt/air	Roughness glass/Pt
0	0	0	0.9
1	0.9	0.6	1.0
2	2.3	0.3	0.6
5	4.6	0.8	0.5
15	12.4	0.8	0.8
50	41.1	1.5	0.7

Table 5.2: Fitted parameters matching the measured curves in Fig. 5.2. The roughness values should to be correctly interpreted.

thickness and the roughness of the two interfaces can be determined, for each sample, by fitting the recorded data with the simulations. The results are summarized in Tab. 5.2, where a special comment on the roughness should be given.

In fact, in XRR the interface roughness is intended as the width of the in-plane averaged refractive index profile variation between two layers. For this reason XRR cannot distinguish between a graded and a rough interface.

In Fig. 5.3, the density (or similarly the refractive index) profile is plotted for the third sample of the described series, the roughness is just intended as the  $\sigma$  of the "erf" profile between two layers. That means, that the roughness values are just parameters to model the density profile, for this reason, there is no contradiction in simulating a roughness bigger than the layer thickness itself. One has also to consider that at very small thicknesses, the model adopted is too naive, in fact, oxidation takes place altering the density profile drastically at this thicknesses. It is anyway interesting to note how XRR is still sensitive to a platinum layer of almost 1 nm nominal thickness.

The XRR can also be intended as a special case of x-ray diffraction performed at the (000) reflection.

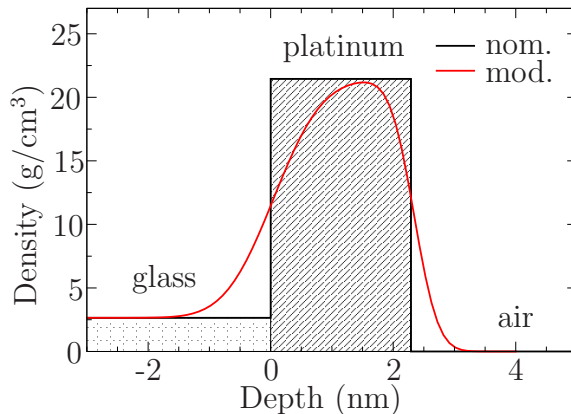


Figure 5.3: Nominal and modelled profile of the 2 nm thick platinum layer on glass.

## 5.2 Dynamical theory of x-ray diffraction

The equations (5.1) are based on the implicit assumption that the scattered field is given by linear surposition of the effects that the incoming beam would have on every electron. This is the kinematical approximation, where the incoming beam is supposed to be unperturbed and the scattered waves do not interact with the sample. The use of this approximation is justified by the weakness of the interaction between x-ray and matter and the scattering intensity can be calculated with success in several situations, like small and non perfect crystals. Different formulations of the kinematical theory can be given, but it is always assumed that the scattered waves do not interact with the sample itself.

In case of thick and perfect samples, this approximation cannot be used, and a theory that takes into account the multiple scattering should be used. These theories are called dynamical.

Following this arguments, the  $2 \times 2$  transfer-matrix method, introduced for optical wavelengths and for x-ray reflectivity, is a dynamical theory. The x-ray diffraction dynamical theory is essentially the solution of the Maxwell's equations in not homogeneous media, because the atom-to-atom variation of the electron density should be taken into account.

In particular, in case of crystals, the solution is searched in the Bloch form

$$\vec{E}(\vec{r}) = \sum_{\vec{g}} \vec{E}_g e^{i\vec{k}_g \cdot \vec{r}} \quad \text{with} \quad \vec{k}_g = \vec{k}_0 + \vec{g} \quad (5.13)$$

where  $\vec{g}$  are the reciprocal space vectors, and  $\vec{k}_0$  belongs to the first Brillouin zone and is unknown. The Maxwell's equations can be written for  $\vec{E}$  using the assumption (5.13) obtaining an infinite system of algebraic equations

$$k^2 \vec{E}_{\vec{g}} - \vec{k}_g \times (\vec{E}_{\vec{g}} \times \vec{k}_g) = -k^2 \sum_{\vec{p}} \chi_p \vec{E}_{g-p}, \quad (5.14)$$

where  $\chi_g$  are the Fourier coefficients of the periodic crystal susceptibility expanded as follows

$$\chi(\vec{r}) = \sum_{\vec{g}} \chi_g e^{i\vec{g} \cdot \vec{r}}. \quad (5.15)$$

The system (5.14) can be solved if one restricts the number of equations, that means the number of vectors  $\vec{g}$  in the series (5.13). Assuming that the series has only one term, only one plane wave propagates in the crystal (one beam approximation). This approximation is valid if the crystal does not diffract and the plane wave represents the transmitted wave. The problem requires to calculate two amplitudes, and the  $2 \times 2$  transfer-matrix formalism is obtained giving the XRR equations. If the series contains two non-zero terms, two plane waves propagates (two beam approximation), the transmitted and the diffracted wave. Four amplitudes are needed and a more complicated  $4 \times 4$  transfer-matrix method should be used.

Three or even more beams are seldom needed in x-ray diffraction, because multiple diffraction is rare when the probing wavelength has the same order of magnitude of the crystal lattice constant.

A short comment regarding the recorded x-ray spectra is needed. The measurements were all performed with a Siemens D5000 equipped with a standard high resolution (+--+) Ge(022) monochromator set on the  $\text{CuK}\alpha_1$  wavelength of 0.1541 nm. The achieved resolution is approximately  $12''$ . All the measured spectra are  $\omega/2\theta$  scans on symmetric reflections, because the perfect pseudomorphicity of the structures made asymmetric reflections not strictly necessary. The detector slit was always set to 0.2 mm, the few exceptions are explicitly documented.

The high perfection of the grown samples consisting of thick crystalline layers make the use of the dynamical theory mandatory. More details about dynamical theory can be found in [42, 44, 45, 46]. Nevertheless, the kinematical theory can be used to understand qualitatively the main feature of measured spectra. A good review work can be found in [47], where HRXRD spectra from superlattice structures are analyzed following the kinematical theory.

The measured x-ray spectra can be compared with the simulated ones calculated with the  $4\times 4$  formalism using a commercial software. In these simulations, the sample structure can be implemented as function of fitting parameters that can be optimized in order to find the best agreement with the measurements [48]. Several examples of this procedure are given in the following chapters.

## 5.3 Detection of thin layers

In a highly perfect pseudomorphic layer system, HRXRD is extremely sensitive to very thin layers, in fact, the diffraction itself occurs because of the constructive interference between the periodically ordered layers. Because of this, the influence on the diffraction spectrum of a very thin layer can be important, even though the scattering of the layer itself is not detectable. A typical example is reviewed in [42], where a thin layer (less than 10 nm) is sandwiched between two thicker layers. Simulations show that the thin layer alters the interference fringes of the spectrum.

This effect is extremely evident in Fig. 5.4. The sample under examination consists of GaAs substrate, GaAs buffer, InAs quantum dot layer, and 80 nm GaAs as cap layer. It is clear that the presence of the quantum dots is not directly detectable by HRXRD, but the existence of the InAs wetting layer can be evidenced by the phase shift introduced to the propagating waves. The analysis of the three spectra shows that almost the same diffraction pattern is periodically obtained by increasing progressively the thickness of the InAs layer in the simulations. Therefore, for every Bragg reflection, several values of the InAs thickness are plausible and are listed in Tab. 5.3.

The (002) and (006) reflections are quasi forbidden in GaAs [44] and for this reason the interference effect is not as strong as for the (004), where the interference fringes due to the 80 nm GaAs cap layer and the GaAs substrate are well defined. It is clear that the only plausible thickness that, from Tab. 5.3, fits the three Bragg reflections simultaneously is the first one. In fact, a thickness bigger than 3 nm has to be excluded, because it is not compatible with the predicted flux originating from the indium effusion cell, that cannot be so high at the given experimental condition. Considering that the (004) reflection is the most faithful, the value of 0.59 nm can be assigned. An InAs wetting layer of 0.59 nm

(002)	(004)	(006)
0.68	0.59	0.70
		1.41
	1.72	2.14
	2.82	2.86
3.24	3.88	3.59
		4.31
5.59	4.95	5.03

Table 5.3: Simulated values of the InAs wetting layer thickness for different Bragg reflections. Just the first value is plausible.

corresponds to 1.7 monolayers. This value is in perfect agreement with the literature value of 1.5–1.6 monolayers [49, 50]. It is interesting that the correct determination of the InAs wetting layer thickness is obtained just with HRXRD measurements.



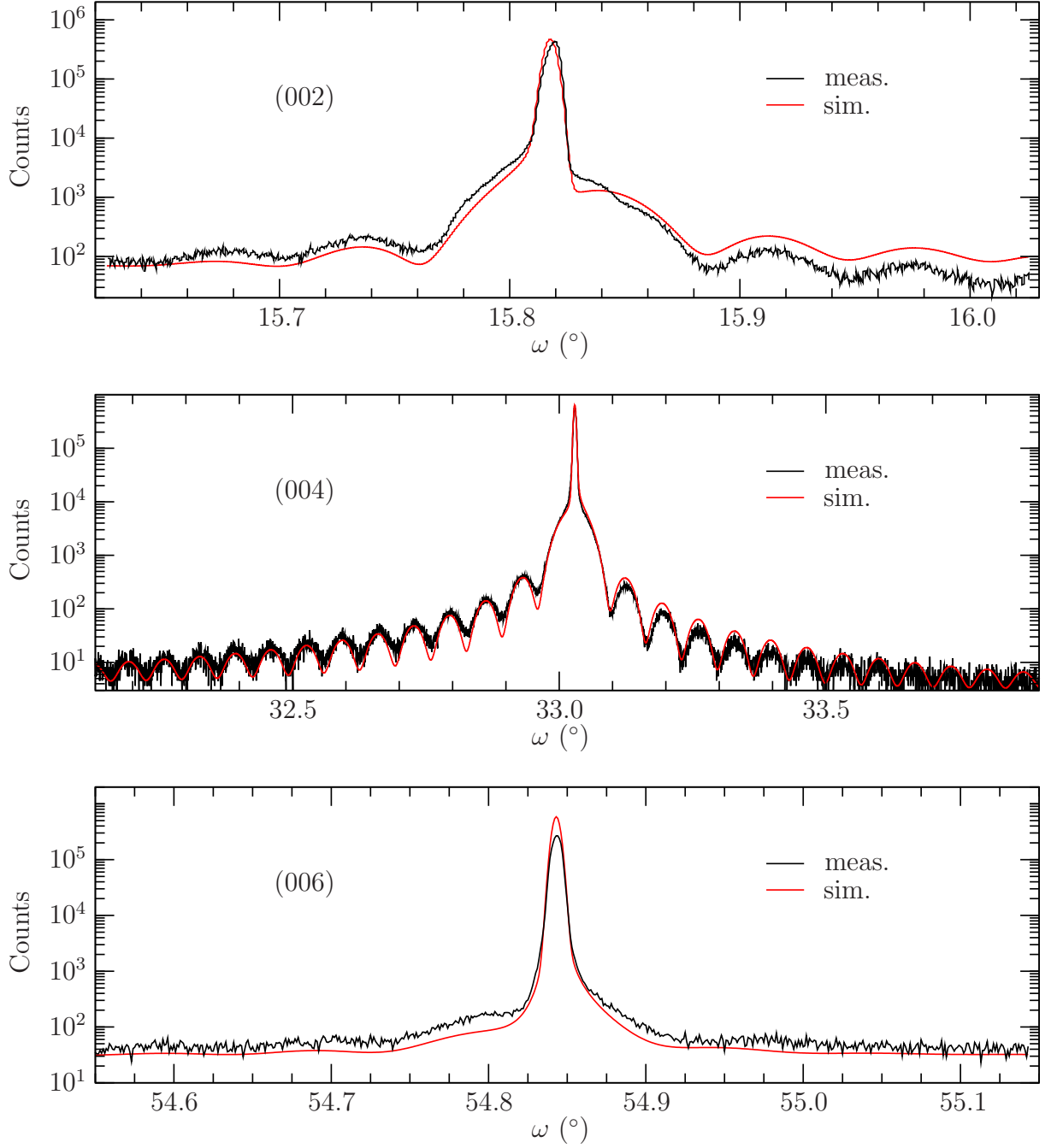


Figure 5.4: HRXRD spectra of the InAs quantum dot layer capped by 80 nm GaAs. The simulations are relative to an InAs thickness of 0.68, 0.59, and 0.70 nm for the (002), (004), and (006) reflections respectively. The (006) spectrum is measured without slits.

# Chapter 6

## The molecular beam epitaxy system

In this chapter, some topics regarding MBE growth and MBE technology are treated in detail focusing on the available systems. Big emphasis is given to the effusion cells and the growth rate calibration methods. In fact, a good calibration of the MBE system is essential for the production of VCSEL and VECSEL devices.

### 6.1 Introduction

In Fig. 6.1 is shown a specific scheme of the double chamber MBE system used in this work. At the bottom of the picture the intro system is sketched, this section can be evacuated by a turbomolecular pump and in few hours the pressure reaches the low  $10^{-8}$  Torr range. This is the only part of the whole unit which is exposed to air, because the samples are, in fact, introduced or taken out almost daily. The samples, which are mounted on molybdenum holders, can be moved in vacuum via special carriers and transferred using magnetic bars. When a satisfactory vacuum level is reached in the intro section, the sample is transferred in the treatment unit, where a base pressure in the  $10^{-10}$  Torr range is obtained with an ion pump. Here the new wafer and the sample holder are degassed at  $370^{\circ}\text{C}$  for at least 90 min. After this process, the sample is moved to the transfer module, from which it can be introduced in the growth chamber.

The growth chambers have a base pressure in the low  $10^{-11}$  Torr range. In the first one, the vacuum is maintained by a cryopump, an ion pump, a titanium sublimator, and of course by the liquid nitrogen cryopanel. A photograph of the cryopanel is shown in Fig. 6.2. In the second growth chamber, the possibility to grow layers containing phosphorus (e.g. GaAsP) is given by the presence of a phosphine injector equipped with a thermal cracking unit. This gas load makes necessary the use of a turbomolecular pump instead of an ion pump. More information about this system can be found in [51]. In both chambers small quantities of gaseous  $\text{CBr}_4$  are used as source for the carbon *p*-doping. Another MBE system of the same type, completely separated from the double chamber, is also available. This third growth chamber is kept in vacuum by a turbomolecular pump, an ion getter pump, and a titanium sublimator. In addition to the equipment that is similar to the ones of the first two systems, nitrogen is available thanks to a radio-frequency plasma source together with antimony, which is provided by a valved-cracked effusion cell.

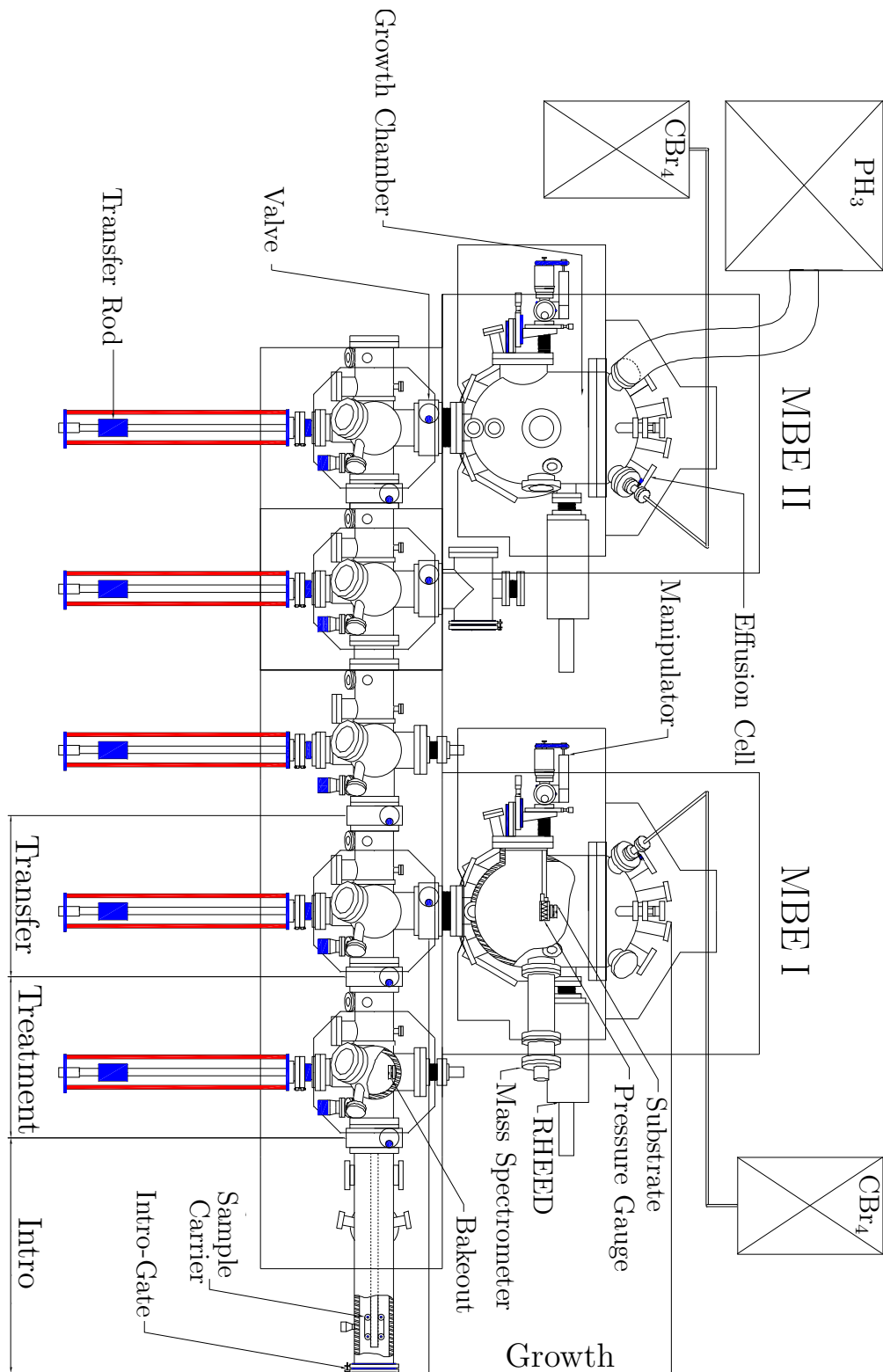


Figure 6.1: Schematic view of the double chamber RIBER 32 MBE system.

A more detailed description of this very special and particularly advanced system can be found in [52]. In each growth chamber, a valved-cracked arsenic solid source and at least one gallium, aluminum, silicon, and indium effusion cells are present. In addition, each growth module is equipped with a quadrupole mass spectrometer, in order to test the system for leakage and to monitor the residual gases, and with a RHEED unit that allows the monitor of the sample crystal surface.

## 6.2 The effusion cells

In Chapter 2, the effusion cells are theoretically described, starting from the ideal Knudsen cell to arrive to more realistic geometries, in this section, the performances of the effusion cells used in the system are in detail analyzed. In Fig. 6.3 a picture of a typical effusion cell is shown.

The effusion cells, that are approximately 30 cm long, work up to a temperature of 1400 °C and are mostly made of refractory materials, like tantalum and molybdenum. The design employs tantalum foils to improve the thermal coupling between the filament and the crucible and also to shield the cryopanel. Electrical insulation is obtained by using pBN and its use is limited by designing self-supporting filament structures. W-26%Re/W-5%Re thermocouples (TCs) are employed, they provide high thermal stability in the whole temperature range of operation. Different heater designs are optimized for different kind of cells, for example, in Fig. 6.4, a photograph of the top part of a normal cell can be compared to the one in Fig. 6.5, where another cell design, optimized for aluminum evaporation, is shown. It can be noticed how the filament does not extend to the top, this kind of cells are called "cold lip" and they improve the source material yield because they prevent the liquid aluminum to diffuse to the top of the crucible.

The crucibles are approximately 9 cm long and have a diameter of about 2 cm and are made of pBN, because of its high chemical stability up to 1400 °C. Their shape is similar to the one depicted in Fig. 2.3 and the nominal capacity is of 35 cc. The crucibles cannot be completely loaded, because in this system they lay almost horizontally. This is not a



Figure 6.2: Photograph of a part of the cryopanel, before insertion in the MBE chamber during maintenance.

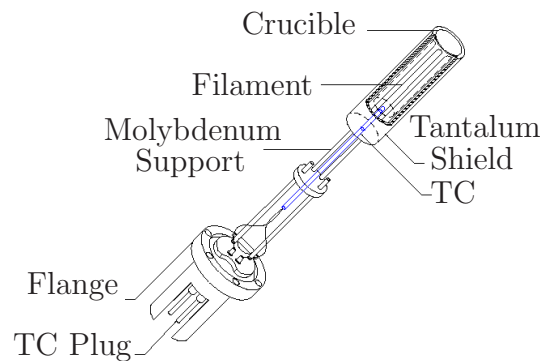


Figure 6.3: Scheme of typical effusion cell.

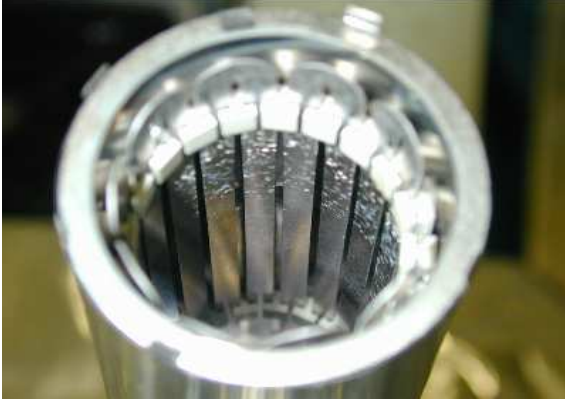


Figure 6.4: Top view photograph of a standard effusion cell, the tantalum heater is visible, together with the pBN insulators.

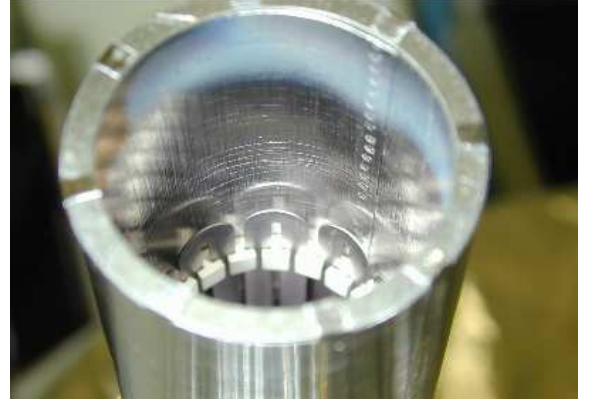


Figure 6.5: Top view photograph of a cold lip cell, to be compared with Fig. 6.4. The filament heater is recessed.

limitation for silicon, because just few grams in a cell are enough for  $n$ -doping. In gallium and indium cells, 50 g and 25 g of source material are loaded respectively. On the other hand, typically not more than 10 g of aluminum is loaded, because aluminum wets the pBN surface and it diffuses toward the top part of the crucible, where it is not longer usable. Among all source materials, aluminum is always the first one that need to be refilled. The cold lip cells alleviate this problem allowing to load up to 16 g aluminum, increasing the number of samples that can be grown between two maintenance acts.

A photograph, from the inside of one of the growth chambers, taken during maintenance, is shown in Fig. 6.6, one can see the shutters, the white pBN crucible of the indium cell and, on its left, liquid gallium deposits on the outer side of the gallium cell shutter. Arsenic deposits are also visible everywhere on the chamber walls. In the photograph shown in Fig. 6.7, the inner chamber walls were cleaned, in fact some arsenic accumulation was mechanically displaced, one can also see that the cells and the shutters were removed.

In the growth chambers the fluxes of the molecular beams are controlled by the cells temperature and by the mechanical shutters in front of them. The cells are heated using DC current sources with a precision of  $0.1^\circ\text{C}$  on the thermocouple reading, via PID controller. The molecular flux can be directly monitored by measuring the BEP (beam equivalent pressure) with an Bayard-Alpert hot-cathode ionization gauge situated on the manipulator in correspondence to the growth position. The beam equivalent pressure of the molecular fluxes generated by one gallium and two aluminum cells is shown in Fig. 6.8, each shutter is opened for three minutes and one can easily see a transient after the shutter is opened. This is due to the abrupt change of the thermal condition of the cell, the flux stabilizes asymptotically, and so the data can be reasonably fitted with the function

$$f(t) = A_\infty + A_1 e^{-(t-t_0)/\tau}, \quad (6.1)$$

where  $t_0$  represent the time when the shutter is opened, and  $\tau$  is the time constant characteristic for the cell. From Fig. 6.8, it is evident that the third cell, a cold lip cell containing aluminum, shows an almost ideal behavior with no overshoot and no



Figure 6.6: Sample view of the cells, the open shutter shows the indium crucible and, on its left, liquid gallium covers partially the gallium cell shutter. On the first row on the right, the arsenic cracker is visible.



Figure 6.7: Sample view after the removal of shutters and cells for maintenance. Some arsenic deposits were removed from the chamber walls, to be compared with Fig. 6.6.

measurable time constant. On the other hand, the first two cells exhibit a time constant of approximately 40 and 30 s respectively and an overshoot of about 15% of the steady flux.

The growth of a 80 nm thick GaAs layer can be analyzed as example, at the typical GaAs growth rate of 600 nm/h, almost 1 nm difference is obtained between the cases with and without transient. Therefore, it is important to consider that these transients can be relevant. The dynamic of the fluxes during the growth of actual devices will be described in detail in Sect. 9.4.

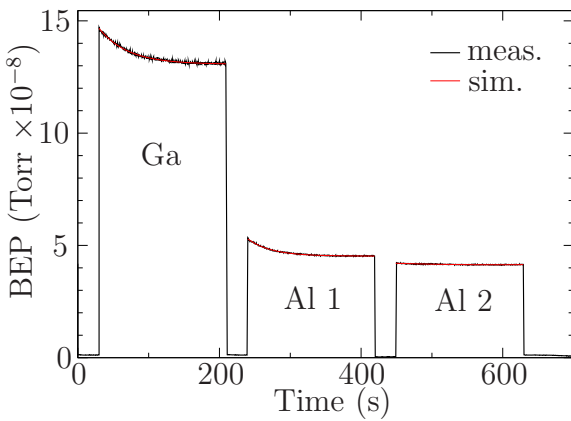


Figure 6.8: Measured fluxes for three different cells, the fluxes are fitted using (6.1). The third cell, a cold lip cell, shows an almost ideal behavior.

### 6.3 Calibration of the sources

The temperature dependence of the molecular flux from an effusion cell is well described by the equations (2.1), (2.2), and (2.3) even in the not ideal case. In fact, in Figs. 6.9 and



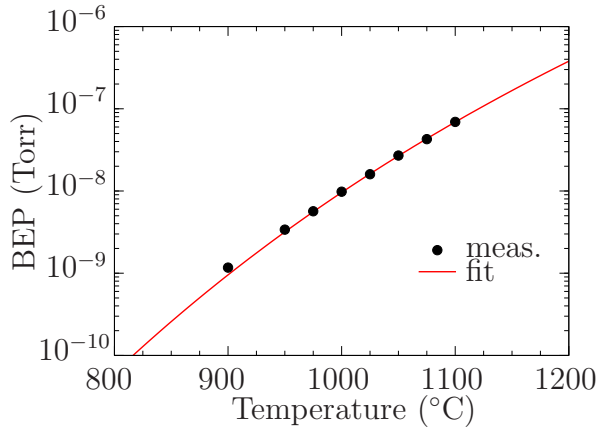


Figure 6.9: Temperature dependence of the flux from an aluminum cell.

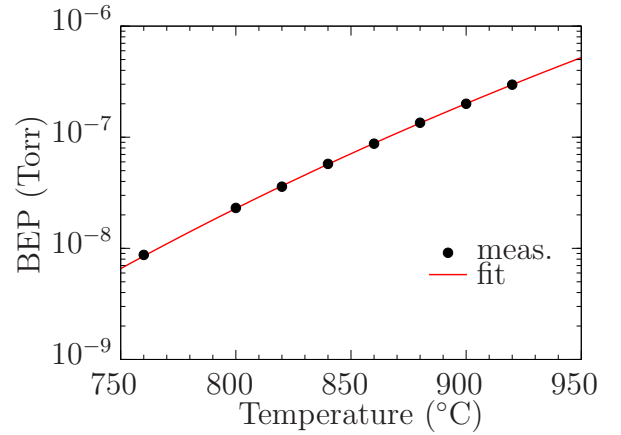


Figure 6.10: Temperature dependence of the flux from a gallium cell.

6.10 the molecular fluxes, from two different cells, are measured at different temperatures. The good agreement with the aforementioned equations allows the estimation of  $\Delta H$ . For the available MBE systems, discrepancies between measured and literature values of  $\Delta H$  were found by [53], but these can be most of all attributed to the temperature measurements done with the thermocouple, which is in contact to the lower part of the crucible. Therefore, the thermocouple temperature can be some tens of degree different than the effective material temperature.

The correspondence between temperature and measured flux is not a constant. In fact, by using a cell the quantity of the source material is slowly decreasing and also the material disposition in the crucible changes altering the flux. In order to obtain the same flux, the temperature should be, growth after growth, slowly increased. It is difficult to monitor this behavior, because one should calculate how many hours a certain cell was at a certain temperature in order to estimate the real depletion and usage. One can just argue that, after nearly one thousand hours of usage, at an AlAs growth rate of approximately 200 nm/h, an aluminum cell need about 20 °C temperature increase to reach the same initial flux. As already mentioned, the depletion of the aluminum cell always occurs first and a sudden decrease of the flux of about 20% can be observed in just few hours. The bottom of the crucible is then almost empty and most of the material is migrated to the top, where it is not anymore usable. For gallium cells the effect is lower and, even at a GaAs growth rate of 600 nm/h, the temperature increase after nearly one thousand hours usage is less than 10 °C.

## 6.4 Calibration of the growth rates

As already discussed in the introductory chapter, the growth rate in III/V compound is ruled by the group III elements, as long as enough group V is present. The group III elements used are gallium, aluminum and indium. For this elements the proportionality between the measured fluxes and the growth rate is strictly valid just if their sticking coefficient is unity. The sticking coefficient is very close to 1 for gallium and for indium

as long the substrate temperature does not exceed  $620^{\circ}\text{C}$  and  $520^{\circ}\text{C}$  respectively. For aluminum it is practically always one. If these conditions are fulfilled during the growth, then calibration samples can be grown to estimate the proportionality factors between cell fluxes and growth rates.

A good design for a calibration sample is the one that allow to calibrate as many cells as possible with the highest precision and reliability. For example a simple periodic structure, 10 times approximately 100 nm GaAs and 100 nm AlAs, is suitable to calibrate one gallium and one aluminum cell at once. The HRXRD measurements of the (002) and (004) reflection on such a structure are shown in Fig. 6.11, the relative optical reflectivity spectrum is shown in Fig. 6.12. All the measurements are recorded on the center of a 2 inches wafer.

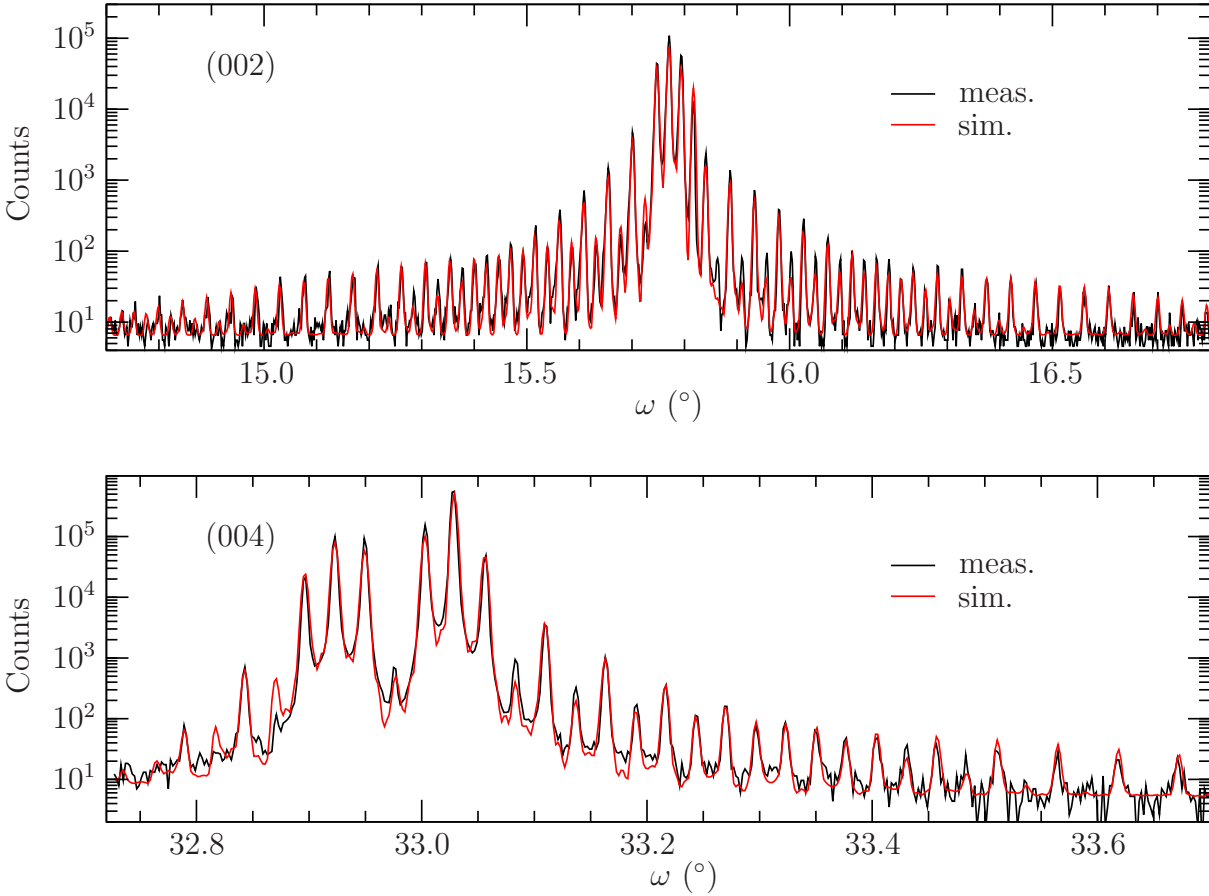


Figure 6.11: HRXRD (002) and (004) spectra and relative simulations of the simple GaAs/AlAs superlattice described in the text.

Two independent sets of growth rates can be extracted by fitting independently the (002) and (004) spectra, these results can be then compared with the reflectivity measurement, which is also very sensitive to the thickness of the layers, when these are of the order of a quarter of wavelength. No automatic fitting procedure was available to analyze the reflectivity data. The two parameters were adjusted visually.



Another simple calibration sample design consists in growing approximately 100 nm AlAs followed by approximately 1500 nm GaAs. In this second example, the reflectivity spectrum is very sensitive to the thickness of the thicker GaAs layer and the thin AlAs layer serves just as interface to produce interference fringes. The thickness of the nominally 100 nm thick AlAs layer can be measured easily with HRXRD, for example with a scan at the (002) reflection. In addition, one can dope the top 500 nm of the GaAs layer, in this way the sample can be also used as doping calibration (see Sect. 6.8). The reflectivity spectrum of such a sample and the (002) HRXRD spectrum are shown in Figs. 6.13 and 6.14. An absolute precision close to 1% is reached with both kind of samples.

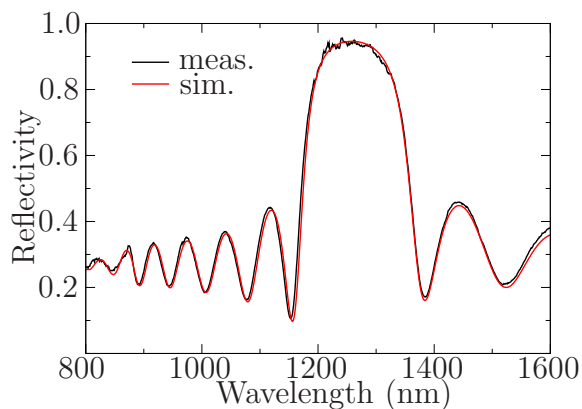


Figure 6.12: Measured and simulated optical reflectivity spectra, for the same structure measured in Fig. 6.11.

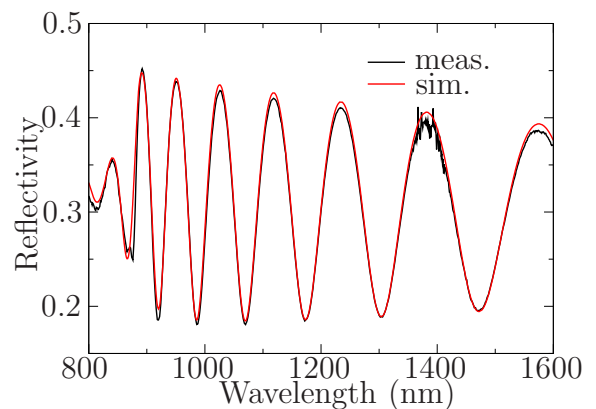


Figure 6.13: Measured and simulated optical reflectivity spectra, for nominal 100 nm AlAs capped by 1500 nm GaAs.

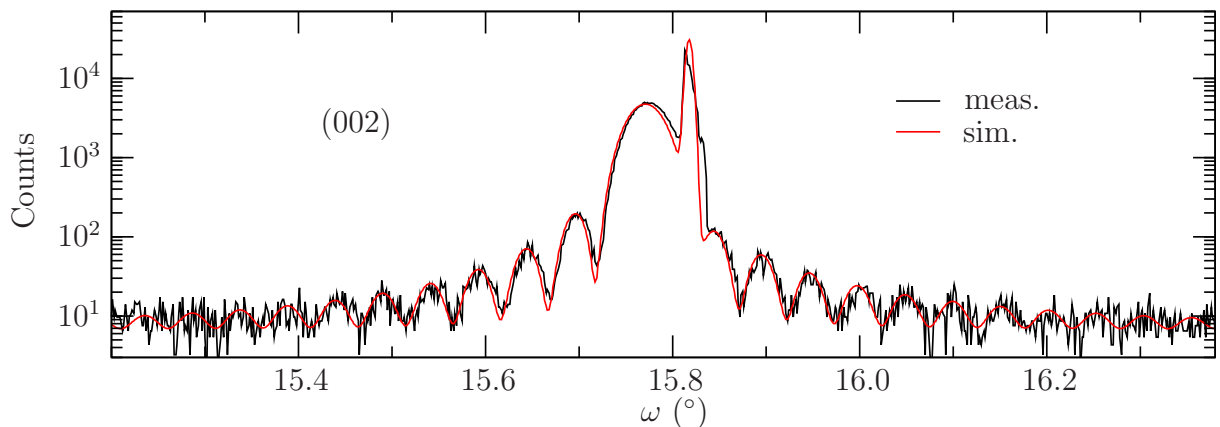


Figure 6.14: HRXRD (002) spectrum and relative simulation on the same sample measured in Fig. 6.13.

The indium molecular flux is typically determined by growing InGaAs/GaAs QWs, because these structures exhibit a strong photoluminescence (PL) response that is very sensitive to the indium content of the  $\text{In}_x\text{Ga}_{1-x}\text{As}$  alloy and, in optoelectronic devices, one is anyway interested in the emission wavelength of the QWs that are used as active

region. Another important aspect is that comparable samples measured under the same conditions, allow the comparison of the PL signals. The comparison of the PL signal of two nominally identical samples is given in Fig. 6.15. In these samples three InGaAs

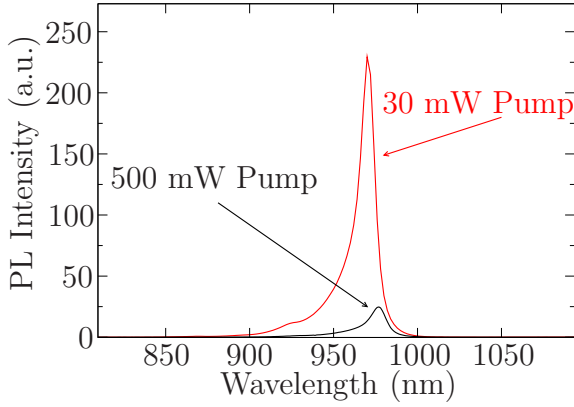


Figure 6.15: Comparison of the PL signal from two nominal identical InGaAs QWs test samples. As indicated two different excitation pump powers were used at 514.5 nm.

8 nm thick QWs, separated by 10 nm GaAs, are confined from both sides by 200 nm thick  $\text{Al}_{0.5}\text{Ga}_{0.5}\text{As}$  layers, finally a 40 nm GaAs layer caps the structure. The difference in the PL signal is of almost two order of magnitude, because one have to consider that one structure was weakly pumped to avoid the saturation of the detector, it is a consequence of the different quality of the grown material. An improvement in the pump system of the growth chamber and a careful degas procedure applied on every component of the system is certainly the reason for the improved PL signal.

The HRXRD (004) reflection of the sample from Fig. 6.15 which shows more intense signal is showed in Fig. 6.16, the indium molar fraction  $x$  in the  $\text{In}_x\text{Ga}_{1-x}\text{As}$  QWs is determined from the simulation to be 15.1%, this procedure is definitely less straightforward than PL measurements. On the other hand, there are some drawbacks in measuring directly the PL signal of QWs. In fact, it is not always possible to excite the quantum well region with a pump beam, the argon laser emitting at 514.5 nm used as excitation source, because it is absorbed from the layers above the QWs if their thickness exceed

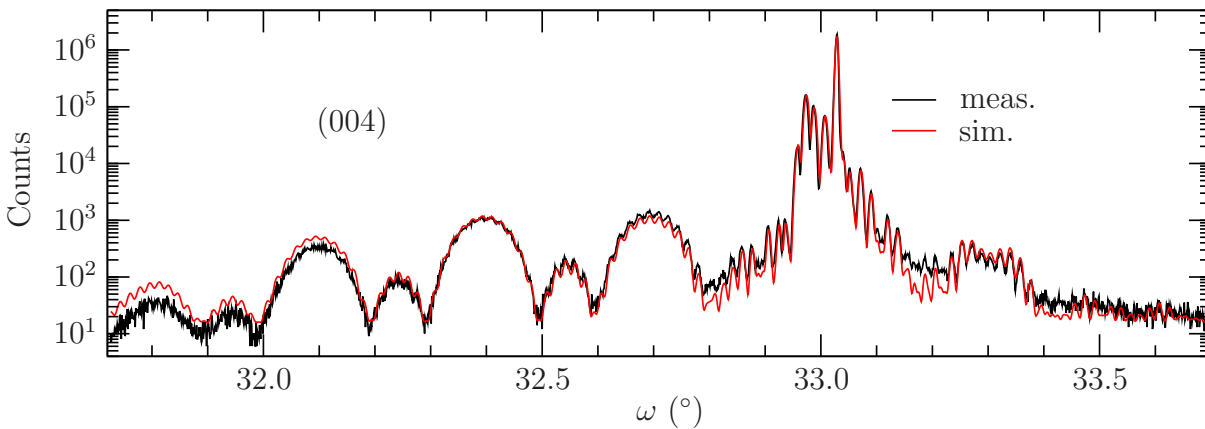


Figure 6.16: HRXRD (004) spectrum of the InGaAs/GaAs QWs sample described in the text, the indium molar fraction  $x$  in the  $\text{In}_x\text{Ga}_{1-x}\text{As}$  alloy is 15.1%.

some microns. This is always the case for typical VCSEL and VECSEL devices. In this case HRXRD, even though more laborious and indirect, allows a precision of 0.1% in the indium fraction determination. HRXRD is non destructive, but no information about the optical quality of the QWs can be obtained.

## 6.5 AlGaAs calibrations based on photoluminescence

As already shown in the last section, photoluminescence is the best method to characterize the QWs. In particular, one can optimize the process parameters, in order to maximize the PL signal measured on comparable samples. In this way, the optimal growth procedure, for example the growth temperature for InGaAs/GaAs QWs can be found, improving the device performances.

In this section, PL measurements are used to determine the aluminum fraction in a homogeneous  $\text{Al}_x\text{Ga}_{1-x}\text{As}$  layer. This measurements have a direct application in the characterizations of VECSELs as it will be shown in chapter 11. A simple test structure was grown, consisting of nominal 200 nm  $\text{Al}_{0.20}\text{Ga}_{0.80}\text{As}$  layer sandwiched between two 30 nm thick AlAs layers and capped by 15 nm GaAs. As shown in Fig. 6.17, a strong bulk PL signal, due to the direct bandgap of  $\text{Al}_{0.20}\text{Ga}_{0.80}\text{As}$ , can be recorded when the structure is pumped with a 514.5 nm argon laser. The PL peak position is a function of the aluminum concentration that can be directly measured.

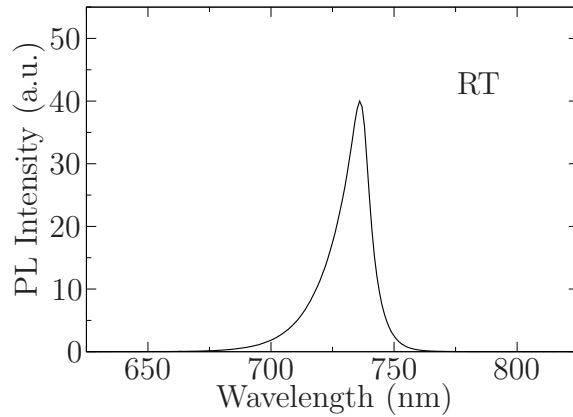


Figure 6.17: Room temperature PL spectrum of the sample described in the text, consisting of nominal  $\text{Al}_{0.20}\text{Ga}_{0.80}\text{As}$ .

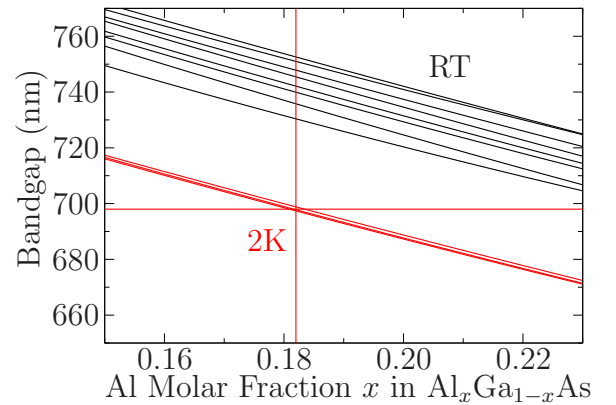


Figure 6.18: Different behavior of the  $\text{Al}_x\text{Ga}_{1-x}\text{As}$  bandgap in function of  $x$ , respectively at RT (black) and 2 K (red), after [55].

In practice, an absolute concentration measurement is difficult to achieve, because it is not easy to model the measured PL spectra recorded at room temperature, where many parameters, that are apparatus dependent, have to be taken into account [54]. As example, in fact, the bandgap is not precisely identified by the energy of the maximum intensity and for this reason it is not easy to give a precise formula for the bandgap of  $\text{Al}_x\text{Ga}_{1-x}\text{As}$  at room temperature. At low temperature the bandgap is defined with higher precision. This situation is described in Fig. 6.18, where different formulae for

the bandgap given by different authors, collected in the review paper of Pollak [55], are plotted as functions of the aluminum molar fraction  $x$ . At low temperature it is easy to measure the bandgap, this can be seen in Figs. 6.19 and 6.20. At low temperatures the bandgap is close to the free exciton peak at 698 nm. From this value using the 2 K curve in Fig. 6.18 one finds for the aluminum molar fraction  $x$  the value of 0.182. It is important to point out that the value measured at 11 K is very close to the 2 K value, because of the general temperature dependence of the bandgap in semiconductors [56]. One can also notice in Figs. 6.19 and 6.20 the appearance of two binded excitons, at less than 15 meV, for temperatures lower than 50 K.

The obtained value of  $x$  can be used to calibrate the PL setup, in fact at room temperature one can associate the intensity maximum at 736 nm to a molar aluminum fraction of 18.2% and, just recognizing that all the curves in Fig. 6.18 have practically the same slope of 0.24%/nm, one can easily measure the aluminum molar fraction of every  $\text{Al}_x\text{Ga}_{1-x}\text{As}$  bulk layer for  $x$  close to 20%.

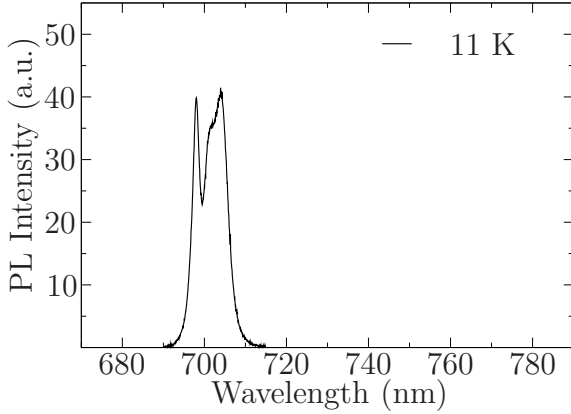


Figure 6.19: Low temperature PL spectrum of the described AlGaAs test structure, at higher wavelengths the bound excitons peaks are stronger than the sharper free exciton transition.

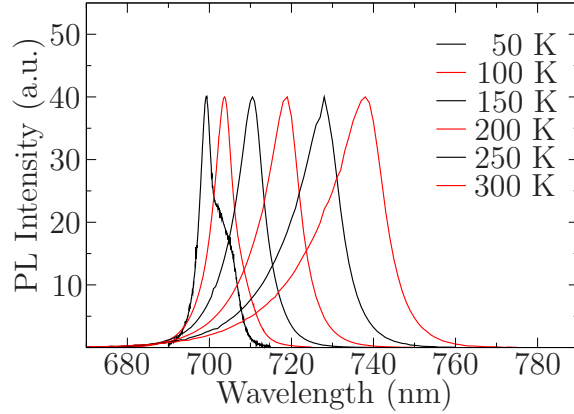


Figure 6.20: Temperature dependence of the PL spectra of the described AlGaAs test structure, at 50 K bound excitons peaks are visible in the right shoulder.

It is useful to compare the obtained result with the x-ray measurements from Figs. 6.21, where recorded and simulated curves are simultaneously shown. In this simulations not all the structural parameters, namely thicknesses and composition, are allowed to vary, in fact the growth was performed with an aluminum and a gallium cells always driven at the same temperature. The gallium or the aluminum cell was shuttered in order to grow AlAs and GaAs respectively, and to grow AlGaAs they were both open. It follows that, in this particular growth recipe, just the AlAs and GaAs growth rates represent the only free parameters and, as long as the shutters operation time table is known, define completely the structure.

One can see that the (002) spectrum contains more fine details than the (004) and the (006), even though the latter are more strain sensitive. This suggests that the (002) is a

reliable tool to extract information regarding the AlGaAs alloy [44]. In fact, the aluminum molar fraction obtained analyzing the (002), (004), and (006) spectra gives  $x = 0.183$ ,  $x = 0.175$  and  $x = 0.172$  respectively, the agreement between PL and the (002) HRXRD measurement is impressive.

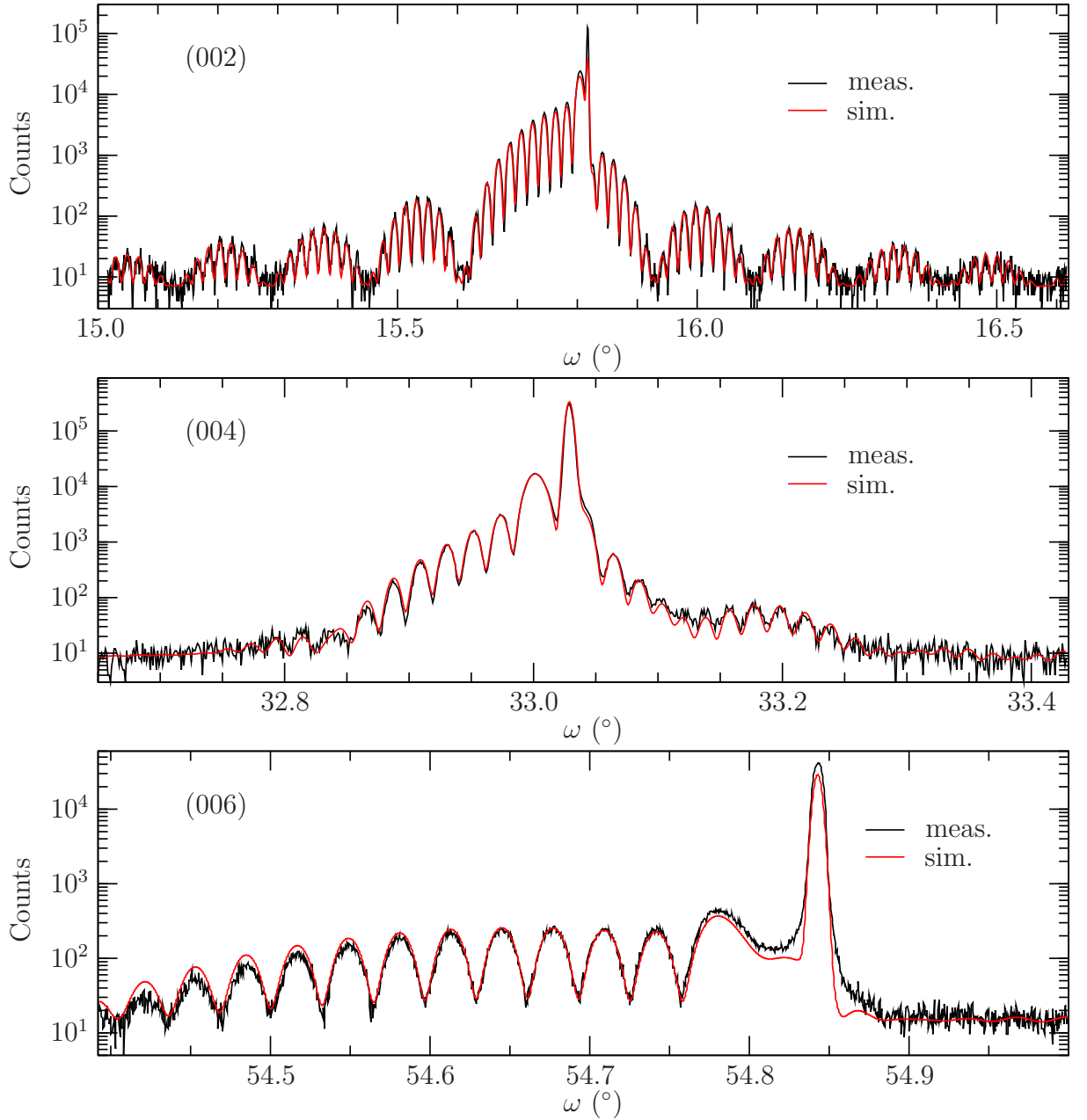


Figure 6.21: Measured and simulated (002), (004), and (006) Bragg reflections of the AlGaAs calibration sample.

## 6.6 Growth rate profile

The layers thicknesses of the MBE grown samples is not uniform. The substrate rotation, at a speed of approximately one turn per second, guarantees an azimuthal homogeneity on the two inches wafers and, therefore, just the radial profile of the layers thicknesses should be investigated. At this scope one can perform several HRXRD and optical reflectivity measurements, at different distances from the wafer center, on the already described calibration samples. The results of such measurements, performed on the simple GaAs/AlAs superlattice from Figs. 6.11 and 6.12, are summarized in Figs. 6.22 and 6.23. In the first figure, just the period of the superlattice is considered and it is extracted, from the optical reflectivity measurements, with easy calculations based on the position of the center of the stopband, and then verified with the transfer-matrix method. No best fit procedure is applied. Nevertheless, the results agree very well with HRXRD measurements, where, as can be seen from the spectra in Fig. 6.11, the angular separation between the satellites peaks, define the superlattice period with high precision. Practically no deviation is observed between the data collected from the (004) and the (002) reflection. The HRXRD

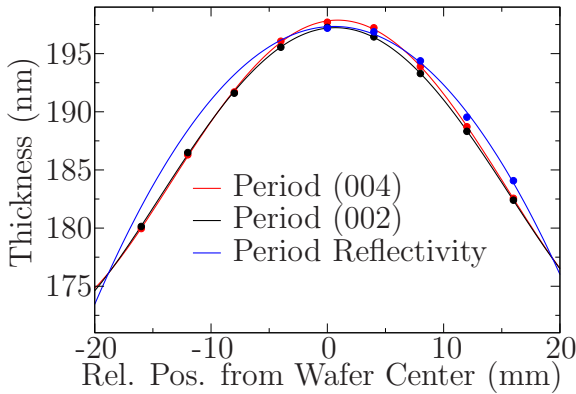


Figure 6.22: Period of the superlattice, from the simple 10 times GaAs/AlAs calibration sample, measured at different radii and with three independent measurements.

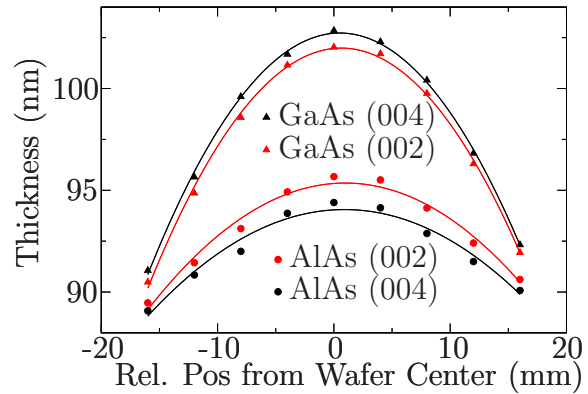


Figure 6.23: GaAs and AlAs layer thicknesses, measured at different radii with HRXRD, on the simple GaAs/AlAs superlattice calibration sample.

measurements were also performed for positions that are symmetric relatively to the wafer center just to test the reproducibility of the method. The measured points are symmetric too. In Fig. 6.23 the fitted thicknesses of the GaAs and AlAs layers constituting the superlattice are plotted separately and in function of the radii for the two Bragg reflections. Here it is possible to find a discrepancy between the results. The deviations between the two measurements are close to 1%, nevertheless, also in this case the (002) spectrum is more reliable, because of its higher material contrast.

The radial thickness profile generated from all the other cells is quite similar to the ones shown in this section for the specific cases of gallium and aluminum. It is quite clear that even though the thickness gradient is very pronounced, the composition of the alloys remains practically constant over the wafer.

A more homogeneous thickness profile could be achieved by tilting the manipulator

position. In fact, when the angle between sample normal and the molecular beams increases, the growth gets more homogeneous at cost of lower growth rates and a less efficient material usage. For industrial application the wafer homogeneity is mandatory, but for research, where no high yield is requested, the presence of a thickness gradient can be advantageous.

## 6.7 Pyrometer

In crystal growth the substrate temperature is one of the most important process variable and should be monitored carefully. This is a difficult task in a MBE system. In fact, in contrast to the effusion cell, where a thermocouple can be put in contact to the bottom of the crucible, the sample holder thermocouple is not in contact with the sample, but it is just very close to it, because this should rotate. Therefore, the measured temperature is quite different than the actual sample surface temperature.

In large heated systems, one can very often assume that the emitted radiation follows the ideal black body spectral distribution. With this approximation, that holds in large ovens, pyrometry can be used successfully to absolutely determine the system temperature. Even though in MBE systems the condition are not so optimal, pyrometry is currently used to control the temperature and to monitor the grown structure [57].

The pyrometer used in this work detects infrared radiation in the spectral range between 910 and 970 nm. In this spectral region, the samples exhibit often a flat maximum or a fast modulation of the optical reflectivity (one has also to consider the temperature effect on a reflectivity spectrum), for this reasons the pyrometer signal can be very sensitive to the grown structure. As example, in Fig. 6.24, two nominal identical VECSEL samples are considered. In the first two plots the pyrometer signals recorded during the growth of the double stopband DBRs are plotted. The corresponding nominal layer structure is summarized in the third plot. The difference in the pyrometer signals reveals a problem in the growth rates used to grow the second sample, these result to be almost 5% larger than expected. The pyrometer signal is also influenced by the cells in use, in fact infrared radiation from the cells can be reflected from the sample altering the detected signal, for example, by shutting one cells. The pyrometer signal can be also influenced by the substrate thickness, by the substrate holder, and from many other factors. The simplest and more reliable method to calibrate the pyrometer is to adjust the emissivity factor of the instrument at 582 °C where the oxide desorption temperature of the GaAs surface can be precisely determined using RHEED (see section 7).

## 6.8 Doping calibration

The doping in GaAs and in the AlGaAs system in general is efficiently performed using silicon and carbon to obtain *n*-type and *p*-type materials respectively [58]. The doping level can be easily measured with the Van der Pauw method [59, 60] on a doped GaAs layer of approximately 500 nm thickness. Silicon is typically evaporated from a standard effusion cell, in fact, in standard conditions, not more than 1100 °C are necessary to obtain a silicon flux which is high enough to dope the samples. In Fig. 6.25, a silicon doping



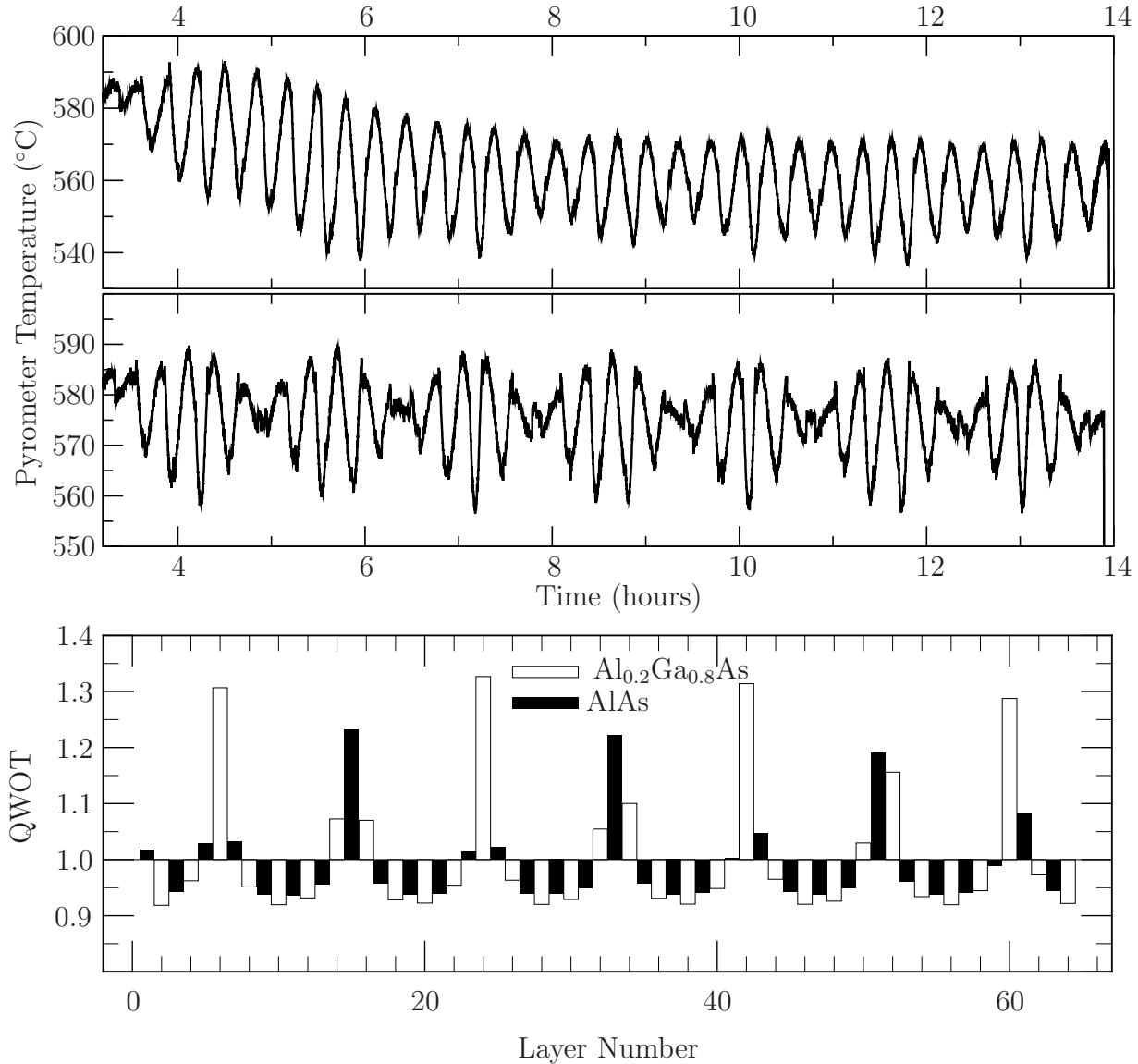


Figure 6.24: Pyrometer signals, recorded during the growth of double DBRs, from two nominal identical samples. In the third plot the relative nominal structure is reported in quarter wavelength optical thickness (QWOT) units for 980 nm wavelength.

calibration curve is shown, the data are normed for a GaAs growth rate of 500 nm/h, because the doping level is of course inversely proportional to the layer growth rate for a fixed doping flux.

Carbon can be introduced in the system as gaseous  $\text{CBr}_4$  and this molecule can be thermally cracked. The temperature that is used for cracking is 125 °C. In order to introduce just very small fluxes of  $\text{CBr}_4$ , a small part of the gas pipe is filled with the gas and its pressure  $P$  is measured and adjusted by an electrovalve in a controlled closed PID loop. Then, flowing through an orifice, the  $\text{CBr}_4$  is injected in the growth chamber or alternatively in a turbomolecular pump by switching run/vent valves. In Fig. 6.26,



the  $p$ -doping level is plotted versus the  $\text{CBr}_4$  pressure in the pipe, the doping level is also normed for a growth rate of 500 nm/h.

It is interesting to analyze the fitted expression obtained for the  $p$ -doping, or equivalently for the gas flow through the orifice, versus the pressure  $P$ . The orifice has diameter of 0.2 mm and a length of 0.6 mm, this dimensions are always comparable with the mean free path of the  $\text{CBr}_4$  molecules at the pressures of interest, limited to less than 1 Torr, which is approximately the gas vapor tension at room temperature, and to more than 1 mTorr, which is the lower limit for the pressure control loop. The mean free path ranges between 0.05 and 5 mm. Following [2, 3] the gas flux  $Q$  through a circular tube is proportional to the pressure difference  $P_1 - P_2$  at its ends

$$Q \propto (P_1 - P_2) \quad (6.2)$$

and it is the sum of two fluxes moving in the opposite directions without any mutual interaction. Therefore, this formula is valid in the molecular regime. For higher pressures, supposing an ideal laminar flow, one can write

$$Q \propto (P_1 + P_2)(P_1 - P_2), \quad (6.3)$$

and considering that in the setup  $P_1 = P$  and  $P_2$  is negligible, because high vacuum is present in the growth chamber or at the turbomolecular pump inlet, one has for the gas flux a quadratic dependancy on the pressure. Consequently, it is reasonable to fit the data from Fig. 6.26 with a power law and expect an exponent between one and two, because neither the molecular flow nor the viscous flow conditions are fulfilled and, in fact, it was found an exponent of approximately 1.3. It is worth to point out that the doping level calibrations have a precision that is estimated just below 10%, in fact the doping level is function of the III/V ratio [58] and also a dependancy on the aluminum molar fraction can be observed [61].

Silicon is ideally incorporated in AlGaAs up to a concentration of approximately  $6 \times 10^{18} \text{ cm}^{-3}$ , at higher concentrations the silicon atoms start to occupy the arsenic site

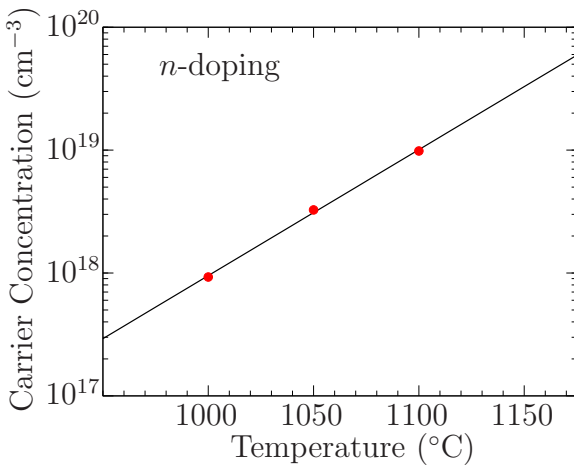


Figure 6.25: Calibration curve for the silicon cell, the doping levels is normed for a GaAs growth rate of 500 nm/h.

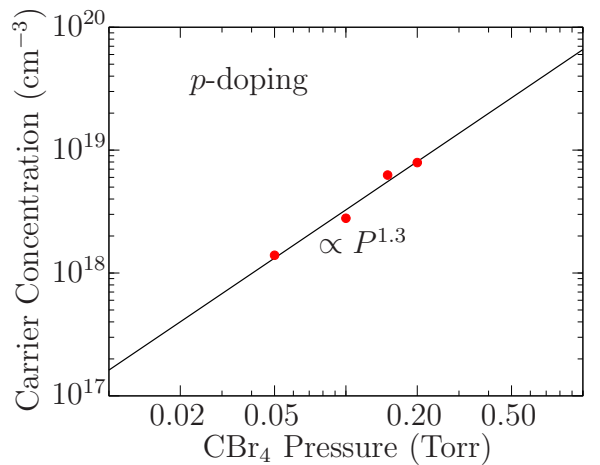


Figure 6.26: The  $p$ -doping, normed for a GaAs growth rate of 500 nm/h, plotted versus the  $\text{CBr}_4$  pressure before the orifice.

instead of the gallium one, resulting in a lower doping capability due to compensation. At even higher silicon concentrations the formation of  $\text{Si}_{\text{As}}\text{-Si}_{\text{Ga}}$  pairs induce the creation of silicon precipitates. On the other hand the carbon doping level can reach  $10^{20}\text{cm}^{-3}$ . All the  $p$ -contact in this work were realized at a GaAs growth rate of less than 100 nm/h in order to reach a doping concentration on GaAs of more than  $10^{20}\text{cm}^{-3}$ . This doping

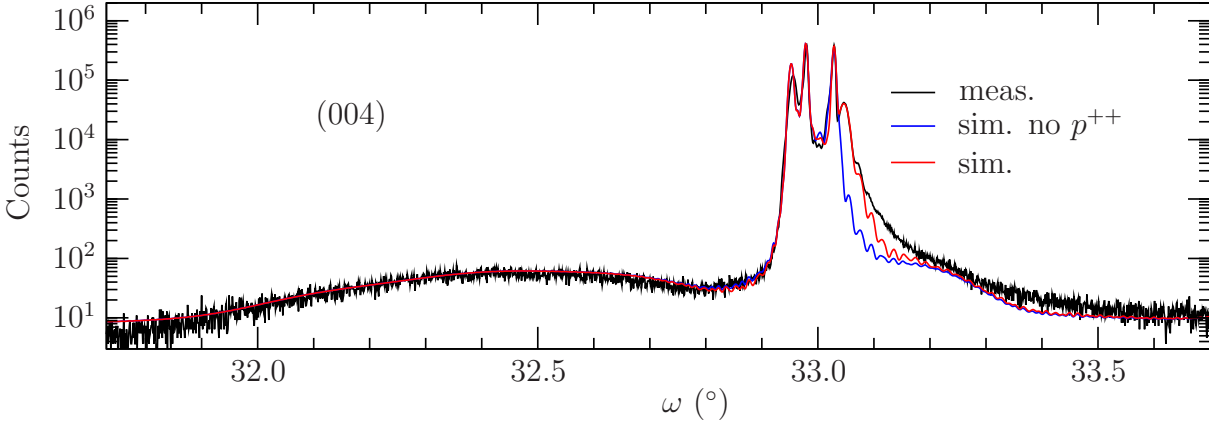


Figure 6.27: HRXRD spectrum of an edge emitter laser structure. Together with the measurement two different simulations are shown. In the first the strain introduced by the top highly carbon doped layer is not considered, in the second it is taken into account.

level concentration is so high that its effect can be evidenced by HRXRD measurements. In Fig. 6.27, the HRXRD spectrum of an edge emitter laser structure is shown. The structure contains a single InGaAs QW. The presence of the QW generates the large and weak peak at low angles, while the cladding AlGaAs layers peaks are visible close to the substrate one. In this sample the absence of DBRs makes more visible the effect of the thin  $p^{++}$  cap layer. Two different simulations of the HRXRD spectra were performed. One without including any influence of the  $p$ -doping, and a second one, where the  $p^{++}$  layers were included. The two layers with a  $p$ -doping concentration graded from  $5 \times 10^{19}$  to  $10^{20}\text{cm}^{-3}$  are well fitted by considering that the carbon in GaAs introduces tensile strain. From the strain measurement obtained by the HRXRD simulation one can calculate the carbon concentration, using the linear approximation for  $\text{GaAs}_{1-x}\text{C}_x$  valid for low  $x$  given by [62]. For the top high doped contact layer a concentration  $x$  of carbon of approximately 0.4% is obtained, this value corresponds to a carbon doping concentration of approximately  $0.9 \times 10^{20}\text{cm}^{-3}$  and it is in good agreement with the nominal and measured value of the holes concentration within 10%.

## 6.9 The arsenic source

As already mentioned in chapter 2, the MBE growth of III/V compound semiconductors is performed with an excess of the group V elements. For this reason it is also not so strictly necessary to determine the arsenic flux with high precision. The arsenic flux can be controlled by an electrically driven needle valve and of course also by the source

temperature which is set close to  $400^{\circ}\text{C}$ . The arsenic evaporated in this conditions is in tetrameric form, and can be efficiently dimerized by the thermal cracking stage of the cell working at  $820^{\circ}\text{C}$ .

The arsenic dimers are normally preferred because of their higher accommodation coefficient compared to the tetramers. This is due to the presence of arsenic dimers on the reconstructed sample surfaces (see chapter 7). Typical arsenic BEP are between  $10^{-6}$  and  $10^{-5}$  Torr, measured with the ionization gauge, this value is probably overestimated due to the low sticking coefficients of the arsenic molecules on the not cooled components of the chamber, like the housing of ionization gauge, that creates spurious reflected arsenic beams.

There is a lower limit for the V/III flux ratio that should be employed to obtain high quality GaAs. This limit can be found by observing the surface transition between the  $(2\times 4)$  As-rich to  $(4\times 2)$  Ga-rich surfaces using RHEED (see chapter 7). This experiment was performed at a growth temperature of  $580^{\circ}\text{C}$  and the surface transition was found to be at an arsenic BEP of approximately  $2 \times 10^{-6}$  Torr for a gallium growth rate of 620 nm/h. This experiment can be destructive for the sample, because gallium droplets can be easily created on the surface.

Even though the arsenic flux cannot be easily absolutely measured, high reproducibility is anyway obtained with the ionization gauge, this is important when other group V elements like P,N,Sb are introduced [51, 52].

The loaded arsenic charge is of approximately 2.5 kg and permits to grow several hundreds of samples without any refill. In Figs. 6.28 and 6.29, the empty and loaded arsenic crucible is shown during the operation of refilling



Figure 6.28: Empty arsenic crucible, at the bottom it is possible to see small orifices.

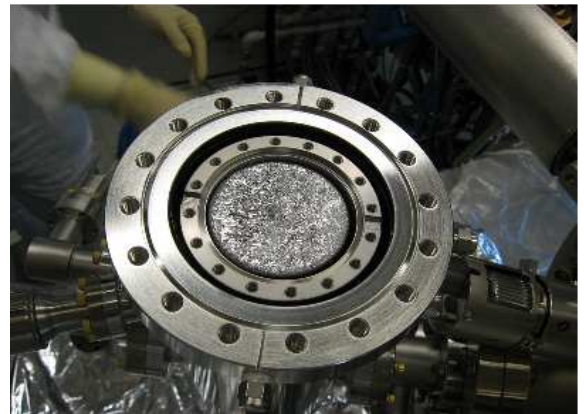


Figure 6.29: Arsenic load in the steel crucible, the weight of the arsenic charge is approximately 2.5 kg.

## 6.10 Residual gas analyzer (RGA)

A vacuum chamber is a dynamic environment and the residual gas inside a MBE chamber is the result of complex processes. Adsorption, desorption, diffusion, and chemical

reactions may take place on the walls exposed to UHV. The exact determination of the composition of the residual gas present in a vacuum chamber is a challenge, many problems have to be considered and solved [3, 63].

In this section some mass spectra, recorded in the growth chamber by a quadrupole analyzer, are shown and discussed, it is evident that a detailed and quantitative analysis of the residual gas in the growth chamber is not possible, nevertheless some important informations can be obtained.

In mass spectrometry different ions, characterized by charge  $q_i$  and mass  $m_i$ , are separated by the action of an electromagnetic field, the equations of motion are

$$m_i \ddot{\vec{r}} = q_i \vec{E}(\vec{r}, t) + \vec{v}(\vec{r}, t) \times q_i \vec{B}(\vec{r}, t). \quad (6.4)$$

It is obvious that any instrument working on this principle is just sensitive to the ratio  $m_i/q_i$ . If the applied fields are time dependent, the instrument is said to be dynamic, if just an electrical field is used, the instrument is referred as electric. In the case of the quadrupole analyzer, a time varying electrical field separates the different species, so one is dealing with a dynamic electrical path stability instrument. The term path stability is used to distinguish between time stability instruments, like the time-of-flight analyzers.

In the given MBE system, an electric quadrupole analyzer is connected to the vacuum chamber but it is not cooled by the cryopanel and it is protected by a metal shield, mainly to avoid arsenic coating. This is a severe limiting factor in the equipment, in fact the quadrupole is weakly pumped by the cryopanel and by the system pumps, therefore its vacuum environment is surely different that the one present at the sample position. The analyzer is stated to work at a pressure lower than  $10^{-5}$  Torr, so that the mean free path of the ions is much longer than the device itself.

The quadrupole analyzer is made of a filament, to extract the electrons, that, after being accelerated, are used to ionize the molecules of the residual gas. The acceleration energies are ranging typically from 60 eV to 150 eV, because in this conditions the ionization cross section for almost all molecules of interest is maximized [63]. After being ionized the molecules are separated from the electrons by mean of a negative plate and are driven in the analyzer. The analyzer consists, in the ideal case, of four surfaces of hyperbolic cross section, like depicted in Fig. 6.30. Typically in a quadrupole analyzer the complicated hyperbolic surfaces are converted in conductive rods, that can be fabricated more easily (Fig. 6.31). The equations of the hyperboloid surfaces are given by

$$f_x(x, y, z) = y^2 - x^2 = -L^2 \quad \text{and} \quad f_y(x, y, z) = y^2 - x^2 = L^2 \quad (6.5)$$

and each equation represents a pair of opposite electrodes. The potential  $A + B \cos \omega t$  is applied to the  $f_x$  branches and the opposite  $-(A + B \cos \omega t)$  to the  $f_y$ ,  $A$  is a DC voltage and the oscillating component has typically the frequency of 0.5–2 MHz of amplitude  $B$ . The electric potential in the region between these surfaces is an harmonic function and it is easy to recognize that

$$V(x, y, z) = \frac{x^2 - y^2}{L^2} (A + B \cos \omega t) \quad (6.6)$$

is the potential that satisfies the boundary conditions at the surfaces  $f_x$  and  $f_y$ . It follows that the equation of motion of a positive ion can be easily derived just calculating the

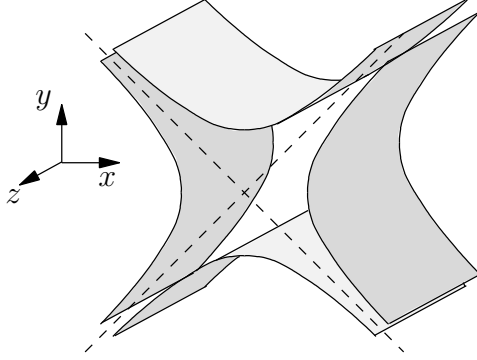


Figure 6.30: Electrodes of an ideal quadrupole analyzer, their surfaces are perfect hyperboloids.

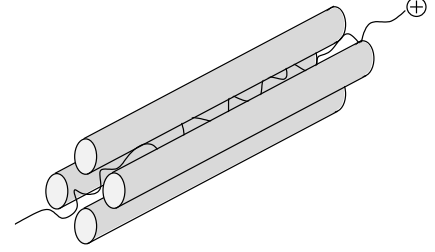


Figure 6.31: Real shape of the electrodes in a quadrupole analyzer, the hyperboloids are typically replaced with rods.

electric field from (6.6), one gets

$$m_i \ddot{x} = -\frac{2x}{L^2}(A + B \cos \omega t)q_i \quad (6.7)$$

$$m_i \ddot{y} = \frac{2y}{L^2}(A + B \cos \omega t)q_i \quad (6.8)$$

$$m_i \ddot{z} = 0 \quad (6.9)$$

where  $m_i$  and  $q_i$  are the mass and the charge of the positive ion respectively. The three equations (6.7, 6.8, 6.9) are separated and the motion along the different axes is independent. The first two equations can be written in the Mathieu canonical form [64]

$$\ddot{x} + (a + 2q \cos 2t)x = 0 \quad \text{and} \quad \ddot{y} - (a + 2q \cos 2t)y = 0, \quad (6.10)$$

with the dimensionless variables  $a$  and  $q$ , defined as

$$q = \frac{4q_i B}{m_i L^2 \omega^2} \quad a = \frac{8q_i A}{m_i L^2 \omega^2}. \quad (6.11)$$

The instrument geometry fixes  $L$  and typically  $\omega$  is also unvaried. This means that at any given  $m_i/q_i$  there is a one-to-one correspondence between the parameters spaces  $(q, a)$  and  $(B, A)$ . Solving numerically the differential equations (6.10), one can show that their solutions divide the  $(q, a)$  plane in regions where the two equations are respectively stable or unstable, like shown in Fig. 6.32. With unstable one means that the solution has the tendency to diverge with the time, with stable one means that the solution is oscillatory. In the case of a positive ion, this will be detected at a certain  $z$  just if the two solutions are simultaneously stable, this happens in an almost triangular-shaped region having the vertices at the points  $(0, 0)$ ,  $(0.706, 0.237)$ , and  $(0.908, 0)$ . Defining now the quadrupole constant  $D$  as

$$D = \frac{L^2 \omega^2}{4} \quad (6.12)$$

it follows that

$$B/D = \frac{m_i}{q_i} q \quad \text{and} \quad A/D = \frac{m_i}{2q_i} a. \quad (6.13)$$

One can now replot the stability diagram using the scaled variables  $B/D$  and  $A/D$  like shown in Fig. 6.33 for  $m_i/q_i$  equal to 1, 2, and 3 and the ion mass is conveniently expressed in atomic mass units (AMU) and its charge as multiple of the electron charge. In

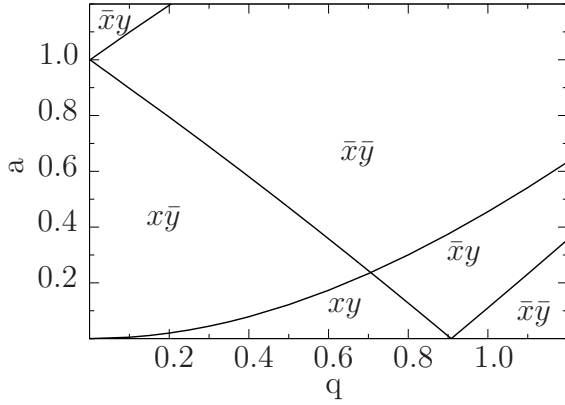


Figure 6.32: Stability plot for equations (6.10). The symbols  $x$  and  $\bar{x}$  mean that the equation for  $x$  is respectively stable and unstable, the same holds for  $y$  and  $\bar{y}$ .

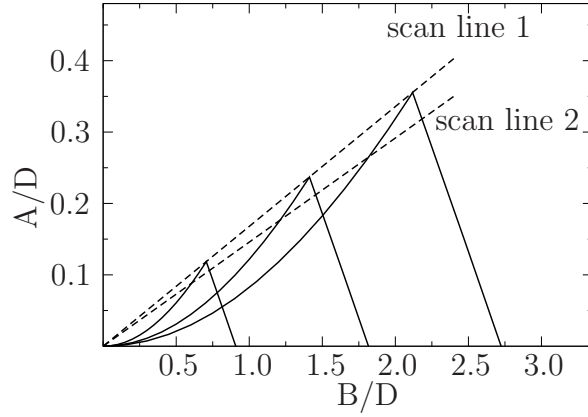


Figure 6.33: Stability regions for  $m_i/q_i = 1, 2, 3$ . The resolving power is infinite for scan line 1 and constant for the scan 2.

Fig. 6.33 the dotted lines represent scans performed by varying  $A$  and  $B$  keeping their ratio constant. It is clear from the plot that with these scans a constant resolving power is achieved, where the resolving power  $R$  can be defined as

$$R = \frac{m_i/q_i}{\Delta(m_i/q_i)}. \quad (6.14)$$

But typically one asks a mass spectrometer to resolve adjacent mass numbers and therefore  $\Delta(m_i/q_i) < 1$  is required for the whole sensitivity range. This implies that in practice the  $A - B$  scan should be chosen so that the resolving power increases linearly with  $m_i/q_i$ , this can be done at cost of a decreasing sensitivity.

In order to interpret correctly the recorded mass spectrograms the table 6.1 can be used for the assignment of the peaks, for a given molecule the relative intensity of the most probable fragmented ions are reported. Even though the table 6.1 is measured for an electron energy of 70 eV and the recorded data were obtained at approximately 100 eV, similar values can be extracted from other calibration tables, for example [65], where the electron energy is 90 eV.

In Fig. 6.34, a spectrum recorded, at a growth chamber pressure of  $4 \times 10^{-11}$  Torr, after more than one week without having performed any growth process is shown. At 2  $m_i/q_i$  a weak hydrogen peak is visible, the very weak signal at 12  $m_i/q_i$  can be related to carbon ions. At 16  $m_i/q_i$  the highest signal is recorded, one can assign the signal to  $O^+$  and  $CH_4^+$ , but a signal component due to the methane ion cannot be so relevant, because of the total absence of other methane fragments, especially the one at 15  $m_i/q_i$ . Therefore, the 16  $m_i/q_i$  peak is probably due just to oxygen. The peaks 17 and 18  $m_i/q_i$  are related to water molecules. The presence of water molecules should be not so high in a liquid nitrogen cooled UHV chamber, and this strong presence can be explained



$m_i/q_i$	$H_2O$	$CO_2$	$O_2$	$N_2$	$CH_4$	fragments
1	0.1				3.8	$H^+$
2					0.6	$H_2^+$
12		6.3			2.1	$C^+$
13					7.4	$CH^+$
14				9.0	15.0	$CH_2^+, N^+$
15					83.0	$CH_3^+$
16	3.1	16.0	14.0		100.0	$CH_4^+, O^+$
17	27.0				1.3	$CH_4^+, HO^+$
18	100.0					$H_2O^+$
19	0.2					$H_2O^+$
22		0.5				$CO_2^{2+}$
28		15.0		100.0		$CO^+, N_2^+$
29		0.2		0.7		$CO^+, N_2^+$
32			100.0			$O_2^+$
33			0.1			$O_2^+$
34			0.4			$O_2^+$
44		100.0				$CO_2^+$
45		1.2				$CO_2^+$
46		0.4				$CO_2^+$

Table 6.1: Fragmentation patterns for different molecules, at a ionization energy of 70V [3].

considering that the quadrupole is mounted outside the cryopanel, and it is protected by a metallic housing in order to avoid severe arsenic coating. A strong water peak is then explained considering that the system bakeout was performed at an effective temperature

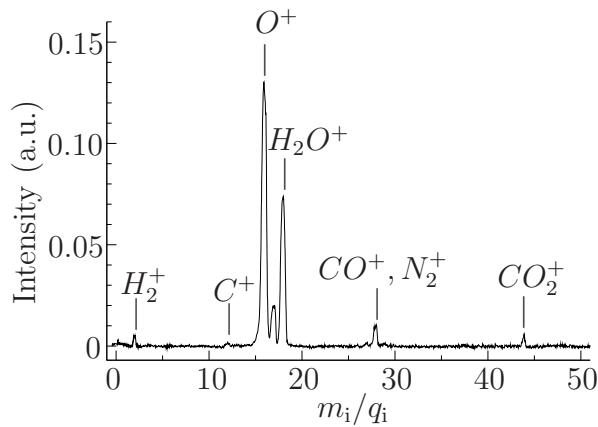


Figure 6.34: Mass spectrogram recorded at a chamber pressure of  $4 \times 10^{-11}$  Torr.

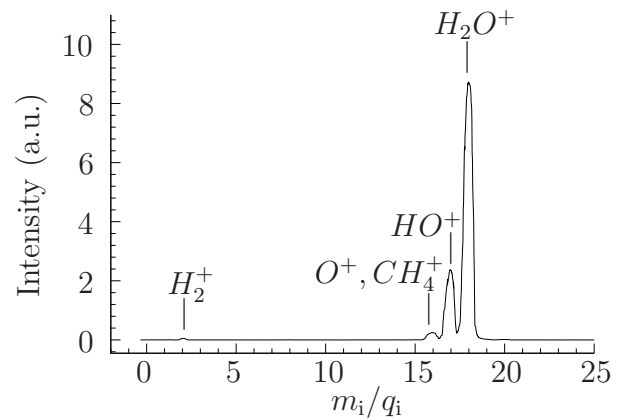


Figure 6.35: Mass spectrogram recorded at a nominal pressure of  $6.2 \times 10^{-7}$  Torr, one day after maintenance.

of approximately 150 °C. At 28  $m_i/q_i$  one sees the  $CO^+$  and  $N_2$  peaks, and finally at 44  $m_i/q_i$  the  $CO_2^+$  peak which is small due the loss in sensitivity.

Two spectra recorded the day after opening the growth chamber, with all components (cells, cryopanel) at room temperature, shows a more complicated spectrum. These are shown in Fig. 6.35 and in Fig. 6.36, where under the same conditions, the second spectrum was collected with ten times higher sensitivity, in order to resolve the weak peaks. Looking

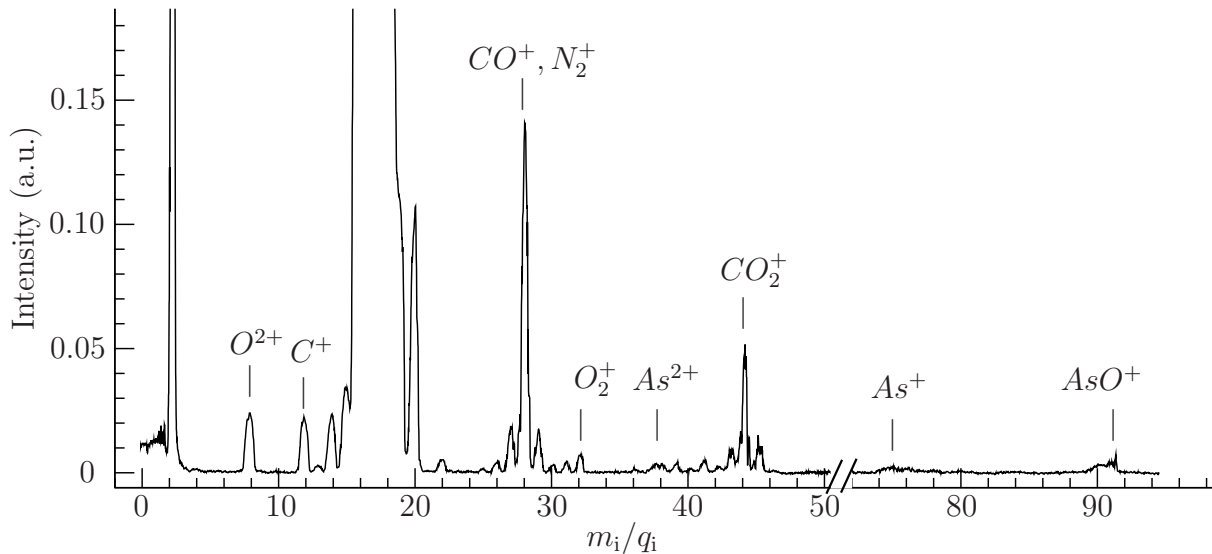


Figure 6.36: Mass spectrogram recorded at a nominal pressure of  $6.2 \times 10^{-7}$  Torr, one day after maintenance, under the same condition of Fig. 6.35, but with ten times higher resolution, in order to visualize the weak peaks.

at the high mass number part of the spectrum at 91  $m_i/q_i$  the arsenic oxide peak is present followed by the arsenic peak at 75  $m_i/q_i$  and 37.5  $m_i/q_i$  barely visible. At 44  $m_i/q_i$  the  $CO_2^+$  peak is again present, and most of the small peaks can be assigned to isopropyl alcohol (19, 27, 29, 31, 39, 41, 42, 43, 45) used to clean the vacuum flanges during the maintenance procedure. The 32  $m_i/q_i$  peak is molecular oxygen  $O_2^+$ . The monitoring of the oxygen peak is very important, because it can be associated to a leak or a virtual leak in the system. The 22  $m_i/q_i$  signal can be assigned to  $CO_2^{2+}$ . Neon  $Ne^+$  can be attributed to the isotopes at 20 and 22  $m_i/q_i$ , while 18, 17 and 16 belong to water. The 16  $m_i/q_i$  peak is originated also from  $CO_2$  and  $O_2$  fragments, but also from methane, because of the presence of the 15  $m_i/q_i$  peak. The 14  $m_i/q_i$  signal belongs to nitrogen and methane. Finally 12, 8, and 2 respectively to carbon, oxygen, hydrogen.

The RGA is of great importance especially to perform leak testing of the system after maintenance, for this purpose the MBE system is always carefully leak tested using helium by setting the quadrupole to the mass number 4.



# Chapter 7

## Reflection high-energy electron diffraction

As already mentioned in chapter 2, a RHEED unit is often integrated in a MBE system. In a RHEED experiment an electron beam with an energy ranging typically from 10 to 50 keV impinges on the sample at an incidence angle of just few degrees and a diffraction pattern can be observed on a phosphorus screen on small scattering angles. Under these conditions the beam is extremely surface sensitive, having a penetration depth of just few angstroms.

The equipment does not occupy precious place in front of the sample, this place is normally used for the effusion cells and the pyrometer port, in fact the RHEED gun and the screen can be built in a MBE system without any interference with other instruments. In addition, the presence of UHV environment is ideal for the propagation of an electron beam. RHEED is a robust surface sensitive in-situ tool, its use does not interfere with the growth processes, and can be used to monitor the diffraction pattern generated by the growing surface, in practice one can monitor the growth conditions.

### 7.1 Electron wavelength

From De Broglie relation one can associate a wavelength  $\lambda$  to a particle of momentum  $p$ , the famous relation holds

$$\lambda = \frac{h}{p}. \quad (7.1)$$

For small kinetic energies classical mechanics just gives

$$E = \frac{p^2}{2m_e} = \frac{m_e v^2}{2} \quad \text{and so} \quad \lambda = \frac{h}{\sqrt{2m_e E}}. \quad (7.2)$$

Considering a 30 keV electron, from the classical formula one gets a speed  $v$  that is already 30% the speed of light. Even at this energy the relativistic corrections do not affect drastically the wavelength, in fact following [66] one can derive the kinetic energy of a body, in our case the electron, starting from the more general Newton formula

$$\vec{F} = \frac{d\vec{p}}{dt} \quad (7.3)$$

and writing the elemental work

$$dE = \vec{F} \cdot d\vec{x} = \frac{d\vec{p}}{dt} \cdot \vec{v} dt = m_e d(\gamma \vec{v}) \cdot \vec{v} \quad \text{where} \quad \frac{1}{\gamma} = \sqrt{1 - \frac{v^2}{c^2}}. \quad (7.4)$$

Integrating by parts and setting the constant to have  $E = 0$  for  $v = 0$ , one gets for the kinetic energy

$$E = m_e(\gamma - 1)c^2. \quad (7.5)$$

The relativistic correction gives for 30 keV a  $\gamma \approx 1.06$  and so an electron speed that is more than 4% smaller than the classical one. A formula for the momentum as function of the energy can also be written as

$$p = \sqrt{2m_e E + \frac{E^2}{c^2}} \quad (7.6)$$

and finally for the wavelength

$$\lambda = \frac{h}{\sqrt{2m_e E + \frac{E^2}{c^2}}}. \quad (7.7)$$

Electrons accelerated at 30 keV have  $\lambda = 6.98 \cdot 10^{-3} \text{ nm}$  ( $\lambda = 7.08 \cdot 10^{-3} \text{ nm}$  without relativistic correction), which means a wavelength that is 22 times smaller than x-ray  $\text{CuK}\alpha$ . The relative  $\vec{k}_i$  vector has modulus  $900.2 \text{ nm}^{-1}$ . This last value should be compared to the length of the crystal axes  $\vec{g}_i$  of the reciprocal space related to the crystal or surface under investigation, which is typically almost 100 times smaller.

## 7.2 Kinematical approach to RHEED

Unlike x-ray or neutrons, that are weakly scattered by matter, the electrons interaction is strong and the penetration depth is small. As seen in chapter 5, strong interactions with the sample results in a not negligible energy exchange between the incoming and the diffracted beam. Beside this, the large values of the incidence electrons momentum  $\vec{k}_i$  is favorable to multiple diffraction because it has to be compared to the reciprocal space vector typical of the sample. Considering that, in standard HRXRD, multiple diffraction is just accidental, this is the rule using high-energy electrons. All these arguments makes the use of the kinematical theory of diffraction unreliable for high energy electrons, nevertheless this theory can be used to explain easily and qualitatively some of the main features of the RHEED experiments [67].

The RHEED geometry is briefly summarized in Fig. 7.1, where an electron beam, characterized by a wave vector  $\vec{k}_i$ , impinges on a crystalline sample at low incidence angle, typically  $0-5^\circ$ . For this reason, the penetration depth of the beam is confined to few monolayers and the sample is seen as a two dimensional crystal. Therefore, the reciprocal space generated by the surface under investigation is not made of isolated points, but is composed of a regular array of parallel rods, perpendicular to the surface. This simplifies the diffraction conditions, in fact, the diffraction conditions on the wave vectors relative to the perpendicular direction are relaxed. As already mention, a further simplification arises from the big radius of the Ewald sphere compared to the modulus of  $\vec{g}_i$  in the reciprocal space.

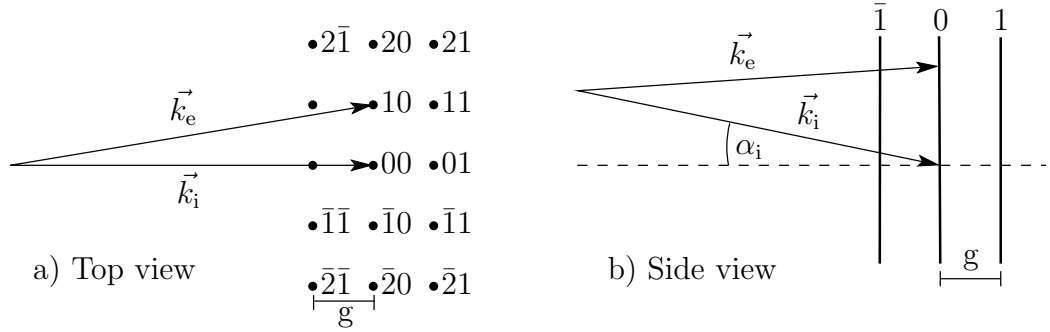


Figure 7.1: RHEED geometry, the page represents the sample surface, and the  $\vec{k}_i$  vector is not correctly scaled. The typical incidence angle  $\alpha_i$  is  $0-5^\circ$ .

### 7.3 RHEED patterns on GaAs (001)

In the following section the RHEED patterns typically observed during the preparation and growth of GaAs on GaAs (001) substrate are shown and briefly commented. To avoid misunderstandings in each photograph the direction of the incoming beam is always explicitly specified. All the photographs were collected with an high sensitivity digital 8-bit camera, and the intensity of pictures is inverted, so that black tones correspond to high intensity and vice versa, the contrast of the images is enhanced to emphasize the diffraction pattern. The real scale of the pictures is calibrated with care, in order to measure real distances on the phosphorus screen, and a grid corresponding to integers and quarter of the reciprocal space vector of the surface  $g$  is always overlapping the photographs. It is also always specified if the temperature, is the thermocouple temperature, or the real temperature, measured by a calibrated pyrometer.

In Fig. 7.2 a naive sketch of the GaAs (001) surface is depicted. The atoms in the

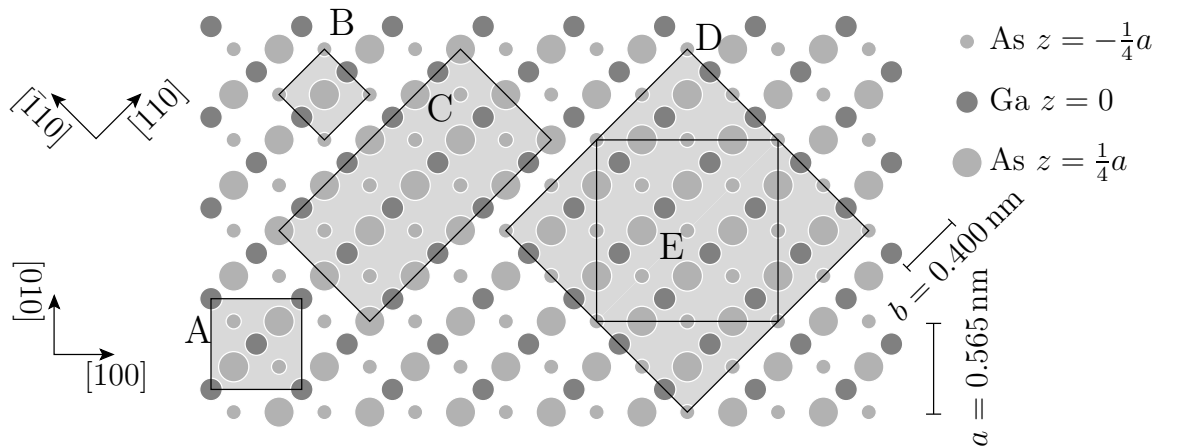


Figure 7.2: Naive sketch of the GaAs (001) surface. The darker circles represent gallium atoms situated at  $z = 0$ , the small and big gray circles represent arsenic atoms situated at  $z = -1/4a$  and  $z = 1/4a$  respectively.

figure belong to three different levels, at  $z = -\frac{1}{4}a$  and at  $z = \frac{1}{4}a$  one finds arsenic atoms, at  $z = 0$ , one finds gallium atoms. In the figure the atoms are supposed to stay in the same position they would have in bulk material. This is unrealistic, because the dangling bonds, present on the surface, force the atoms to arrange themselves in the specific surface reconstructions.

Following the conventions introduced in surface crystallography by E.A. Wood [68], the substrate net parallel to the surface is used as reference and, from Fig. 7.2, one can recognize that the square  $B$  can be taken as unit cell for the surface. Its lattice constant  $b$  is given by  $b = a/\sqrt{2} = 0.400 \text{ nm}$ , which corresponds, in reciprocal space, to the length of the vector  $g = 2\pi/b = 15.71 \text{ nm}^{-1}$ .

The used GaAs substrates were "epi-ready", which means that the substrate surface is polished and cleaned chemically, and, after that, a native oxide is generated in controlled conditions. No differences were observed between substrates coming from different manufacturers. The substrate was loaded in the growth chamber, heated up to  $370^\circ\text{C}$ , when the arsenic valve was opened. Then the temperature was increased gradually. Just diffuse scattering could be observed on the RHEED screen. In Fig. 7.3 a photograph was taken at a thermocouple temperature of  $530^\circ\text{C}$ , just the weak specular reflection could be observed at any azimuth. This is typical of an amorphous oxidized surface that does not possess a periodic mesh. A moderate increase of the thermocouple temperature of

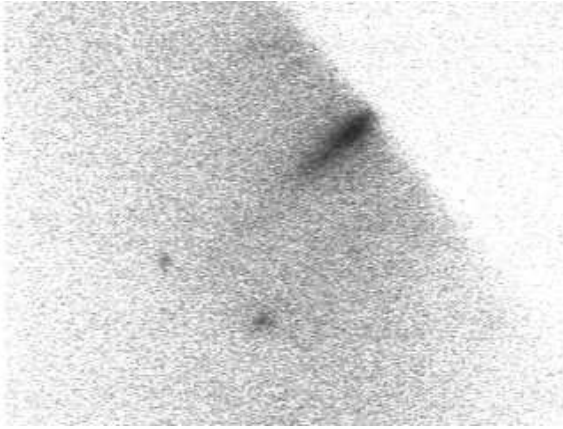


Figure 7.3: Weak diffuse scattering due to the native oxide at  $530^\circ\text{C}$  thermocouple temperature. The signal is independent of the azimuth.

just  $5^\circ\text{C}$  in half a minute was then sufficient to remove the oxide layer and a diffraction pattern appeared as can be seen in Figs. 7.4 and 7.5. The two pictures look quite similar, in fact no strong difference can be seen between the azimuth  $[110]$  and  $[\bar{1}10]$ , except that when the incoming beam propagates along the  $[110]$  the diffraction lines are sharper than in the  $[\bar{1}10]$  case, where the shape of the diffracted spots slightly reminds the traces of a duck. This is a direct consequence of the preparation of the surfaces that was not reconstructed, and it was not atomically flat. It is interesting that the small differences between the two pictures are a consequence of the lack of the four-fold symmetry about the  $[001]$  direction, which is already evident.

The dimensions of the surface mesh can be estimated just by considering the RHEED geometry. As one can see in Fig. 7.1, one can measure experimentally  $g$  and so  $b$ ,

$$d = \frac{g}{k_i} D \quad \text{and} \quad b = \frac{\lambda}{d} D, \quad (7.8)$$

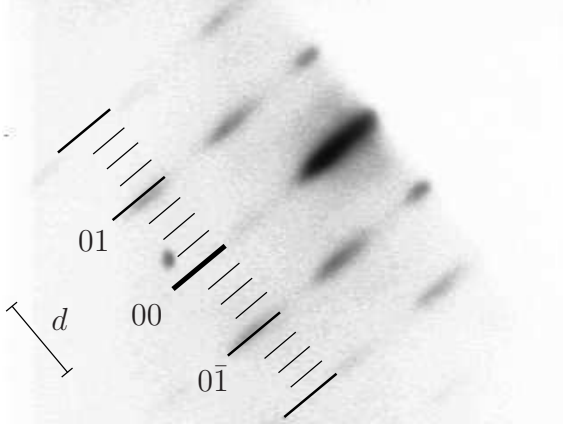


Figure 7.4: RHEED pattern after oxide desorption,  $\vec{k}_i$  along  $[110]$  at  $535^\circ\text{C}$  thermocouple temperature.

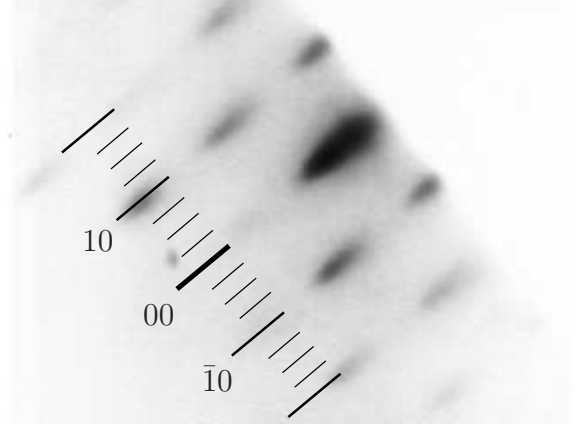


Figure 7.5: RHEED pattern after oxide desorption,  $\vec{k}_i$  along  $[\bar{1}10]$  at  $535^\circ\text{C}$  thermocouple temperature.

where  $\lambda$  is given by (7.7) at 30 keV,  $D$  is the sample–screen distance of 320 mm and  $d=5.59$  mm is the distance measured on the screen between two neighbors rods, for example the 00 and 01. Substituting these numerical values in (7.8) the value of 0.400 nm is obtained for  $b$ , this values is in perfect agreement with what is expected for gallium arsenide.

The aforementioned oxide desorption temperature can be used to calibrate the pyrometer, by setting an effective emissivity, and to measure the thermocouple offset, which is strongly system dependent, in fact the surface oxide desorption occurs at  $582\pm 1^\circ\text{C}$  [69, 70]. The desorption temperature is also known to be optimal for the growth of GaAs and AlGaAs, so care should be taken in observing the appearance of the diffraction pattern.

As the GaAs growth was started on the substrate, the RHEED patterns appeared spotted, this is an indication that the new surface was still not smooth. At a typical growth rate of 600 nm/h, after 1–2 minutes the RHEED pattern appeared streaky, indicating a surface made of smooth flat terraces. The appearance of streaks with separation  $d/2$  in Fig. 7.6 and  $d/4$  in Fig. 7.7 are the indication of a  $(2\times 4)$  reconstruction. The surface mesh has, in this reconstruction, sides of length 0.80 and 1.60 nm (rectangle  $C$ ) respectively and it is oriented like sketched in Fig. 7.2. The streaks are identified with multiple fractions of the original reciprocal space vector  $g$  of the surface.

There are several physical models for the  $(2\times 4)$  surface, because the arsenic dimers, that are not sketched in the figure, are taking the place of some of the arsenic atoms building different reconstructions. Three different  $(2\times 4)$  reconstructions are observable by varying the substrate temperature [67, 71]. At the desorption temperature the  $(2\times 4)\beta$  is recognizable for the presence of all the quarter fractional lines in Fig. 7.7. Increasing or decreasing the substrate temperature by  $40\text{--}50^\circ\text{C}$  leads to the  $(2\times 4)\alpha$  and  $(2\times 4)\gamma$  surface reconstruction respectively, where the half fractional line tend to disappear. This can be barely recognized in Fig. 7.8.

The different reconstructions can be used to identify good growth conditions, as it is accepted that the  $(2\times 4)\beta$  is optimal for GaAs growth [58].

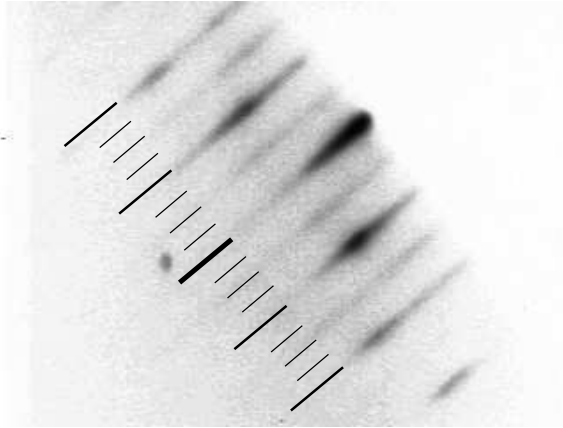


Figure 7.6: RHEED pattern during GaAs growth at the oxide desorption temperature,  $\vec{k}_i$  along  $[110]$ .

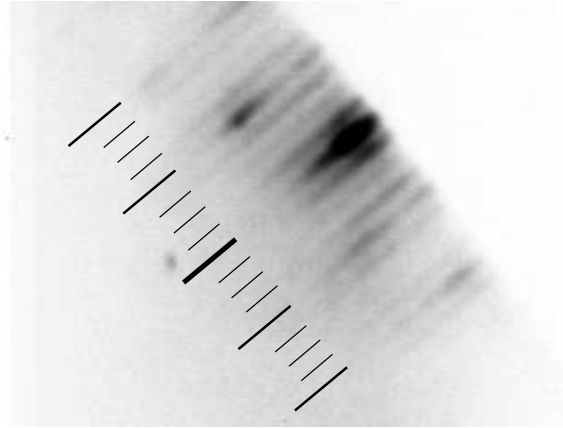


Figure 7.7: RHEED pattern during GaAs growth at the oxide desorption temperature,  $\vec{k}_i$  along  $[\bar{1}10]$ .

The presence of dimers on the GaAs surface explains why arsenic dimers are kinetically favored respect the tetramers to be accommodated on the surface. An inversion of the diffraction patterns showed in Figs. 7.6 and 7.7 is obtained decreasing the arsenic flux, resulting in a Ga-rich  $(4 \times 2)$  surface. As already mentioned in section 6.9 this growth conditions are not suitable for good crystal quality.

Approximately one minute after growth-stop, a smooth surface, flat at a monolayer level, without the presence of terraces, was generated. This is due to the high mobility of the gallium atoms on the surface at  $580^\circ\text{C}$  pyrometer temperature. In this conditions the RHEED pattern, which is extremely surface sensitive, change its morphology, and the streaks were transformed in sharp points aligned on a circle, as can be seen in Fig. 7.9. The circle is just the projection on the screen of the intersections between the reciprocal space streaks and the Ewald sphere associated to the incoming beam, as clearly shown in Fig. 7.10. The radius of the circle can be directly measured on the screen resulting in a value of  $R = 7.0\text{ mm}$ , therefore, it is easy to calculate the incidence angle of the beam  $\alpha_i$ ,

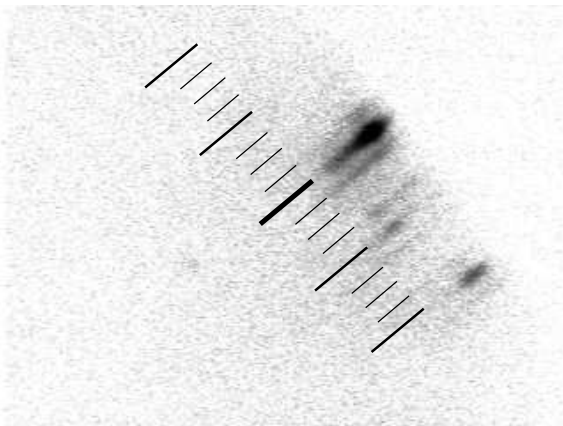


Figure 7.8: RHEED pattern of the  $(2 \times 4)\gamma$  reconstruction, recorded with  $\vec{k}_i$  along  $[\bar{1}10]$  and at  $\simeq 510^\circ\text{C}$  pyrometer temperature.



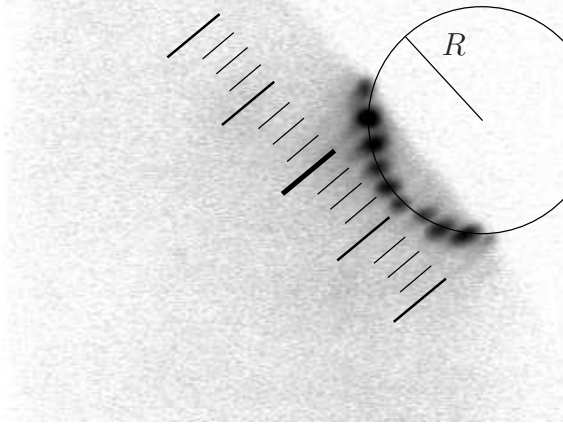


Figure 7.9: RHEED pattern recorded at 580 °C pyrometer temperature, with  $\vec{k}_i$  along  $[\bar{1}10]$ , after one minutes of growth-stop. The pattern is composed of sharp spots aligned on a circle.

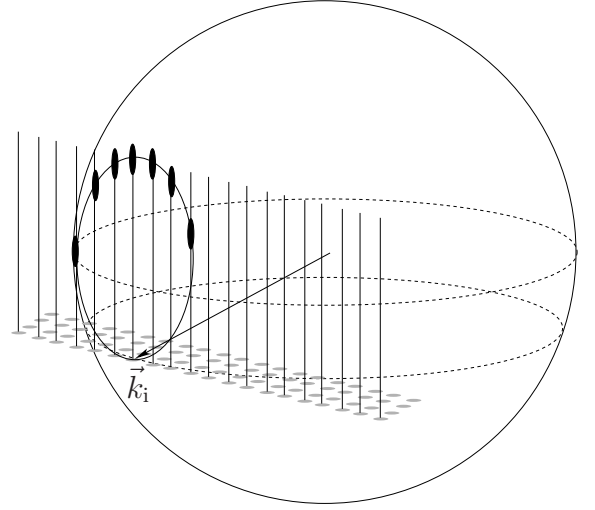


Figure 7.10: Reciprocal space rods intersecting the Ewald sphere determining the diffracted beams.

obtaining

$$\alpha_i = \frac{R}{D} = 1.25^\circ. \quad (7.9)$$

It was mentioned in section 2.1 that the growth of atomically flat monolayers can be detected from the oscillations of the RHEED signal intensity. This can be seen in Figs. 7.11 and 7.12, where the RHEED signal on the phosphorus screen was integrated on a rectangular region that includes a diffraction streak and then plotted versus the time. After a growth-stop of at least one minute, in order to have a starting atomically flat surface, the opening of the gallium shutter created, successively, always new monolayers and the relative RHEED oscillation.

The shape of the recorded curves is very sensitive to the beam position and to the average sampling area of the screen. The characteristic damping of the oscillations is due to the loss of coherence during the growth, in fact, depending on the growth kinetic, a monolayer can start to nucleate in some region before others, explaining the damping. Moreover, the region sampled by the electron beam is strongly elongated, because of the small incidence angle, resulting in an enhanced spatial averaging that accelerates the damping. The oscillations are clearly evident, and the data can be fitted with a sinusoidal function of decreasing amplitude. From the two plots a growth rate of 680 nm/h can be measured with high precision, just considering that a complete oscillation corresponds to  $a/2 = 0.283$  nm, namely, a complete gallium and arsenic monolayers. This growth rate cannot be compared to the expected growth rate of 620 nm/h at 8 mm from the wafer center, because the RHEED measurements are performed without substrate rotation, and also the exact position of the electron beam on the sample is not known. In Fig. 7.13 the same measurement shown in Fig. 7.12 is plotted on a longer time range, one can see that

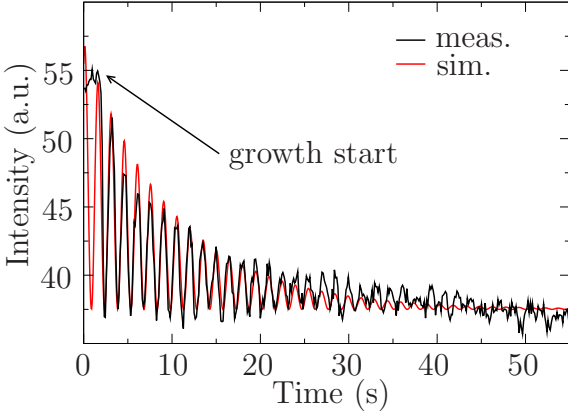


Figure 7.11: RHEED oscillations. The measured GaAs growth rate is 680 nm/h.

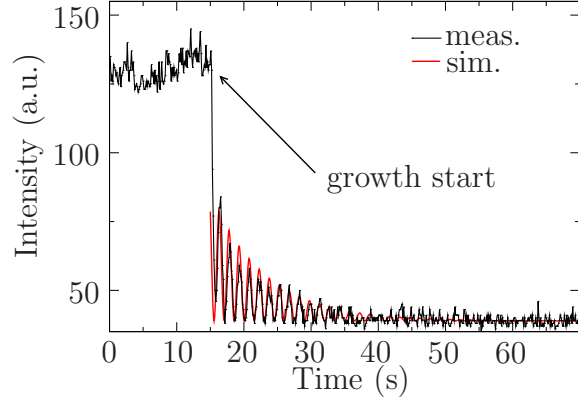


Figure 7.12: RHEED oscillation recorded integrating the signal on a different region respect Fig. 7.11. The measured growth rate is also 680 nm/h.

the intensity  $I(t)$  of the RHEED signal recovered the starting value approximately after 100 s the gallium shutter was closed. The time constant  $\tau$  of this process is related to the mobility of the gallium atoms on the surface and can be roughly estimated using the function

$$I(t) = I_{\infty} - I_1 e^{-(t-t_0)/\tau}. \quad (7.10)$$

A  $\tau$  value of approximately 25 s can be so obtained. After the recovery, a smooth atomic surface with pattern similar to the one shown in Fig. 7.9 was again obtained.

At pyrometer temperatures lower than 480 °C the diffraction pattern changes again in the so called  $c(4 \times 4)$  reconstruction. The patterns in Figs. 7.14 and 7.15 were recorded at 100 °C thermocouple temperature without performing any growth. The reconstruction possess the four-fold symmetry, in fact, there is equivalence between the  $[\bar{1}10]$  and  $[110]$  azimuth and between the  $[100]$  and  $[010]$  azimuth respectively. It is interesting to notice that the absence of quarter order diffraction streaks in Fig. 7.14 is typical of this reconstruction [71] that is proved with other surface sensitive techniques, like STM (scanning tunneling microscopy) [67]. In fact, the smallest primitive unit cell of this surface is represented in Fig. 7.2 by the square labeled by  $E$ , it follows that along the  $[100]$  and  $[010]$

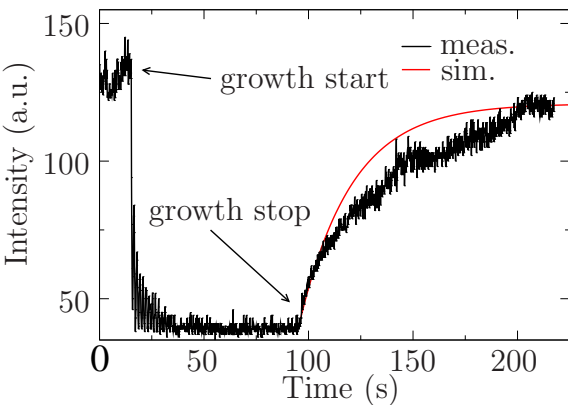


Figure 7.13: Same measurements as Fig. 7.12, but plotted on a wider time range. The RHEED signal recovery after growth-stop at  $\simeq 100$  s can be observed. The recovery time can be roughly estimated as 25 s.



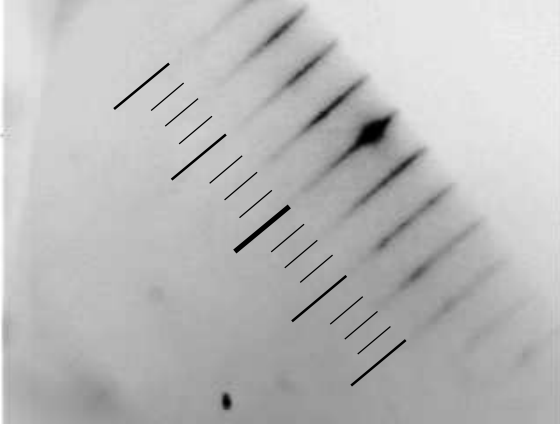


Figure 7.14: RHEED pattern of the  $c(4 \times 4)$  reconstruction recorded at  $100^\circ\text{C}$  thermocouple temperature. The  $\vec{k}_i$  is along  $[\bar{1}10]$  but the same pattern is visible for  $\vec{k}$  along the  $[110]$ .

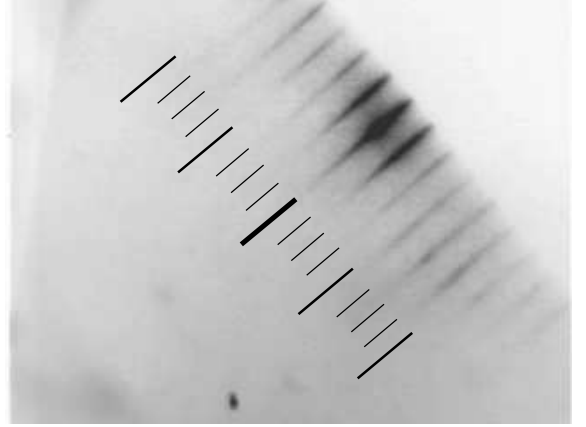


Figure 7.15: RHEED pattern of the  $c(4 \times 4)$  reconstruction recorded at  $100^\circ\text{C}$  thermocouple temperature. The  $\vec{k}_i$  is along  $[100]$  but the same pattern is visible for  $\vec{k}_i$  along the  $[010]$ .

directions a periodicity of  $2a = 2\sqrt{2}b = 1.131\text{ nm}$  is expected. This can be verified by evaluating the diffraction pattern Fig. 7.15 where the spacing between the streaks is equal to  $\sqrt{2}d/4$ . It follows that in reciprocal space along the  $[110]$  and the  $[\bar{1}10]$  directions a spacing of  $d/2$  can be observed as it can be easily proved from Fig. 7.14.

# Chapter 8

## High Performance VCSELs emitting at 760 nm

This chapter regards VCSELs emitting at 760 nm wavelength. In sect. 8.2 and 8.4, the device structure and the fabrication steps are carefully analyzed. These descriptions can be used as model for all the other devices that will be introduced in the following chapters, where all the differences will be punctually emphasized.

### 8.1 Introduction

In recent years, VCSELs emitting in the 760 nm wavelength range have attracted considerable attention for different applications, among which the most important is oxygen sensing [72, 73, 74]. VCSELs emitting at 780 nm incorporating AlGaAs QWs with only  $200\mu\text{A}$  threshold current and almost 1.1 mW single-mode output power were already demonstrated almost a decade ago [75], at the same wavelength single-mode output power of 3.4 mW was reached using metal aperture [76]. Nevertheless, for 760 nm emission wavelength, it is difficult to obtain devices with output powers in the milliwatt range, because of the reduced refractive index contrast in the DBRs, and the low carrier confinement in the QWs. The AlGaAs active region was claimed to be responsible for the low performances of these devices and novel QW materials were proposed, for example AlInGaAs/AlGaAs [77] or even quantum dots [78]. Despite of this, in what follows it is shown that the AlGaAs material system can be successfully employed to produce high-performance short-wavelength VCSELs.

For spectroscopic applications, such as oxygen sensing, devices that show hop-free mode operation tunable in a wide wavelength range are necessary. In particular not only single-mode operation is required but also the polarization switch, typical of VCSELs, should be removed. The presented AlGaAs 760 nm VCSELs show good performances and, if special fabrication steps are applied, they are valid spectroscopic sources for cheap in-situ oxygen sensing applications.

## 8.2 Layer structure

The active region of the laser is composed of three 8 nm thick  $\text{Al}_{0.14}\text{Ga}_{0.86}\text{As}$  QWs separated by 10 nm thick  $\text{Al}_{0.40}\text{Ga}_{0.60}\text{As}$  barriers. For current confinement, a 25 nm thick AlAs oxidation layer is placed above the QW region in a node of the calculated standing wave pattern. The DBRs are graded in composition and doping concentration in order to minimize the optical absorption and to decrease the electrical resistance. The  $n$ -doping level is varied between  $1.3 \times 10^{18}$  and  $2.7 \times 10^{18} \text{ cm}^{-3}$ , while the  $p$ -doping is varied between  $2.1 \times 10^{18}$  and  $5.6 \times 10^{18} \text{ cm}^{-3}$ . Moreover,  $\delta$ -doping is included both in the  $n$ - and the  $p$ -side in the vicinity of the standing wave nodes.

The mirrors incorporate 40.5  $n$ -type and 26  $p$ -type layer pairs. The highest refractive index in the DBRs is given by  $\text{Al}_{0.30}\text{Ga}_{0.70}\text{As}$  layers which exhibit an absorption edge at 690 nm with a sufficient safety margin to avoid absorption at the emission wavelength. The first 32  $n$ -type pairs consists of AlAs to enhance the refractive index contrast, while  $\text{Al}_{0.93}\text{Ga}_{0.07}\text{As}$  is used in the remaining  $n$ -pairs as lowest index material in the DBRs. This composition provides enough tolerance for the subsequent mesa etching process to avoid the oxidation of the AlAs layers in the  $n$ -DBR. The  $p$ -contact layer consists of 14 nm thick GaAs with a carbon doping concentration exceeding  $10^{20} \text{ cm}^{-3}$ . The growth temperature was  $580^\circ\text{C}$  during the entire process. In addition, a top quarter-wave ( $\lambda/4$ ) extra layer is grown, yielding antiphase reflection from the semiconductor–air interface. This extra layer is partially or totally removed at the output facet, as explained in detail in sect. 8.4.

In Fig. 8.1, the aluminum concentration profile together with the standing wave pattern, simulated for the emission wavelength of 760 nm, is plotted for the central part of the VCSEL structure. In Fig. 8.2 a SEM (scan electron microscope) picture of the complete sample cross section is shown, it is possible to see the difference between the lower 32 and the upper 8  $n$ -type pairs, and the  $p$ -doped DBR.

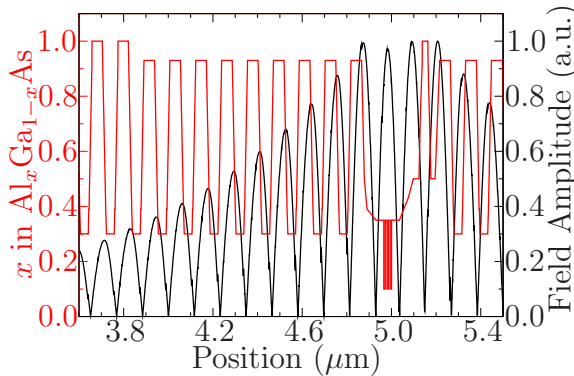


Figure 8.1: Aluminum concentration profile and simulated standing wave pattern in the central part of the structure for the emission wavelength of 760 nm.

## 8.3 Wafer-level characterization

Since the growth rate in the given MBE system exhibits a gradient along the radial direction, resonance wavelengths between 717 and 790 nm are obtained on the same wafer. Fig. 8.3 shows the reflectivity spectra for samples without (curve a) and with the  $\lambda/4$  antiphase layer (curve b). The measurements are performed at wafer positions where the

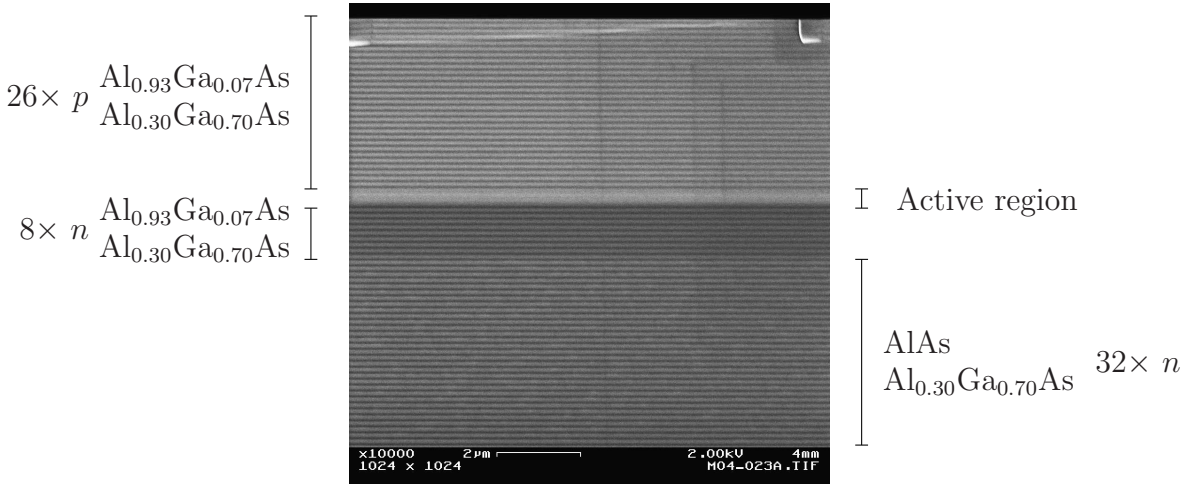


Figure 8.2: SEM section of one of the samples described in the text. It is possible to distinguish the two different kinds of  $n$ -doped DBRs and the 26  $p$ -doped top pairs.

resonance dips occur at approximately 765 nm. The sample with the antiphase layer has a reduced resonance reflectivity of 65%.

Fig. 8.4 shows the photoluminescence spectrum, recorded at room temperature, corresponding to the sample with antiphase layer, under 514.4 nm argon ion laser excitation and after the removal of the top  $p$ -doped DBR by wet etching. The photoluminescence spectra are less sensitive to the thickness gradient over the wafer than the resonance wavelengths, because the given variations in the QW thickness do not significantly shift the energy levels. therefore, the aluminum composition is almost constant over the wafer. The photoluminescence peak is located at approximately 748 nm wavelength. This value is optimized to obtain the best performance for 760 nm laser emission at room temperature.

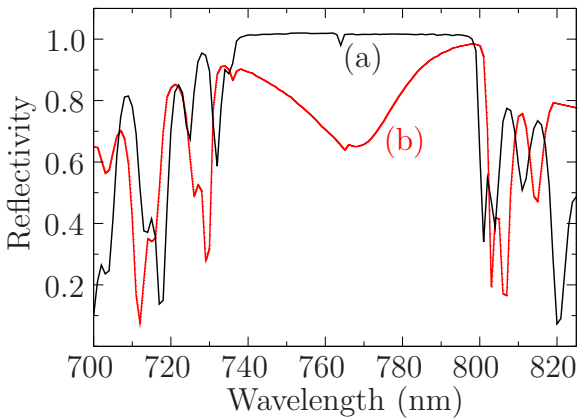


Figure 8.3: Reflectivity spectra for standard (a) and for antiphase (b) samples.

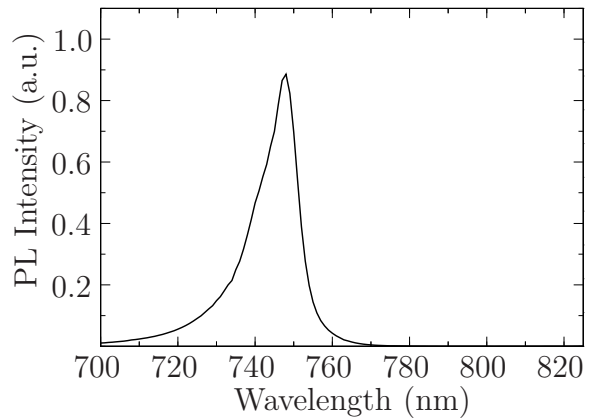


Figure 8.4: Room temperature photoluminescence spectrum of an etched sample.

## 8.4 Lasers fabrication

The fabrication process started with wet mesa etching. The etching process was stopped below the 25 nm thick AlAs oxidation layer and circular mesas with different diameters between 48 and 54  $\mu\text{m}$  were defined. Oxidation in a  $\text{N}_2/\text{H}_2\text{O}$  atmosphere at a temperature of 400  $^\circ\text{C}$  resulted in oxide apertures ranging between 2 and 8  $\mu\text{m}$ . On the top side TiPtAu ring contacts and on the bottom side broad-area GeAuNiAu contacts were deposited.

In the following, the term standard device refers to a VCSEL obtained after etching the extra  $\lambda/4$  layer. The high top mirror reflectivity will thus be restored. On the other hand, devices with superior single-mode performance can be obtained by removing this layer only in a center circular region of a few micrometer diameter. In this case, higher order modes will be strongly suppressed since they experience a reduced reflectivity and additional absorption in the  $\lambda/4$  thick GaAs layer. These devices are called inverted circular relief VCSELs. Instead of etching only a circular disk into the central region of the extra  $\lambda/4$  GaAs layer, one can also implement a surface grating with the same diameter. A photograph of one of this special device together with an AFM measurement of the inverted relief are shown in Fig. 8.5. With these inverted grating relief VCSELs, not only an enhancement of the single-mode performance but also a stable polarization can be achieved. More details on these devices can be found in [79].

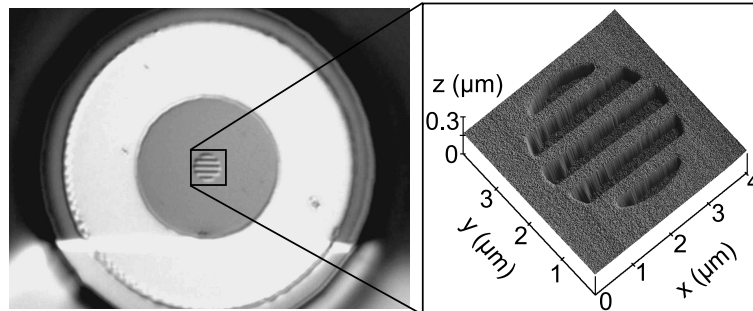


Figure 8.5: Optical microscope photograph and AFM measurement on an inverted relief VCSEL.

## 8.5 Standard and inverted relief 760 nm VCSELs

In Fig. 8.6 is presented the light–current–voltage (LIV) characteristics of a standard VCSEL with 8  $\mu\text{m}$  oxide diameter. The laser shows a threshold current of 1.5 mA and a differential quantum efficiency of 35%. The maximum output power of 5.6 mW is reached at 16 mA current. Fig. 8.6 also displays the optical spectrum at 17 mA, indicating transverse multimode operation at approximately 768 nm emission wavelength.

In Fig. 8.7 the LIV characteristics of a 4  $\mu\text{m}$  active diameter VCSEL with a 3  $\mu\text{m}$  diameter inverted circular relief shows a threshold current of 0.7 mA and single-mode operation up to 2.0 mW with a side-mode suppression ratio (SMSR) of at least 30 dB, as shown by the spectrum recorded at 4.4 mA. A kink in the output power characteristic,

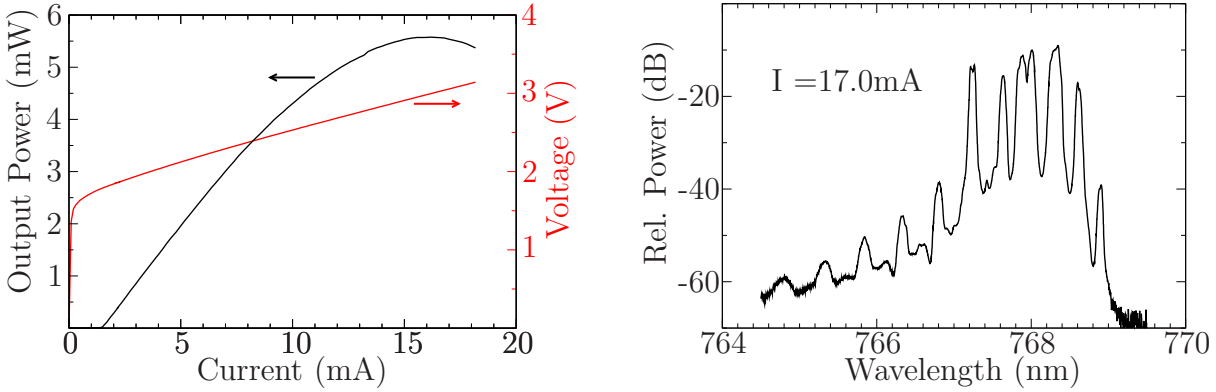


Figure 8.6: LIV characteristics (right) and spectrum (left) of a standard multimode VCSEL with an active diameter of  $8 \mu\text{m}$ .

here at about 5 mA current, is typical for such VCSELs when higher modes appear. Besides emission wavelengths around 760 nm, laser operation could also be observed for wavelengths far away from the gain maximum, due to the mentioned radial gradient. Fig. 8.8 depicts the characteristics of a device with an inverted circular relief of  $3 \mu\text{m}$  diameter and  $4 \mu\text{m}$  oxide aperture lasing at 720 nm in multimode operation, as evidenced by the spectrum taken at 6.6 mA. Despite the large detuning between the gain maximum and the cavity resonance of more than 40 nm, the device still shows 16% differential quantum efficiency, 0.6 mW maximum output power, and 2.8 mA threshold current. Also from the same sample, devices lasing at 717 nm with a maximum output power of 0.3 mW can be observed [80].

The wavelength dependences of the maximum single-mode output power and of the threshold current are shown in Figs. 8.9 and 8.10 for standard and inverted relief VCSELs respectively. For easy comparison, the same scale is used. Both types of VCSELs have an oxide aperture diameter of  $4 \mu\text{m}$ . The relief diameter is  $3 \mu\text{m}$  and its depth is 64 nm. As can be inferred from the minima of the threshold currents of both types of lasers, the best spectral overlap of the gain curve and the cavity resonance is given for emission

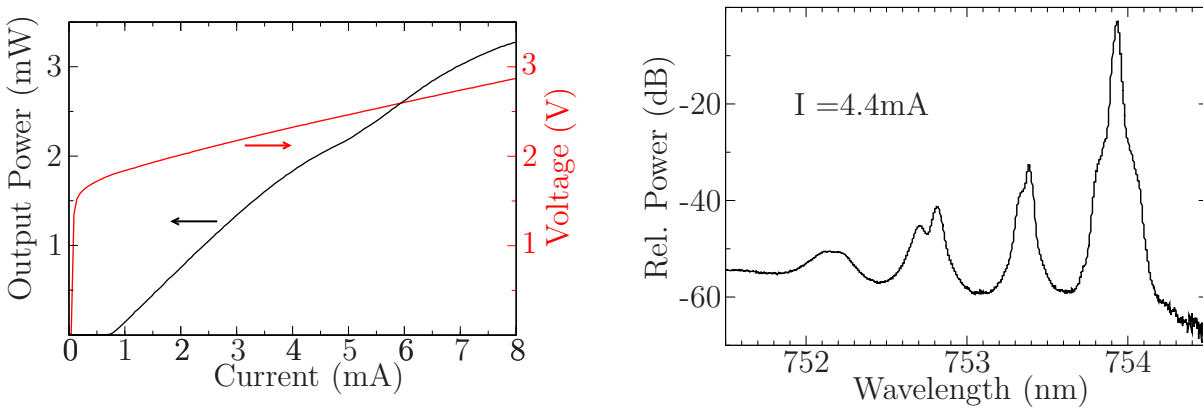


Figure 8.7: LIV characteristics (right) and spectrum (left) of a  $4 \mu\text{m}$  active diameter VCSEL with a  $3 \mu\text{m}$  diameter inverted relief, which is single-mode up to 4.4 mA.

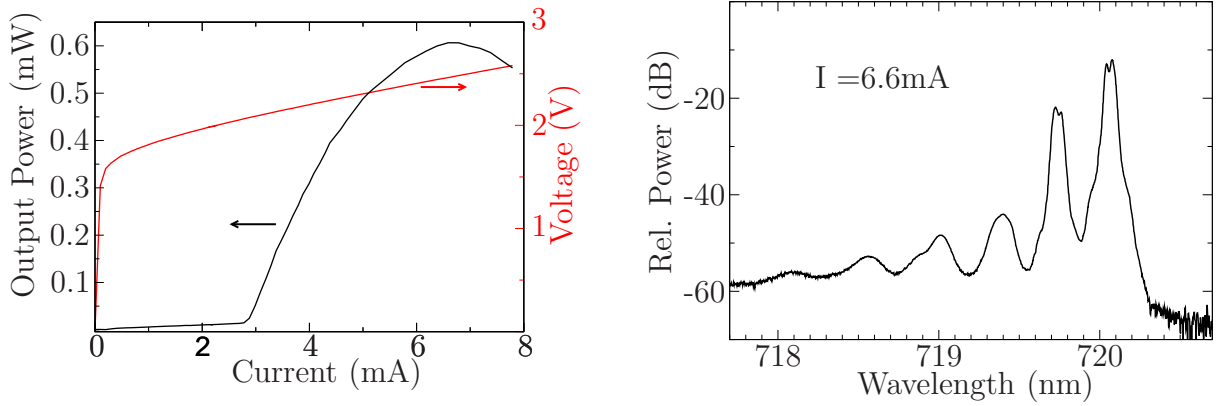


Figure 8.8: LIV characteristics (right) and spectrum (left) of a  $3 \mu\text{m}$  diameter inverted relief device with  $4 \mu\text{m}$  active diameter, lasing at  $720 \text{ nm}$ .

wavelengths between  $760$  and  $780 \text{ nm}$ . For smaller or larger emission wavelengths, the threshold current increases due to detuning between gain peak and cavity resonance. The magnitudes of the threshold currents and their wavelength dependences are very comparable for both types of lasers. The minimum threshold current is found in the  $771$  to  $778 \text{ nm}$  range and is  $420 \mu\text{A}$  in both cases. In contrast, the maximum single-mode output powers of standard and inverted relief VCSELs differ significantly. On average, the power is approximately doubled for the inverted circular relief lasers which clearly demonstrates the effectiveness of this technique. Close to  $760 \text{ nm}$  wavelength, i.e. in the spectral region important for oxygen sensing, standard devices show about  $0.9 \text{ mW}$  power, whereas more than  $1.9 \text{ mW}$  are obtained from the circular inverted relief VCSELs.

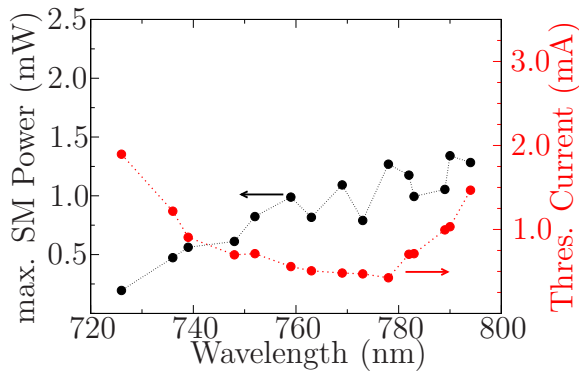


Figure 8.9: Wavelength dependence of the maximum single-mode (SM) output power and of the threshold current of standard VCSELs with about  $4 \mu\text{m}$  active diameter.

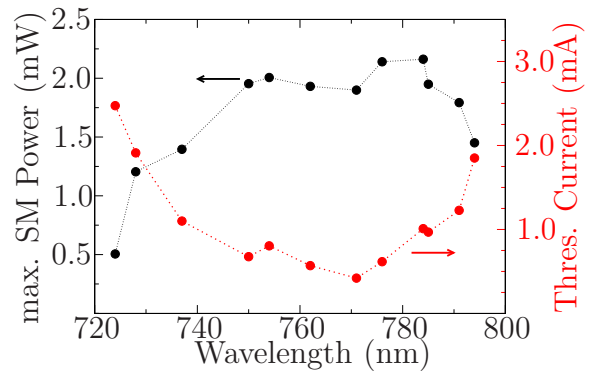


Figure 8.10: Wavelength dependence of the maximum single-mode power and of the threshold current of inverted relief VCSELs with  $3 \mu\text{m}$  relief diameter and about  $4 \mu\text{m}$  active diameter, to be compared with Fig. 8.9.



## 8.6 Inverted grating relief 760 nm VCSELs

In this section, devices with the inverted grating relief are considered. All the devices have an oxide aperture of  $4\mu\text{m}$  and, as can be seen from Fig. 8.5, a relief diameter of  $4\mu\text{m}$  and a grating period of  $0.8\mu\text{m}$  and  $0.7\mu\text{m}$  with a duty cycle of 50%. Gratings depths of 34, 44, 53, 64, and  $74\text{nm}$  were realized, but there is almost no dependence of the devices performances on the etch depth. The gratings are obtained by e-beam lithography, because just a small amount of devices were produced, nevertheless submicrometric standard lithography would be possible for mass production.

In Fig. 8.11, the polarization resolved LIV curve of one typical device is shown as function of the device temperature. One can easily see how the grating along the  $[\bar{1}10]$  crystallographic direction forces the VCSEL to lase with a polarization that is practically orthogonal to this direction. The lasing operation is single-mode up to  $5\text{mA}$ , where the

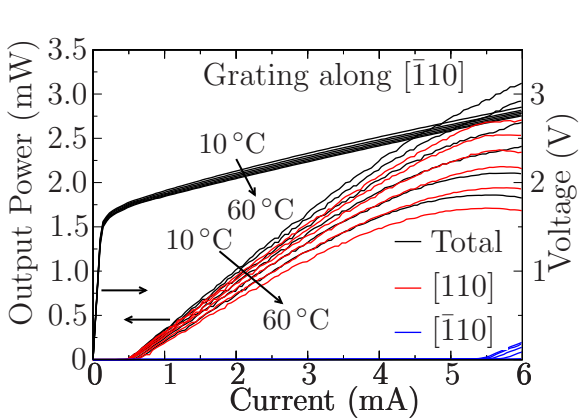


Figure 8.11: LIV curves of a  $4\mu\text{m}$  active diameter VCSEL with an inverted grating relief of  $3\mu\text{m}$  and a period of  $0.8\mu\text{m}$  and an etch depth of  $44\text{nm}$ . The curves are polarization resolved and plotted as function of different device temperatures.

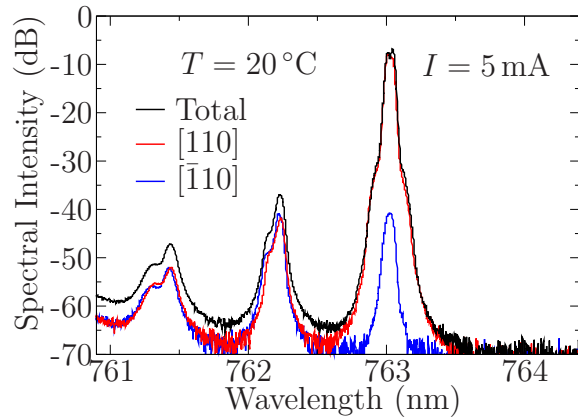


Figure 8.12: Polarization resolved spectrum of the same VCSEL of Fig. 8.11 for a device temperature of  $20^\circ\text{C}$  at a current of  $5\text{mA}$ .

SMSR is still  $30\text{dB}$  as shown in Fig. 8.12, and the peak-to-peak OPSR (orthogonal-polarization suppression ratio) in the spectra is  $33\text{dB}$ , which corresponds to the limit of the employed polarizer.

In Figs. 8.13 and 8.14, the wavelength tunability of the device considered previously is analyzed by varying the current from  $1\text{mA}$  to  $5\text{mA}$  at a fixed device temperature of  $35^\circ\text{C}$  and by varying the device temperature from  $10^\circ\text{C}$  to  $60^\circ\text{C}$  at a fixed current of  $5\text{mA}$ . This is a preliminary prove that this laser is a valid spectroscopic source because it remains single-mode with a SMSR of  $30\text{dB}$  over the whole tuning range. The current and temperature tuning coefficients are  $0.6\text{nm}/\text{mA}$  and  $0.06\text{nm}/\text{K}$  respectively. In Fig. 8.15, always from the same device, the OPSR is plotted in function of the current together with LI curve relative to a temperature of  $20^\circ\text{C}$ , one can see how the OPSR is higher than  $26\text{dB}$  for current between  $2.5$  and  $5\text{mA}$ .

Finally in Fig. 8.16 a histogram shows the distribution of the maximum single-mode



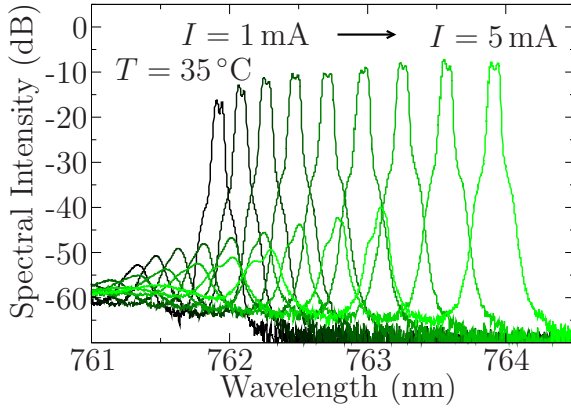


Figure 8.13: Spectra of the laser from Fig. 8.11 at device temperature of 35°C for currents varying from 1 mA to 5 mA in steps of 0.5 mA.

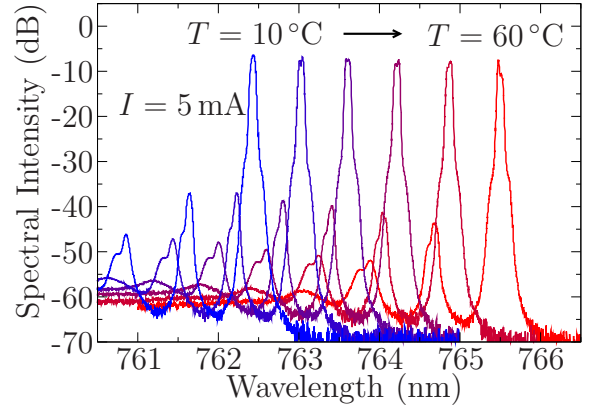


Figure 8.14: Spectra of the laser from Fig. 8.11 at a current of 5 mA for device temperatures varying from 10°C to 60°C in steps of 10°C.

output power measured for many devices comparable with the one of Fig. 8.11, these devices have the same oxide aperture and the same inverted grating relief parameters, but they differ slightly in emission wavelength which is ranging between 750 nm and 790 nm. The large gradient thickness present in the MBE system reduces the possibility of making a large statistic on devices with comparable wavelength and, furthermore, one has to consider that on the same wafer devices with different oxide apertures and grating relief parameters were fabricated. This drastically reduces the number of comparable lasers. For a complete overview of the statistical analysis of the performances of the 760 nm VCSELs one should refer to [79].

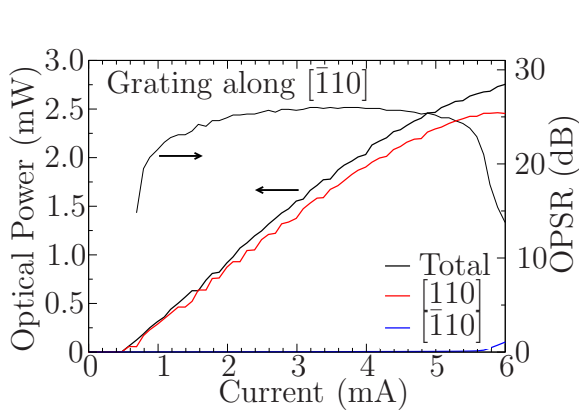


Figure 8.15: Polarization resolved LI curves and OPSR of the VCSEL in Fig. 8.11 for a substrate temperature of 20°C.

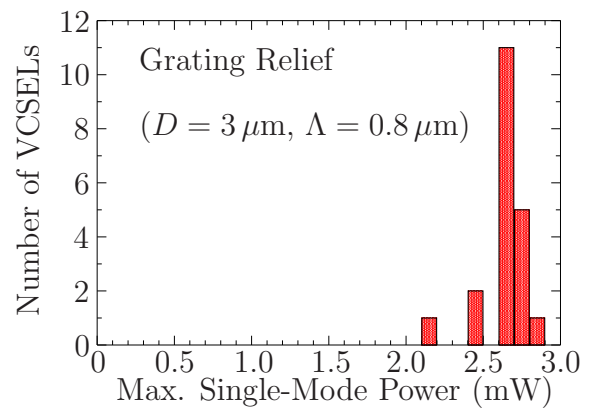


Figure 8.16: Distribution of the maximum single-mode output power for VCSELs comparable to the one in Fig. 8.11 at a substrate temperature of 20°C.

## 8.7 Oxygen sensing

The devices described in the last section are good spectroscopic sources for oxygen sensing, where a VCSEL is used to scan the absorption lines of the gas molecules by detecting the laser beam passed through the gas under investigation. VCSELs or DFB (distributed feedback) lasers were already used for this scope [81, 82, 83, 84]. The advantage of this method is the possibility to perform non local measurements that are spatially integrative, and also to allow them at very high gas temperatures. The use of a VCSEL, which is a tunable light source that substitutes a spectrometer, brings together the advantages of low cost with high versatility due to small volumes, easy tunability via injection current or device temperature modulations.

The *A*-band of the oxygen spectrum, the so called atmospheric transition for oxygen, is typically used for sensing. It is given by the transitions between the triplet electronic ground state  $X^3\Sigma_g^+(\nu = 0)$  and the singlet excited electronic state  $b^1\Sigma_g^+(\nu = 0)$ , the transitions do not excite the ground vibrational levels that remains  $\nu = 0$ .

The used nomenclature can be briefly resumed considering that, the ground electronic state is denoted with *X*, excited electronic states with the same or different multiplicity of the ground state are indicated with progressive capital letters *A, B, C...*, or small letters *a, b, c...* respectively.

The multiplicity is given by  $2S + 1$ , where  $\vec{S}$  is the spin of the molecule.

The projection of the orbital angular momentum  $\vec{L}$  on the molecular axis is given by  $\Sigma, \Pi, \Delta, \Phi...$  for respectively 0, 1, 2, 3....

The inversion symmetry relative to the molecule center is denoted by the indexes *g/u* for the parities +1, -1 respectively, the symmetry under reflection in a plane containing the internuclear axis is indicated by + and -.

The final state of the transition is characterized by a vibrational number  $\nu = 0, 1, 2, 3...$ , which corresponds to the *A, B, C, D...* band respectively, and if the starting state of the transition has vibrational number  $\nu \neq 0$  one has the so called hot bands.

All the transitions of the band are defined by the rotational degree of freedom of the molecule that is characterized by the angular momentum  $\vec{N}$ . Because of coupling between  $\vec{S}$  and  $\vec{N}$ , the total angular momentum  $\vec{J} = \vec{N} + \vec{S}$  is a good quantum number and one has

$$J = N \quad S = 0 \quad (8.1)$$

that represent a singlet excited state, and a triplet for the ground state that is splitted as follows

$$\begin{aligned} J &= N + 1 \\ J &= N \quad S = 1 \\ J &= N - 1. \end{aligned} \quad (8.2)$$

A simulated transmission spectrum of the *A*-band  $X^3\Sigma_g^+ \rightarrow b^1\Sigma_g^+$  of oxygen is shown in Fig. 8.17, the lines are tabulated in the HITRAN96 database [85] and are divided in pairs. Symmetry arguments shows that those transitions are electric dipole forbidden and the magnetic dipole term is approximately 5 orders of magnitude smaller than allowed transitions. To identify the transitions one has to consider that, in the excited state, just even values of *N* are allowed by the wavefunction symmetry and in the ground state just

the odd ones. The given selection rules are  $\Delta N = \pm 1$  and  $\Delta J = 0, \pm 1$  [87] and, therefore, each transition is identified by the quantum numbers  $N$  and  $J$  of the initial state and their relative increment denoted by  $P, Q, R$  for  $-1, 0, 1$  respectively. Using this notation one can label each transition in the band with the sequence  $\Delta N N \Delta J J$ . Following these conventions, the spectrum in Fig. 8.17 is divided in a  $R$ -branch at higher energies and a  $P$ -branch at lower, characterized by  $\Delta N = 1$  and  $\Delta N = -1$  respectively. It is evident that the latter is preferred for oxygen sensing because of the higher spacing between the lines. One can also notice that the given selection rule explains the presence of the pairs of lines in both branches, in fact in the  $R$ -branch the allowed transitions are  $R m R m$  and  $R m Q m + 1$  and in the  $P$ -branch  $P m P m$  and  $P m Q m - 1$ , where  $m$  is an odd integer. For  $m = 1$  in the  $P$ -branch just the transition  $P1P1$  exists and this is the only line that does not belong to a doublet, as one can see in Fig. 8.17 and in Table 8.1.

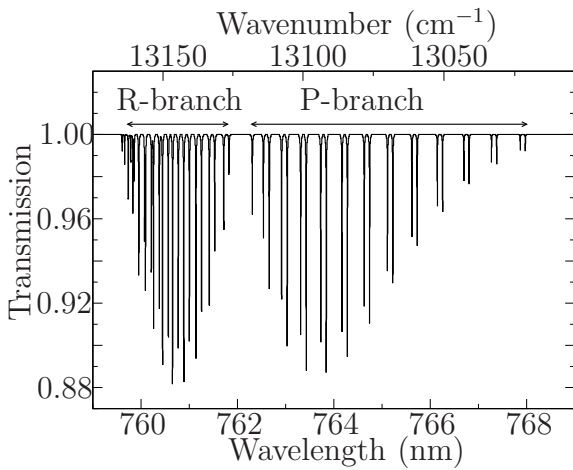


Figure 8.17: Oxygen A-band simulated transmission spectrum at an optical path length of 1 m at standard conditions and an oxygen concentration of 100%.

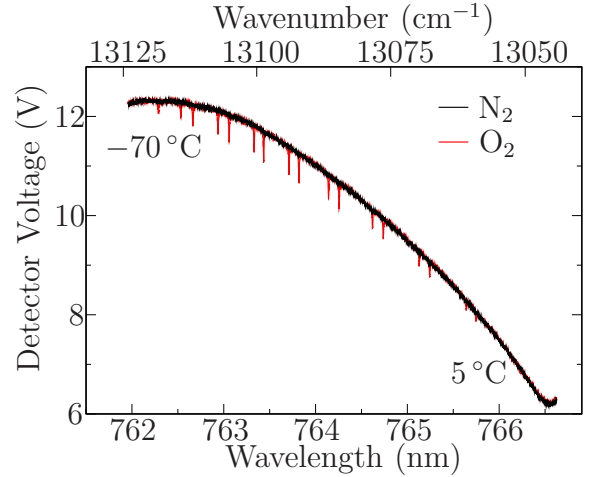


Figure 8.18: Laser signal measured through an absorption cell of 0.5 m length filled with nitrogen (black) or oxygen (red) at 1 bar. The wavelength scan is obtained by rising the device temperature from of  $-70^\circ\text{C}$  to  $5^\circ\text{C}$ .

In Fig. 8.18 the laser transmission signal through nitrogen and oxygen was recorded through 0.5 m optical length at standard conditions. The plotted signal is the output voltage directly measured from the detector. The presence of 15 absorption lines of oxygen from the  $P1P1$  to the  $P15P15$  is easy to recognize. The wavelength scan was obtained by tuning the VCSEL by changing the device temperature. In the experiment the temperature was changed in 12 s from  $-70^\circ\text{C}$  to  $5^\circ\text{C}$ . Further elaboration of the raw data allows the extraction of the transmission spectra of the gas, as shown in Figs. 8.19 and 8.20, where two spectra, recorded in different conditions, show marked differences. A polarization stable behavior without any mode hop was obtained over a tune range of the VCSEL emission wavelength of more than 7 nm, by varying the device temperature from  $-70^\circ\text{C}$  to  $100^\circ\text{C}$ .

Transmission spectra of gases are very sensitive to temperature and pressure. In fact the occupation probability of an energy level is function of the temperature, and the

<i>P</i> -branch			<i>R</i> -branch		
Position (cm <sup>-1</sup> )	Position (nm)	Assignment	Position (cm <sup>-1</sup> )	Position (nm)	Assignment
—	—	—	13126.39346	761.824	<i>R1R1</i>
13118.04555	762.309	<i>P1P1</i>	13128.26932	761.715	<i>R1Q2</i>
13114.10087	762.538	<i>P3Q2</i>	13131.49186	761.528	<i>R3R3</i>
13112.01639	762.659	<i>P3P3</i>	13133.44172	761.415	<i>R3Q4</i>
13107.62884	762.914	<i>P5Q4</i>	13136.21715	761.254	<i>R5R5</i>
13105.61746	763.032	<i>P5P5</i>	13138.20517	761.139	<i>R5Q6</i>
13100.82204	763.311	<i>P7Q6</i>	13140.56811	761.002	<i>R7R7</i>
13098.84907	763.426	<i>P7P7</i>	13142.58405	760.885	<i>R7Q8</i>
13093.65678	763.729	<i>P9Q8</i>	13144.54100	760.772	<i>R9R9</i>
13091.71093	763.842	<i>P9P9</i>	13146.58038	760.654	<i>R9Q10</i>
13086.12583	764.168	<i>P11Q10</i>	13148.13604	760.564	<i>R11R11</i>
13084.20390	764.280	<i>P11P11</i>	13150.19683	760.445	<i>R11Q12</i>
13078.22816	764.630	<i>P13Q12</i>	13151.34898	760.378	<i>R13R13</i>
13076.32856	764.741	<i>P13P13</i>	13153.43079	760.258	<i>R13Q14</i>
13069.96200	765.113	<i>P15Q14</i>	13154.17969	760.215	<i>R15R15</i>
13068.08212	765.223	<i>P15P15</i>	13156.28118	760.093	<i>R15Q16</i>
13061.32737	765.619	<i>P17Q16</i>	13156.62279	760.073	<i>R17R17</i>
13059.46714	765.728	<i>P17P17</i>	13158.74399	759.951	<i>R17Q18</i>
13052.32403	766.147	<i>P19Q18</i>	13158.68085	759.955	<i>R19R19</i>
13050.48078	766.255	<i>P19P19</i>	13160.81486	759.831	<i>R19Q20</i>
13042.94893	766.698	<i>P21Q20</i>	13160.33962	759.859	<i>R21R21</i>
13041.12509	766.805	<i>P21P21</i>			
13033.19668	767.271	<i>P23Q22</i>			
13031.39038	767.378	<i>P23P23</i>			

Table 8.1: Position and assignment of the lines of the oxygen A-band at 296 K after [87].

intensity ratio between two different lines, characterized by the rotational numbers  $N_1$  and  $N_2$ , is given by the Boltzmann distribution

$$\frac{I_{N_1}}{I_{N_2}} = \frac{2N_1 + 1}{2N_2 + 1} e^{-\beta(E_{N_1} - E_{N_2})} \quad (8.3)$$

where  $T$  is the absolute temperature,  $k_B$  the Boltzmann constant and  $\beta = (k_B T)^{-1}$  and  $2N + 1$  is the degeneracy of a level characterized by  $N$ . The formula (8.3) allows measurement of the gas temperature. More complicated is the modeling of the line shape, in fact there are several mechanisms that are responsible for the line broadening. Despite the statistical equilibrium the occupation of an energy level is related to spontaneous emission

processes and to the dynamic of the inelastic collisions between molecules. Therefore, one can define a lifetime  $\tau$  of the specific energy level, this lead to an uncertainty in the energy due to the uncertainty relation. As result of the exponential decay of the level occupations it is associated a lorentzian broadening of the transitions energies, these effects have to be added to the Doppler broadening due to molecule velocity distribution and that is just a function of the temperature [86]. The elastic collisions between molecules are responsible of an additional broadening associated with a small shift of the line positions. All these effects are strongly pressure and temperature dependent.

In Figs. 8.19 and 8.20 two spectra were recorded at different pressures, the raw measurements are similar to the one shown in Fig. 8.18 but, after elaboration of the data, the transmission spectra can be extracted and 19 lines are investigated. The data fits well with the simulation and in particular one can extrapolate the pressure broadening coefficient for each line. These values agree to the literature data within 6%, this means that the oxygen gas preassure can be determined with the same precision, and an high reliability in the measurement is obtained by considering several absorption lines. At pressures higher that 10 bar the pressure broadening is responsible of considerable line coupling transitions, and the spectra can be not longer easily simulated.

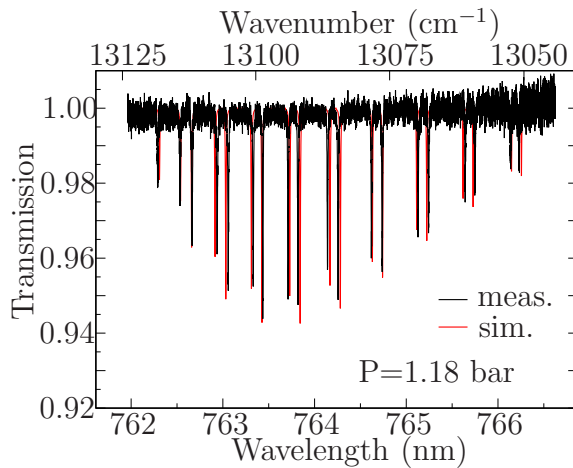


Figure 8.19: Measured and simulated transmission spectrum at an optical path length of 0.5 m at 1.18 bar and an oxygen concentration of 100%.

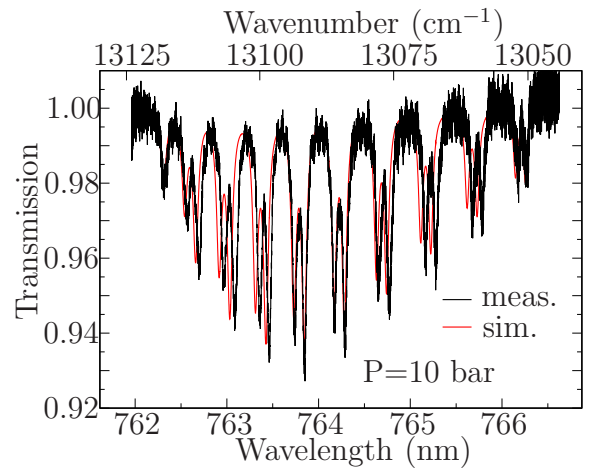


Figure 8.20: Measured and simulated transmission spectrum at an optical path length of 0.5 m at 10 bar and an oxygen concentration of 100%.

By modulating the injection current of the VCSELs at 1 kHz, wavelength scans on a single absorption line were performed, considering that the automatic evaluation algorithm allowed just the sampling of 20 measurements per second, oxygen concentration in the range 0–10% were performed with a precision of  $4000 \text{ ppm} \cdot \text{m} \cdot \text{Hz}^{1/2}$ , that means a precision of 0.4% in one second, sampling on a length of 1 m. In further experiments a detection limit of 16 ppm was reached using an Herriott cell, that provides an effective optical path of 5 m using the second-harmonic detection spectroscopy. All details and informations concerning, these temperature, pressure, and concentration measurements can be found in [88, 89, 90].

# Chapter 9

## VCSEL devices emitting at 850 nm

Oxide-confined VCSELs emitting at 850 nm wavelength are of great importance for short distance data transmission, but other applications, such as optical spectroscopy, optical sensing, and also biophotonic, are emerging utilization fields for this devices. In fact, one has the advantage of an established technology based on GaAs QWs and on the almost unstrained AlGaAs material system. Despite the standardization of these devices, special designs require an accurate attention in the growth technique and in the fabrication. In this chapter some special kind of 850 nm VCSELs are presented followed by a detailed analysis of the DBRs compositional profiles performed with HRXRD.

### 9.1 High-power single-mode 850 nm VCSELs

In Fig. 9.1, a scheme of a typical 850 nm emitting VCSEL is shown. The devices, that were grown at 580 °C on *n*-substrates, consist of an optical resonator which is composed of 23 Al<sub>0.90</sub>Ga<sub>0.10</sub>As/Al<sub>0.20</sub>Ga<sub>0.80</sub>As *p*-doped and 38.5 *n*-doped Bragg mirror pairs with graded interfaces in order to reduce the electrical resistance. Three  $\delta$ -doping sheets per period are always settled close to the node of the standing wave pattern, and the doping is modulated in order to improve the electrical performance without drastically increment the optical absorption due to free carriers. The active region is composed of three GaAs 8 nm thick QWs surrounded by 10 nm Al<sub>0.27</sub>Ga<sub>0.73</sub>As layers. In order to provide an higher current injection, an oxide aperture is fabricated by selective oxidation of an highly *p*-doped AlAs layer of 32 nm thickness which is situated on a node of the standing wave pattern. A plot of the AlGaAs composition close to the active region, together with the doping concentration is shown in Fig 9.2.

To improve the single-mode maximum output power the inverted relief technic is used. An extra  $\lambda/4$  antiphase GaAs layer was grown on the top of a standard structure, the reflectivity of the top mirror is in this way drastically reduced. A comparison between reflectivity spectra of comparable VCSEL structures, standard and with the extra  $\lambda/4$  GaAs layer, is shown in Fig 9.3. The fabrication process is optimized to obtain a circular inverted relief of diameter between 3 and 4  $\mu\text{m}$ . The nominal depth of the relief is 58 nm and it is calculated in order to minimize the threshold gain of the laser. A self-alignment technique is used to position the relief and the etching was performed using a citric acid solution. Beside the inverted relief devices also reference devices were fabricated by

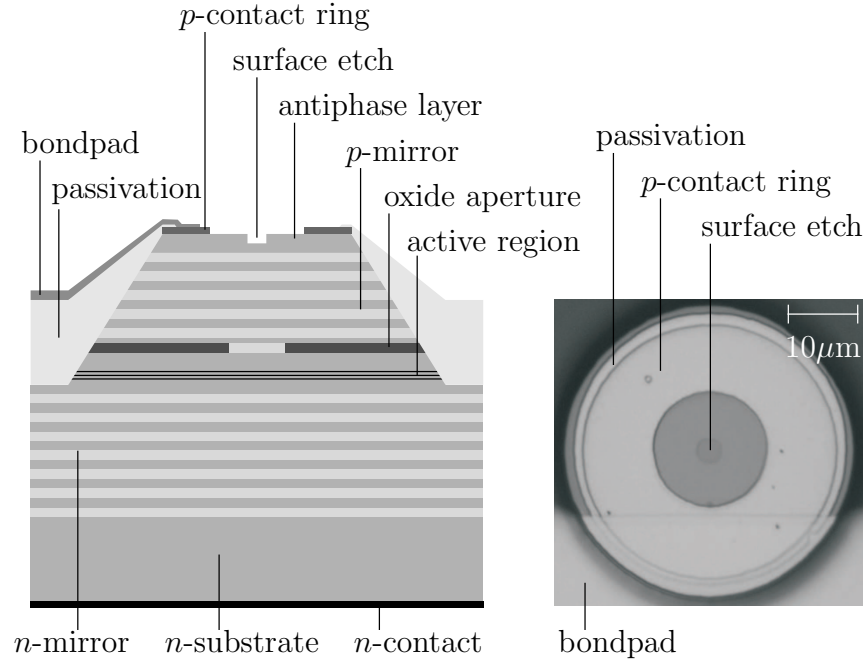


Figure 9.1: Cross section scheme of a VCSEL (left), top view photograph of a VCSEL with inverted surface relief (right).

etching the antiphase layer across the whole output facet. For a detailed description of the fabrication process one can refer to [91].

In standard single-mode VCSELs the oxide aperture is limited to 3-4 μm, because larger oxide apertures result in higher maximum output power but multimode operation. In an inverted relief device, the oxide aperture can be increased up to 6 μm with a relative increase of the maximum single-mode output power.

In Fig 9.4 an output characteristic of a reference device of 6 μm active diameter shows

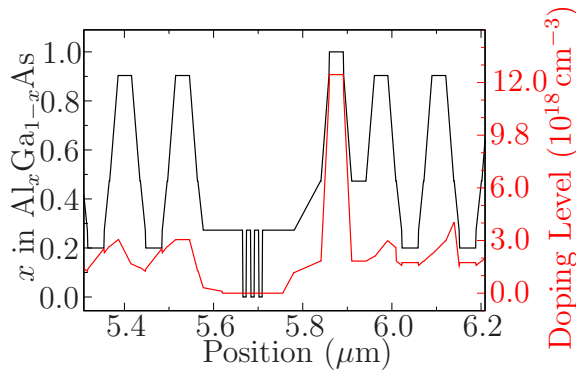


Figure 9.2: Nominal aluminum molar fraction  $x$  in the  $\text{Al}_x\text{Ga}_{1-x}\text{As}$  alloy and doping profile of the presented devices.

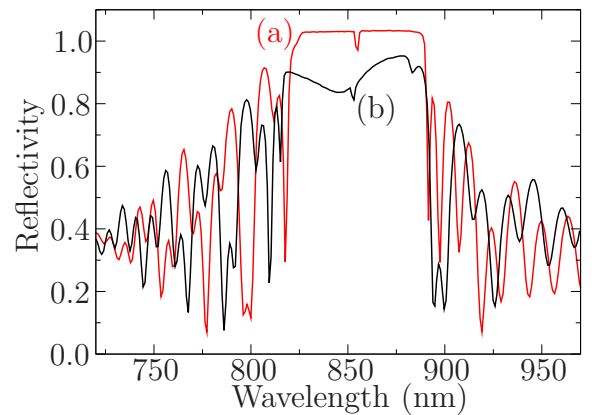


Figure 9.3: Reflectivity spectra for a standard (a), and an inverted relief structure (b).



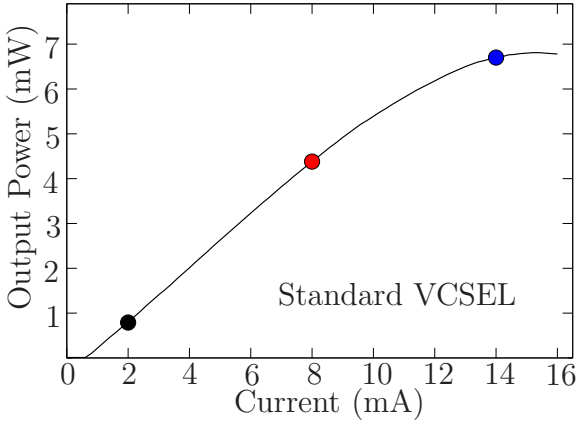


Figure 9.4: LI characteristic of a standard reference device having an oxide aperture of  $6\mu\text{m}$ .

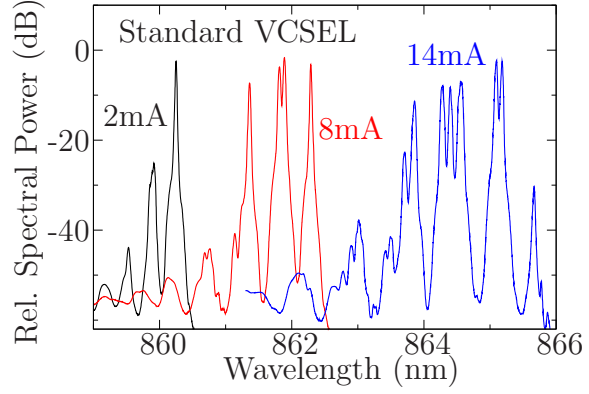


Figure 9.5: Spectra of the standard reference device of  $6\mu\text{m}$  oxide aperture diameter at three different injection currents.

a threshold current of  $0.7\text{ mA}$  and a maximum output power of  $6.8\text{ mW}$  at  $14\text{ mA}$  injection current. Even just above the threshold the device exhibits no single mode operation as shown in Fig. 9.5, where three spectra, recorded at three different injection currents, are shown.

In Fig 9.6 the same measurements are performed for an inverted relief device nearby the reference one. The relief diameter is  $3.3\mu\text{m}$  and has a depth of  $58\text{ nm}$ , and the oxide aperture is again of  $6\mu\text{m}$ . In this case one can see that the threshold current is clearly increased to  $3.1\text{ mA}$ , but the device shows single-mode operation with SMSR higher than  $30\text{ dB}$  up to the thermal rollover, as one can see in Fig. 9.7. The record maximum single-mode output power delivered is of  $6.3\text{ mW}$  at  $12\text{ mA}$  driving current. This value should be compared with the  $6.1\text{ mW}$  in [92].

In Figs. 9.8 and 9.9, the far field patterns of the two aforementioned devices driven

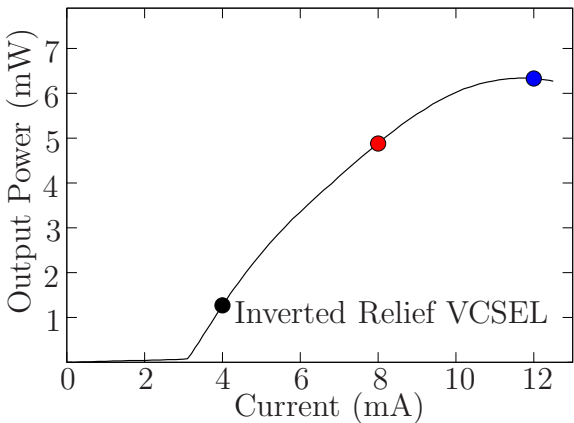


Figure 9.6: LI characteristic of an inverted relief device having an oxide aperture diameter of  $6\mu\text{m}$  and a relief diameter of  $3.3\mu\text{m}$ .

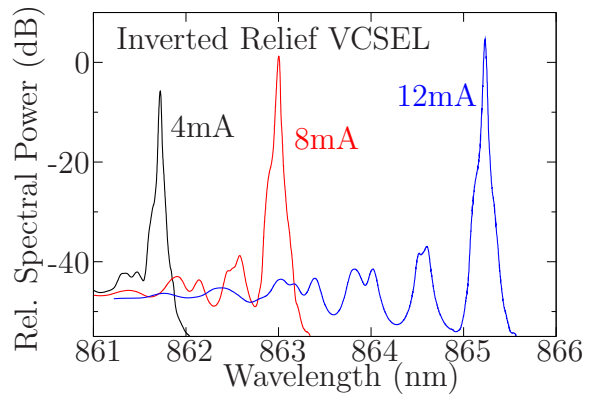


Figure 9.7: Spectra of the inverted relief device, with  $6\mu\text{m}$  oxide aperture and  $3.3\mu\text{m}$  relief diameter at three different injection currents.



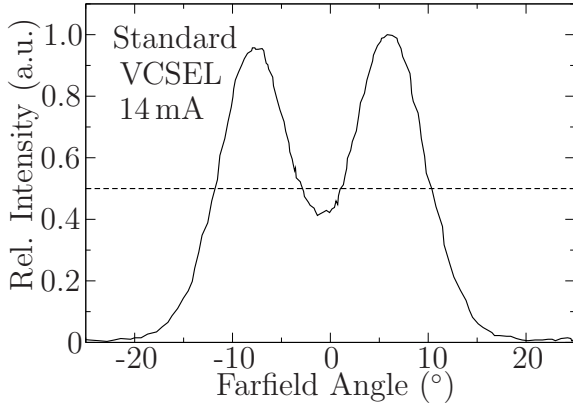


Figure 9.8: Far-field pattern of a  $6\text{ }\mu\text{m}$  active diameter reference VCSEL without relief at 14 mA driving current.

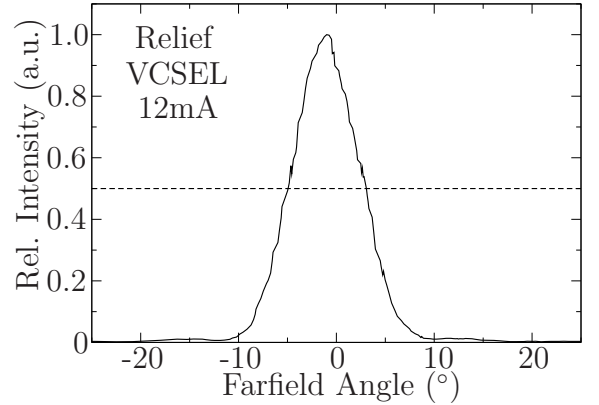


Figure 9.9: Far-field pattern of a  $6\text{ }\mu\text{m}$  active diameter VCSEL with  $3.3\text{ }\mu\text{m}$  relief diameter at 12 mA driving current.

at the maximum output power, are plotted. One can see that the inverted relief VCSEL shows at 12 mA a Gaussian shaped beam profile with a FWHM (full width half maximum) of  $7.6^\circ$ , furthermore, side lobes are practically absent.

Densely packed individually addressable VCSEL array with a minimum pitch down to  $24\text{ }\mu\text{m}$ , based on a similar design, were demonstrated as a multiple optical traps [93].

## 9.2 Monolithically integrated transceivers

In this section, monolithically integrated transceiver for optical-fiber bidirectional data transmission are presented. Each transceiver consists of a photodiode, sensitive to 850 nm wavelength, closely packed with a VCSEL emitting at the same wavelength. The laser structure is similar to the standard one presented in sect. 9.1, and the receiver is a MSM (metal-semiconductor-metal) photodiode.

In Fig. 9.10, two optical microscope photographs are showing ready devices, corresponding to different designs. In both pictures, one can recognize the big circular photodiode structures, where the metallic finger-contacts are clearly visible, and the VCSEL upper facets placed on the side or in the center of the considered structures. The incident light generates electron-hole pairs in the GaAs detector absorbing region. Therefore, a current is generated between the metallic fingers, connected alternatively at the two bond-pads, when a voltage difference of few volts is applied. The diameter of the detecting area is set to  $110\text{ }\mu\text{m}$  in order to have an optimal coupling with GI MMF (graded-index multimode fibers) of  $100\text{ }\mu\text{m}$  core diameter. This glass fibers are well suited for Gbit/s data transmission over distances in the 100 m range due the high bandwidth-length product. Despite the simplicity of the detector structure, a long technological work was performed and many different generations of devices were grown and processed.

The metallic fingers have a width of  $1\text{ }\mu\text{m}$  and a spacing of  $2\text{ }\mu\text{m}$ , so approximately 1/3 of the photodiode surface is not effective, but the small spacing is required for good high frequency response. An antireflection coating improves the sensitivity of the devices and mitigates the crosstalk in full-duplex data transmission. The geometry of the improved

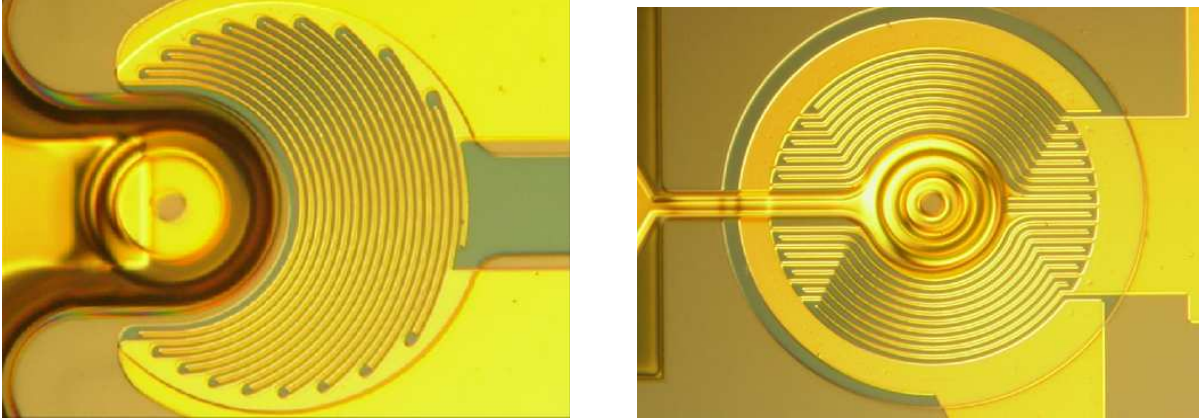


Figure 9.10: Optical microscope photographs of two different VCSEL-photodiode designs. The big circular structures have  $110\text{ }\mu\text{m}$ . Left previous design, right improved design.

design, right in the figure, allows a better coupling to the optical fiber, compared to the old one on the left.

In Fig. 9.11 a scheme of the improved device layer structure is depicted. An etch stop-layer consisting in  $300\text{ nm}$  AlAs layer serves to free the VCSEL surface after some lithographical steps. The layer labeled with (e) is just a spacer, its function is to reduce the capacitive coupling between the detector and the underlying doped VCSEL. Previous designs without the spacer layer show worse dynamical detector performances. The layer (d) is the GaAs absorbing layer, its thickness is chosen making a compromise between sensitivity, that requires a thick GaAs layer, and good frequency response of the detector, that requires a thin one. The thin layer (c), having graded increasing aluminum concentration up to  $\text{Al}_{0.30}\text{Ga}_{0.70}\text{As}$ , and layer (b) work as Schottky barrier. On the top of the structure the thin GaAs layer (a) prevents oxidation. It is important to point out that the presence of the buried VCSEL structure improves the sensitivity of the photodiode, in fact, the not absorbed light is reflected back in the absorbing layer by the stopband of the VCSEL.

In Fig. 9.12 a SEM photograph of a cross section of a device during the processing is shown. One can recognize the  $n$ -mirror, the active region, and the  $p$ -mirror of the VCSEL structure. and the effect of the oxidation process. Therefore, the oxide aperture is clearly visible between the DBRs and the AlAs stop-layer is also oxidized. The  $\text{Al}_{0.90}\text{Ga}_{0.10}\text{As}$  part of each DBR pair is just marginally oxidized. The picture refers to the old design, where the spacing layer (e) is absent, and the AlAs stop-layer is  $200\text{ nm}$  thick.

The static characteristics of a VCSEL belonging to the described structure are reported in Fig. 9.13 as function of the temperature. The lasers have an oxide aperture diameter of  $10\text{ }\mu\text{m}$ , and the operation is tested up to  $100^\circ\text{C}$ , where the optical output power still exceed  $3\text{ mW}$ . The small-signal response of these lasers at a bias current of  $6\text{ mA}$  exhibits a bandwidth exceeding  $7\text{ GHz}$  as can be seen in Fig. 9.14.

The digital data transmission experiments are performed by coupling each end of a GI MMF between two transceiver chips. The received eye diagrams obtained in full-duplex mode, modulating the VCSELs by two pattern generators at the same clock signal, are showed in Figs. 9.15 and 9.16. In the first digram the eye is still open at  $500\text{ Mbit/s}$

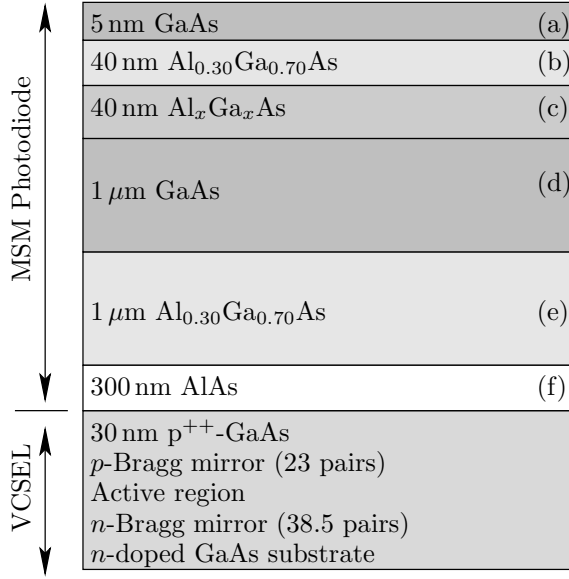


Figure 9.11: VCSEL with integrated MSM photodiode layer structure. The layer thickness is not correctly scaled.

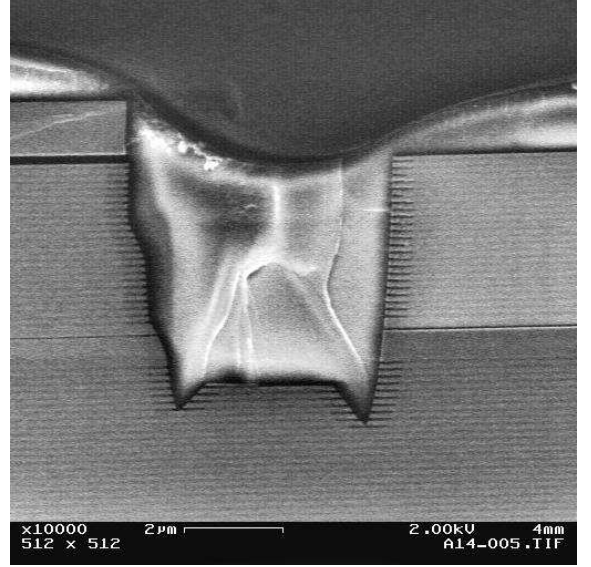


Figure 9.12: Cross section SEM photograph of a device during processing.

over a fiber length of 300 m. Over a fiber of 50 m an open eye diagram is still present at 2.5 GHz. Considering that the improved photodiodes have a bandwidth approaching 3 GHz, the bidirectional data transmission is then limited by the GI MMF, having a bandwidth-length product of 100 GHz·m.

The growth of the mentioned VCSEL structures, followed by the additional growth of the photodiodes layers, requires the choice of the right substrate temperature during the growth of the absorbing material. Absorbing layers grown at the standard substrate temperature of 580 °C results in MSM photodiodes with poor dynamical response. The optimal substrate growth temperature was found to be 400 °C. In fact, in Fig 9.17 the

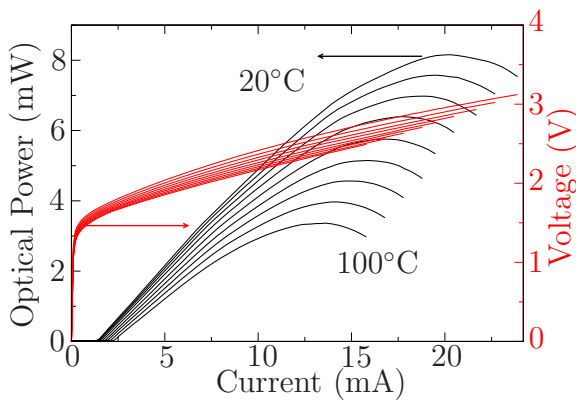


Figure 9.13: LIV characteristics of the 10  $\mu\text{m}$  active diameter 850 nm VCSEL for different temperatures.

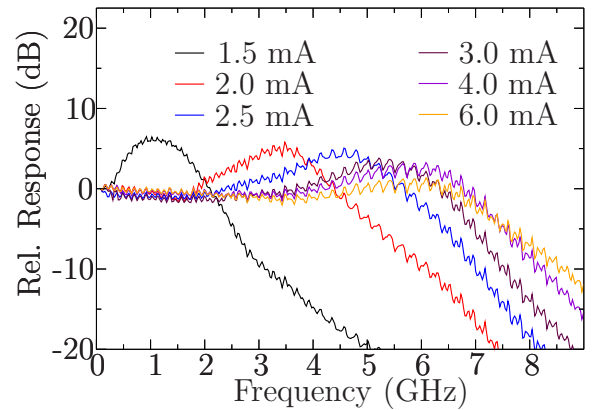


Figure 9.14: Small-signal response of a VCSEL for various bias currents.

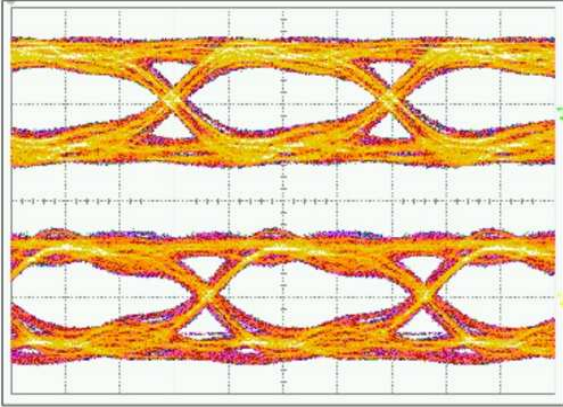


Figure 9.15: Full-duplex mode experiment trough 300 m GI MMF at 500 Mbit/s.

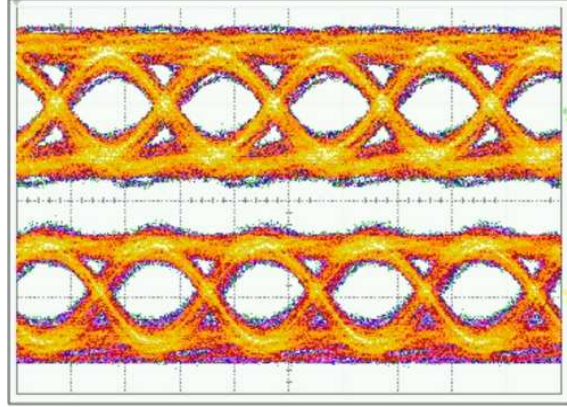


Figure 9.16: Full-duplex mode experiment trough 50 m GI MMF at 2.5 Gbit/s.

HRXRD spectra of four different structures are shown. They were grown on a highly *p*-doped GaAs layer on *n*-doped high-quality substrate, such a simplified buffer emulates the electrical behavior of the buried VCSEL, which would be present in the complete structure. The structures were grown at different temperatures, and in one sample the thickness of the absorbing layer is halved, as can be seen by observing the fine fringes of the relative spectrum.

The photodiodes grown at 390°C and 400°C show the best frequency response, while, by a growth temperature of 340°C the resulting crystal structure is already seriously damaged. This can be seen by the broadening in the HRXRD spectrum. Considering that the samples grown at 490°C and 580°C should exhibit the best crystal quality, one

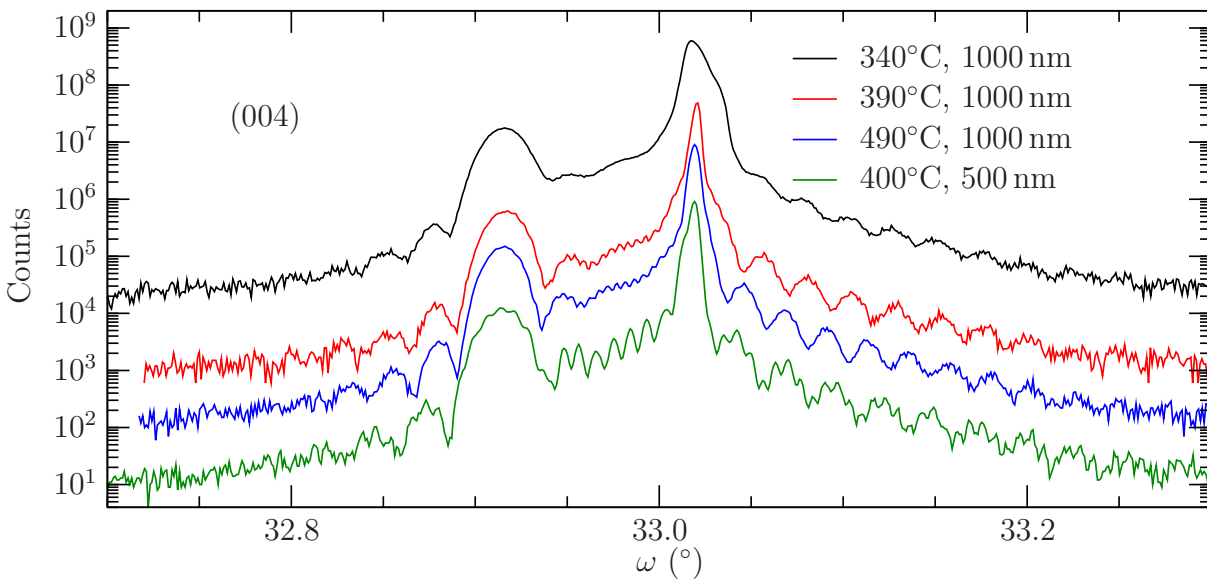


Figure 9.17: HRXRD (004) spectra of four photodiode structures, the growth temperature and the thickness of the absorbing GaAs layer is indicated.



can evince that an optimum concentration of point defects present at 400 °C, non verifiable with HRXRD, improves the high frequency behavior of the photodiodes probably by influencing the lifetime of the carriers. More details about the characterization and fabrication of these devices can be found in [94, 95].

These samples were also used to recalibrate the aluminum molecular beam flux, in fact the AlAs layer is responsible of the fringes with lower frequency in the relative spectra, therefore, the differences in periods are due to the subsequent thickness adjustments.

### 9.3 Flip-chip highly packed VCSEL arrays

In this section the implementation of arrays of highly packed VCSELs based on the flip-chip technology is summarized. This design allows to simultaneously couple the light emitted from three 850 nm VCSELs into a 50  $\mu\text{m}$ -core diameter multimode fiber (MMF).

The array implementation consists of  $(4 \times 4) \times 3$  individually addressable VCSELs, where each triple is a pixel in a  $(4 \times 4)$  array of 250  $\mu\text{m}$  step. This can be coupled into a  $(4 \times 4)$  50  $\mu\text{m}$  optical fiber bundle with 250  $\mu\text{m}$  fiber-to-fiber spacing. This design is very convenient for parallel data transmission, where the three VCSELs per channel are individually addressable offering a redundancy that increases drastically the channel lifetime. A cross section sketch of the complete pixel architecture is depicted in Fig. 9.18, while a SEM photograph is shown in Fig. 9.19.

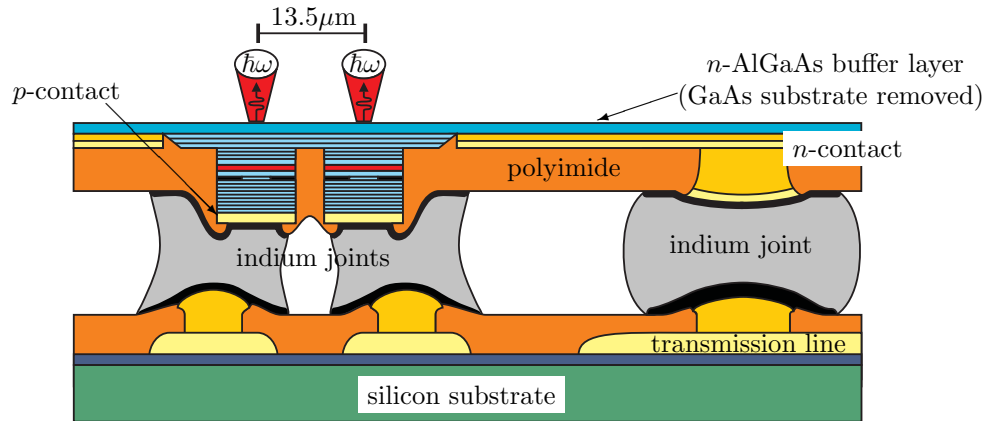


Figure 9.18: Cross section sketch of the complete pixel architecture.

These devices are bottom emitters, therefore the number of pairs of the  $n$ - and  $p$ -doped DBRs are basically inverted in comparison to the devices of the previous section. As shown in the Fig. 9.18, the main laser emission is from the  $n$ -side. The complex fabrication process takes advantage of a self-align  $p$ -contacts that is used as mask for the CAIBE (chemical assisted ion beam etching) procedure in order to etch the mesa with good sidewall quality. After the oxidation, to define the active aperture, a structured silicon substrate is then flip-chip bonded to the laser chip, and finally the GaAs substrate is removed chemically. At the end of the process one finds on the emission side a 3  $\mu\text{m}$  thick  $n$ -doped AlGaAs as contact for the laser diodes. The molar aluminum concentration of

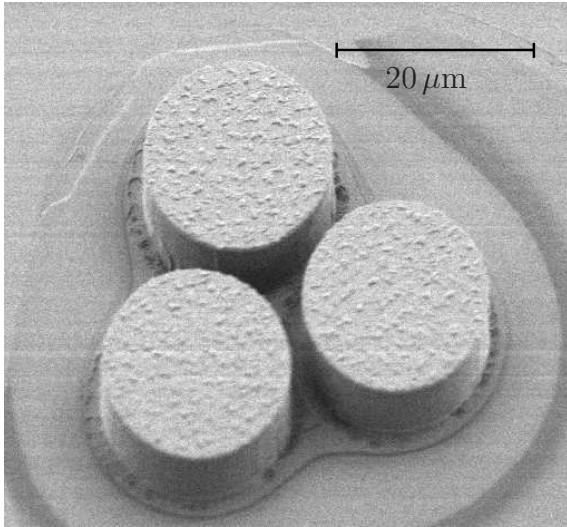


Figure 9.19: SEM photograph, of a triple of VCSELs during fabrication, the self-aligned  $p$ -contact are already deposited and the mesa are etched. The three mesas have an outer diameter of  $19\mu\text{m}$  and are separated by  $1.5\mu\text{m}$  at the smallest distance.

less than 15% is chosen to avoid oxidation but it is higher than 10% to be not absorbant for the 850 nm laser emission. Pixels with VCSELs having active diameter of  $4\mu\text{m}$ , lateral oxidation depth of  $4\mu\text{m}$ , and mesa separated by just  $1.5\mu\text{m}$  are demonstrated [96]. For this configuration a center-to-center distance of only  $13.5\mu\text{m}$  is reached. Quasi-error-free transmission of 10 Gbit/s over 500 m trough  $50\mu\text{m}$  MMF is also demonstrated.

One can think of using the three VCSELs simultaneously, increasing this way the transmitter lifetime due to the redundancy of the devices. Nevertheless, a more sophisticated approach can be used. In fact, some spontaneous emission is coupled by the shared  $n$ -type mesa in the idle devices when just one VCSEL is driven. The coupling is also favored by the small pitch. As result, an unbiased photocurrent flows in the idle devices monitoring the emission of the lasing VCSEL. The single VCSEL health can be so monitored and in case of failure another VCSEL from the pixel can be activated.

Details about the structure, the fabrication steps, and the experimental results can be found in [96, 97].

## 9.4 The real VCSELs profile

In this section a detailed analysis of the compositional profile of the presented VCSELs emitting at 850 nm is performed using HRXRD.

In Fig. 9.2, the aluminum molar fraction is plotted just for the cavity region, while a detailed plot of the nominal compositional profile of a DBR period is given in Fig. 9.20 for the  $n$ -pairs. Starting after the first  $\delta$ -doping sheet, the shutters of two aluminum cells and one gallium cell are opened together in order to grow  $\text{Al}_{0.27}\text{Ga}_{0.73}\text{As}$ , then the composition is ramped linearly with the thickness until the  $\text{Al}_{0.47}\text{Ga}_{0.53}\text{As}$  alloy is reached, this is done by increasing the aluminum and decreasing the gallium cells temperatures linearly with the time. The second  $\delta$ -doping sheet is obtained by closing the shutters of the aluminum and gallium cells, after that, a ramp from  $\text{Al}_{0.47}\text{Ga}_{0.53}\text{As}$  to  $\text{Al}_{0.90}\text{Ga}_{0.10}\text{As}$  is followed by the third  $\delta$ -doping. When the shutters of the group III cells are opened again, their temperature is kept constant and an  $\text{Al}_{0.90}\text{Ga}_{0.10}\text{As}$  constant composition

layer is grown. At this point the aluminum fraction is symmetrically ramped down, but without performing any  $\delta$ -doping, until the composition  $\text{Al}_{0.20}\text{Ga}_{0.80}\text{As}$  is reached and kept constant for 37 nm. After the growth of this layer, the shutters of the group III cells are closed for the  $\delta$ -doping and the cycle starts again.

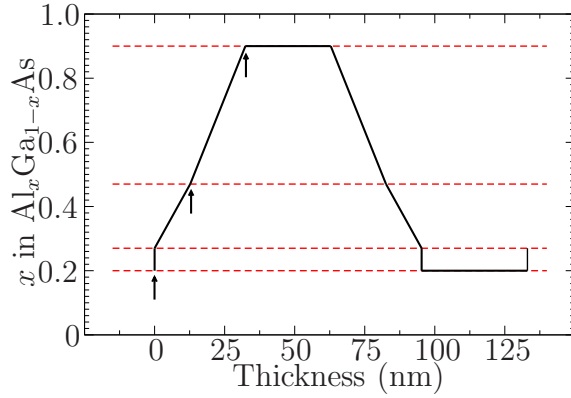


Figure 9.20: Nominal compositional profile of a DBR period in a 850 nm VCSEL, the arrows represent  $\delta$ -doping. Four linear composition-graded layers per period are present.

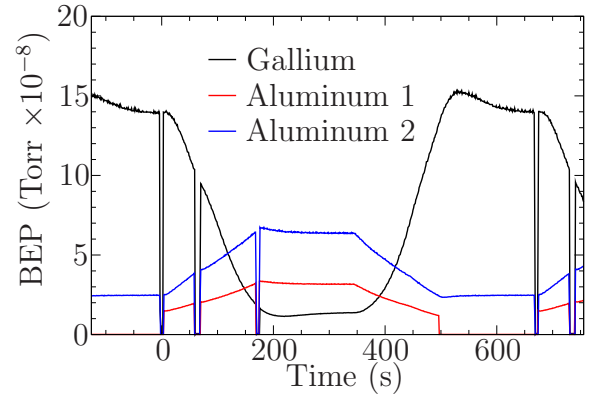


Figure 9.21: Measured fluxes from the three effusion cells used to grow the nominal structure shown in Fig 9.20, one DBR pair is grown in approximately 670 s.

As it will be exhaustively shown in the follows, the HRXRD spectra of grown VCSELs evidence that the aluminum profile of the DBRs differs from the nominal one. There are several causes for this behavior. In fact, the cells are programmed to increase their temperature linearly, and their fluxes are not linear functions of the temperature, in addition to that, the effusion cells have a certain response time and their dynamical behavior should be considered.

One has to mention that in the VCSEL modeling there is no particular reason to choose the linear-graded profile, therefore, there is no reason to try to correct the layer structure in order to better match the one shown in Fig 9.20. Small deviations of the profile does not affect significantly the optical reflectivity spectrum. In fact, as long as the periodicity of the DBR is guaranteed, the structure will exhibit anyway a stopband with high maximum reflectivity for optical wavelength.

It follows that one can accidentally grow graded DBRs with high reflectivity at the designed wavelength using the wrong molecular fluxes from the different cells. This can affect the length of the VCSEL cavity or other features of the structure.

It is so of great interest to determine the real compositional profile of the VCSEL DBRs. A precise idea of this can be obtained by measuring the fluxes of the three cells when these are driven in the same way it would happen during the growth. The ion gauge described in chapter 6 is used for these measurements, and the fluxes, expressed in BEP, are plotted in Fig. 9.21. One can recognize from the figure the occurrence of the three  $\delta$ -doping, and one can see that when the gallium flux increases, the aluminum fluxes decrease and viceversa, and that an overshoot of gallium can be seen at approximately

530 s after the period start. Using the calibration table it is possible to convert the fluxes in growth rates and finally the aluminum fraction  $x$  in the  $\text{Al}_x\text{Ga}_{1-x}\text{As}$  as function the time is just given by

$$x(t) = \frac{G_{\text{Al1}}(t) + G_{\text{Al2}}(t)}{G_{\text{Al1}}(t) + G_{\text{Al2}}(t) + G_{\text{Ga}}(t)}, \quad (9.1)$$

where  $G(t)$  is the growth rate of AlAs or GaAs in function of time correspondent to a specific cell. Integrating the total growth rate over the time one gets the grown tickness at a specific time  $t$ , which results in

$$d(t) = \int_0^t (G_{\text{Al1}}(t') + G_{\text{Al2}}(t') + G_{\text{Ga}}(t')) dt', \quad (9.2)$$

and eliminating  $t$  from (9.1) and (9.2), one obtains the compositional profile  $x(d)$ . This is shown in comparison with the nominal one in Fig 9.22. The  $x(t)$  measured for four

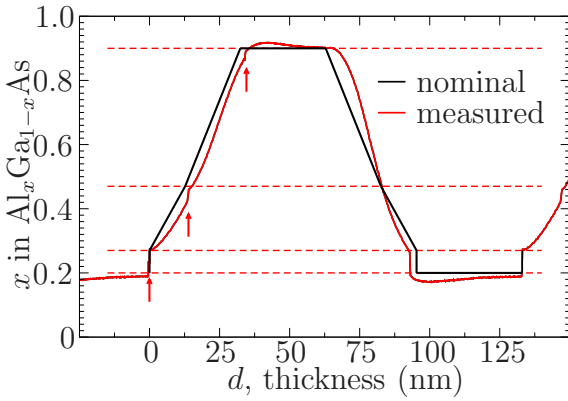


Figure 9.22: Comparison between the nominal and measured compositional profile in a 850 nm VCSEL DBR period, the arrows represent  $\delta$ -doping, the measured profile is obtained by flux measurements.

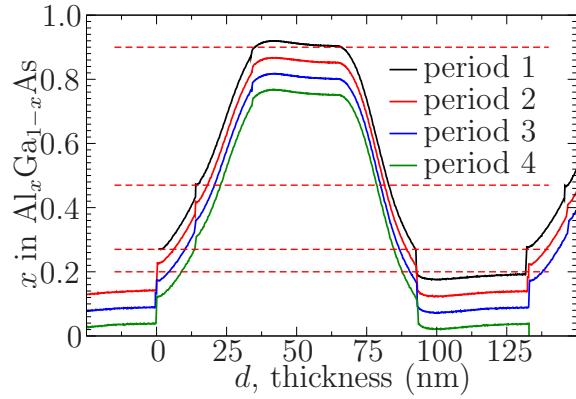


Figure 9.23: Comparison between the profiles of four adjacent DBR periods determined from flux measurements, the profiles are shifted of 5% each to simplify the visualization.

periods is shown in Fig. 9.23, where one can see that the reproducibility, and so the periodicity of the DBR is strictly confirmed. A simplified sample made of 34  $n$ -pairs was grown to analyze in detail the periodic structure, the relative HRXRD spectra are shown in Fig. 9.25. One can see that the nominal structure fitted following the linear graded compositional profile shows high order satellite peaks that are not present in the measurements. From the kinematical theory, the satellite peaks are related to the Fourier components of the electron density of the periodic superlattice, they represent its structure factor. So it is logic to accredit to a smother profile the suppression of the satellites. Despite almost all the VCSELs have graded compositional profile to reduce the electrical resistance, the HRXRD spectra of the DBRs of this important devices are seldom analyzed in literature. The problem is marginally treated by [99] and more in detail by [98], that introduces the idea of an easy biparabolic function to mimic smooth profiles.



The bipolarabolic profile is very easy to implement and can be defined as follows

$$\begin{aligned} x(d) &= x_1 + \frac{(x_2 - x_1)(d - d_1)^2}{(d_2 - d_1)^2} & \text{for } d_1 \leq d \leq d_2 \\ x(d) &= x_3 + \frac{(x_2 - x_3)(d - d_3)^2}{(d_3 - d_2)^2} & \text{for } d_2 \leq d \leq d_3, \end{aligned} \quad (9.3)$$

where the indexes 1 and 3 are referred to the starting and final point respectively, and the index 2 is referred to the junction point of the two parabolas, as can be seen in Fig. 9.24. The continuity of the profile is directly given by the formulae (9.3) and six parameter are necessary to define the curve. One can also pretend the continuity of the first derivative reducing the free parameter to five, this condition is

$$\frac{x_3 - x_2}{d_3 - d_2} = \frac{x_2 - x_1}{d_2 - d_1}. \quad (9.4)$$

In Figs. 9.25, 9.26, and 9.27, the measured and simulated HRXRD spectra for the test 34  $n$ -pairs DBR and for a complete VCSEL structure, like the one described in sect.9.1, are shown. In both cases one can see that the linear-graded nominal profile is not adequate to fit the spectra. By looking at Fig. 9.20, it is clear that 7 parameters are needed to fit the nominal profile, considered symmetric. On the other hand using a 5 parameters bipolarabolic profile, like the one shown in Fig. 9.24, one can see that again 7 parameters are needed to fit the complete profile also considered symmetric. By comparison between the insets in Figs. 9.26 and 9.27 it is clear that at least 15 lamellae are needed for a satisfactory fit, this is reasonable because, as one can see in Fig. 9.24, the 15 lamellae staircase is still a rough approximation of the measured profile.

It is important to specify, that is experimentally impractical to obtain the compositional profile by flux measurements before the growth of each sample, as shown, this can be extracted by HRXRD, giving precise information that can be used for the next growth.

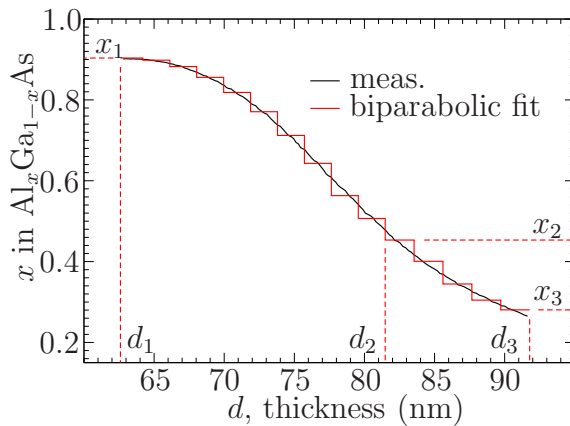


Figure 9.24: Discretized bipolarabolic compositional profile used to fit the HRXRD spectra from the VCSEL in Figs. 9.26 and 9.27, overlapped to the profile obtained by flux measurements. The number of used lamellae is 15.

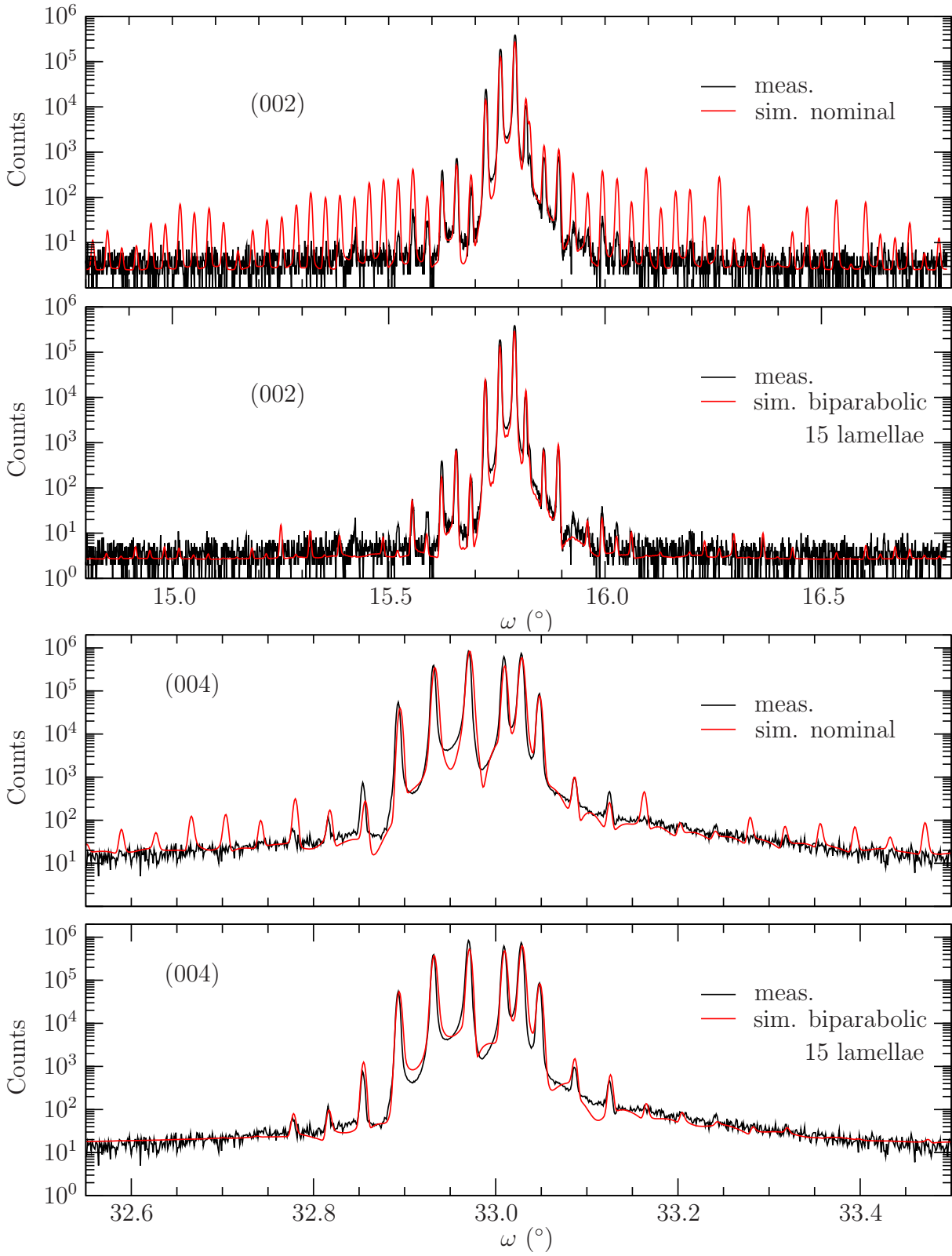


Figure 9.25: HRXRD (002) and (004) spectra of the 34  $n$ -pairs DBR. The relative simulations of the same measurements regard the nominal linear-graded and bipolarabolic profiles respectively.

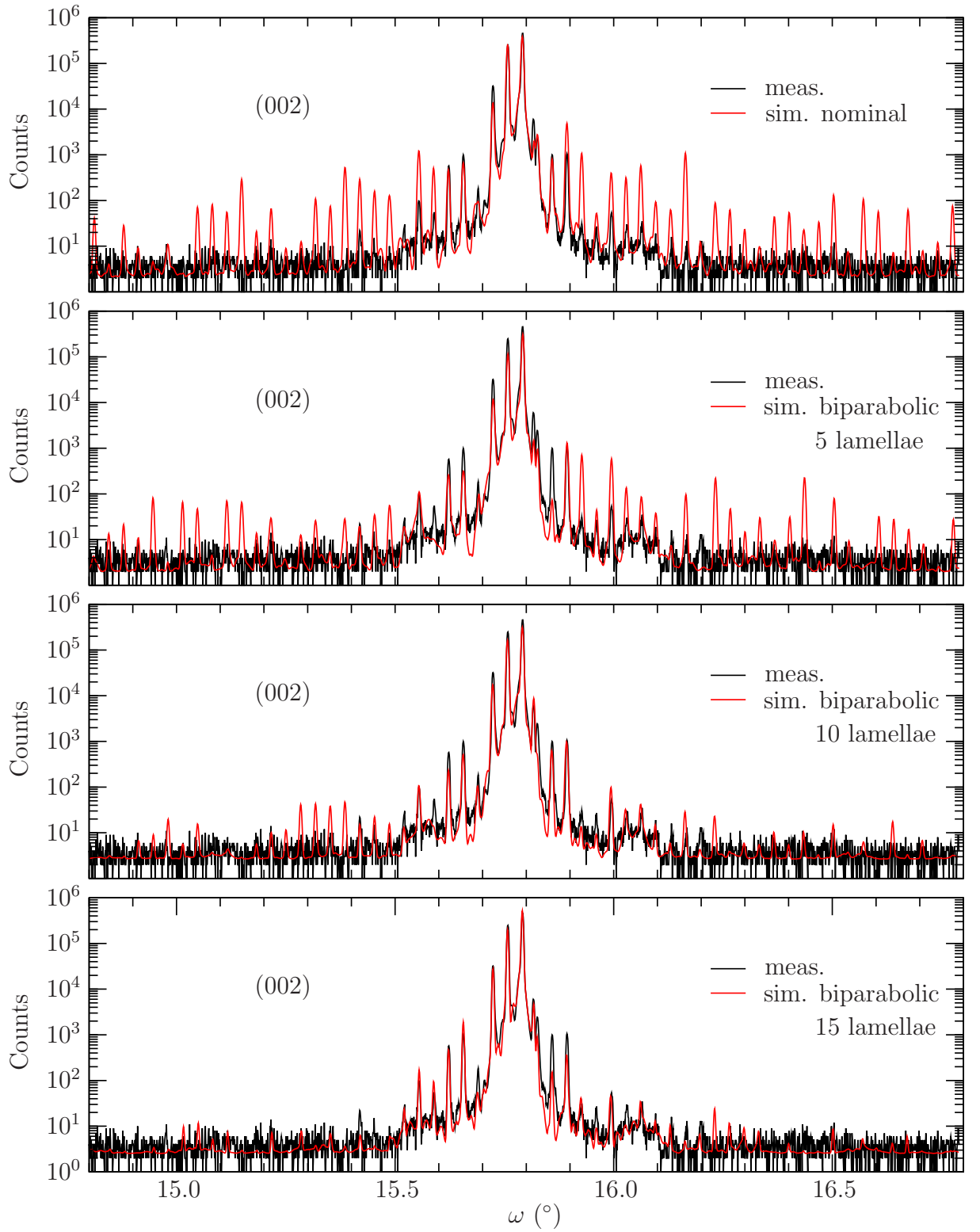


Figure 9.26: HRXRD (002) spectra of a complete 850 nm VCSEL structure. The relative simulations of the same measurement regard nominal linear-graded and bipolarabolic with 5, 10, and 15 lamellae respectively.

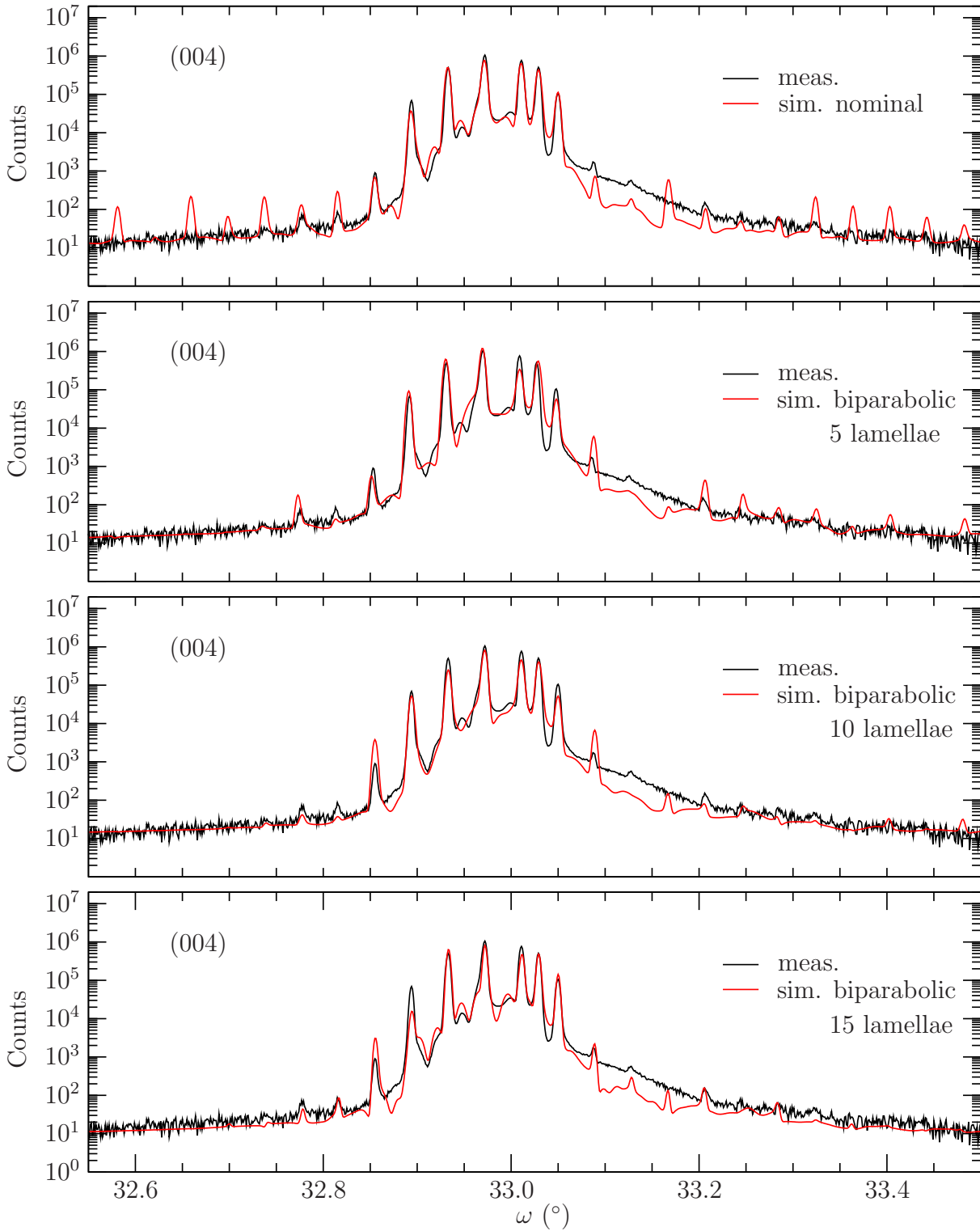


Figure 9.27: HRXRD (004) spectra of a complete 850 nm VCSEL structure. The relative simulations of the same measurement regard nominal linear-graded and bipolarabolic with 5, 10, and 15 lamellae respectively.

# Chapter 10

## VCSEL devices emitting at 980 nm

In this section, VCSEL devices emitting at 980 nm followed by electrically pumped VECSELs based on a similar layer structure are presented.

### 10.1 VCSEL layer structure for 980 nm emission

The emission wavelength of 980 nm characterizes deeply the design of these devices, in fact the GaAs substrate is almost transparent to the laser beam and therefore, the fabrication of bottom emitting devices is possible. It follows that the substrate should not be necessarily removed in contrast to the devices described in sect. 9.3. This simplifies the device fabrication and improves its performance due to a better heat extraction and a more homogeneous current injection.

The standard bottom emitter VCSEL device has 20  $n$ -DBR pairs on the substrate side and 30  $p$ -DBR pairs on top. One can see that, in comparison to VCSELs emitting at shorter wavelengths, a lower number of pairs is needed because of the higher refractive index contrast that can be achieved. In fact, GaAs is transparent at 980 nm and can be used as high refractive index material. The  $\text{Al}_{0.90}\text{Ga}_{0.10}\text{As}$  alloy is used, as usual, as low refractive index material in order to allow the selective oxidation of the 25 nm thick highly  $p$ -doped AlAs layer to provide current confinement. The compositional profile of the pairs is, similarly to the previously described VCSELs structure, also smooth to reduce the electrical resistance. Two  $\delta$ -doping sheets per period are placed in the nodes of the standing wave pattern.

Laser structures based on different designs were grown. The main differences are summarized in the figures from 10.1 to 10.4, where the refractive index and the field amplitude of the simulated standing wave patterns at 980 nm wavelength are plotted versus the depth position for the four structures. The first structure contains three 8 nm thick  $\text{In}_{0.15}\text{Ga}_{0.75}\text{As}$  QWs separated by 10 nm GaAs layers. In the second structure, another group of three QWs is added at a distance of 139 nm from the first one in order to place all the six QWs approximately on the maxima of the electric field. Therefore, this length corresponds to an optical thickness of half wavelength. The third structure is similar to the first one, but two tensile-strained 30 nm thick  $\text{GaAs}_{0.875}\text{P}_{0.125}$  layers are situated respectively before and after the active region providing a partial strain compensation of the compressively strained InGaAs QWs. In addition, the third structure exhibits a

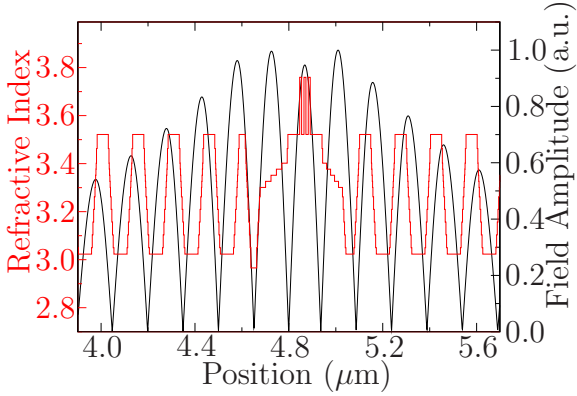


Figure 10.1: Refractive index and simulated standing wave pattern for a standard 980 nm VCSELs. The AlAs layer for oxide confinement corresponds to the lowest refractive index.

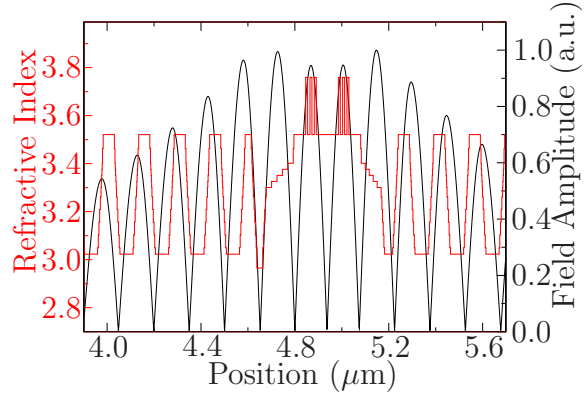


Figure 10.2: Refractive index and simulated standing wave pattern, for a structure with a second triplet of  $\text{In}_{0.15}\text{Ga}_{0.75}\text{As}$  QWs separated by 139 nm.

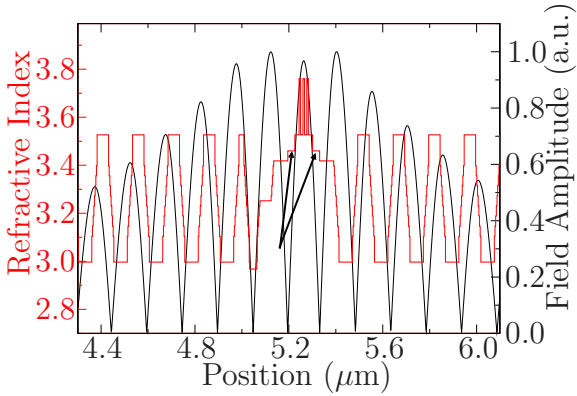


Figure 10.3: Structure to be compared to the one in Fig. 10.1, the arrows indicates the 30 nm thick  $\text{GaAs}_{0.875}\text{P}_{0.125}$  strain compensation layers. An improvement of the cavity design reduced the threshold current.

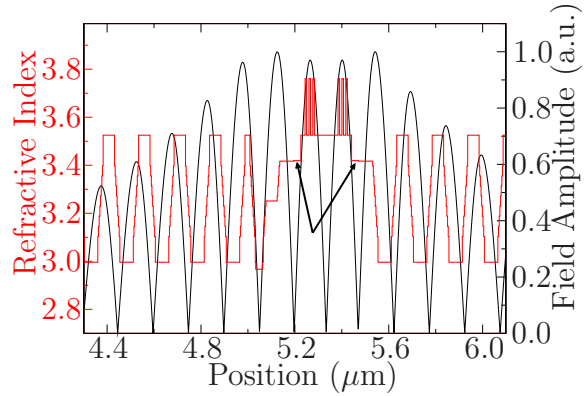


Figure 10.4: Structure to be compared to the one in Figs. 10.2 and 10.3, the arrows indicates the 30 nm thick  $\text{GaAs}_{0.75}\text{P}_{0.25}$  strain compensation layers. The cavity design is also improved.

different refractive index profile of the cavity compared to the first one. This design, simulated with the transfer matrix method, reduces the threshold gain. The fourth structure is an improvement of the second one, it includes two 30 nm thick  $\text{GaAs}_{0.75}\text{P}_{0.25}$  strain layers to partially compensate the strain of the six QWs and exhibits the same cavity improvements of the third structure.

## 10.2 Fabrication and performances of the devices

The main steps of the devices fabrication are shortly described in the follows. The mesas are etched on the  $p$ -doped side, and the oxidation process defines the VCSEL apertures.

The  $p$ -contacts are then evaporated covering completely the top of the mesas. One has to polish the backside of the substrate in order to provide an optically flat emission facet. This operation can be performed by chemical-mechanical partial removal of the substrate, its thickness is reduced from the standard  $350\text{ }\mu\text{m}$  to less than  $200\text{ }\mu\text{m}$ . Large area  $n$ -contacts are then deposited on the back side of the substrate leaving an opening for light emission. At this point, the device can be soldered  $p$ -side down to a copper heat sink using indium. The fabrication process ends with the deposition of an antireflection coating on the emission facet to reduce the unwanted feedback given by the GaAs-air interface.

The LIV curves of two comparable VCSELs of  $134\text{ }\mu\text{m}$  active diameters, obtained from design one and two, having respectively three and six InGaAs QWs are shown in Figs. 10.5 and 10.6. The  $2\times 3$  QWs design shows an higher maximum output power of  $335\text{ mW}$  at

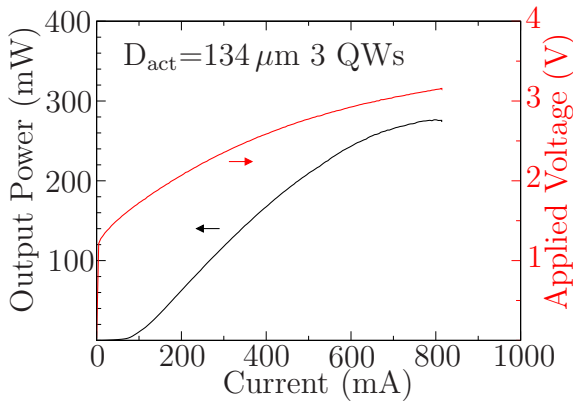


Figure 10.5: LIV characteristics of  $134\text{ }\mu\text{m}$  active diameter 3 QWs VCSEL device (design from Fig. 10.1).

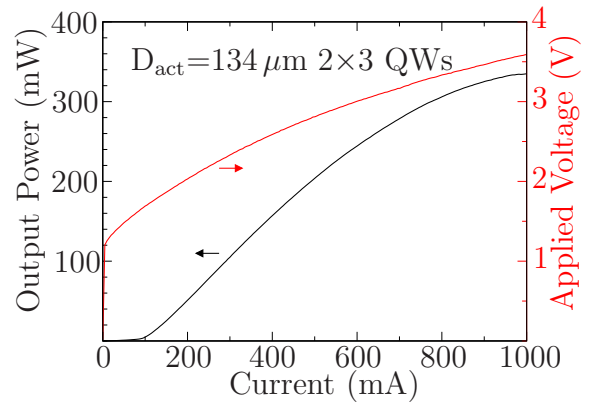


Figure 10.6: LIV characteristics of  $134\text{ }\mu\text{m}$  active diameter  $2\times 3$  QWs VCSEL device (design from Fig. 10.2).

approximately  $1000\text{ mA}$  compared to the  $275\text{ mW}$  of maximum output power at  $800\text{ mA}$  of the 3 QWs design, despite the latter shows a better threshold current. The higher output power of the  $2\times 3$  QWs design is not an obvious fact. In order to deeply understand the experimental results, a detailed modeling of the electrical behavior, of the QWs injection, of the losses in the resonator and in the QWs, and even of the internal heat dissipation in the devices should be made.

The introduction of the strain compensation layers in the third design of Fig. 10.3 improves the stability and the reliability of the devices, which show no degradation after more than one week continuous operation. Based on this design, a  $4\times 4$  array of VECSELs having  $49\text{ }\mu\text{m}$  active diameters showing more than  $0.8\text{ W}$  output power was demonstrated.

## 10.3 Electrically pumped VECSELs

As already mentioned in chapter 4, VECSELs are characterized by an external optical cavity. In this section, an electrically pumped VECSEL device is described. The VECSEL device concept is similar to the already described VCSELs but one has to reduce the number of the  $n$ -DBR pairs, in order to have an optical feedback with the external mirror.



The presented device incorporates 10  $n$ -doped DBR pairs and 3 strain compensated QWs (design 3). The fabrication steps are similar to the bottom emitting VCSELs of sect. 10.2, where the  $n$ -contact is now evaporated on the epitaxial side (intracavity contact) with electroplated gold. Polyimide insulation layers are used for chip planarization. The main difference is that the high quality  $n$ -doped substrate should be removed in this VECSEL design. In fact, the doping concentration of the standard GaAs substrate is higher than  $10^{18} \text{ cm}^{-3}$ , and the relative free carrier absorption of the order of  $3 \text{ cm}^{-1}$  would introduce in the external cavity a detrimental optical loss. For this reason, in the epitaxial design an AlAs stop layer should be grown to allow the substrate removal process.

The LIV curves and the relative laser emission spectrum of a VECSEL with  $75 \mu\text{m}$  active diameter are plotted in Figs. 10.7 and 10.8 respectively. The radius of curvature of the external mirror is 10 mm and its reflectivity is 90%. As one can see, the laser emission is single-mode up to 110 mA and more that 12 mW output power are obtained.

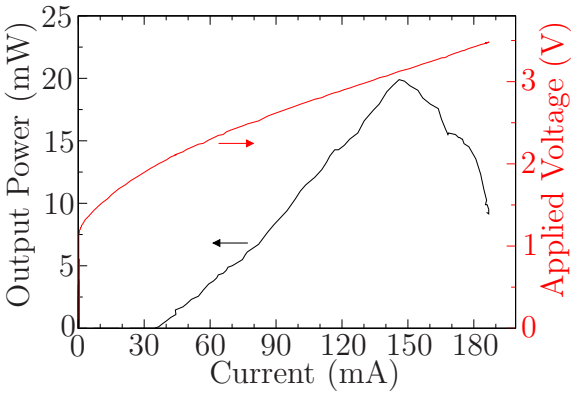


Figure 10.7: Strain compensated 3 QWs VECSEL of  $75 \mu\text{m}$  active diameter and 10  $n$ -doped DBR pairs. The external mirror has 10 mm radius of curvature and a reflectivity of 90%.

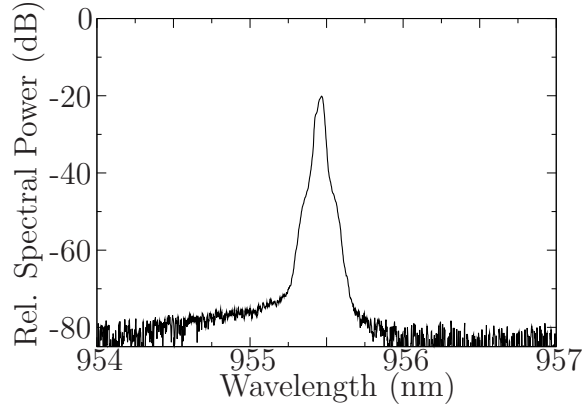


Figure 10.8: Spectrum of the VECSEL from Fig. 10.7 measured at an injection current of 110 mA and showing single-mode emission of more than 12 mW.

Other electrically pumped VECSEL designs including a higher feedback of the external mirror, obtained by further reduction of the  $n$ -DBR pairs, and taking advantage of the improved mechanical stability and heat extraction given by the use of high quality GaAs undoped substrate, that does not need to be removed because of its low optical absorption, are described together with all the fabrication details in [100].

The HRXRD spectrum of a VCSEL structure consisting of 17  $n$ -doped DBR pairs and  $2 \times 3$  strain compensated QWs is shown in Fig. 10.9 as a characterization example. One can see, on the low angle side of the spectrum, the peculiar pattern of the  $2 \times 3$  strained QWs that is composed of  $\text{In}_{0.176}\text{Ga}_{0.824}\text{As}$  as resulted from the HRXRD simulation. The indium molar fraction results to be at least 1% higher than the wanted value, and therefore, a shift of the gain curve of 5-10 nm makes this devices not optimal. On the high angle side of the spectrum, the pattern generated from the GaAsP layers indicates a composition of  $\text{GaAs}_{0.82}\text{P}_{0.18}$ , resulting in a undercompensation of the QWs strain. Following the indication obtained from the HRXRD measurements, the indium and the phosphorus



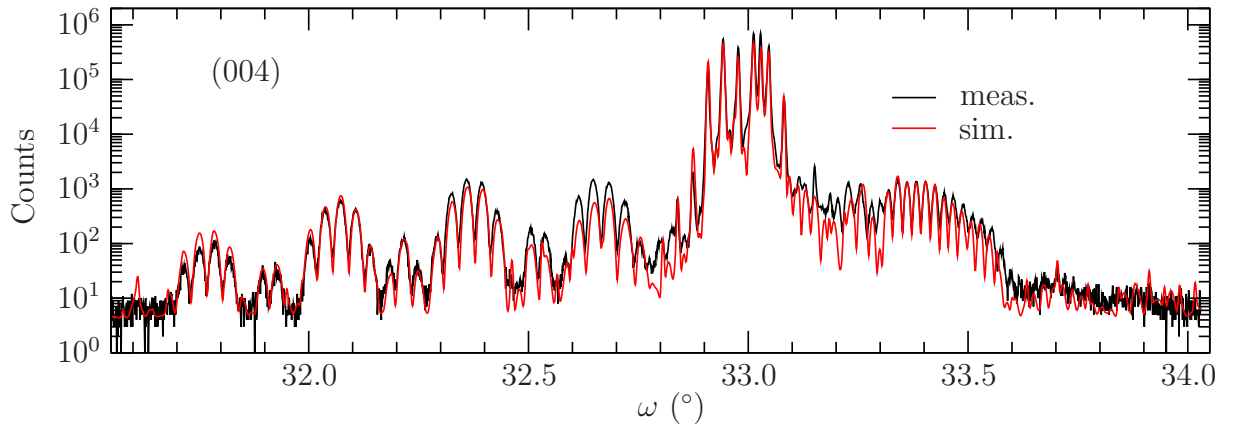


Figure 10.9: HRXRD of a strain compensated  $2 \times 3$  QWs VCSEL with 17  $n$ -doped DBR pairs.

fluxes were respectively reduced and increased in the successive growth process in order to grow the optimal structure.

# Chapter 11

## VECSELs

This Chapter is dedicated to VECSEL devices, focusing on the methods to characterize the epitaxial growth with special attention to HRXRD.

A detailed description of the design and performances of these VECSEL devices can be found in [26].

### 11.1 Device design and fabrication

As already mentioned in chapter 4, part of this work is devoted to barrier pumped and QW pumped VECSEL devices. Starting from the barrier pumped VECSELs and referring to Fig. 4.3, an emission wavelength of approximately 980 nm is realized with six 7.5 nm thick  $\text{In}_{0.15}\text{Ga}_{0.85}\text{As}$  QWs, separated by half wavelength in optical thickness GaAs layers, in order to place each QW at a maximum of the standing wave pattern. The GaAs is also the barrier material that absorbs the 808 nm laser pump beam. The cavity is sandwiched between the external mirror, placed at a distance of some centimeters, and the epitaxially grown DBR. The DBR is undoped and  $\text{Al}_{0.20}\text{Ga}_{0.80}\text{As}$  and AlAs are used as high and low refractive index materials respectively. Furthermore, a special design of the DBR allows to have a high reflectivity also for the 808 nm pump beam under an incidence angle of approximately  $26^\circ$  measured from the sample normal. The layer structure of such reflectors is quasi periodic, in order to exhibit two stopbands, as can be seen in a scheme of the layer sequence given in the third plot of Fig. 6.24.

Considering that VECSELs are high power devices, where output power higher than 10 W are typical, the thermal management is of primary importance. For this reason, the devices are grown in reverse order, therefore, on the substrate side one finds the active region followed by the DBR, the chip is then mounted from the DBR side on a heat sink and the substrate is then removed chemically.

It is important to mention the strategy that can be used to characterize the epitaxial growth, as already mentioned in chapter 6, and it is based on the exact knowledge of the sample that the grower has and can be used to analyze the HRXRD spectra. In fact, the layer thicknesses and the compositions of the different layers are not independent, but are linked in the growth procedure. For this reason, a VECSEL structure, like the one previously presented that is composed of almost 80 layers, can be described by using just 5 independent parameters. In this particular case, one can consider five molecular fluxes

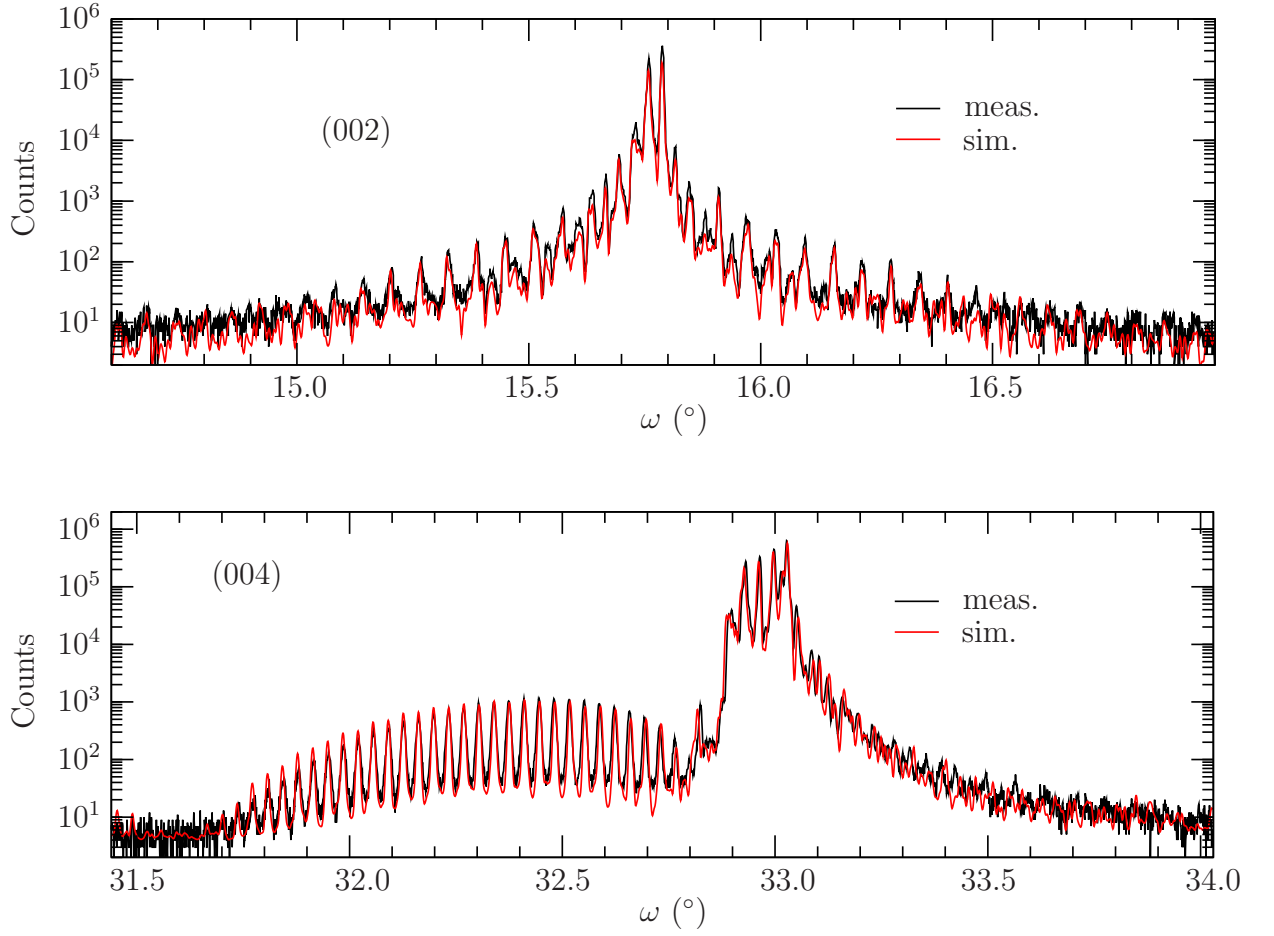


Figure 11.1: Measured HRXRD (002) and (004) spectra of a 980 nm barrier pumped VECSEL and the respective simulations based on five independent parameters.

deriving from indium, gallium, and aluminum cells and two additional ones originating from a second aluminum cell driven at two different temperatures during the growth.

Therefore, the measured HRXRD spectra shown in Fig. 11.1 can be exactly fitted by simulated spectra based on five free parameters. The simultaneous fits of the (002) and (004) Bragg reflections is easy to perform, in fact, while the (002) reflection is very sensitive to the DBR layers, the (004) is more characterized from the indium concentration in the QWs, as can be seen on the left side of the spectrum, which is typical of compressively strained layers. The simulation gives an indium molar fraction  $x$  of 15.7% for the  $\text{In}_x\text{Ga}_{1-x}\text{As}$  QWs. In addition, the high frequency modulation of the indium related layers is mainly given by the distance between the QWs, and considering that the barrier layers are composed of GaAs, the information about gallium and indium are extracted in an almost direct way from the (004), making more stable the parameters determination. From the simulation results that the gallium flux had a deviation of just -0.5% respect the aspired value. On the other hand, for the two aluminum cells deviations of approximately +3% and -3% are found.

The optical reflectivity spectrum, of the effectively grown layer stack calculated from

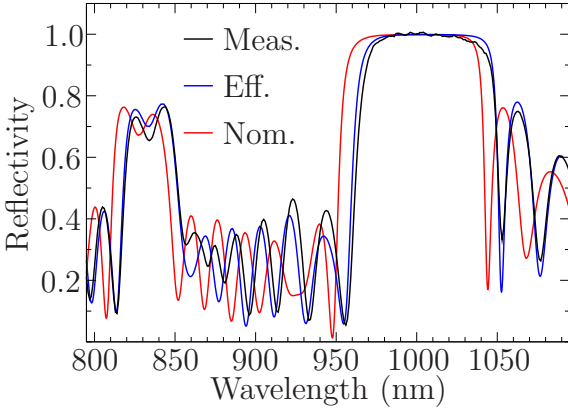


Figure 11.2: Reflectivity spectra of a 980 nm VECSEL. Measured (black curve), simulated according to the effective structure determined from HRXRD measurements (blue curve), and simulated according to the nominal structure (red curve). All spectra refer to wafer center but the nominal design is conceived for 8 mm from the wafer center.

the molecular fluxes measured from HRXRD, can be simulated using the transfer matrix method and compared to the measured and nominal ones. This is done in Fig. 11.2, it is interesting to compare the three curves considering the aforementioned flux deviations from the nominal layer structure. One has to consider that the nominal layer thickness is calculated for a wafer position of 8 mm from the wafer center and so the reflectivity spectrum of the nominal structure (red curve in the figure) exhibits the main stopband centered at a wavelength higher than 980 nm. On the other hand, one can see that the measured (black curve) and simulated spectrum obtained from HRXRD measurements (blue curve) are shifted to even higher wavelengths. Just with the support of the HRXRD it is possible to argue that the aluminum cells are responsible for this deviation, that could be corrected in the successive growth run.

In Fig. 11.2 one can also see the second stopband designed for the pump wavelength of 808 nm. The spectra in Fig. 11.2 are measured and simulated for an angle of  $10^\circ$  from the normal, while the second stopband is centered at 808 nm at for an incidence angle of the pump beam of approximately  $26^\circ$ .

The error in the aluminum molecular fluxes does not affect strongly the composition of the nominal  $\text{Al}_{0.20}\text{Ga}_{0.80}\text{As}$  layers in the DBR, that can be directly and independently measured performing a photoluminescence measurement as shown in sect. 6.5. In fact, the DBR consists of AlAs that confine AlGaAs layers, that exhibit the typical PL spectrum shown in Fig. 11.3. The maximum PL intensity at 730 nm corresponds to an aluminum molar fraction of approximately 20% and can be used as fast independent check of the

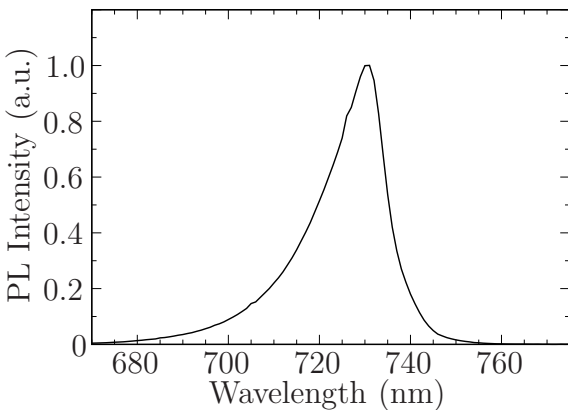


Figure 11.3: Photoluminescence signal recorded by pumping the DBR with an argon ion laser of 514.5 nm wavelength.

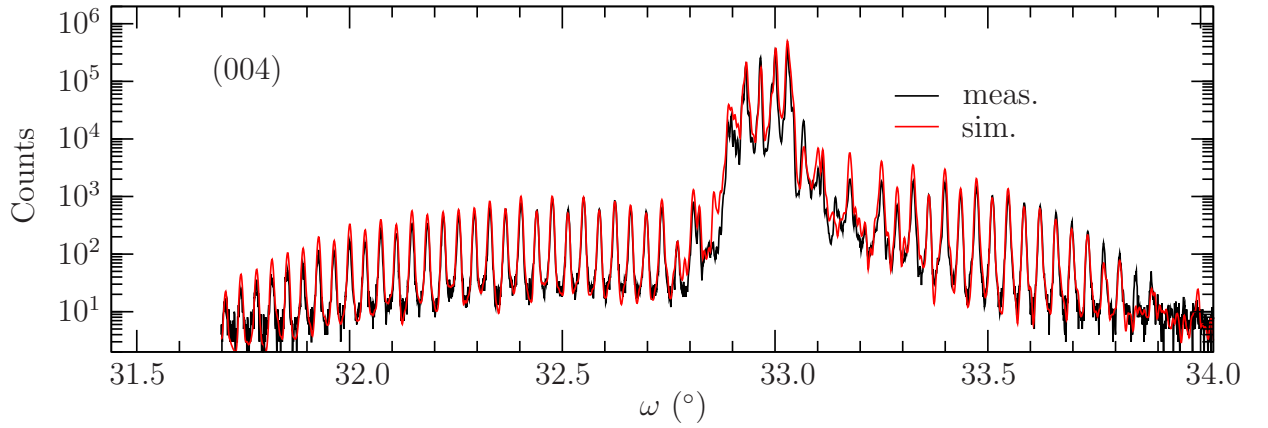


Figure 11.4: Measured and simulated (004) of a 6 QWs strain compensated VECSEL structure.

validity of the HRXRD simulations.

Devices fabricated following this concept show an output power of 3.6 W [101], and a similar design employs in addition strain compensating GaAsP layers between the QWs allowing a drastic improvement of the laser performances. Therefore, strain compensated VECSEL exhibiting 13.2 W infrared emission and, by introducing LBO non linear crystal in the cavity, 407 mW blue emission are demonstrated by [26].

For this devices the same simulation strategies on the HRXRD spectra can be applied, as example, in Fig. 11.4 the (004) HRXRD spectra of a 6 QWs strain compensated VECSEL structure is shown together with the simulation. The strain sensitivity of the (004) Bragg reflection allows the easy estimation of the indium molar fraction in the QWs that results to be composed of  $\text{In}_{0.159}\text{Ga}_{0.841}\text{As}$ . The strain compensating layers between the QWs result to be  $\text{GaAs}_{0.824}\text{P}_{0.176}$  of approximately 13 nm thickness, that compensates 95% of the QWs strain.

## 11.2 Quantum well pumped VECSELs

In this section, the structures of QW pumped VECSELs for an emission wavelength of 850 nm are described, the layer structures of two different design are shown in Figs. 11.5 and 11.6. The QWs are directly pumped so close as possible to the emission wavelength in order to reduce heat generation. The absorption is enhanced by placing the QWs at the antinodes of the standing wave patterns for pump and laser beam simultaneously, this can be done by making the internal semiconductor cavity resonant for both the laser and the pump radiation. In addition, the semiconductor surface is placed at a node of the laser field to minimize resonator losses.

The DBR consists of 35 standard periodic  $\text{AlAs}/\text{Al}_{0.20}\text{Ga}_{0.80}\text{As}$  pairs. The first structure has a periodic gain structure constituted of 12 single QWs, while in the second design take place 7 double QWs. The QWs are 8 nm thick GaAs separated by  $\text{Al}_{0.30}\text{Ga}_{0.70}\text{As}$ . The internal resonator is completed by  $\text{TiO}_2/\text{SiO}_2/\text{TiO}_2$  dielectric coating for the devices

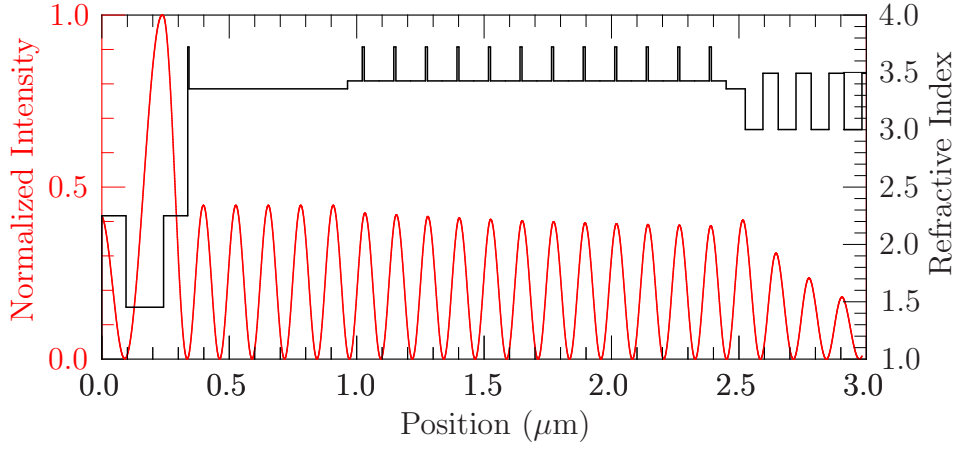


Figure 11.5: Device structure of a QW pumped VECSEL having 12 single GaAs QWs. The top side of the internal resonator is made of  $\text{TiO}_2/\text{SiO}_2/\text{TiO}_2$ .

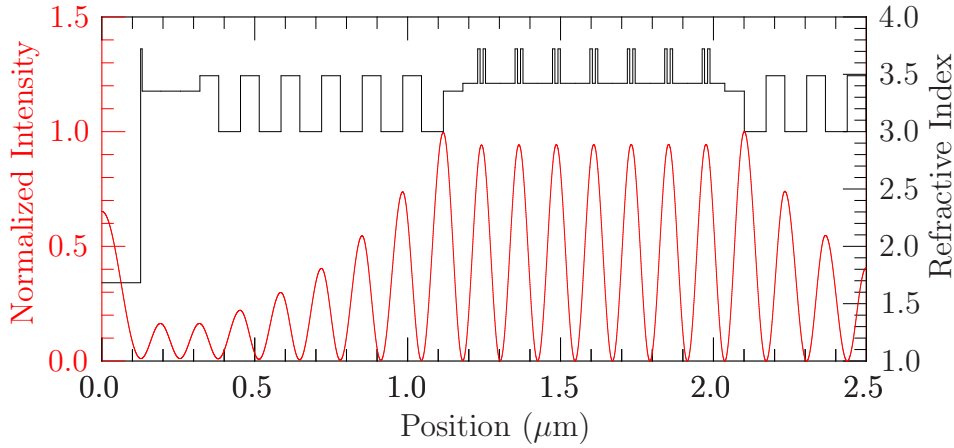


Figure 11.6: Device structure of a QW pumped VECSEL having 7 double GaAs QWs. The top side of the internal resonator is made of 6 pairs of  $\text{AlAs}/\text{Al}_{0.20}\text{Ga}_{0.80}\text{As}$ .

of Fig. 11.5 and by 6  $\text{AlAs}/\text{Al}_{0.20}\text{Ga}_{0.80}\text{As}$  pairs capped by  $\text{Al}_2\text{O}_3$   $\lambda/4$  layer for the devices of Fig. 11.6. As already seen for other devices, the structure are grown in inverted order to allow an efficient mounting on a heat sink. To characterize the devices a tunable Ti:sapphire laser is used as pump source, therefore, by changing the angle of the pump beam, the optimal resonant condition can be achieved for different pump wavelengths.

In Fig. 11.7 the output power of the first device type is plotted versus the absorbed pump power and different curves are plotted as function of the transmittivity  $T_m$  of the external mirror. A slope efficiency  $\eta_d$  of 66% is obtained for a transmittivity of 2% resulting in a output power of more than 0.7 W.

In Fig. 11.8 the same kind of plot is shown for the second design. Here a slope efficiency of 67% is reached at a transmittivity of 3.8%, this is a record value for semiconductor VECSELs. In the two figures one can also note that the differential quantum efficiency

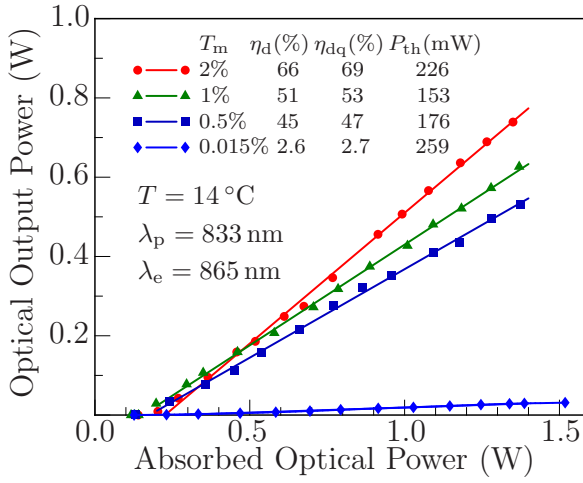


Figure 11.7: Laser output power versus the absorbed pump power for a device based on Fig. 11.5 design.

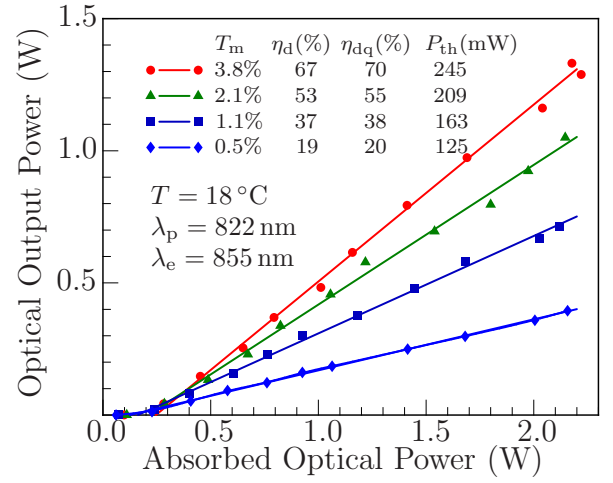


Figure 11.8: Laser output power versus the absorbed pump power for a device based on Fig. 11.6 design.

$\eta_{dq}$  is very close to  $\eta_d$  because of the small quantum defect typical of QW pumped devices.

Despite the performances of the two lasers seem to be similar, a great difference in absorption efficiency can be found. In fact in Figs. 11.7 and 11.8 the effectively absorbed pump power are considered, but just 45% of the incident pump power is absorbed by the first device in comparison to the 80% of the second one. This consideration makes the second design very interesting, in fact, by analyzing the absorption efficiency in function of the Ti:sapphire pump wavelength, one finds that the absorption band of the device has a FWHM (full width half maximum) of 4 nm. This result is attractive, because instead of the tunable small linewidth Ti:sapphire pump laser, one could use cheaper diode lasers with wider bandwidth.

In Fig. 11.9, the optical output power is plotted versus the net incident pump power for the second device, at a pump power of 3.2 W corresponds an output power of 1.6 W, so 50% optical to optical efficiency  $\eta_{opt}$  is reached. These measurements is taken with recycling of the pump beam, that means that the reflected pump beam is redirected again

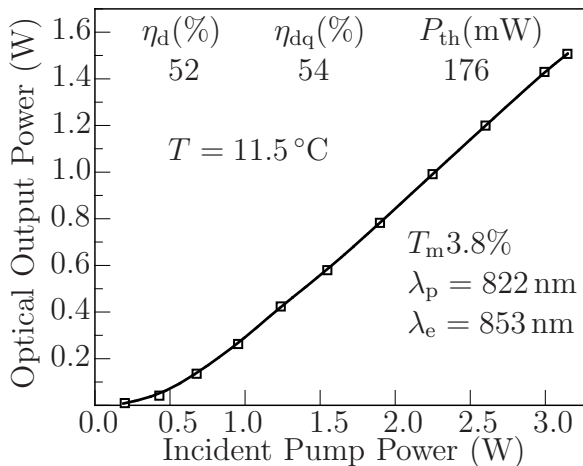


Figure 11.9: Output power versus incident pump power of the second device with simple reimaging of the pump power not absorbed in the first pass.

to the sample. Considering that the absorption efficiency is already as high as 80%, this brings just a small improvement in  $\eta_{\text{opt}}$ .

### 11.3 HRXRD on VECSELs, a special case

The power of HRXRD simulation can be applied also to analyze special situations. In Fig. 11.10, the HRXRD spectra of a QW pumped VECSEL laser structure is shown. The spectra do not fit the nominal structure and the satellites peaks relative to the periodic DBR, composed of 33 pairs of AlAs/ $\text{Al}_{0.20}\text{Ga}_{0.80}\text{As}$ , are splitted. Also the reflectivity spectrum shows a problem in the growth.

Flux measurements performed after the growth of the sample showed a decrease of the flux originating from one aluminum cell, this information is compatible to the fact that the cell was close to its exhaust time. One can try to model the decrease of the

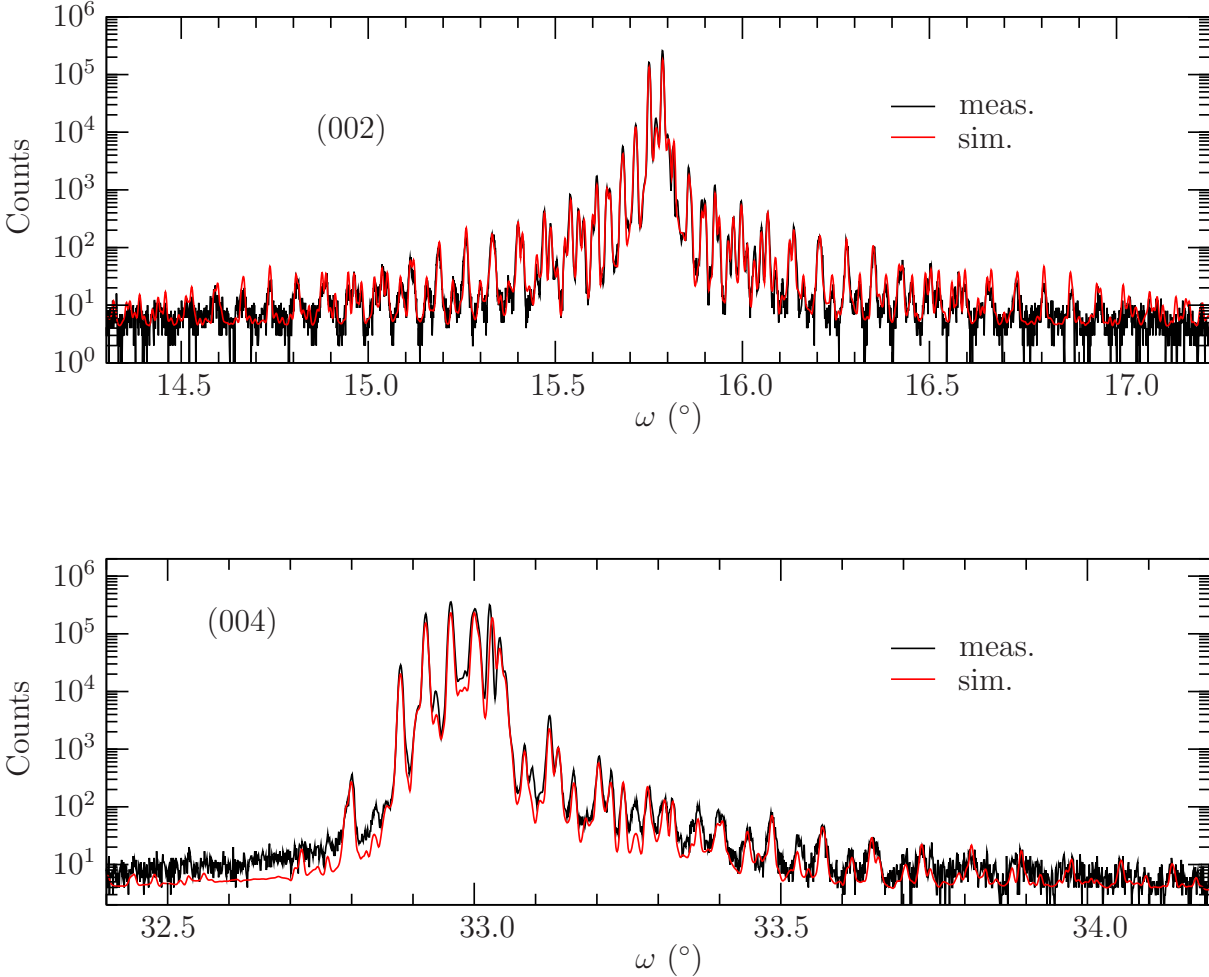


Figure 11.10: HRXRD spectra of a QW pumped VECSEL with 33 pairs periodic DBR, the flux from one of the used aluminum cell is fitted following the expression (11.1).



aluminum cell flux during the growth of the DBR by choosing the function

$$f(n) = f_0 \left( 1 - \frac{a_1}{1 + e^{(a_2 - n)/a_3}} \right), \quad (11.1)$$

where  $f(n)$  is the cell flux during the growth of the  $n$ -th DBR pair,  $f_0$  is the starting stable flux of the cell and  $a_1$ ,  $a_2$  and  $a_3$  are free parameters to be determined. There is no specific reason to use the functional form (11.1) for the cell flux, but this behavior is plausible for an aluminum cell. In fact, as already discussed in chapter 6, it is known that the exhaust of the aluminum source start with the depletion of the bottom part of the crucible, but the cell can still deliver a certain flux  $f_0(1 - a_1)$  due to the presence of aluminum migrated at the top of the cell, this is a clear indication that new material should be loaded.

In Fig. 11.10 the HRXRD spectra of the VECSEL are simulated including the depletion of the aluminum cell by varying the three parameters  $a_i$ . The fit agrees very well with the simulation and a plot of the aluminum flux in function of the DBR pair number is plotted in Fig. 11.11 for independent fits performed on the (002) and on the (004) reflections. The two curves are similar and both show a decrease of 25% of the flux during the time needed to grow few DBR pairs. Both simulations render for  $a_2$  a value close to 22, and for  $a_3$  1.0 and 1.5 is obtained for the (002) and (004) respectively. Considering that a pair is grown is 901 s, the decay time for aluminum flux can be estimated between 15 and 22 minutes. The fitted  $a_i$  parameter are obviously contingent on the particular effusion cell, but this can prove the fast decay of the flux of an exhausted aluminum cells, such behavior was often just partially observed during previous experiments.

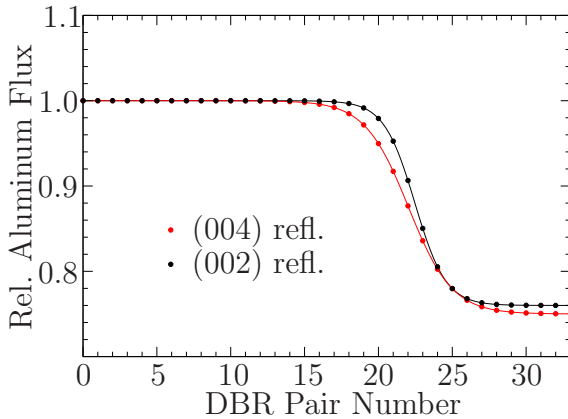


Figure 11.11: Relative aluminum flux originating from an effusion cell during the growth of a periodic DBR. The behavior is obtained by independent (002) and (004) HRXRD measurements. The aluminum cell is exhausted and new material should be loaded. A flux loss of approximately 25% can be observed.

# Chapter 12

## Conclusions

The purpose of this thesis is the MBE growth and characterization of multilayer structures for vertically emitting laser devices. In order to achieve this goal a patient experimental work was devoted to the samples characterization and to improve the growth processes. The knowledge of the growth recipes allows the simulations of HRXRD spectra restricting the use of free parameters to the ones that have a physical meaning, like the molecular fluxes originated from the effusion cells. The correct modeling of the growth process allows to extract reliable information about the samples also in complex situations, like shown in the study of the real compositional profile in VCSELs. The analysis of HRXRD improves the grown structures, because they are closer to the design values and permits the production of reliable devices after the processing. In this works many example of this strategy are given.

Hundreds of samples were grown for completely different classes of devices. In what follows the main results are summarized.

The design and growth of 760 nm emitting VCSEL structures, allowed the fabrication of devices with high performances, like multimode VCSELs with output power of 5.6 mW for devices with oxide aperture of  $8\text{ }\mu\text{m}$ . Single-mode devices with 420  $\mu\text{A}$  threshold and more than 1.9 mW output power were produced using the inverted relief technique. Moreover for 760 nm emission, polarization-stable single-mode power of 2.6 mW using the technique of the inverted grating relief were demonstrated. These devices are valid spectroscopic sources for oxygen sensing, thanks to a tunability of more than 7 nm on a temperature range between -70 and 100°C. Using these VCSELs, oxygen detection with a sensitivity as low as 16 ppm was performed, making possible not only the remote measurements of the oxygen concentration, but also measurements of gas temperature and pressure. Pressure measurements with 6% precision was demonstrated for pressure lower than 10 bar.

VCSELs exhibiting continuous laser emission at less than 720 nm were fabricated using the AlGaAs material system.

Single-mode emission of 6.3 mW was realized using the inverted relief technique for 850 nm VCSELs.

Monolithically integrated miniaturized transceiver chips including 850 nm VCSELs and a MSM photodiodes were fabricated. Bidirectional digital data transmission (full duplex mode) at 2.5 Gbit/s over 50 m graded-index multimode fiber was demonstrated.

Very high flip-chip VCSEL packing densities, enabling redundancy via three VCSELs

---

per channel together with simple intracell VCSEL monitoring, was reached achieving  $13.5\,\mu\text{m}$  center-to-center device pitches.

A new 980 nm bottom emitting VCSEL design was developed introducing a new active region containing two groups of 3 QWs, with and without GaAsP strain compensation. These devices can be used for high power applications, in fact  $4\times 4$  array of these VCSELs with  $49\,\mu\text{m}$  apertures resulted in more than 0.8 W output power. Single devices with an oxide aperture of  $134\,\mu\text{m}$  and 335 mW output power confirm the improvement in the design.

For the same wavelength, electrically pumped VECSELs showing more than 12 mW single-mode output power were fabricated. Thank to the presence of the external cavity, these devices are also suitable for frequency doubling.

The growth of optically pumped VECSELs, based on InGaAs QWs for 980 nm emission wavelength, were realized without and with strain compensation. Strain compensation, new mounting techniques, and new heat sinks provided a drastic improvement of the output power. HRXRD is the easy and direct tool to measure and characterize the strained layers together with the DBRs.

The growth of QW pumped VECSEL structures designed for an emission at 850 nm resulted in devices showing a slope efficiency of 67% and optical-to-optical efficiency of 50% at an output power of 1.6 W.

# Appendix A

## Publications

- I. Kardosh, F. Rinaldi, J. Hertkorn, and R. Michalzik, “Beam properties and  $M^2$  measurements of high-power VCSELs”, in Proc. *Semiconductor and Integrated Optoelectronics Conf., SIOE 2005*, paper 33. Cardiff, Wales, UK, March 2005.
- A. Kroner, F. Rinaldi, I. Kardosh, and R. Michalzik, “Towards ultra-compact optical tweezers without external optics”, in Proc. (CD ROM) *Conf. on Lasers and Electro-Optics Europe, CLEO/Europe 2005*, paper CL4-2-FRI, one page. Munich, Germany, June 2005.
- R. Michalzik, M. Stach, H. Roscher, F. Rinaldi, M. Riedl, and J.M. Ostermann, “Advanced short-wavelength vertical-cavity lasers and arrays for optical interconnection” (invited), in Proc. *The Fourth International Conf. on Optical Communications and Networks, ICOCN 2005*, pp. 116–119. Bangkok, Thailand, Dec. 2005.
- R. Michalzik, J.M. Ostermann, M. Riedl, F. Rinaldi, H. Roscher, and M. Stach, “Novel VCSEL designs for optical interconnect applications” (invited), in Proc. *The 10th Optoelectronics and Communications Conf., OECC 2005*, pp. 328–329. Seoul, Korea, July 2005.
- J.M. Ostermann, F. Rinaldi, P. Debernardi, and R. Michalzik, “VCSELs with enhanced single-mode power and stabilized polarization for oxygen sensing”, *IEEE Photon. Technol. Lett.*, vol. 17, pp. 2256–2258, 2005.
- F. Rinaldi, J.M. Ostermann, P. Debernardi, and R. Michalzik, “Single-mode and polarisation-stable inverted grating relief VCSELs for 760 nm oxygen sensing”, in Proc. *Semiconductor and Integrated Optoelectronics Conf., SIOE 2005*, paper 14. Cardiff, Wales, UK, March 2005.
- M. Stach, L. Stöferle, F. Rinaldi, and R. Michalzik, “Monolithically integrated optical transceiver chips at 850 nm wavelength consisting of VCSELs and MSM photodiodes” (invited), in Proc. (CD ROM) *Conf. on Lasers and Electro-Optics Europe, CLEO/Europe 2005*, paper CI2-4-THU, one page. Munich, Germany, June 2005.
- M. Stach, L. Stöferle, F. Rinaldi, and R. Michalzik, “3 Gbit/s data transmission with monolithically integrated optical transceiver chips for very short reach applications”,

- 
- in Proc. *31st Europ. Conf. on Opt. Commun., ECOC 2005*, vol. 3, pp. 529–530. Glasgow, Scotland, UK, Sept. 2005.
- S.-S. Beyertt, T. Kübler, U. Brauch, A. Giesen, E. Gerster, F. Rinaldi, and P. Unger, “Semiconductor thin-disk laser — Comparison of spacer and quantum-well pumping”, *20th Anniversary Meeting Advances Solid-State Photonics*. Vienna, Austria, Febr. 2005. Published in *OSA Trends in Optics and Photonics* vol. 98, em Advanced Solid-State Lasers ed. by C. Denman and I. T. Sorokina (Optical Society of America, Washington, DC 2005), pp. 294–298, 2005.
  - J. Wöllestein, M. Braun, S. Hartwig, A. Peter, A. Lambrecht, J.M. Ostermann, F. Rinaldi, and R. Michalzik, “Oxygen measurements by using a novel vertical-cavity surface-emitting laser” (in German: “Industrielle Sauerstoffmessung mit einem neuartigen oberflächenemittierenden Laser”), *tm – Technisches Messen*, vol. 72, pp. 440–448, 2005.
  - A. Gadallah, M. Stach, F. Rinaldi, S. Lorch, I. Kardosh, P. Gerlach, and R. Michalzik, “Fabrication and characterization of GaAs-based transceiver chips for bidirectional optical data transmission”, in Proc. *XXVI Conf. on Solid State Physics and Materials Science* of the Egyptian Materials Research Society, *Eg-MRS 2006 & Workshop on Nanostructures: Science, Fabrication, Characterization and Devices*, p. 128. Alexandria, Egypt, Sept. 2006.
  - A. Kroner, A. Gadallah, I. Kardosh, F. Rinaldi, and R. Michalzik, “Integrated VCSEL trap arrays for microfluidic particle separation and sorting”, in Proc. *EOS Topical Meeting on Biophotonics and Biomedical Optics*, pp. 140–141. Paris, France, Oct. 2006.
  - A. Kroner, J.F. May, I. Kardosh, F. Rinaldi, H. Roscher, and R. Michalzik, “Novel concepts of vertical-cavity laser-based optical traps for biomedical applications”, in *Biophotonics and New Therapy Frontiers*, R. Grzymala, O. Haeberlé (Eds.), Proc. SPIE 6191, pp. 619112–1–12, 2006.
  - A. Kroner, I. Kardosh, F. Rinaldi, and R. Michalzik, “Towards VCSEL-based integrated optical traps for biomedical applications”, *Electron. Lett.*, vol. 42, no. 2, pp. 93–94, 2006.
  - R. Michalzik, A. Kroner, J.M. Ostermann, M. Riedl, F. Rinaldi, H. Roscher, and M. Stach, “High-performance vertical-cavity laser diodes enabling new applications” (invited), in Proc. *Eighth International Conf. on Optoelectronics, Fiber Optics and Photonics, Photonics 2006*, vol. 2, p. 246. Hyderabad, India, Dec. 2006.
  - F. Rinaldi, J.M. Ostermann, A. Kroner, M.C. Riedl, and R. Michalzik, “760 nm high-performance VCSEL growth and characterization”, in *Micro-Optics, VCSELs, and Photonic Interconnects II: Fabrication, Packaging, and Integration*, H. Thienpont, M.R. Taghizadeh, P. Van Daele, J. Mohr (Eds.), Proc. SPIE 6185, pp. 61850X–1–7, 2006.

- W. Schwarz, I. Kardosh, F. Rinaldi, and R. Michalzik, “Cavity optimization of electrically pumped VECSELs”, in *Proc. Semiconductor and Integrated Optoelectronics Conf., SIOE 2006*, paper 40. Cardiff, Wales, UK, April 2006.
- M. Stach, F. Rinaldi, M. Chandran, S. Lorch, and R. Michalzik, “Monolithically integrated GaAs-based transceiver chips for bidirectional optical data transmission”, *Electron. Lett.*, vol. 42, no. 12, pp. 716–718, 2006.
- M. Stach, F. Rinaldi, M. Chandran, S. Lorch, and R. Michalzik, “Bidirectional optical interconnection at Gb/s data rates with monolithically integrated VCSEL–MSM transceiver chips,” *IEEE Photon. Technol. Lett.*, vol. 18, pp. 2386–2388, 2006.
- M. Stach, M. Chandran, F. Rinaldi, S. Lorch, I. Kardosh, H. Roscher, P. Gerlach, and R. Michalzik, “Monolithically integrated transceiver chips for bidirectional optical interconnection”, in *Micro-Optics, VCSELs, and Photonic Interconnects II: Fabrication, Packaging, and Integration*, H. Thienpont, M.R. Taghizadeh, P. Van Daele, J. Mohr (Eds.), *Proc. SPIE 6185*, pp. 61850Q-1–6, 2006.
- M. Stach, F. Rinaldi, M. Chandran, S. Lorch, and R. Michalzik, “Bidirectional optical data transmission over multimode fiber with monolithically integrated transceiver chips”, in *Proc. 7th International Conf. on Optical Technologies, Optical Sensors & Measuring Techniques, OPTO 2006*, pp. 99–102. Nürnberg, Germany, May/June 2006.
- M. Stach, F. Rinaldi, A. Gadallah, S. Lorch, I. Kardosh, P. Gerlach, and R. Michalzik, “1 Gbit/s bidirectional data transmission over 100 m graded-index glass optical fiber with monolithically integrated transceiver chips”, in *Proc. 32nd Europ. Conf. on Opt. Commun., ECOC 2006*, vol. 3, pp. 493–494. Cannes, France, Sept. 2006.
- M. Stach, F. Rinaldi, S. Lorch, and R. Michalzik, “Novel optoelectronic components for bidirectional optical Gbit/s computer networks” (in German: “Neuartige optoelektronische Komponenten für bidirektionale optische Gbit/s-Computernetzwerke”), in *Proc. 9th Workshop on Optics in Computing Technology, ORT 2006*, Siegen, Germany, Oct. 2006.
- M. Stach, F. Rinaldi, S. Lorch, and R. Michalzik, “Gbit/s-range bidirectional optical data transmission at 850 nm wavelength for automotive and in-house networks based on novel transceiver chips and PCS or graded-index glass fibers” (in German: “Bidirektionale optische Datenübertragung im Gbit/s-Bereich bei 850 nm Wellenlänge für Automotive- und Inhaus-Netze basierend auf neuartigen Transceiver-Bauelementen sowie PCS-Fasern oder Gradientenindex-Glasfasern”), *13th ITG Symposium on Communication Cable Networks*, Köln, Germany, Dec. 2006. In *ITG-Fachbericht Kommunikationskabelnetze*, vol. 197, pp. 163–166, 2006.
- J. Wöllenstein, M. Braun, H. Böttner, S. Hartwig, A. Lambrecht, A. Peter, J. Ostermann, F. Rinaldi, and R. Michalzik, “On oxygen spectroscopy using surface-emitting lasers”, (in German: “Zur Sauerstoffspektroskopie mit oberflächenemittierenden

- 
- Lasern”), in *Proc. Sensoren und Messsysteme 2006, 13. ITG-/GMA-Fachtagung*, pp. 503–506. Freiburg, Germany, Mar. 2006
- R. Michalzik, M. Stach, F. Rinaldi, and S. Lorch, ”Monolithic integration of VCSELs and MSM photodiodes for bidirectional multimode fiber communications” (*invited*), in *Vertical-Cavity Surface-Emitting Lasers XI*, K.D. Choquette, J.K. Guenter (Eds.), *Proc. SPIE* 6484, pp. 648409-1-10, 2007.
  - F. Rinaldi, J.M. Ostermann, A. Kroner, and R. Michalzik, ”High-performance AlGaAs-based VCSELs emitting in the 760 nm wavelength range”, *Optics Communications*, vol. 270, pp. 310-313, 2007.
  - A. Kroner, F. Rinaldi, J.M. Ostermann, and R. Michalzik, ”High-performance single fundamental mode AlGaAs VCSELs with mode-selective mirror reflectivities”, *Optics Communications*, vol. 270, pp. 332-335, 2007.
  - R. Michalzik, M. Stach, F. Rinaldi, and S. Lorch, ”Novel VCSEL-based transceiver chips for bidirectional optical interconnects using butt-coupled multimode fibers”, in *Proc. 5. ITG-Workshop Photonische Aufbau- und Verbindungstechnik*, pp. 33-37. Berlin, Germany, March 2007.
  - B. Scherer, J. Wlenstein, M. Weidemller, W. Salzmann, J.M. Ostermann, F. Rinaldi, and R. Michalzik, ”Oxygen measurements at high pressures using a low cost, polarization stabilized, widely tunable vertical-cavity surface-emitting laser”, in *Smart Sensors, Actuators, and MEMS III*, T. Becker, C. Can N.S. Barker (Eds.), *Proc. SPIE* 6589, pp. 658908-1-10, 2007.
  - M. Stach, F. Rinaldi, J. Scharpf, S. Lorch, and R. Michalzik, ”1 Gbit/s bidirectional optical data transmission over 50 m semi-GI PCS fiber with monolithically integrated transceiver chips”, in *Proc. EOS Conf. on Trends in Optoelectronics, Sub-conf. on Information and Communication*, pp. 61-62. Munich, Germany, June 2007.
  - H. Roscher, F. Rinaldi, A. Weigl, and R. Michalzik, ”Record-low thermal resistance, 12.5 Gbit/s capable flip-chip bonded 850 nm wavelength 2-D VCSEL arrays”, in *Proc. (CD ROM) Conf. on Lasers and Electro-Optics Europe, CLEO/Europe 2007*, paper CB4-4-TUE, one page. Munich, Germany, June 2007.
  - A. Kroner, F. Rinaldi, R. Rösch, and R. Michalzik, ”Densely packed VCSEL arrays tailored for optical particle manipulation”, in *Proc. (CD ROM) Conf. on Lasers and Electro-Optics Europe, CLEO/Europe 2007*, paper CB4-1-TUE, one page. Munich, Germany, June 2007.
  - S.-S. Beyertt, U. Brauch, F. Demaria, N. Dhidah, A. Giesen, T. Kübler, S. Lorch, F. Rinaldi, and P. Unger, ”Efficient Gallium-Arsenide Disk Lasers,” *IEEE Journal of Quantum Electronics*, vol. 43, no. 10, pp. 869–875, 2007.



- M. Stach, F. Rinaldi, D. Wahl, D. Rimpf, S. Lorch, and R. Michalzik, "1Gbit/s full-duplex bidirectional optical data transmission over 500 m of 50 m-core graded-index multimode fiber with novel monolithically integrated transceiver chips", *in Proc. 33rd Europ. Conf. on Opt. Commun.*, ECOC 2007, vol. 5, pp. 127-128. Berlin, Germany, Sept. 2007.
- H. Roscher, F. Rinaldi, and R. Michalzik, "Small-pitch flip-chip-bonded VCSEL arrays enabling transmitter redundancy and monitoring in 2-D 10-Gbit/s space-parallel fiber transmission", *IEEE J. Select. Topics Quantum Electron.*, vol. 13, pp. 1279-1289, 2007.
- M. Stach, F. Rinaldi, D. Wahl, D. Rimpf, S. Lorch, and R. Michalzik, "Monolithically integrated miniaturized transceiver chips for bidirectional graded-index fiber systems" (in German: "Monolithisch integrierte miniaturisierte Transceiver-Chips fr bidirektionale Gradientenindexfaser-Systeme"), *14th ITG Symposium on Communication Cable Networks, Köln, Germany, Dec. 2007. In ITG-Fachbericht Kommunikationskabelnetze*, vol. 204, pp. 115-119, 2007.
- A. Kroner, F. Rinaldi, R. Rösch, I. Kardosh, and R. Michalzik, "Towards a compact particle manipulation system based on arrays of vertical-cavity laser diodes", *Non-linear Microscopy and Optical Control*, NMOC 2008, Mnster, Germany, Feb. 2008, to be presented.



# Bibliography

- [1] R.A. Swalin, *Thermodynamics of solids*. New York: John Wiley & Sons, 1972.
- [2] A. Roth, *Vacuum Technology*. Amsterdam, Netherland: North-Holland publishing company, 1982.
- [3] J.F. O'Hanlon, *A User's Guide to Vacuum Technology*. New York: John Wiley & Sons, 1989.
- [4] W.L. Winterbottom and J.P. Hirth, "Diffusional contribution to the total flow from a Knudsen cell," *J. Chem. Phys.*, vol. 37, no. 4, pp. 784–793, 1962.
- [5] K. Motzfeldt, "The thermal decomposition of sodium carbonate by the effusion method," *J. Phys. Chem.*, vol. 59, pp. 139–147, 1955.
- [6] D.T.J. Hurle, "Revised calculation of point defect equilibria and non-stoichiometry in gallium arsenide," *J. Phys. Chem. Solids*, vol. 40, pp. 613–626, 1979.
- [7] C.T. Foxon, J.A. Harvey, and B.A. Joyce, "The evaporation of GaAs under equilibrium and non-equilibrium condition using a modulated beam technique," *J. Phys. Chem. Solids*, vol. 34, no. 10, pp. 1693–1701, 1973.
- [8] H.A.J. Oonk, *Phase Theory*, vol. 3. Amsterdam, Netherlands: Elsevier Scientific Publishing Company, 1981.
- [9] F.A. Kröger, *The Chemistry of Imperfect Crystals*, vol. 1. Amsterdam, Netherlands: North Holland Publishing Company, 1973.
- [10] P.S. Kop'ev and N.N. Ledentsov, "Molecular beam epitaxy of heterostructures made of III/V compounds," *Sov. Phys. Semicond.*, vol. 22, no. 10, pp. 1093–1101, 1988.
- [11] J.M. van Hove and P.I. Cohen, "Mass action control of AlGaAs and GaAs growth in molecular beam epitaxy," *Appl. Phys. Lett.*, vol. 47, no. 7, pp. 726–728, 1985.
- [12] S. Gonda and Y. Matsushima, "Molecular beam epitaxy of GaP and GaAsP," *Jap. J. Appl. Phys.*, vol. 15, no. 11, pp. 2093–2101, 1976.
- [13] L.D. Landau and E.M. Lifshitz, *Theory of Elasticity*, Pergamon press, 1986.
- [14] J.F. Nye, *Physical Properties of Crystals*, Oxford at the Clarendon press, 1967.

- [15] A. Ballato, "Poisson's ratio for tetragonal, hexagonal, and cubic crystals," *IEEE Transaction on Ultrasonics, ferroelectrics, and Frequency Control*, vol. 43, pp. 56–62, 1996.
- [16] I. Vurgaftman, J.R. Meyer, and L.R. Ram-Mohan, "Band parameters for III-V compound semiconductors abd their alloys," *Applied Physics Review*, vol. 89, no.11, pp. 5815–5875, 2001.
- [17] M. Ohring *Material science of thin films*, Academic Press, second edition, 2002.
- [18] <http://www.k-space.com/>
- [19] F.C. Frank and J.H. van der Merwe, "One-dimensional dislocations. I. Static theory," *Proceeding of the Royal Society*, vol. 198, no.1053, pp. 205–216, 1949.
- [20] J. Weertman and J.R. Weertman *Elemantary dislocation theory*, Oxford University Press, 1992.
- [21] J.W. Matthews and A.E. Blakeslee "Defects in epitaxial multilayers," *Journal of Crystal Growth*, vol. 27, pp. 118–125, 1974.
- [22] J.W. Matthews and A.E. Blakeslee "Defects in epitaxial multilayers II," *Journal of Crystal Growth*, vol. 29, pp. 273–280, 1975.
- [23] J.W. Matthews and A.E. Blakeslee "Defects in epitaxial multilayers III," *Journal of Crystal Growth*, vol. 32, pp. 265–273, 1976.
- [24] W.D. Nix "Mechanical Properties of Thin Films" *Metallurgical Transactions A*, vol. 20A, pp. 2217–2245, 1989.
- [25] E. Kasper and H.-J. Herzog, "Elastic strain and misfit dislocation density in  $\text{Si}_{0.92}\text{Ge}_{0.08}$  films on silicon substrates ," *Thin Solid Film*, vol. 44, pp. 357–370, 1977.
- [26] F. Demaria, *Schicht- und Resonator design von Halbleiterscheibenlasern*, Ph.D. thesis, University of Ulm, 2008.
- [27] J. Chilla, S. Butterworth, A. Zeitschel, J. Charles, A. Caprara, M. Reed, and L. Spinelli, "High power optically pumped semiconductor lasers," *Proc. SPIE*, vol. 5332, pp. 143–150, 2004.
- [28] S. Cho, G. Kim, J. Kim, K. Kim, S. Lee, J. Yoo, T. Kim, and Y. Park, "Compact and efficient green VECSEL based on novel optical end-pumping scheme', *IEEE Phot. Tech. Lett.*, vol. 19, no. 17, pp. 1325–1327, 2007.
- [29] S. Hilbich, W. Seelert, V. Ostroumov, C. Kannengiesser, R. v. Elm, J. Müller, and B. Lübeck, "New wavelengths in the yellow orange range between 545 nm to 580 nm generated by an intracavity frequency-doubled optically pumped semiconductor laser', *Proc. SPIE*, vol. 6451, pp. 64510C-1–7, 2007.

- 
- [30] E. Gerster, I. Ecker, S. Lorch, C. Hahn, S. Menzel, and P. Unger, "Orange-emitting frequency-doubled GaAsSb/GaAs semiconductor disk laser", *J. Appl. Phys.*, vol. 94, no. 12, pp. 7397–7401, 2003.
- [31] R.W. Boyd, *Nonlinear optics*, Academic Press, 1992.
- [32] D.A. Kleinman, "Nonlinear dielectric polarization in optical media", *Phys. Rev.*, vol. 126, no. 6, pp. 1977–1979, 1962.
- [33] N. Yamada, Y. Kanedo, S. Nakagawa, D.E. Mars, T. Takeuchi, and N. Mikoshiba, "Continuous-wave operation of a blue vertical-cavity surface-emitting laser based on second-harmonic generation", *Appl. Phys. Lett.*, vol. 68, no. 14, pp. 1895–1897, 1996.
- [34] R. Michalzik and K.J. Ebeling, "Operating principles of VCSELs," in *Vertical-Cavity Surface-Emitting Laser Devices*, edited by H. Li and K. Iga, Springer-Verlag, Berlin, pp. 53–98, 2003.
- [35] M. Kuznetsov, F. Hakimi, R. Sprague, and A. Moradian, "Design and characteristics of high-power ( $>0.5$ -W cw) diode-pumped vertical-external-cavity surface-emitting semiconductor lasers with circular TEM<sub>00</sub> beams," *IEEE J. Select. Topics Quantum Electron.* vol. 5, no. 3, pp. 561–573, 1999.
- [36] P. Unger, "Introduction to power diode lasers," in *High-power diode lasers, fundamentals, technology, applications*, edited by R. Diehl, Springer-Verlag, Heidelberg, 2000.
- [37] K.D. Choquette, K.M. Geib, H.C. Chui, B.E. Hammons, H.Q. Hou, T.J. Drummond, and R. Hull, "Selective oxidation of buried AlGaAs versus AlAs layers," *Appl. Phys. Lett.*, vol. 69, no. 10, pp. 1385–1387, 1996.
- [38] S.-S. Beyertt, U. Brauch, F. Demaria, N. Dhidah, A. Giesen, T. Kübler, S. Lorch, F. Rinaldi, and P. Unger, "Efficient Gallium-Arsenide Disk Lasers," *IEEE Journal of Quantum Electronics*, vol. 43, no. 10, pp. 869–875, 2007.
- [39] H.A. Macleod, *Thin-Film Optical Filters*, Bristol: Institute of Physics Publishing (IoP), 3. ed., 2001.
- [40] R. Michalzik, W. Schmid, S. Mahmoud, and R. Jäger, University Of Ulm, Institute of Optoelectronics.
- [41] L.G. Parratt, "Surface studies of solids by total reflection of X-rays", *Physical Review*, vol. 30, no. 4, pp. 359–369, 1954.
- [42] V. Holý, U. Pietsch, and T. Baumbach, *High-Resolution X-Ray Scattering from Thin Films and Multilayers*, Springer, 1999.
- [43] M. Tolan, *X-Ray Scattering from Soft-Matter Thin Films*, Springer, 1999.
- [44] P.F. Fewster, *X-Ray Scattering from Semiconductors*, Imperial College Press, 2000.

- [45] B.E. Warren, *X-Ray Diffraction*, Addison Wesley, 1969.
- [46] A. Authier, *Dynamical Theory of X-Ray Diffraction*, Oxford University Press, 2001.
- [47] E.E. Fullerton, I.K. Schuller, H. Vanderstraeten, and Y. Bruynseraede, “Structural refinement of superlattices from x-ray diffraction”, *Physical Review B*, vol. 45, no. 16, pp. 9292–9319, 1992.
- [48] LEPTOS V 4.02, Bruker AXS, 2006.
- [49] R. Heitz, T.R. Ramachandran, A. Kalburge, Q. Xie, I. Mukhametzhanov, P. Chen, and A. Madhukar, “Observation of reentrant 2D to 3D morphology transition in highly strained epitaxy: InAs in GaAs”, *Physical Review Letters*, vol. 78, no. 21, pp. 4071–4074, 1997.
- [50] F. Patella, F. Arciprete, M. Fanfoni, A. Balzarotti, and E. Placidi, “Apparent critical thickness versus temperature for InAs quantum dot growth on GaAs(001)”, *Applied Physics Letters*, vol. 88, 161903, 2006.
- [51] M.C. Riedl, Ph.D. thesis, University of Ulm, to be published.
- [52] I. Ecker, *Molekularstrahlepitaxie GaAs-basierender Mischungshalbleiter für 1300 nm-nahe Laserdiodenemission*, Ph.D. thesis, University of Ulm, 2004.
- [53] R. Jäger, *Molekularstrahlepitaxie hocheffizienter Leucht- und Laserdioden*. Ph.D. thesis, University of Ulm, 2002.
- [54] P.Y. Yu and M. Cardona, *Fundamentals of semiconductors*, Springer, 1996.
- [55] F.H. Pollak, “Energy gaps of AlGaAs,” in *Properties of aluminium gallium arsenide*, edited by S. Adachi, London:IEE, Inspec, 1993.
- [56] Y.P. Varshni, “Temperature dependence of the energy gap in semiconductors”, *Physica*, vol. 34, pp. 149–154, 1967.
- [57] J. Muszalski, “Pyrometric interferometry during MBE growth of laser heterostructures,” *Thin Solid Films*, vol. 367, pp. 299–301, 2000.
- [58] E.C. Larkins and J.S. Harris, Jr. “Molecular beam epitaxy of high-quality GaAs and AlGaAs,” in *Molecular beam epitaxy*, edited by R.F.C. Farrow, Noyes Publications, New Jersey, U.S.A., 1995.
- [59] L.J. van der Pauw, “A method of measuring specific resistivity and Hall effect of discs of arbitrary shape”, *Philips Research Report*, vol. 13, no. 1, pp. 1–9, 1958.
- [60] L.J. van der Pauw, “A method of measuring specific resistivity and Hall effect on lamellae of arbitrary shape”, *Philips Technical Review*, vol. 20, pp. 220–224, 1958.
- [61] C. Giannini, C. Gerardi, L. Tapfer, A. Fisher, and K.H. Ploog, “Carbon incorporation in GaAs and  $\text{Al}_x\text{Ga}_{1-x}\text{As}$  layers grown by molecular beam epitaxy,” *J. Appl. Phys.*, vol. 74, no. 1, pp. 77–81, 1993.

- 
- [62] C.R. Abernathy, S.J. Pearton, R. Caruso, F. Ren, and J. Kovalchik, “Ultrahigh doping of GaAs by carbon during metalorganic molecular beam epitaxy”, *Appl. Phys. Lett.*, vol. 55, no. 17, pp. 1750–1752, 1989.
- [63] D.M. Hoffman, B. Singh, and J.H. Thomas III, *Handbook of Vacuum Science and Technology*, Academic Press, 1998.
- [64] E.L. Ince, *Ordinary differential equations*, Dover Publications, 1956.
- [65] Balzers quadrupol mass spectrometer, operative manual.
- [66] R.P. Feynman, *The Feynman Lectures on Physics*, Addison-Wesley Publishing Company, 1963.
- [67] W. Braun, *Applied RHEED*, Springer-Verlag, 1999.
- [68] E.A. Wood, “Vocabulary of surface crystallography”, *Journal of applied physics*, vol. 35, no. 4, pp. 1306–1312, 1964.
- [69] A.J. Spring Thorpe, S.J. Ingre, B. Emmerstorfer, P. Mandeville, and W.T. Moore, “Summary abstract: Measurement of GaAs surface oxide desorption temperatures’, *J. Vac. Sci. Technol. B*, vol. 5, no. 3, pp. 739, 1987.
- [70] A.J. Spring Thorpe, S.J. Ingre, B. Emmerstorfer, P. Mandeville, and W.T. Moore, “Measurement of GaAs surface oxide desorption temperatures’, *Appl. Phys. Lett.*, vol. 50, no. 2, pp. 77–79, 1987.
- [71] H.H. Farrell and C.J. Palmström, “Reflection high energy electron diffraction characteristic absences in GaAs(100)(2×4)-As: A tool for determining the surface stoichiometry”, *J. Vac. Sci. Technol. B*, vol. 8, no. 4, pp. 903–907, 1990.
- [72] P. Vogel and V. Ebert, “Near shot noise detection of oxygen in the A-band with vertical-cavity surface-emitting lasers,’ *Appl. Phys. B*, vol. 72, pp. 127–135, 2001.
- [73] H.P. Zappe, M. Hess, M. Moser, R. Hövel, K. Gulden, H.P. Gauggel, and F. Monti di Sopra, “Narrow-linewidth vertical-cavity surface-emitting lasers for oxygen detection’, *Appl. Opt.*, vol. 39, no. 15, pp. 2475–2479, 2000.
- [74] T. Leinonen, J. Viheriälä, J. Lyytikäinen, P. Leinonen, M. Dumitrescu, and M. Pessa, “MBE-grown 760-nm VCSELs for oxygen sensing’, *Proc. CLEO/Europe 2005*, paper CB-15-MON, 2005.
- [75] H.-E. Shin, Y.-G. Ju, J.-H. Shin, J.-H. Ser, T. Kim, E.-K. Lee, I. Kim, and Y.-H. Lee, “780nm oxidised vertical-cavity surface-emitting lasers with Al<sub>0.11</sub>Ga<sub>0.89</sub>As quantum wells’, *Electron. Lett.*, vol. 32, no. 14, pp. 1287–1288, 1996.
- [76] N. Ueki, A. Sakamoto, T. Nakamura, H. Nakayama, J. Sakurai, H. Otoma, Y. Miyamoto, M. Yoshikawa, and M. Fuse, “Single-transverse-mode 3.4-mW emission of oxide-confined 780-nmVCSELs’, *Photonics Technology Letters, IEEE*, vol. 11, no. 12, pp. 1539–1541, 1999.

- [77] J. Gilor, I. Samid, and D. Fekete, "Threshold current density reduction of strained AlInGaAs quantum-well laser', *IEEE J. Quantum Electron.*, vol. 40, no. 10, pp. 1355–1364, 2004.
- [78] T.W. Schlereth, S. Gerhard, W. Kaiser, S. Höfling and A. Forchel, "High-performance Short wavelength ( $\sim 760$  nm) AlGaInAs quantum-dot lasers', *IEEE Phot. Tech. Lett.*, vol. 19, no. 18, pp. 1380–1382, 2007.
- [79] J.M. Ostermann, F. Rinaldi, P. Debernardi, and R. Michalzik, "VCSELs with enhanced single-mode power and stabilized polarization for oxygen sensing', *IEEE Photon. Technol. Lett.*, vol. 17, no. 11, pp. 2256–2258, 2005.
- [80] F. Rinaldi, J.M. Ostermann, A. Kroner, and R. Michalzik, "High-performance AlGaAs-based VCSELs emitting in the 760 nm wavelength range', *Optics Communications*, vol. 270, no. 2, pp. 310–313, 2006.
- [81] V. Weldon, J. O’Gorman, J.J. Pérez-Camacho, J. Hegarty, J.C. Connolly , and N.A. Morris, "Oxygen sensing using single-frequency DFB laser diodes at  $\lambda = 761$  nm', *Sensors and Actuators B*, vol. 42, pp. 163–168, 1997.
- [82] V. Weldon, J. O’Gorman, J.J. Pérez-Camacho, D. McDonald, J. Hegarty, J.C. Connolly , N.A. Morris, R.U. Martinelli, and J.H. Abeles, "Laser diode based oxygen sensing: A comparison of VCSEL and DFB laser diodes emitting in the 762 nm region', *Infrared Physics & Technology*, vol. 38, pp. 325–329, 1997.
- [83] V. Weldon, J. O’Gorman, J.J. Pérez-Camacho, and J. Hegarty, "Oxygen sensing using single frequency GaAs-AlGaAs DFB laser diodes and VCSELs', *Electronics Letters*, vol. 32, no. 3, pp. 219–221, 1996.
- [84] J. Wang, S.T. Sanders, J.B. Jeffries, and R.K. Hanson, "Oxygen measurements at high pressures with vertical cavity surface-emitting lasers', *Applied Physics B*, vol. 72, pp. 865–872, 2001.
- [85] <http://cfa-www.harvard.edu/hitran/>
- [86] B.H. Bransden and C.J. Joachain, *Physics of Atoms and Molecules*, Longman Scientific & Technical, 1983.
- [87] L.R. Brown and C. Plymate, "Experimental line parameters of the oxygen A band 760 nm', *Journal of Molecular Spectroscopy*, vol. 199, pp. 166–179, 2000.
- [88] B. Scherer, J. Wöllenstein, M. Weidemüller, W. Salzmänn, J.M. Ostermann, F. Rinaldi, and R. Michalzik, "Oxygen measurements at high pressures using a low-cost polarisation-stabilized widely tunable vertical-cavity surface-emitting laser', *Proc. SPIE*, vol. 6589, 2007
- [89] B. Scherer, J. Wöllenstein, M. Weidemüller, W. Salzmänn, J.M. Ostermann, F. Rinaldi, and R. Michalzik, "Measurement of the pressure broadening coefficients of



- the oxygen A-band using a low cost, polarization stabilized, widely tunable vertical-cavity surface-emitting laser', *Microsyst. Technol.*, DOI:10.1007/s00542-007-0440-z, 2007
- [90] J. Wöllestein, M. Braun, S. Hartwig, A. Lambrecht, A. Peter, J.M. Ostermann, F. Rinaldi, and R. Michalzik, "Industrielle Sauerstoffmessung mit einem neuartigen oberflächenemittierenden Laser', *Technisches Messen*, vol. 72, no. 7–8, pp. 440–448, 2005.
  - [91] A. Kroner, F. Rinaldi, J.M. Ostermann, and R. Michalzik, "High-performance single fundamental mode AlGaAs VCSELs with mode-selective mirror reflectivities," *Optics Communications*, vol. 270, no. 2, pp. 332–335, 2007.
  - [92] Å. Haglund, J.S. Gustavsson, J. Vukusic, P. Modh, and A. Larsson, "Single fundamental mode output power exceeding 6 mW from VCSELs with a shallow surface relief," *IEEE Photon. Technol. Lett.*, vol. 16, no. 2, pp. 368–370, 2004.
  - [93] A. Kroner, F. Rinaldi, R. Rösch, and R. Michalzik, "Novel concepts of vertical-cavity laser-based optical traps for biomedical applications," in *Biophotonics and New Therapy Frontiers*, R. Grzymala, O. Haeberlé (Eds.), Proc. SPIE 6191, pp. 619112 1–12, 2006.
  - [94] M. Stach, F. Rinaldi, D. Wahl, D. Rimpf, S. Lorch, and R. Michalzik, "Monolithically integrated miniaturized transceiver chips for bidirectional graded-index fiber systems" (in German: "Monolithisch integrierte miniaturisierte Transceiver-Chips für bidirektionale Gradientenindexfaser-Systeme"), *14th ITG Symposium on Communication Cable Networks, Köln, Germany, Dec. 2007. In ITG-Fachbericht Kommunikationskabelnetze*, vol. 204, pp. 115–119, 2007.
  - [95] M. Stach, F. Rinaldi, M. Chandran, S. Lorch, and R. Michalzik, "Bidirectional optical interconnection at Gb/s data rates with monolithically integrated VCSEL-MSM transceiver chips', *IEEE Photon. Technol. Lett.*, vol. 18, pp. 2386–2388, 2006.
  - [96] H. Roscher, F. Rinaldi, and R. Michalzik, "Small-pitch flip-chip-bonded VCSEL arrays enabling transmitter redundancy and monitoring in 2-D 10-Gbit/s space-parallel fiber transmission', *IEEE J. Select. Topics Quantum Electron.*, vol. 13, pp. 1279–1289, 2007.
  - [97] H. Roscher, F. Rinaldi, A. Weigl, and R. Michalzik, "Record-low thermal resistance, 12.5 Gbit/s capable flip-chip bonded 850 nm wavelength 2-D VCSEL arrays', in *Proc. (CD ROM) Conf. on Lasers and Electro-Optics Europe, CLEO/Europe 2007*, paper CB4-4-TUE, one page. Munich, Germany, June 2007.
  - [98] S.G. Patterson, G.S. Petrich, R.J. Ram, and L.A. Kolodziejski, "X-ray diffraction analysis of bandgap-engineered distributed Bragg reflectors', *Journal of Electronic Materials*, vol. 28, no. 10, pp. 1081–1083, 1999.
  - [99] P. Kidd, "Investigation of the precision in x-ray diffraction analysis of VCSEL structures', *Jour. of Mat. Science: Materials in Electronics*, vol. 14, pp. 541–550, 2003



- [100] I. Kardosh, Ph.D. thesis, University of Ulm, to be published.
- [101] E. Gerster, *Optisch gepumpte Halbleiter-Scheibenlaser in den Materialsystemen In-GaAs/GaAs und GaAsSb/GaAs*, Ph.D. thesis, University of Ulm, 2005.

# Curriculum Vitae

## Personal Data

Name: Fernando Rinaldi  
Birthdate/birthplace: 6th November 1973/ Catanzaro, Italy  
Nationality: Italian

## Education

09/1978–06/1983 Scuola Elementare Statale, Decollatura, Italy  
09/1983–06/1986 Scuola Media Statale, Decollatura, Italy  
09/1986–06/1991 Liceo Scientifico Statale, Decollatura, Italy  
10/1991–09/1998 Academic studies in Physics ,  
University 'La Sapienza' Roma, Italy  
01/2002–02/2008 Research at the Institute of Optoelectronics,  
University of Ulm, Germany

## Scientific Experience

10/1997–11/1997 Research work at the VUV SUPERLUMI beamline  
at the DESY synchrotron, Hamburg  
10/1999–04/2001 Research work on x-ray diffraction,  
at the ENEA laboratories, Frascati, Italy  
04/2001–12/2001 Training and mobility of researcher (TMR) project  
on Si-Ge by DaimlerChrysler, Ulm, Germany

Ulm, 23rd. January 2008